Internal variability of the thermohaline ocean circulation

Lianke te Raa

Cover: Texel, sunset over the North Sea (photograph by G. A. te Raa)

ISBN 90-393-3345-9

Internal variability of the thermohaline ocean circulation

Interne variabiliteit van de thermohaliene oceaancirculatie

(met een samenvatting in het Nederlands)

PROEFSCHRIFT

ter verkrijging van de graad van doctor aan de Universiteit Utrecht
op gezag van de Rector Magnificus, Prof. dr. W. H. Gispen,
ingevolge het besluit van het College voor Promoties
in het openbaar te verdedigen op

woensdag 21 mei 2003 des ochtends om 10.30 uur

door

Lianke Alinda te Raa

geboren op 26 juni 1975 te Eindhoven

Promotoren: **Prof. dr. ir. H. A. Dijkstra**
Prof. dr. W. P. M. de Ruijter
Instituut voor Marien en Atmosferisch onderzoek Utrecht (IMAU),
Faculteit Natuur- en Sterrenkunde, Universiteit Utrecht

Dit proefschrift werd mede mogelijk gemaakt door financiële steun van de Nederlandse organisatie voor Wetenschappelijk Onderzoek (NWO).

Contents

Chapter 1

Introduction

1.1 Climate variability

Climate affects our daily lives in many ways and is of great importance to society, although we might usually not even realize it. Not only is the general weather and natural vegetation determined by the local climate, but also the global agricultural productivity is adjusted to and optimized for present climatic conditions. The safety of many people living in low-lying countries like the Netherlands is closely connected to the sea-level height, which is strongly influenced by climate. Changes in climate may therefore have not only ecological, but also large economical and social consequences. This realization has been strengthened by the current concern about the anthropogenic (human-induced) climate change. To predict future changes in climate, necessary for the development of policy, knowledge and understanding of anthropogenic as well as natural climate variability is needed (National Research Council, 1995).

It has been well established that the climate system exhibits (natural) variability on a multitude of time scales, ranging from a few years to several hundreds of thousands of years. This is illustrated schematically in the 'artist's impression' of a climate spectrum, shown in Fig. 1.1. One of the most well-known climate variations on relatively short time scales is the so-called El Niño phenomenon, which is associated with anomalous warming of the equatorial Pacific near the coast of Peru every 3 to 4 years. El Niño is part of an oscillation of the equatorial coupled ocean-atmosphere system called the El Niño-Southern Oscillation (ENSO). The effects of ENSO can now sometimes be predicted already a few months in advance. On the other hand, an example of climate variability on a very long time scale is formed by the glacial cycles, which have occurred during the last two million years and involve rather dramatic changes between warm interglacial periods and the much colder ice ages.

At the moment, climate variability on decadal (say 10–15 yr), interdecadal (say 20–85 yr), and centennial (say 150–850 yr) time scales is receiving a lot of attention. Increased emissions of CO_2 and other greenhouse gases are expected to lead to an increase in the globally averaged surface temperature of 1.4 °C to 5.8 °C over the period 1990 to 2100 (IPCC, 2001). Considerable anthropogenic climate changes are thus expected on time scales of decades to

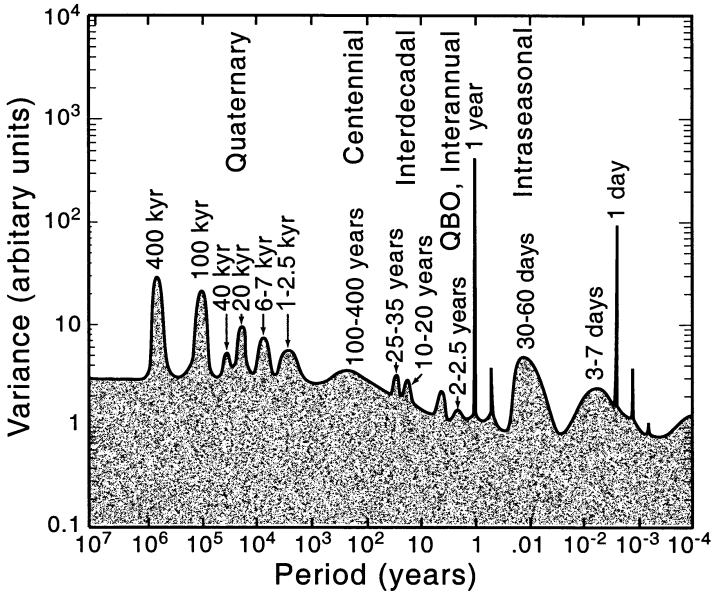

Figure 1.1: *An 'artist's rendering' of the composite power spectrum of climate variability showing the amount of variance in each frequency range (from Ghil (2002)).*

centuries. In order to reduce the uncertainty in these estimated climate changes, accurate predictions of natural climate variability at these time scales are necessary.

A wealth of information on the past climate can be found in the earth's natural archives, in the form of proxy records. Climate proxy data are records of climate-dependent natural phenomena (e.g. tree-ring thickness), providing an indirect measure (Bradley, 1999) of a certain climate variable (e.g. local surface temperature). Variability at interdecadal as well as centennial time scales has, for instance, been found in the oxygen-isotope ($\delta\,^{18}$O) records derived from ice cores, tree-ring index series, pollen records and sea-ice extent (Stocker and Mysak, 1992). Mann *et al.* (1995) find variability on a 15–35 yr, as well as on a 50–150 yr time scale in a study of several proxy data. Hibler and Johnson (1979) report variability with a 20-yr period in δ^{18}O records from Greenland ice cores. In a study of two $\delta\,^{18}$O-records from Arctic ice cores from locations 600 km apart, Fisher (1982) found spectral peaks at periods of 625, 417, 330 and 185 years, as well as at 2500 years, that could not be attributed to local effects. A high-resolution oxygen-isotope record from a stalagmite from Ireland reveals multicentury variability with peaks around 625 yr, 170 yr and 80 yr (McDermott *et al.*, 2001). Tree-ring data show that it has been relatively warm during the Middle Ages (Bradley, 1999) and that temperatures decreased in the centuries that followed. The latter gave rise to a relatively cold period called the Little Ice Age (Grove, 1988), which lasted roughly from 1500 to 1850.

The longest instrumental record, the 335-yr time series of Central England Temperatures (Plaut *et al.*, 1995), is still far too short to extract information about variability at centennial

time scales from it. However, the instrumental record does provide ample evidence of decadal and interdecadal climate variability. Variability with a period of about 14 years has been found in Atlantic sea-surface temperature (SST) data (Sutton and Allen, 1997; Moron *et al.*, 1998) and seems to be associated with propagating anomalies in the Gulf Stream region. Evidence for variability at time scales of about 15 and 25 years has been found in surface air temperatures (Plaut *et al.*, 1995). Also in records of global air temperature (Ghil and Vautard, 1991), a signal with a period of about 15 years has been identified.

Multidecadal variations in North-Atlantic SST, sea-level pressure (SLP) and surface winds were found by Kushnir (1994), who analyzed more than 100 years of data from the Comprehensive Ocean-Atmosphere Data Set (COADS). Negative SST anomalies prevailed from about 1900 to 1920 and from about 1970 to 1980, whereas the 1930–1960 period was characterized by warm anomalies. Associated with these temporal SST changes is a basin-scale spatial pattern with maxima in the Labrador Sea and northeast of Bermuda. This analysis was extended by Tourre *et al.* (1999) through the use of a longer instrumental data set based on the Kaplan *et al.* (1998) statistical reanalysis of SLP and SST data in the Atlantic back to 1856. A spectral peak around a period of 50–60 years was located in the data fields, although it was not clearly resolvable from the secular variance. The spatial SST and SLP patterns associated with this peak are shown in Fig. 1.2. At a certain phase (indicated as phase $0\,^\circ$ in Fig. 1.2) positive SST anomalies are found in the central North Atlantic. The SLP anomalies are positive in the subtropical North Atlantic and negative at higher latitudes, corresponding to enhanced westerlies. The region of positive SST anomalies expands (phase $90\,^\circ$) and the area with the maximum amplitudes shifts to the northwest. In this phase, negative SLP anomalies occur over most of the basin.

In a spatio-temporal analysis of the global SST record for the 20th century, multidecadal SST changes were also found by Moron *et al.* (1998). An increase in global SSTs in the early part of the 20th century started in the subpolar North Atlantic. Although North-Atlantic SSTs have decreased since the early 1970s, the globally averaged SST has increased over the past few decades. An analysis of the change in heat content over the upper 300 m for the Atlantic (Levitus *et al.*, 2000) also demonstrates a warming trend of the upper ocean since 1950.

Before being able to make accurate predictions about possible future interdecadal or centennial climate changes, we will have to know the causes of the natural climate variability at these time scales. In general, climate variability can be caused by external factors or generated internally in the climate system. The climate system consists of various subsystems, of which the oceans, the atmosphere and the cryosphere (all the ice near the earth's surface) are the most important for (inter)decadal and centennial climate variability. An external cause of climate variability is the variation of the earth's orbital parameters on time scales of 20 kyr (1 kyr=10^3 yr), 40 kyr and 400 kyr (Berger, 1978). The resulting changes in solar irradiance on these time scales are associated with the occurrence of the ice ages (Imbrie and Imbrie, 1980). Also on interdecadal time scales periodic variations in solar irradiance have been proposed to cause climate changes (Lean and Rind, 1998). However, the actual strength of fluctuations in solar forcing is still controversial and statistically significant relationships between climate proxy data and solar irradiance are often hard to establish (Stuiver, 1980; Stocker and Mysak, 1992).

Internal climate variability arises from interactions within and between the different climate subsystems. Abrupt reorganizations of the climate system have been proposed to cause

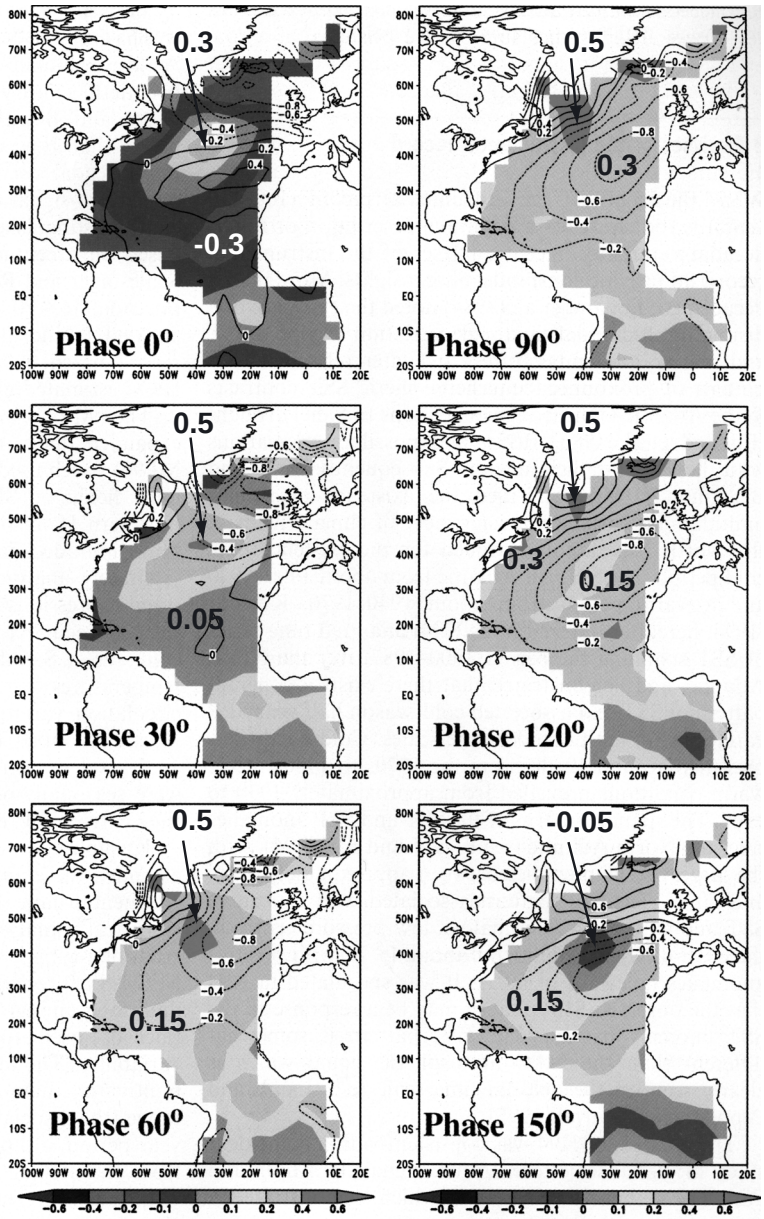

Figure 1.2: *Reconstruction of the multidecadal signal in SST and SLP in the Kaplan* et al. *(1998) data set. The shading and bold numbers denote SST (units are °C), while the contours depict SLP (units are hPa). Each panel is separated in time by approximately 4.3 years (adapted from Delworth and Mann (2000), original figure in color).*

rapid climate changes. These reorganizations can be interpreted as sudden changes between (quasi-)equilibrium states due to a small change in a parameter. An example is the sudden onset of the Younger Dryas, the cold period during which almost glacial conditions returned, around $11,000$ yr BP. Such abrupt changes are hard to predict, as they depend rather sensitively on small changes in parameters.

A standard explanation of interannual to decadal climate variability is that high-frequency variations in the atmosphere are 'integrated' by the slower reacting ocean, leading to low-frequency variability (Hasselmann, 1976). In this mechanism, only the atmosphere plays an active role and the ocean responds passively. However, variability caused by this mechanism does not have a preferred time scale nor a preferred pattern, as is the case for the observed interdecadal and centennial variability. Therefore, the Hasselmann mechanism cannot fully explain the variability at these time scales.

The existence of preferred time scales and preferred spatial patterns in observations indicates that internal modes of variability are likely to be involved. These could be internal modes within one climate subsystem, as well as coupled modes involving two or more subsystems (in this thesis, the words 'coupled mode' are used only to indicate a mode in which two subsystems are both actively involved, i.e. if there is a 'two-way' interaction). As variations in the oceans, and in particular in the ocean circulation, occur on time scales of months to thousands of years, internal variability of the ocean is likely to be crucial for our understanding of climate variability on time scales of several decades to centuries. Because of its large thermal inertia, the ocean can act as a vast reservoir of heat, thereby damping the relatively fast fluctuations in atmospheric temperature. Moreover, as the (large-scale) ocean circulation contributes significantly to the total meridional heat transport of the combined ocean-atmosphere system, variability in the ocean circulation can induce significant climate variability.

1.2 The large-scale ocean circulation

The large-scale ocean circulation is driven by wind-stress forcing at the surface and by fluxes of heat and freshwater at the ocean-atmosphere interface. Horizontal currents, which are mainly driven by the wind stress, dominate the near-surface circulation, whereas the much slower motions of the deep ocean are largely driven by the surface buoyancy flux. A classical picture of the near-surface circulation is shown in Fig. 1.3. In all oceans, the circulation in both the northern and southern hemisphere is characterized by basin-wide cells, the so-called gyres. These gyres have intense western boundary currents and slower, more diffuse eastern boundary currents. In the North Atlantic and the North Pacific there is a strong anti-cyclonic subtropical gyre and a weaker subpolar gyre, with an eastward flowing jet between the two gyres. The western boundary current in the North-Atlantic Ocean, the Gulf Stream, transports about 150 Sv (1 Sv $\equiv 10^6$ m^{3}s^{-1}) of water northward at 60°W (Johns *et al.*, 1995). Other important features of the large-scale surface circulation are the equatorial current system, with the eastward Equatorial Countercurrent between westward equatorial currents in both the Atlantic and the Pacific Oceans, and the eastward Antarctic Circumpolar Current (ACC).

The fluxes of heat and freshwater at the ocean surface give rise to large-scale gradients of temperature and salinity, which produce density gradients both in horizontal and vertical

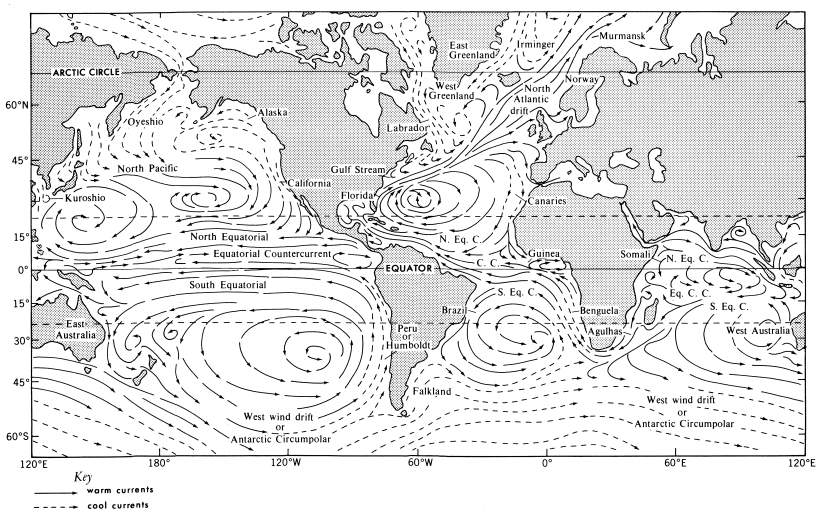

Figure 1.3: *Schematic diagram of the global ocean's near-surface circulation (from Peixoto and Oort (1992)).*

direction. The circulation driven by the resulting pressure gradients is called the thermohaline circulation (THC), or overturning circulation. The net heat flux at the ocean-atmosphere interface is the difference between incoming solar radiation and outgoing longwave radiation, latent heat and sensible heat. The total downward annual-mean heat flux into the ocean is plotted in Fig. 1.4. Near the equator, the ocean gains heat from the atmosphere, whereas

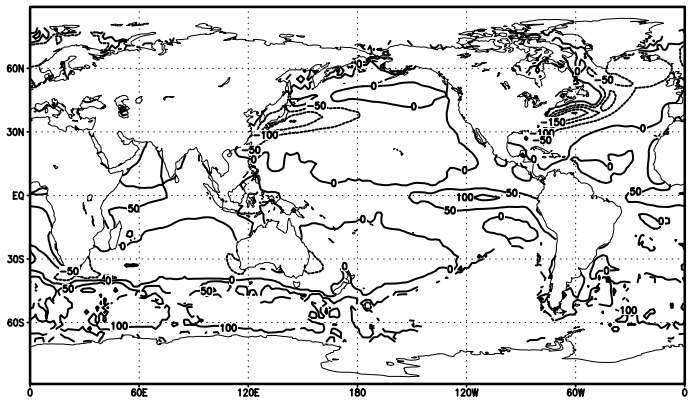

Figure 1.4: *Net downward annual-mean heat flux (in W m^{-2}) into the ocean, obtained from the Oberhuber (1988) data set.*

at higher latitudes the ocean loses heat. The strongest heat loss takes place in the region of the western boundary currents. The freshwater flux is the net result of evaporation minus

precipitation and continental run-off. The subtropics are dominated by evaporative freshwater loss (Fig. 1.5), whereas in the tropics and at high latitudes precipitation causes net freshwater gain.

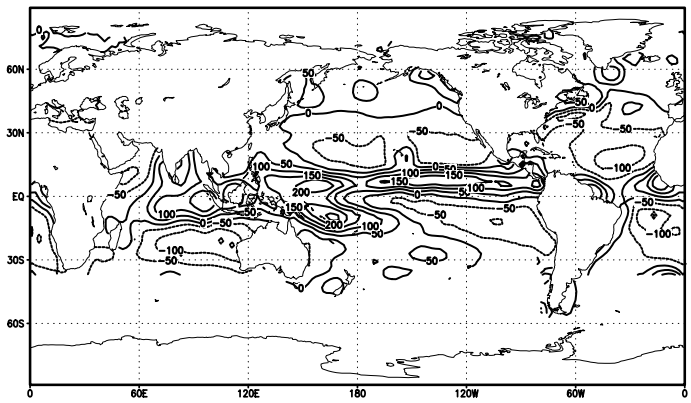

Figure 1.5: *Downward annual-mean freshwater flux into the ocean (in mm/month), obtained from Oberhuber (1988).*

The North Atlantic is a central area for the global thermohaline circulation. Here, intense cooling of the relatively saline surface water, which is transported northward by the Gulf Stream, causes the water column to become unstably stratified. At certain locations in the northern North-Atlantic Ocean, mainly in the Labrador Sea and in the Greenland Sea, this results in deep convection. Mixing of the surface water with deeper water produces the relatively dense North Atlantic Deep Water (NADW). This water mass is transported southward at depths between roughly 2 and 4 km in a deep western boundary current. Most of the NADW crosses the equator and flows over the even denser Antarctic Bottom Water (AABW). The AABW is formed at a few locations around Antarctica and fills the deepest parts of all ocean basins.

Together, the wind-driven and thermohaline circulation form a complex three-dimensional circulation involving surface and deep currents in all ocean basins, which has been named the 'ocean conveyor' (Gordon, 1986; Broecker, 1991). A schematic plot of the global ocean circulation is shown in Fig. 1.6, where the vertical structure of the flow has been simplified by dividing the flow into surface and deep currents. The NADW crosses the equator in the Atlantic, joins the ACC and enters the Indian and the Pacific Oceans. Here, it slowly mixes with the surrounding waters, becomes lighter and finally returns to the formation region in the North Atlantic via the surface-current system.

Variability of the wind-driven ocean circulation is associated with adjustment of surface currents and occurs on time scales of months to decades. Internal variability of the thermohaline ocean circulation has much larger time scales, of the order of decades to millennia. Internal thermohaline variability is therefore a likely candidate to be involved in climate variability at interdecadal to centennial time scales.

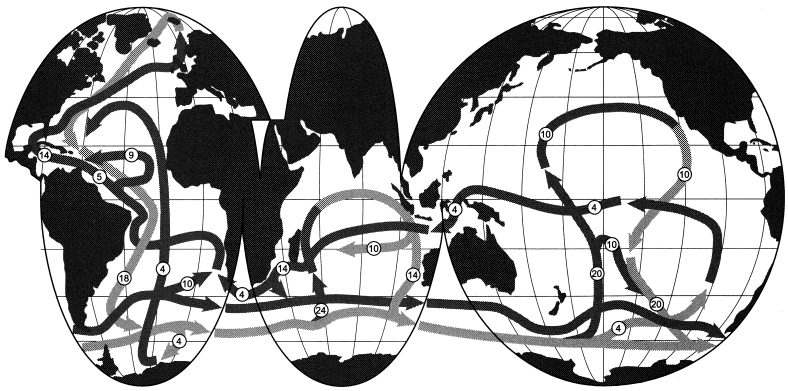

Figure 1.6: *Sketch of the global ocean circulation as a 'conveyor belt'. Dark (light) shaded paths indicate flow in the surface (deep) ocean. Numbers indicate volume transport in Sverdrups. This figure is based on Schmitz (1995), but taken from Bradley (1999).*

1.3 Internal thermohaline variability

Indications for (inter)decadal thermohaline variability have for instance been found in measurements of the overflow from the Nordic Seas (Dickson and Brown, 1994), convective activity (Schlösser *et al.*, 1991), repeated ship measurements (Bryden *et al.*, 1996), and ocean weather stations (Sy *et al.*, 1997; Joyce and Robbins, 1996). However, direct measurements of the circulation away from the coast and outside main shipping routes are still hardly performed on a regular basis. Moreover, on time scales longer than several decades, only very few subsurface observations are available and also the number of SST observations is rather limited. Future developments in the retrieval of proxy data will hopefully increase the number of sufficiently long high-resolution proxy records substantially. However, the exact reconstruction of climate variables from proxy data will remain problematic and the spatial coverage of the proxy records poor. The sparseness of the oceanographic data set causes large uncertainties in time scales and spatial patterns of observed (thermohaline) ocean variability.

Consequently, the physical mechanisms underlying the variability cannot be understood from the observational record only. Moreover, it is also not possible to test the causal relations that are involved in a laboratory experiment. Therefore, numerical models are essential to simulate the climate system and to investigate the physical mechanism(s) causing the variability. These models simulate the various components of the climate system, by solving numerically the evolution equations that describe the behavior of the system. Internal variability of the thermohaline circulation has been investigated in a hierarchy of models. Starting at the top, with the most complex models, this hierarchy includes:

(i) Low-resolution coupled general circulation models (CGCMs) of the ocean-atmosphere-sea-ice system (e.g. Delworth *et al.* (1993)), in which many physical processes are represented, although some, such as sub-grid scale mixing, are highly parameterized.

(ii) Low-resolution ocean-only GCMs, which are forced by a prescribed wind-stress pattern and fluxes of heat and freshwater at the ocean surface (e.g. Chen and Ghil (1995)). The forcing functions are a schematic representation of the influence of the atmosphere on the ocean. Usually the forcing is either steady (time-independent), to represent the time-averaged atmospheric conditions, or consists of a steady part with a stochastic (random) component added to it, so that also the effect of high-frequency atmospheric fluctuations is represented.

(iii) Planetary geostrophic ocean-only models, in which inertial terms have been neglected in order to filter out the relatively fast inertia-gravity waves and dispersive Rossby waves. This makes the numerical computations more efficient and gives a good representation of the interior ocean circulation (e.g. Colin de Verdière (1988)).

(iv) Strongly simplified models. Among these are strictly two-dimensional and zonally averaged ocean models, in which the effects of wind forcing and rotation are ignored or parameterized, respectively (e.g. Wright and Stocker (1992); Dijkstra and Molemaker (1997)). The simplest models in which thermohaline variability can be represented are the conceptual box models, in which the ocean is represented by two or more well-mixed boxes that exchange properties through a density-driven transport (e.g. Stommel (1961); Welander (1982)).

A further subdivision within each of these levels can be made in terms of the model configuration that is used, for instance, whether or not bottom topography is included in an ocean-only GCM. A large number of modeling studies has been performed to investigate internal variability of the thermohaline circulation with each of these types of models. In these studies, many physical mechanisms have been proposed that could possibly explain (inter)decadal and centennial climate variability. In some cases, the variability was self-sustained, whereas in others it could be excited by stochastic components in the forcing.

In a 600-yr long integration of the coupled Geophysical Fluid Dynamics Laboratory (GFDL) Modular Ocean Model (MOM), interdecadal variability with an average period of about 50 years was found and analyzed by Delworth *et al.* (1993) and Delworth and Greatbatch (2000). In Fig. 1.7a, the spectrum of the first 200 years of the THC-index time series from the study in Delworth *et al.* (1993) is shown. This THC-index is defined as the maximum of the annual-mean meridional overturning (the volume transport in the meridional-vertical plane). Enhanced variability is visible in a broad band around a period of 50 years. The spatial pattern of SST change associated with fluctuations in the thermohaline circulation (Fig. 1.7b) shows two maxima of opposite sign in the western and central North Atlantic and is in quite good agreement with variability observed by Kushnir (1994).

The study of Delworth and Greatbatch (2000) shows that the atmosphere seems merely to respond to the oceanic variability, but has no active role in the modeled variability. Delworth *et al.* (1993) describe a mechanism for this variability in which density anomalies in the sinking region of the North Atlantic, combined with changes in overturning and gyre circulation, are mentioned as the physical mechanism of the oscillation. A positive salinity anomaly in the sinking region strengthens the thermohaline circulation and leads to enhanced northward heat transport, creating a pool of anomalously warm water in the top kilometer in the middle of the North Atlantic. The associated anti-cyclonic circulation leads to a decreased transport

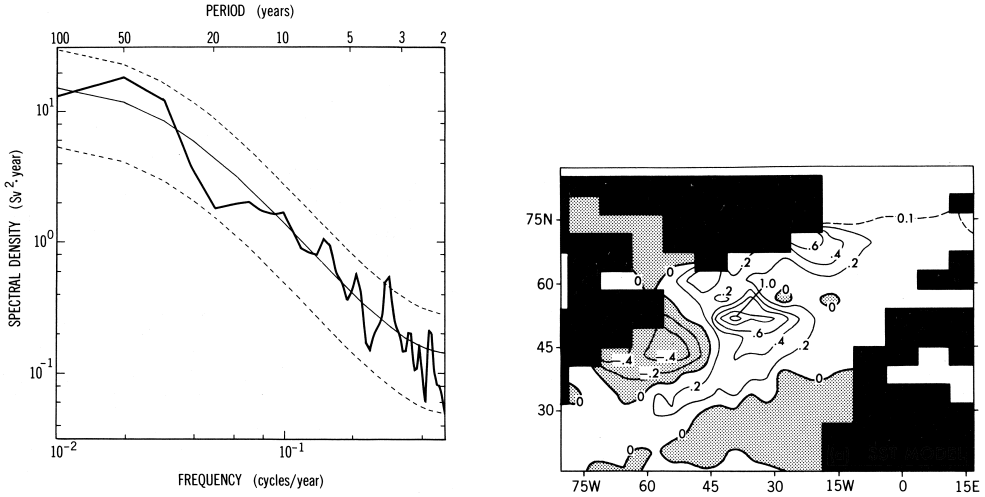

(a) (b)

Figure 1.7: *(a) Spectrum of the first 200 years of the thermohaline circulation index time series with the GFDL MOM model (heavy, solid line). Thin, solid line denotes the least-squares best fit of a theoretical red noise spectrum to the spectrum of the thermohaline circulation. Dashed lines denote 95% confidence limits about the red noise spectrum. (b) Differences in annual-mean SST in MOM between four decades with anomalously large THC-index values and four decades with anomalously small THC-index values. Units are degrees Celsius. Values less than zero are stippled. Figures taken from Delworth* et al. *(1993).*

of saline water into the sinking region, resulting in a negative salinity anomaly after half an oscillation period. In the coupled NCAR Climate System Model (CSM), variability with a 30 to 50-yr period was found in a 300-yr long integration (Capotondi, 2000). The patterns and evolution characteristics of this variability are very similar to those found by Delworth *et al.* (1993) and hence Capotondi (2000) concludes that the mechanism driving the CSM-variability is the same as that proposed by Delworth *et al.* (1993).

In a study with the uncoupled MOM ocean GCM in an idealized single-hemispheric basin configuration, Chen and Ghil (1995) found an interdecadal oscillation with a period varying from 20 yr to about 50 yr, depending on the choice of parameters. The oscillation is characterized by anti-cyclonic movement of density anomalies in the northwestern part of the domain and occurs when there is either net evaporation at high latitudes or constant heat-flux forcing. The mechanism is as follows: if the overturning circulation is anomalously weak, dense water accumulates at high latitudes due to the net evaporation or constant cooling applied there. This dense anomaly induces strong convection and results in a strengthening of the overturning circulation.

Interactions between the wind-driven gyres and the thermohaline circulation drive the decadal oscillations reported by Weaver and Sarachik (1991a,b) and Weaver *et al.* (1993) in a similar single-hemispheric basin configuration of MOM. Temperature and salinity anomalies travel eastward and are picked up by the subpolar gyre, which transports them into the sinking

region, where they influence the strength of the meridional overturning. The advective time scale leads to the decadal (8–9 yr) period. The existence of this decadal variability was shown to depend sensitively on the shape and strength of the freshwater-flux forcing (Weaver *et al.*, 1993). Yin and Sarachik (1995) obtained a 14-yr oscillation in a single-hemispheric basin configuration of MOM. They proposed a mechanism in which subsurface advective heating due to the northeastern current associated with deep convection warms the (subsurface) water at high latitudes and induces convection from below. The enhanced convection induces cyclonic surface flows at high latitudes, which advect subpolar freshwater southward from the northern boundary into the convective regions. This ends the phase of anomalous strong convection.

Self-sustained oscillations with a period of about 20 yr were found in a simulation with MOM in a North-Atlantic configuration with continental geometry by Weaver *et al.* (1994). The time scale of this oscillation is set by the cooling time of the Labrador Sea, which is the most important region in this oscillation. Interdecadal oscillations associated with viscous Kelvin waves were found in a study with an OGCM by Greatbatch and Peterson (1996). An important element is a relatively weak stratification due to convective mixing near the northern boundary of the domain, which slows down the propagating Kelvin-like waves enough to yield variability with interdecadal periods.

Centennial variability has also been found in various OGCM studies. Mikolajewicz and Maier-Reimer (1990) describe a 320-yr oscillation in the global Hamburg Large-Scale Geostrophic (LSG) model, the latter driven by a stochastic forcing. This oscillation was explained by the advection of (mainly) salinity anomalies around the overturning loop, analogous to the overturning or loop oscillation described by Welander (1986). Others have argued that the centennial-scale LSG-variability is an expression of a flip-flop oscillation (Pierce *et al.*, 1995; Osborn, 1997). The latter oscillation was first found by Welander (1982) in a conceptual box model, consisting of two boxes which exchanged heat and salt vertically. The oscillation is characterized by a slow and diffusive build-up of potential energy that is suddenly released in a violent overturning event and is thus fundamentally different from the advective loop oscillation. A damped oscillatory mode with a 530-yr period was identified by Sirkes and Tziperman (2001), using the adjoint model of the MOM model. The physical mechanism of this mode was proposed to be dominated by two-dimensional processes in the meridional-vertical plane. Centennial-to-millennial oscillations, characterized by long periods without deep-water formation followed by short periods of intense overturning, were found by Weaver *et al.* (1993) and others. These oscillations were called deep-decoupling oscillations or flushes and resemble the conceptual flip-flop oscillation of Welander (1982).

Planetary geostrophic models have also been used extensively in the study of internal thermohaline variability. Greatbatch and Zhang (1995) obtain a 50-yr oscillation in a planetary geostrophic single-hemispheric ocean model, forced only by constant heat fluxes. Their oscillation has features similar to those of the variability in Delworth *et al.* (1993), and therefore Greatbatch and Zhang (1995) argue that salinity is not necessary for the variability described by Delworth *et al.* (1993). Instead, they suggested that a stronger overturning circulation shortens the surface residence time of a water parcel, thereby changing its temperature and subsequently affecting the strength of the overturning circulation again.

Viscous boundary-trapped waves were considered to be essential in the interdecadal oscillations found in a planetary geostrophic model forced by fixed buoyancy fluxes in a study

by Winton (1996). Colin de Verdière and Huck (1999) suggested that a more general type of waves, with propagation speeds depending on the background stratification, is involved in interdecadal variability. Baroclinic instability of the western boundary current is mentioned as the energy source of these waves (Colin de Verdière and Huck, 1999). Using a tangent linear model of their planetary geostrophic model, Huck and Vallis (2001) show that an interdecadal mode of variability of the thermohaline circulation exists in their model. This mode has the same characteristics as the variability found by Colin de Verdière and Huck (1999) and Huck *et al.* (1999).

Oscillations with centennial time scales have also been found in a planetary geostrophic model forced by a steady freshwater flux (Winton and Sarachik, 1993). The oscillations are associated with the advection of salinity anomalies by the meridional overturning and are related to the loop oscillation described by Welander (1986).

Using a conceptual two-box model, Yin (1995) argues that the interdecadal oscillation found by Yin and Sarachik (1995) in MOM can be explained as a flip-flop oscillation (Welander, 1982). Although generated by internal dynamics of the model, the flip-flop oscillation is not an internal mode of the system, but a switch between two unstable stationary states (Yin, 1995). Griffies and Tziperman (1995) find interdecadal oscillations in a stochastically forced four-box model, which seem to depend on a phase lag between temperature and salinity anomalies, in combination with positive and negative feedbacks of salinity and temperature, respectively. They suggest that the variability found by Delworth *et al.* (1993) can be interpreted in a similar way.

Despite the enormous amount of modeling studies performed to investigate the internal variability of the thermohaline circulation, several problems remain. The dominant periods as well as the associated spatial patterns of the thermohaline variability are still uncertain. There is no satisfactory theory explaining the time scales and spatial patterns of this variability. Finally, an interpretation framework within which the results of numerical model studies are linked to each other and to the observations is lacking.

1.4 This thesis

The main objective of this thesis is to investigate the internal variability of the North-Atlantic thermohaline circulation on interdecadal and centennial time scales in a systematic way. For making progress in understanding this variability, an approach in which a hierarchy of models is used is necessary. Such an approach should first focus on certain idealized limiting cases, in which the physical mechanism underlying the variability can be understood in detail. The most important —and most difficult— step is to identify certain characteristics or typical features of the variability which are central to the mechanism, like energy transfer or phase propagation, that carry over to variability in the 'real' climate system. If the variability in more realistic and more complex cases has the same characteristics, then, most likely, it can be attributed to the mechanism identified in the limiting case. By subsequently considering more realistic configurations within the same model and then going up in the model hierarchy, variability in very complex CGCMs might be related to a well-understood mechanism. The role of such CGCMs is to simulate the observed variability as accurately as possible. In this way, these simulations supplement the scarce observational data set and provide the spatial

patterns and temporal evolution of the variability. Ultimately, such an approach might provide a convincing physical explanation for the observed variability.

In the traditional numerical models used in the study of the variability of the thermohaline circulation, the time-dependent equations describing the fluid motions are integrated forward in time with some time-stepping technique. The resulting time series are analyzed using statistical tools, for example time-series analysis or pattern-reconstruction techniques, to extract statistical properties of the variability. The drawback of this approach is that causal relations between the physical quantities responsible for the variability are hard to determine. In contrast, the modeling approach that is used for most of the work described in this thesis is based on the theory of dynamical systems (Guckenheimer and Holmes, 1983). In this theory, the (either unstable or weakly stable) oscillatory normal modes are central to temporal behavior of the flows. First, stationary solutions of a certain model in the hierarchy are computed. As a next step, the stability of these solutions with respect to infinitesimally small perturbations is determined. Oscillatory eigenmodes determined from such a linear stability analysis provide the oscillatory spatial patterns to which the flow can become unstable, whereas the oscillation period follows from the (imaginary part of) the eigenvalue. The idea behind the use of linear stability analysis is that, as long as the system is not too far into the non-linear regime, the variability is to a large extent determined by these oscillatory eigenmodes. For a further introduction to dynamical systems theory, the reader is referred to appendix A.

From the results in the literature, it seems that an uncoupled, single-hemispheric ocean basin is the simplest model configuration in which interdecadal thermohaline variability resembling the Delworth *et al.* (1993) variability can be found. Salinity, wind forcing, continental geometry and bottom topography all seem to be non-essential. The limiting case of purely thermally driven flows in a single-hemispheric flat-bottomed sector basin is therefore chosen as the starting point for the studies in this thesis. The flow is studied in a rather viscous regime, allowing for all continental boundary layers to be resolved properly. The internal modes of variability of the flow in this idealized configuration are studied in detail, and they are related to variability in other, less idealized, model configurations.

The central questions addressed in this thesis are:

- What are the internal oscillatory modes of the thermally driven flow in a single-hemispheric basin?
- What are the physical characteristics of these internal modes of variability?
- What is the physical mechanism of propagation of the anomaly patterns?
- What is the effect of salinity on the mechanism and stability properties of these modes?
- Can the variability in more complex model configurations be related to the existence of these modes?

In chapter 2, the two numerical models used in this thesis are described, together with the applied methodology. The first model is an implicit model (Dijkstra *et al.*, 2001), which can be used for the computation of steady-state solutions and their linear stability, as well as for (implicit) time integrations. The second model used in this thesis is the MOM OGCM (Pacanowski and Griffies, 1998), which can easily be adapted for different model configurations. As a test of how well the large-scale circulation and stratification are captured in

the idealized model configuration, particular scaling behavior of both models is tested and compared with theoretically derived scaling relations.

Chapter 3 deals with the question whether interdecadal variability of purely thermally driven flows in a single-hemispheric sector basin can be explained by an internal mode of that system. With the implicit model, steady-state solutions of this system are computed and the linear stability of the flows under a prescribed heat-flux forcing is investigated. The most unstable oscillatory mode, which has an interdecadal period, is described in detail and characteristic features of the mode are identified. Also the physical mechanism of the interdecadal mode is determined.

In chapter 4, two steps along a path up in the model hierarchy are taken. Firstly, the implicit ocean model is coupled to a simple energy-balance model for the atmosphere and it is shown that this does not affect the existence of the interdecadal mode. Secondly, also salinity is included and the effect of the transport of salt on the mechanism and stability properties of the interdecadal mode is discussed.

Chapter 5 returns to the configuration of the limiting case of thermally driven flows in the uncoupled implicit ocean model. The central question in this chapter is what kind of other modes of variability exist in the thermally driven single-hemispheric basin and whether they can cause variability on centennial time scales. A second type of modes, with centennial oscillation periods, is found and the physical mechanism of these modes is described. Next, transient flow computations are performed to investigate how the internal modes affect the total circulation.

In chapter 6, a second path up in the model hierarchy is followed, towards a more realistic regime in which also the effects of continental geometry and bottom topography are included. To this end, transient flow computations with the MOM model are performed. The starting point is again the viscous thermally driven flow in the idealized-basin configuration. By considering characteristic features of the physical mechanism of the interdecadal mode in the idealized case, the variability in MOM is related to the interdecadal mode described in chapter 3. Next, the variability is followed up in the model hierarchy towards a less viscous regime and subsequently to a situation in which continental geometry and bottom topography are also included. Finally, a summary and a synthesis of the results are given in chapter 7.

Chapter 2

Model formulation and approach

In this chapter, the two numerical models used in this thesis are introduced. Both models are based on the primitive-equations formulation for the flow, but the discretization schemes and solution methods are different. The equations governing the behavior of the flow are formulated and a description of the models is given. Although the standard model configuration is rather idealized, it is expected that both models give a qualitatively correct representation of the large-scale circulation and stratification. This is tested by considering particular scaling behavior of both models.

2.1 Governing equations

The equations in both models are the Boussinesq equations in spherical coordinates ϕ, θ and z, with application of the hydrostatic approximation. The flow domain is a sector $[\phi_W, \phi_E] \times [\theta_S, \theta_N]$ of average depth D on a sphere that has radius r_0 and rotates with angular velocity Ω. The ocean velocities in eastward and northward directions are indicated by u_* and v_*, respectively, the vertical velocity is indicated by w_*, the pressure by p_*, the temperature by T_* and the salinity by S_*. A linear equation of state is assumed, with expansion coefficients α_T and α_S, reference temperature T_0, salinity S_0 and density ρ_0. The dimensional equations are then given by

$$\begin{aligned}
\frac{Du^*}{dt^*} - \frac{u^* v^* \tan\theta}{r_0} &= 2\Omega v^* \sin\theta - \frac{1}{\rho_0 r_0 \cos\theta}\frac{\partial p^*}{\partial \phi} + A_V \frac{\partial^2 u^*}{\partial z^{*2}} \\
&+ A_H \left(\nabla_H^2 u^* - \frac{u^*}{r_0^2 \cos^2\theta} - \frac{2\sin\theta}{r_0^2 \cos^2\theta}\frac{\partial v^*}{\partial \phi} \right) \qquad (2.1a) \\
\frac{Dv^*}{dt^*} + \frac{u^{*2} \tan\theta}{r_0} &= -2\Omega u^* \sin\theta - \frac{1}{\rho_0 r_0}\frac{\partial p^*}{\partial \theta} + A_V \frac{\partial^2 v^*}{\partial z^{*2}} \\
&+ A_H \left(\nabla_H^2 v^* - \frac{v^*}{r_0^2 \cos^2\theta} + \frac{2\sin\theta}{r_0^2 \cos^2\theta}\frac{\partial u^*}{\partial \phi} \right) \qquad (2.1b) \\
\frac{\partial p^*}{\partial z^*} &= -\rho^* g \qquad (2.1c)
\end{aligned}$$

$$0 = \frac{\partial w^*}{\partial z^*} + \frac{1}{r_0 \cos\theta}\left(\frac{\partial u^*}{\partial \phi} + \frac{\partial (v^* \cos\theta)}{\partial \theta}\right) \tag{2.1d}$$

$$\frac{DT^*}{dt^*} - \nabla_H \cdot (K_H \nabla_H T^*) = \frac{\partial}{\partial z^*}\left(K_V \frac{\partial T^*}{\partial z^*}\right) \tag{2.1e}$$

$$\frac{DS^*}{dt^*} - \nabla_H \cdot (K_H \nabla_H S^*) = \frac{\partial}{\partial z^*}\left(K_V \frac{\partial S^*}{\partial z^*}\right) \tag{2.1f}$$

$$\rho^* = \rho_0(1 - \alpha_T(T^* - T_0) + \alpha_S(S^* - S_0)) \tag{2.1g}$$

with the notation

$$\frac{DF}{dt^*} = \frac{\partial F}{\partial t^*} + \boldsymbol{u^*} \cdot \nabla F = \frac{\partial F}{\partial t^*} + \frac{u^*}{r_0 \cos\theta}\frac{\partial F}{\partial \phi} + \frac{v^*}{r_0}\frac{\partial F}{\partial \theta} + w^*\frac{\partial F}{\partial z^*}$$

$$\nabla_H \cdot (K_H \nabla_H F) = \frac{1}{r_0^2 \cos\theta}\left[\frac{\partial}{\partial \phi}\left(\frac{K_H}{\cos\theta}\frac{\partial F}{\partial \phi}\right) + \frac{\partial}{\partial \theta}\left(K_H \cos\theta \frac{\partial F}{\partial \theta}\right)\right]$$

$$\nabla_H^2 = \nabla_H \cdot \nabla_H$$

where F is an arbitrary scalar. In these equations, $\boldsymbol{u^*} = (u^*, v^*, w^*)^T$ is the velocity vector (the superscript T denotes the transpose), g the gravitational acceleration, A_H and A_V are the horizontal and vertical eddy viscosities and K_H and K_V are the horizontal and vertical mixing coefficients of heat and salt, which are also called horizontal and vertical eddy diffusivities.

The ocean circulation is driven by heat and freshwater fluxes at the surface and by a wind stress $\vec{\tau}(\phi, \theta) = \tau_0(\tau^\phi, \tau^\theta)$, where τ_0 is the amplitude (in Nm^{-2}) and (τ^ϕ, τ^θ) provides the spatial pattern. The downward heat flux is denoted by Q^*_{oa} (in Wm^{-2}) and the freshwater flux Q^*_{FW} (in ms^{-1}) is converted to an equivalent salt flux by multiplying by the reference salinity. At the ocean-atmosphere surface, the boundary conditions then become

$$\rho_0 A_V \frac{\partial u^*}{\partial z^*} = \tau_0 \tau^\phi; \quad \rho_0 A_V \frac{\partial v^*}{\partial z^*} = \tau_0 \tau^\theta; \quad w^* = 0 \tag{2.2a}$$

$$\rho_0 C_{po} K_V \frac{\partial T^*}{\partial z^*} = Q^*_{oa}; \quad K_V \frac{\partial S^*}{\partial z^*} = Q^*_{FW} S_0 \tag{2.2b}$$

where C_{po} is the specific heat capacity of the ocean.

In uncoupled ocean models, the downward heat flux is often assumed to be proportional to the temperature difference between the ocean surface temperature T^*_{surf} and a prescribed 'effective' atmospheric temperature T^*_S, so that

$$Q^*_{oa} = \mu(T^*_S - T^*_{surf}) \tag{2.3}$$

where μ is an ocean-atmosphere exchange coefficient (Haney, 1971). The coefficient μ is related to the restoring time scale for temperature τ_T through $\mu = C_{po}\rho_0 H_m/\tau_T$, with H_m the thickness of the layer in the ocean over which the heat is distributed. Equation (2.3) is called a restoring boundary condition. A more realistic option is that Q^*_{oa} is computed by an atmospheric model, which is coupled to the ocean model. For the freshwater flux a prescribed (dimensionless) function F_S with dimensional amplitude F_0 is used.

The transfer of heat, freshwater and momentum from the surface downward occurs in thin boundary layers, like the Ekman layer for momentum transfer. Although these may

be resolved explicitly, this requires a very high vertical resolution near the surface. Hence, here the methodology as used in many low-resolution ocean general circulation models is followed, in which the surface forcing is distributed as a body forcing over a certain depth of the upper ocean, using a vertical profile function $G(z)$. Therefore, the right-hand sides of the horizontal momentum (2.1a) and (2.1b), temperature (2.1e) and salinity (2.1f) equations are extended with source terms $Q_\tau^{*\phi}$, $Q_\tau^{*\theta}$, Q_T^* and Q_S^*, respectively, which are given by

$$Q_\tau^{*\phi} = G(z)\frac{\tau_0}{\rho_0 H_m}\tau^\phi; \qquad Q_\tau^{*\theta} = G(z)\frac{\tau_0}{\rho_0 H_m}\tau^\theta \tag{2.4a}$$

$$Q_T^* = \begin{cases} G(z)\,(T_S^* - T^*)/\tau_T & \text{restoring} \\ G(z)\,Q_{oa}^*/(C_{po}\rho_0 H_m) & \text{coupled} \end{cases} \tag{2.4b}$$

$$Q_S^* = G(z)\frac{F_0}{H_m}F_S \tag{2.4c}$$

where a typical vertical scale of variation of the function $G(z)$ is given by H_m.

2.2 The THCM model

The implicit model that will be used in chapters 3 to 5 is the ThermoHaline Circulation Model (THCM, see Dijkstra *et al.* (2001)), which has recently been developed at the Institute for Marine and Atmospheric Research Utrecht in the Netherlands. It consists of an ocean model and a diffusive energy-balance model for the atmosphere. These two model components are described separately in the next two sections.

2.2.1 The THCM ocean model

The THCM ocean model uses a dimensionless version of equations (2.1) to (2.4). A non-dimensional temperature T and salinity S are introduced through $T_* = T_0 + \Delta T\, T$ and $S_* = S_0 + \Delta S\, S$, with scales ΔT and ΔS for temperature and salinity, respectively. The non-dimensional pressure p is obtained through $p_* = -\rho_0 g z + 2\Omega r_0 U \rho_0\, p$ and non-dimensional velocities are written as u, v, and w. A characteristic horizontal velocity is indicated by U, and equations (2.1a) to (2.1g) are further non-dimensionalized using scales r_0, D, U, DU/r_0 and r_0/U for horizontal length, vertical length, horizontal velocity, vertical velocity and time, respectively and become

$$\begin{aligned} \varepsilon_R\left(\frac{Du}{dt} - uv\tan\theta\right) - \eta_f v\sin\theta &= -\frac{1}{\cos\theta}\frac{\partial p}{\partial\phi} + E_V\frac{\partial^2 u}{\partial z^2} \\ &+ E_H\left(\nabla_H^2 u - \frac{u}{\cos^2\theta} - \frac{2\sin\theta}{\cos^2\theta}\frac{\partial v}{\partial\phi}\right) \end{aligned} \tag{2.5a}$$

$$\begin{aligned} \varepsilon_R\left(\frac{Dv}{dt} + u^2\tan\theta\right) + \eta_f u\sin\theta &= -\frac{\partial p}{\partial\theta} + E_V\frac{\partial^2 v}{\partial z^2} \\ &+ E_H\left(\nabla_H^2 v - \frac{v}{\cos^2\theta} + \frac{2\sin\theta}{\cos^2\theta}\frac{\partial u}{\partial\phi}\right) \end{aligned} \tag{2.5b}$$

$$\frac{\partial p}{\partial z} = Ra(T - \lambda S) \tag{2.5c}$$

$$0 = \frac{\partial w}{\partial z} + \frac{1}{\cos\theta}\left(\frac{\partial u}{\partial \phi} + \frac{\partial (v\cos\theta)}{\partial \theta}\right) \tag{2.5d}$$

$$\frac{DT}{\partial t} - \nabla_H \cdot (P_H \nabla_H T) = \frac{\partial}{\partial z}\left(P_V \frac{\partial T}{\partial z}\right) + Q_T G(z) \tag{2.5e}$$

$$\frac{DS}{\partial t} - \nabla_H \cdot (P_H \nabla_H S) = \frac{\partial}{\partial z}\left(P_V \frac{\partial S}{\partial z}\right) + Q_S G(z) \tag{2.5f}$$

In all studies performed with THCM, the circulation is only driven by fluxes of heat and freshwater at the surface, so the source terms in the dimensionless momentum equations (2.5a) and (2.5b) have been set to zero. Using the scaling as above, the source terms in the equations for temperature and salinity become

$$Q_T = \begin{cases} Bi\,(\eta_T T_S - T) & \text{restoring} \\ Q^*_{oa}\, r_0/(C_{po}\rho_0 H_m U \Delta T) & \text{coupled} \end{cases} \tag{2.6a}$$

$$Q_S = \gamma F_S \tag{2.6b}$$

where $Bi = r_0/(U\tau_T)$ and the parameter $\gamma = F_0 r_0/(U\Delta S H_m)$ is the freshwater flux strength. The dimensionless parameter η_T is introduced to control the amplitude of T_S. On the continental boundaries, the heat and salt fluxes are zero and no-slip or slip conditions can be prescribed

$$\phi = \phi_W, \phi_E: \quad \frac{\partial T}{\partial \phi} = \frac{\partial S}{\partial \phi} = 0; \quad (1-\chi)v + \chi\frac{\partial v}{\partial \phi} = 0 \tag{2.7a}$$

$$\theta = \theta_S, \theta_N: \quad \frac{\partial T}{\partial \theta} = \frac{\partial S}{\partial \theta} = 0; \quad (1-\chi)u + \chi\frac{\partial u}{\partial \theta} = 0 \tag{2.7b}$$

where the parameter χ has been introduced to be able to switch between no-slip ($\chi = 0$) and slip ($\chi = 1$) conditions. In the standard case, no-slip boundary conditions are prescribed ($\chi = 0$). The bottom of the ocean is impervious to heat and salt and slip conditions are assumed, according to

$$z = -1: \quad \frac{\partial T}{\partial z} = \frac{\partial S}{\partial z} = \frac{\partial u}{\partial z} = \frac{\partial v}{\partial z} = 0 \tag{2.8a}$$

The parameters in equations (2.5) and (2.6) are the Rossby number ε_R, the Rayleigh number Ra, the vertical and horizontal Ekman numbers E_V and E_H, the buoyancy ratio λ, the vertical and horizontal inverse Péclet numbers P_V and P_H, the Biot number Bi and the freshwater flux strength γ. Expressions for these parameters are

$$\varepsilon_R = \frac{U}{2\Omega r_0};\ Ra = \frac{\alpha_T \Delta T g D}{2\Omega U r_0};\ E_V = \frac{A_V}{2\Omega D^2};\ E_H = \frac{A_H}{2\Omega r_0^2};\ \lambda = \frac{\alpha_S \Delta S}{\alpha_T \Delta T}$$

$$P_H = \frac{K_H}{U r_0};\ P_V = \frac{K_V r_0}{U D^2};\ Bi = \frac{r_0}{U\tau_T};\ \gamma = \frac{F_0 r_0}{U\Delta S H_m}$$

The parameter η_f in equations (2.5a) and (2.5b) is introduced to control the strength of the rotation rate; it is set to $\eta_f = 1.0$ in the standard case. When the rotation rate is decreased

to zero, velocities increase characteristically by a factor $1/E_H$, as a result of the change in dominant balance in the momentum equations. Following Weijer and Dijkstra (2001), the Rayleigh number is therefore rescaled in case $\eta_f \neq 1.0$ according to

$$Ra = [\eta_f + (1 - \eta_f)E_H]\frac{\alpha_T \Delta T g D}{2\Omega U r_0} \tag{2.9}$$

Apart from η_f and χ and the parameter η_T in the temperature forcing function, the system appears to contain 9 parameters. However, only 8 of these are independent; the characteristic horizontal velocity U can be chosen as a function of other parameters.

As convection, which occurs in case of an unstable stratification, is not explicitly resolved in the hydrostatic approximation, this process has to be parameterized. Here, implicit mixing is used as the form of convective adjustment (Yin and Sarachik, 1994). This means that when the flow becomes unstably stratified, the vertical mixing coefficient of heat is increased, i.e.

$$P_V = P_V^0 + P_V^c \, \mathcal{H}(\frac{\partial \rho}{\partial z}; \epsilon_H) \tag{2.10}$$

where P_V^0 is the background inverse Péclet number, P_V^c is the convective inverse Péclet number, which is much larger than P_V^0. $\mathcal{H}$ is a continuous approximation to the Heaviside function, for which we use

$$\mathcal{H}(x; \epsilon_H) = \frac{1}{2}(1 + \tanh \, \frac{x}{\epsilon_H}) \tag{2.11}$$

with $\epsilon_H = 0.1$. For convenience, the background inverse Péclet number will be indicated by P_V instead of P_V^0 in the rest of this thesis. Similarly, the background vertical eddy diffusivity K_V^0 will be indicated by K_V.

2.2.2 The THCM atmospheric model

The THCM ocean model can be coupled to a simple diffusive energy-balance model for the atmosphere. In this case, the atmospheric heat flux Q_{oa}^* is provided by the energy-balance model, instead of the restoring boundary condition.

The energy-balance model used is similar to that in North (1975a) and there is no land surface. The equation for the (dimensional) atmospheric surface temperature T_a^* on the domain $[\phi_W, \phi_E] \times [\theta_S, \theta_N]$ is given by

$$\begin{aligned} \rho_a H_a C_{pa} \frac{\partial T_a^*}{\partial t^*} = {} & \rho_a H_a C_{pa} D_0 \nabla_H \cdot (D(\theta) \nabla_H T_a^*) - (A + B T_a^*) \\ & + \frac{\Sigma_0}{4} S_\odot(\theta)(1 - \alpha(\theta))(1 - C_0) + \mu(T^* - T_a^*) \end{aligned} \tag{2.12}$$

where ρ_a is the atmospheric density, C_{pa} the atmospheric heat capacity, H_a an atmospheric scale height, D_0 a constant eddy diffusivity, Σ_0 the solar constant, C_0 the solar scattering coefficient and T^* the temperature at the uppermost ocean level. The functions $D(\theta)$, $S_\odot(\theta)$ and $1 - \alpha(\theta)$ are the spatial patterns of the atmospheric eddy diffusivity, the shortwave radiative heat flux and the co-albedo; A and B are constants in the parameterization of the longwave radiative flux. At the lateral boundaries no-flux conditions are prescribed.

The exchange of heat between atmosphere and ocean is modeled by a constant exchange coefficient μ, with

$$\mu = \rho_a C_{pa} C_H \mid U_a \mid \tag{2.13}$$

where C_H is the Stanton number and $\mid U_a \mid$ a mean surface wind speed. The downward heat flux into the ocean is then given by

$$Q^*_{oa} = \frac{\Sigma_0}{4} S_\odot(\theta)(1-\alpha(\theta))C_0 - \mu(T^* - T^*_a) \tag{2.14}$$

In this way, the following integral conditions are satisfied in steady state

$$\int_{\phi_W}^{\phi_E} \int_{\theta_S}^{\theta_N} Q^*_{oa} \cos\theta \, d\phi \, d\theta = 0 \tag{2.15a}$$

$$\int_{\phi_W}^{\phi_E} \int_{\theta_S}^{\theta_N} (\frac{\Sigma_0}{4} S_\odot(\theta)(1-\alpha(\theta)) - (A + BT^*_a)) \cos\theta \, d\phi \, d\theta = 0 \tag{2.15b}$$

Equation (2.12) is non-dimensionalized by writing $T^*_a = T_0 + \Delta T \, T_a$ and becomes

$$\begin{aligned} \frac{\partial T_a}{\partial t} = \hat{D}_0 \nabla_H \cdot (D(\theta) \nabla_H T_a) - \frac{R}{\Delta T}(A + BT_0 + B\Delta T T_a) + \\ \frac{\Sigma_0}{4} S_\odot(\theta) \frac{R}{\Delta T}(1-\alpha(\theta))(1-C_0) + \mu R(T - T_a) \end{aligned} \tag{2.16}$$

where the notations $\hat{D}_0 = D_0/(U r_0)$ and $R = r_0/(\rho_a H_a C_{pa} U)$ have been used.

2.2.3 Numerical implementation

The model THCM solves the equations numerically, using techniques from dynamical systems theory (see appendix A for more information on dynamical systems theory). The numerical algorithm consists of two main parts. The first part is a continuation algorithm, by which branches of stationary solutions can be traced for changing values of a model parameter (the control parameter). The second part of the numerical algorithm consists of an eigenvalue solver to determine the linear stability of the computed stationary solutions. The growth rates σ of the perturbations are monitored versus values of the control parameter.

The set of partial differential equations (2.5) and (2.16) is discretized on a $N \times M \times (L+1)$ Arakawa C-grid, together with the appropriate boundary conditions. After discretization a system of nonlinear differential equations with algebraic constraints results, which can be written as

$$\mathbf{M} \, \frac{d\mathbf{u}}{dt} = \mathbf{F}(\mathbf{u}, \boldsymbol{q}) \tag{2.17}$$

Here $\mathbf{u}$ is the d-dimensional state vector ($d = 6 \times N \times M \times (L+1)$). It consists of the unknowns (u, v, w, p, T, S) at each grid point, with $(u_a, v_a, w_a, p_a, T_a, q_a)$ for the grid points of the atmospheric layer, where u_a, v_a, w_a are the atmospheric velocities, p_a the atmospheric pressure and q_a the atmospheric moisture. In the model version used in this thesis, only the atmospheric temperature is active and u_a, v_a, w_a, p_a and q_a are dummy variables. Further, $\boldsymbol{q}$

is the q-dimensional vector of parameters, $\mathbf{F}$ is a nonlinear mapping from $R^d \times R^q \rightarrow R^d$ and $\mathbf{M}$ is a linear operator. Stationary solutions satisfy the equation

$$\mathbf{F}(\mathbf{u}, \boldsymbol{q}) = \mathbf{0} \tag{2.18}$$

which is a system of d nonlinear algebraic equations. To compute a branch of stationary solutions in a control parameter, say ν, a pseudo-arclength method (Keller, 1977) is used. The branches of stationary solutions $(\mathbf{u}(s), \nu(s))$ are parameterized by an 'arclength' parameter s. Since this introduces an extra unknown, an additional equation is needed and the tangent in the point $(\mathbf{u}_0, \nu_0)$ is normalized along the branch, i.e.

$$\dot{\mathbf{u}}_0^T(\mathbf{u} - \mathbf{u}_0) + \dot{\nu}_0^T(\nu - \nu_0) - \Delta s = 0 \tag{2.19}$$

where Δs is the step length and a dot indicates differentiation to s. The Newton-Raphson method is used to converge to the branch of stationary solutions. This method finds isolated steady solutions, regardless of their stability. The linear systems are solved with the GMRES method (an iterative linear systems solver) using an MRILU preconditioning technique (Dijkstra *et al.*, 2001).

After a steady state has been computed, the linear stability of the solution can be determined and transitions that mark qualitative changes, such as transitions to multiple equilibria (pitchfork bifurcations or limit points) or periodic behavior (Hopf bifurcations), can be detected. The linear stability analysis amounts to solving a generalized eigenvalue problem of the form

$$\alpha' \mathcal{A}_J \mathbf{u} = \beta' \mathcal{B} \mathbf{u} \tag{2.20}$$

where $\mathcal{A}_J$ is the Jacobian matrix (the derivative of $\mathbf{F}$ to $\mathbf{u}$) and $\mathcal{B} = -\mathbf{M}$. The matrices $\mathcal{A}_J$ and $\mathcal{B}$ are in general non-symmetric matrices, and α' and β' are complex numbers. If $\mathcal{B}$ is nonsingular, the problem reduces to an ordinary eigenvalue problem for the matrix $\mathcal{B}^{-1}\mathcal{A}_J$. Because only real matrices are considered, there are d eigenvalues which are either real or occur as complex conjugate pairs. However, if $\mathcal{B}$ is singular, the eigenvalue structure may be more complicated; the set of eigenvalues may be finite, empty or even the whole complex plane (Golub and Van Loan, 1983). In the particular model here, $\mathcal{B}$ is a singular diagonal matrix because time derivatives are absent in the continuity equation and vertical momentum equation. The problem (2.20) is solved by the Jacobi-Davidson QZ (JDQZ) method (Sleijpen and Van der Vorst, 1996). With this method one can compute several eigenvalues and optionally eigenvectors near a specified target. Details of the method are described in Sleijpen and Van der Vorst (1996) and the implementation of JDQZ in an earlier version of the continuation code in Van Dorsselaer (1997). In case $\alpha' \neq 0$ in (2.20), we will use the notation $\sigma = \sigma_r + i\sigma_i = \beta'/\alpha'$ to indicate the eigenvalue.

Time-dependent behavior can be studied with the THCM model by integrating the system (2.17) implicitly. Using a time step Δt and the time index n, the fully-implicit scheme becomes for $\omega \in [0, 1]$,

$$\mathbf{M}\frac{\mathbf{u}^{n+1} - \mathbf{u}^n}{\Delta t} + (1 - \omega)\mathbf{F}(\mathbf{u}^n) + \omega\mathbf{F}(\mathbf{u}^{n+1}) = 0 \tag{2.21}$$

For $\omega = 1/2$ and $\omega = 1$, these are the implicit midpoint (Crank-Nicholson) method and backward Euler method, respectively. The equations for $\mathbf{u}^{n+1}$ are solved by the Newton-Raphson

method. As the second-order Crank-Nicholson method is unconditionally stable, relatively large time steps can be taken, which are only limited by accuracy and the convergence domain of the Newton process. A more detailed description of the solution methods can be found in Dijkstra (2000).

2.3 The MOM model

The Modular Ocean Model (MOM) is the second model which has been used in this thesis. It has been developed at the Geophysical Fluid Dynamics Laboratory in Princeton (U.S.A.) and is one of oldest ocean models (Bryan and Cox, 1967; Cox, 1984). Over the past decades, it has been used in many climate studies and studies of the ocean circulation. For the work in this thesis, version 3.1 of MOM has been used.

The dimensional equations (2.1a) to (2.1g) are discretized on an Arakawa B-grid of $N \times M \times L$ points. The resulting system is solved with a traditional time-stepping procedure using a leap-frog scheme. Occasionally, an Euler time step is performed to eliminate the computational mode. The equations are split into those for the barotropic part (the external mode), the baroclinic part and the tracers (temperature and salinity). The time steps used for these equations are referred to as Δt_E, Δt_I and Δt_T, respectively and can be chosen differently (asynchronous integration) to speed up convergence of the model (Bryan, 1984). For an extensive description of the splitting of the equations, the discretization and the solution methods in MOM, the reader is referred to Pacanowski and Griffies (1998).

The rigid-lid version of the model is used, in which the vertical velocity is exactly zero at the ocean-atmosphere boundary. In this case, the equation for the barotropic part is a two-dimensional Poisson equation, which is solved by a conjugate-gradient solver. At the continental boundaries, heat and salt fluxes are zero and no-slip conditions are imposed. Also at the bottom heat and salt fluxes are zero, and here slip conditions are assumed. An implicit mixing scheme is used as the variant of convective adjustment, in which the vertical eddy diffusivity is increased in unstably stratified regions.

2.4 Standard configuration and forcing

The configuration described here is the standard configuration for both THCM and MOM. In subsequent chapters, usually only the settings and parameters that have been changed with respect to this standard configuration will be mentioned.

The model domain is a single hemispheric $64°$-wide sector in longitude (with $\phi_W = 74°$W and $\phi_E = 10°$W) between the latitudes $\theta_S = 10°$N and $\theta_N = 74°$N, which has constant depth $D = 4000$ m (Fig. 2.1). In the standard configuration, solutions are computed on an equidistant $16 \times 16 \times 16$ grid, which yields a horizontal resolution of $4\,° \times 4°$ and a vertical resolution of 250 m.

The ocean model is uncoupled and the default forcing is a restoring boundary condition for temperature, with the prescribed surface temperature $T_S^*(\theta)$ given by

$$T_S^*(\theta) = T_0 + \eta_T \Delta T \, \cos \pi \hat{\theta}; \quad \hat{\theta} = \frac{\theta - \theta_S}{\theta_N - \theta_S} \tag{2.22}$$

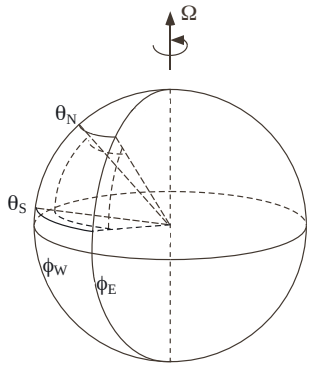

Figure 2.1: *Sketch of the model domain on a sphere rotating with angular frequency* Ω*.*

The dimensionless surface temperature T_S is thus given by

$$T_S(\theta) = \cos \pi \hat{\theta} \tag{2.23}$$

For the profile of the freshwater-flux forcing F_S a sine function is used, with an additional term through which the freshwater input in the north can be modified

$$F_S(\theta) = \sin 2\pi \hat{\theta} + \eta_s e^{20(\hat{\theta}-1)} \tag{2.24}$$

where η_s is a parameter determining the shape of the profile of F_S. The analytical expression of Bryan (1987) is used for the wind stress

$$\begin{aligned} \tau^{\phi} &= 0.2 - 0.8\,(\sin 6\,\theta) - 0.5\,(1 - \tanh 10\,\theta) \\ &\quad - 0.5\left(1 - \tanh\left[10\left(\frac{\pi}{2} - \theta\right)\right]\right) \end{aligned} \tag{2.25a}$$

$$\tau^{\theta} = 0 \tag{2.25b}$$

In the standard set-up, the freshwater-flux forcing and the wind-stress forcing are set to zero ($F_0 = 0$ ms^{-1} and $\tau_0 = 0$ Nm^{-2}, respectively). The salinity field has then a constant value $S^* = S_0$ everywhere in the basin.

The vertical profile function $G(z)$ in equations (2.4), (2.5e) and (2.5f) is chosen as

$$G(z) = \mathcal{H}(z - z_{L-1}; \epsilon_H) \tag{2.26}$$

with z_{L-1} being the depth of the level just below the top and $\mathcal{H}$ as in (2.11) with $\epsilon_H = 10^{-6}$.

Most of the parameters are fixed at values as used in typical large-scale ocean general circulation models and these values are listed in Table 2.1. The horizontal eddy viscosity A_H is rather large, compared to that used in most GCM studies. The value of A_H is bounded from below by the thickness of the boundary layers which develop near the continents. Near the western boundary, the Munk frictional boundary-layer thickness at a latitude θ_0 scales with $(A_H/\beta_0)^{1/3}$, where $\beta_0 = 2\Omega \cos\theta_0/r_0$ monitors the variation of the Coriolis parameter. With a horizontal resolution of $4^\circ \times 4^\circ$, this leads to a typical lower bound

2Ω	=	$1.4 \cdot 10^{-4}$	[s^{-1}]	r_0	=	$6.4 \cdot 10^6$	[m]
D	=	$4.0 \cdot 10^3$	[m]	g	=	9.8	[ms^{-2}]
T_0	=	15.0	[°C]	S_0	=	35.0	[-]
α_T	=	$1.0 \cdot 10^{-4}$	[K^{-1}]	α_S	=	$7.6 \cdot 10^{-4}$	[-]
ρ_0	=	$1.0 \cdot 10^3$	[kg m^{-3}]	τ_T	=	$7.5 \cdot 10^1$	[days]
A_H	=	$1.6 \cdot 10^7$	[m^2s^{-1}]	A_V	=	$1.0 \cdot 10^{-3}$	[m^2s^{-1}]
K_H	=	$1.0 \cdot 10^3$	[m^2s^{-1}]	K_V	=	$2.3 \cdot 10^{-4}$	[m^2s^{-1}]
H_m	=	250.0	[m]	K_V^c	=	$3.3 \cdot 10^{-3}$	[m^2s^{-1}]
F_0	=	0.0	[ms^{-1}]	τ_0	=	0.0	[Nm^{-2}]

Table 2.1: *Standard values of the dimensional parameters used in the numerical computations.*

of $A_H = 5 \cdot 10^5$ m^2s^{-1} at $\theta_0 = 45°$N. However, near the continental walls also thin upwelling and downwelling layers with a typical width of $(A_H/f_0)^{1/2}$ will develop, where $f_0 = 2\Omega \sin\theta_0$, which restricts the value of A_H to be larger than $1 \cdot 10^7$ m^2s^{-1}. Therefore, a value of $A_H = 1.6 \cdot 10^7$ m^2s^{-1} has been used here.

In coarse-resolution ocean models using a horizontal resolution of $4° \times 4°$, typically values of $A_H = 1.5 \cdot 10^5$ m^2s^{-1} are taken. As not all lateral boundary layers near the continental boundaries can be resolved in that case, wiggles are likely to occur near the continental boundaries. Test computations with THCM at a horizontal resolution of $4° \times 4°$ showed that pronounced wiggles were present in a steady-state solution with $A_H = 1.6 \cdot 10^5$ m^2s^{-1}. The MOM model turned out to be much less sensitive to these wiggles. In a steady-state solution computed with MOM at $4° \times 4°$ with $A_H = 1.6 \cdot 10^5$ m^2s^{-1}, only in a narrow region near the eastern boundary some wiggles could be seen, and only in the zonal and vertical velocity fields. This difference between MOM and THCM is most likely related to the different computational grids used in both models (an Arakawa B-grid in MOM and an Arakawa C-grid in THCM) and is currently being investigated.

The use of the large value of A_H will lead to solutions with a very broad western boundary current, but the dominant balances determining the (interior) circulation and stratification are not expected to be significantly influenced by this high horizontal eddy viscosity. In the next section, it is investigated if the qualitative features of the large-scale circulation and stratification can be represented correctly, in spite of the high value of the eddy viscosity. To this end, the scaling relations for the steady state solutions in THCM and in MOM are computed and compared to theoretically derived relations. The effect of the high value of the horizontal eddy viscosity on the modeled variability will be considered in chapter 6. It will be shown that the high value of A_H used in the standard configuration here does not have any qualitative effects on the internal variability found.

The characteristic horizontal velocity U used in the non-dimensionalization in THCM is chosen as $U = 0.1$ ms^{-1} (see Table 2.1), which yields a Rossby number ε_R that is rather small, of $O(10^{-4})$. Hence, for computational efficiency the Rossby number has been set to zero in all computations with THCM. This means that the equations reduce to the planetary

geostrophic equations. Several test computations showed that this approximation does not have any qualitative nor quantitative effects on the results. In all simulations performed with MOM, inertia was retained. The values of the scales ΔT, ΔS and U, and the dimensionless parameters used in THCM are given in Table 2.2. Note that the values of ΔT and η_T are

ΔT	=	1.0	[K]	ΔS	=	1.0	[-]	U	=	0.1 [ms^{-1}]
Ra	=	$4.2 \cdot 10^{-2}$		η_T	=	$1.0 \cdot 10^{1}$		ε_R	=	0.0
E_H	=	$2.7 \cdot 10^{-3}$		P_H	=	$2.9 \cdot 10^{-3}$		η_f	=	1.0
E_V	=	$4.3 \cdot 10^{-7}$		P_V	=	$9.2 \cdot 10^{-4}$		χ	=	0.0
Bi	=	$1.0 \cdot 10^{1}$		P_V^c	=	$1.3 \cdot 10^{-2}$		λ	=	0.0
γ	=	0.0		η_s	=	0.0				

Table 2.2: *Standard values of parameters used in the numerical computations with THCM.*

chosen such that the dimensional meridional temperature difference over the sector, which is given by $2\eta_T \Delta T$, is 20 K in the standard case.

2.5 Scaling behavior

The scaling behavior of the steady-state solutions has been investigated both in THCM and in MOM for the standard configuration. A dimensional meridional overturning streamfunction Ψ_M can be defined by integrating the continuity equation (2.1d) zonally, which yields

$$\cos\theta \int_{\phi_W}^{\phi_E} v^* \, d\phi = \frac{1}{r_0} \frac{\partial \Psi_M}{\partial z*}; \quad r_0 \cos\theta \int_{\phi_W}^{\phi_E} w^* \, d\phi = -\frac{1}{r_0} \frac{\partial \Psi_M}{\partial \theta} \tag{2.27}$$

The maximum of the meridional overturning over the field, Ψ_M^{max}, is used to measure the strength of the overturning circulation. The thermocline depth h is defined here as the depth at which a fraction η of the temperature difference between the surface and the bottom has been achieved, as seen from the surface

$$T_{-h} = T_{surf} - \eta \, (T_{surf} - T_{bot}) \tag{2.28}$$

where T_{-h} is the temperature at $z = -h$, T_{surf} and T_{bot} are the temperature at the surface and at the bottom, respectively, and η is some constant, which was taken 0.9. The situation is sketched in Fig. 2.2. In all scaling relations, the zonally averaged value of h at $\theta = 22\,^\circ$N was taken as a measure of the thermocline depth. No qualitative changes in the scaling relations occurred if $\theta = 42^\circ$N was used instead.

2.5.1 Classical scaling theory

Classical scaling arguments for the thermocline which do not consider the wind forcing nor the freshwater-flux forcing (Welander, 1971) use the thermal wind balance, the continuity

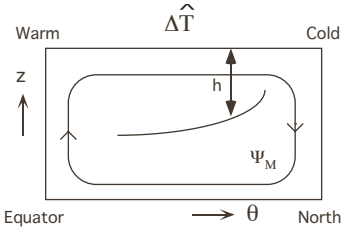

Figure 2.2: *Schematic side-view of the circulation and stratification in a single-hemispheric basin. A characteristic north-south temperature difference is indicated by* $\Delta\hat{T}$.

equation and an advection/diffusion balance of heat at the thermocline to yield

$$\frac{fV}{H} \sim g\alpha\frac{\Delta\hat{T}}{r_0} \tag{2.29a}$$

$$\frac{V}{r_0} \sim \frac{W}{H} \tag{2.29b}$$

$$\frac{V\Delta\hat{T}}{r_0}, \frac{W\Delta\hat{T}}{H} \sim \frac{K_V\Delta\hat{T}}{H^2} \tag{2.29c}$$

Here $f = 2\Omega\sin\theta$ is the Coriolis parameter and H, V and W are scales for the thermocline depth, the horizontal and the vertical velocity, respectively. Further, r_0 has been used as a horizontal length scale of the flow and $\Delta\hat{T}$ is a characteristic meridional temperature difference that drives the circulation. These equations lead to scaling relations for the thermocline depth and the horizontal and vertical velocity, according to

$$H \sim \left(\frac{fr_0^2K_V}{g\alpha_T\Delta\hat{T}}\right)^{\frac{1}{3}} \; ; \; V \sim \frac{K_Vr_0}{H^2} \; ; \; W \sim \frac{HV}{r_0} \tag{2.30}$$

If a scale for the meridional overturning is denoted by Φ_M, the classical scaling theory yields

$$\Phi_M \sim VHr_0 \sim K_V^{2/3}r_0^{4/3}\left(\frac{\Delta\hat{T}g}{2\Omega}\right)^{1/3} \tag{2.31}$$

The vertical diffusivity K_V is often used as a control parameter to check these scaling relations. According to the classical scaling theory $H \sim K_V^{1/3}$ and $\Phi_M \sim K_V^{2/3}$. In a single-hemispheric ocean GCM driven by both buoyancy and wind forcing, Bryan (1987) indeed found $\Phi_M \sim K_V^{2/3}$. Colin de Verdière (1988) obtained the relation $H \sim K_V^{1/3}$ in a planetary geostrophic model without wind forcing. Using the MOM model in a double-hemispheric configuration, Vallis (2000) shows that the classical relations $H \sim K_V^{1/3}$ and $\Phi_M \sim K_V^{2/3}$ are obtained for the case without wind forcing.

If the circulation is driven by both wind and buoyancy forcing, a complicated situation arises: for large vertical diffusivity, buoyancy forcing dominates over wind forcing, while for small values of the vertical diffusivity the wind forcing is dominant. In the latter case, the thermocline depth is determined advectively, and different scaling relations are found

theoretically (Welander, 1971). A detailed numerical investigation of this situation has been performed by Samelson and Vallis (1997) and Vallis (2000). As in most of the studies in this thesis wind forcing is absent, we will compute scaling relations for the case without wind forcing, so that a behavior according to the classical scaling relations is expected.

2.5.2 Scaling relations in THCM

The standard configuration has been used for the computation of scaling relations in THCM. All parameters have values as indicated in Table 2.1, except for K_H, which is increased to $K_H = 1800$ m^{2}s^{-1}. As the meridional temperature difference implied by the restoring boundary condition is $2\eta_T \Delta T$ (with $\Delta T = 1.0$ K, see equation (2.22)), the parameter η_T is a measure of the strength of the buoyancy forcing. To investigate the scaling behavior of the steady solutions, the dependence of the meridional overturning and the thermocline depth on η_T and K_V has been computed. Deviations from classical scaling relations are expected to arise from the use of convective adjustment, which is —unquestionably— an ill-conditioned parameterization of convection in the ocean. Hence, in the results below convective adjustment is first switched off.

A branch of steady-state solutions is computed by increasing the parameter η_T from 0 to its standard value $\eta_T = 10.0$. The meridional overturning streamfunction of the steady state at $\eta_T = 10.0$ is plotted in Fig. 2.3a. It is dominated by a large cell with northward surface flow and sinking around $65°$N, and has a maximum amplitude of 16 Sv. A weak cell that rotates

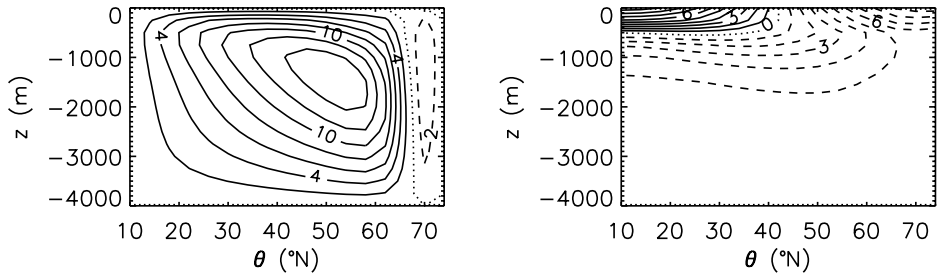

(a) (b)

Figure 2.3: *Steady state solution without convective adjustment. (a) Meridional overturning streamfunction (in Sverdrups). (b) Temperature (dimensionless) for a north-south vertical plane through the middle of the basin ($\phi = 42°$W). The dimensional temperature T^* (in $°C$) can be obtained from* $T^* = 15.0 + \Delta T\, T$.

in opposite direction is present north of $65°$N, due to the absence of convective adjustment. A meridional temperature section along $\phi = 42°$W (Fig. 2.3b) shows a thermocline in the upper 1000 m. Unstable stratification occurs in a layer near the surface north of $45°$N and close to the northern boundary.

The relation between Ψ_M^{max} and η_T is plotted in Fig. 2.4a and shows two regimes: a fit of the first 4 data points yields $\Psi_M^{max} \sim \eta_T^{0.94}$, whereas a fit of the last 7 data points

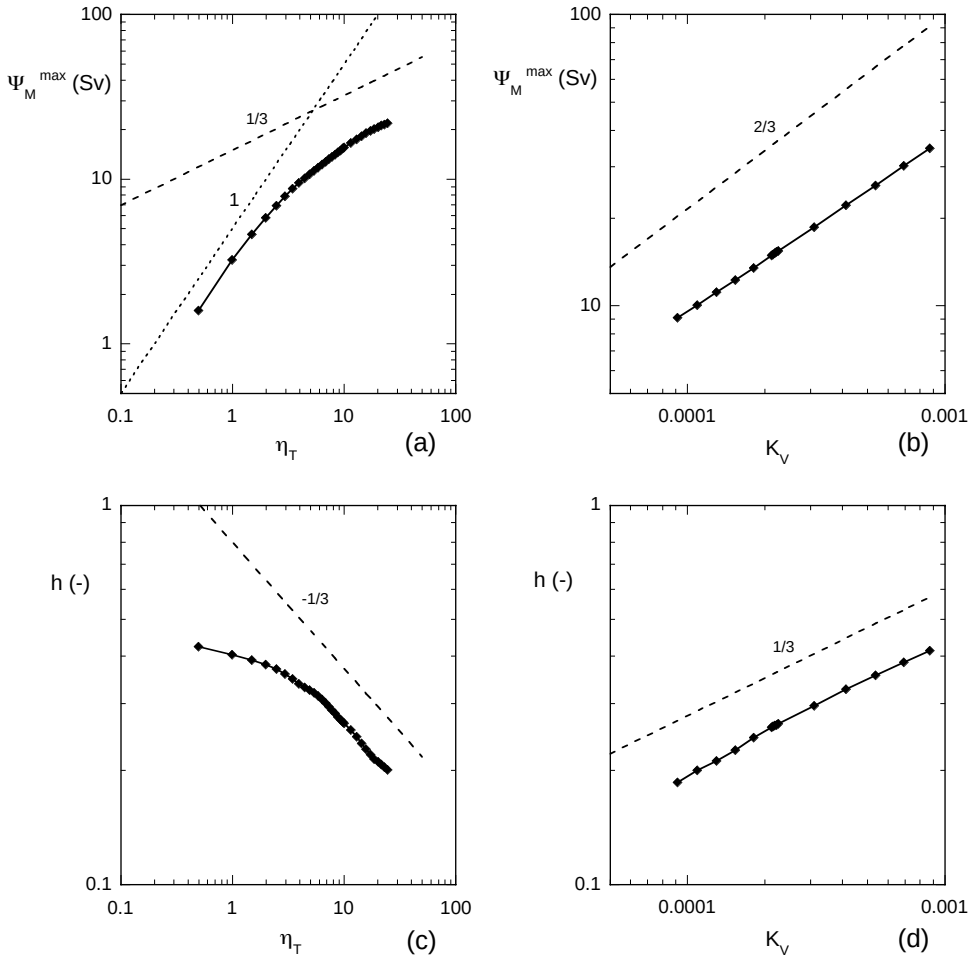

Figure 2.4: *Scaling relations for the solution without convective adjustment. (a) Maximum of the meridional streamfunction (in Sverdrups) as a function of the strength of the buoyancy forcing η_T. (b) Maximum value of the meridional overturning streamfunction as a function of the vertical diffusivity K_V. (c) Dimensionless thermocline depth as a function of η_T. The thermocline depth has been nondimensionalized by scaling with the total depth of the basin. (d) Dimensionless thermocline depth as a function of K_V.*

($\eta_T > 15.7$) yields $\Psi_M^{max} \sim \eta_T^{0.33}$. Thus in the limit of very weak forcing strength, the meridional overturning depends linearly on the strength of the temperature forcing, while for realistic forcing strength (η_T around 10) the classical scaling relation is found. Two regimes are also found in the relation between the thermocline depth and η_T (Fig. 2.4c). A fit of the last 17 points yields $h \sim \eta_T^{-0.33}$, in close correspondence with the classical result. For small values of η_T there is only a weak dependence of h on η_T. The dependence on K_V is also rather close to the classical scaling relations: fits of Ψ_M^{max} and h to K_V yield $\Psi_M^{max} \sim K_V^{0.60}$

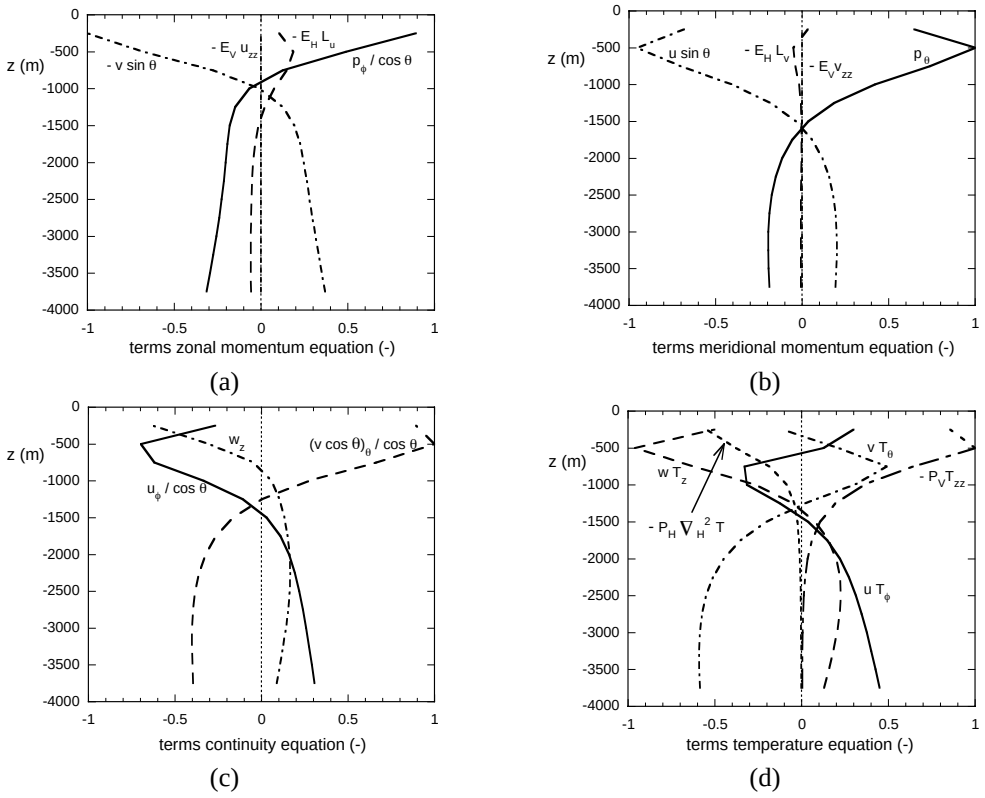

Figure 2.5: *Vertical profile of the (dimensionless) terms in the equations at* $(\phi, \theta) = (48°W, 28°N)$ *for the solution without convective adjustment. The plots are scaled with the maximum values in each plot and subscripts denote differentiation to that variable. (a) Zonal momentum equation. The operator* L_u *is a linear operator denoting horizontal friction. (b) Meridional momentum equation. The linear operator* L_v *denotes horizontal friction. (c) Continuity equation. (d) Temperature equation.*

and $h \sim K_V^{0.35}$ (Figs. 2.4b and 2.4d).

To see if the dominant balances that underly the classical scaling relations apply in the THCM model, the pointwise balances were analyzed for the solution of Fig. 2.3 ($\eta_T = 10.0$ and $K_V = 2.3 \cdot 10^{-4}$ m^{2}s^{-1}). In Fig. 2.5, vertical profiles of the terms in the equations at the point $(\phi, \theta) = (48°\text{W}, 28°\text{N})$ are shown. The dominant balances at this location are a typical example of the balances in the part of the upwelling region lying south of about $40°$ N and outside the viscous 'boundary layers'. The geostrophic balance holds in both the zonal and meridional direction (Fig. 2.5a and b). The horizontal friction terms are not negligible, but do not have a significant effect on the dominant balance. The hydrostatic balance is satisfied by construction and is therefore not shown. At most vertical levels, the three terms in the continuity equation are of the same order of magnitude (Fig. 2.5c). In the temperature equation, two regimes in the vertical can be distinguished (Fig. 2.5d). In the upper 1000 m, the thermocline region, vertical advection of heat is balanced by vertical

diffusion of heat, while below 1500 m depth diffusion becomes negligible and the balance is advective. Between 1000 m and 1500 m depth, an intermediate regime is found in which all terms are of the same order of magnitude. Although there are broad viscous boundary layers in which the dominant balance in the horizontal momentum equations is no longer purely geostrophic, the dominant balances assumed in the classical scaling theory are satisfied in the interior.

The linear relation between overturning and forcing strength in the weak forcing regime is explained by the fact that for very weak forcing the balance in the temperature equation is purely diffusive (not shown), which yields

$$K_H \frac{\Delta\hat{T}}{r_0^2} \sim K_V \frac{\Delta\hat{T}}{H^2} \tag{2.32}$$

The depth of the thermocline is then independent of the flow and scales according to

$$H \sim r_0 \left(\frac{K_V}{K_H} \right)^{\frac{1}{2}} \tag{2.33}$$

Together with geostrophic and hydrostatic equilibrium, this yields

$$\Phi_M \sim \frac{\alpha_T \Delta\hat{T} g K_V r_0^2}{f K_H} \tag{2.34}$$

which shows indeed a linear dependence of Φ_M on $\Delta\hat{T}$.

The effect of convective adjustment on the scaling behavior was tested by computing scaling relations (Fig. 2.6) for $P_V^c = 1.3{\cdot}10^{-2}$, which corresponds to $K_V^c = 3.3{\cdot}10^{-3}$ m^{2}s^{-1}. For η_T around 10, the dependence of the meridional overturning on the temperature forcing still follows the classical scaling relation; a fit to the last 4 data points yields $\Psi_M^{max} \sim \eta_T^{0.35}$ (Fig. 2.6a). A fit of h to η_T for the last 4 points yields $h \sim \eta_T^{-0.19}$ (Fig. 2.6c). Furthermore, fits yield $\Psi_M^{max} \sim K_V^{0.50}$ and $h \sim K_V^{0.43}$ (Figs. 2.6b and 2.6d). Convective adjustment thus introduces non-classical scaling behavior, but the strength of the meridional overturning still follows the classical scaling relations reasonably close.

2.5.3 Scaling relations in MOM

The dependence of the maximum meridional overturning on the strength of the buoyancy forcing η_T has also been computed with MOM, for the same configuration as used in the previous section. The relation between Ψ_M^{max} and η_T is first computed without convective adjustment. For different values of η_T the model is integrated until a steady state has been reached. The maximum meridional overturning is plotted against η_T in Fig. 2.7a. The scaling relation closely corresponds to the one found in THCM (compare to Fig. 2.4a), with a linear regime for weak forcing, and a dependence close to the classical one-third power law for realistic forcing strength ($\eta_T = 10$). In the case with convective adjustment (Fig. 2.7b), where $K_V^c = 10^2$ m^{2}s^{-1} has been used, the relation between meridional overturning and forcing strength is almost the same. The fact that both THCM and MOM give almost identical results close to the classical scaling relations provides confidence that both models can represent the large-scale circulation and stratification rather well.

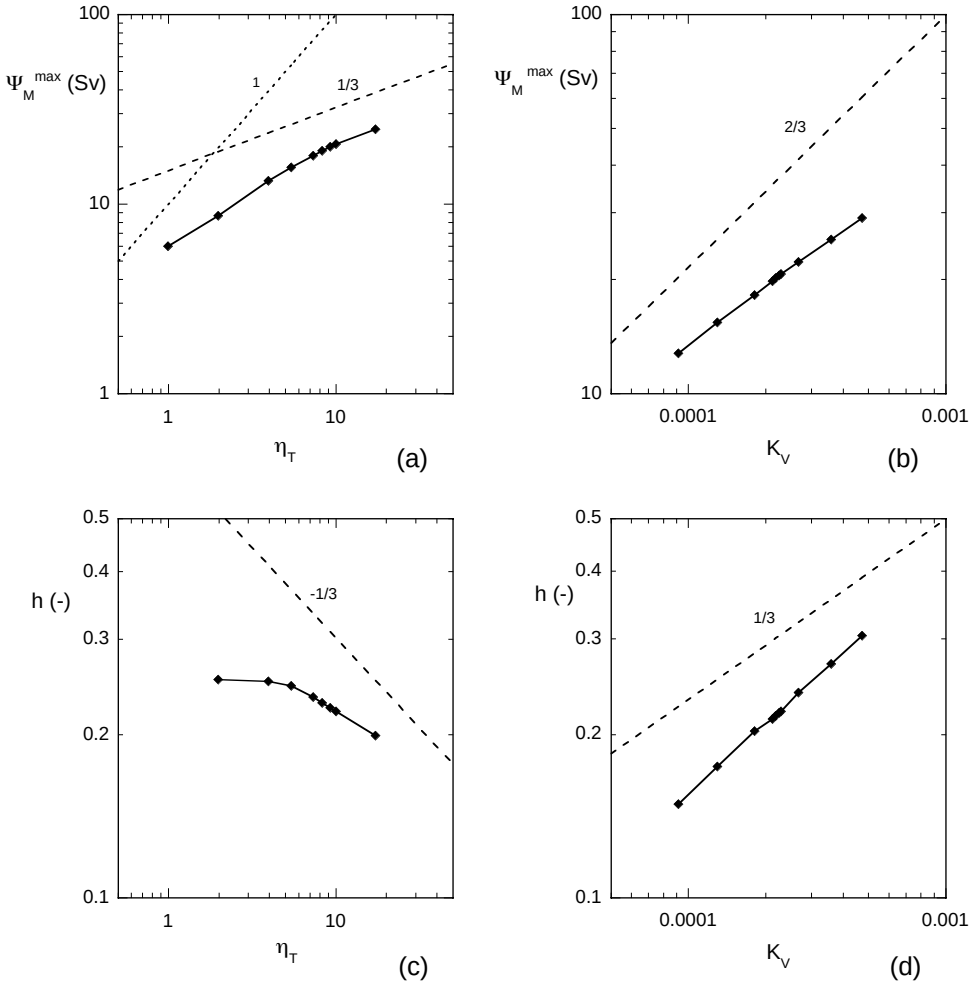

Figure 2.6: *Scaling relations for the solution with convective adjustment. (a) Maximum of meridional overturning streamfunction (in Sverdrups) as a function of the strength of the buoyancy forcing η_T. (b) Maximum value of the meridional overturning streamfunction as a function of the vertical diffusivity K_V. (c) Dimensionless thermocline depth as a function of η_T. (d) Dimensionless thermocline depth as a function of K_V.*

The fact that, despite the high value of A_H, the classical scaling result is found in both models indicates already that the high eddy viscosity does not influence the qualitative behavior of the large-scale circulation and stratification. This was investigated further by computing the relation between Ψ_M^{max} and η_T with the MOM model for the case with $A_H = 1.6 \cdot 10^5$ m^{2}s^{-1} and convective adjustment (Fig. 2.7c). No major differences occur between the scaling relation for $A_H = 1.6 \cdot 10^5$ m^{2}s^{-1} and the one with $A_H = 1.6 \cdot 10^7$ m^{2}s^{-1}, with an approximately linear dependence of Ψ_M^{max} on η_T for weak forcing strength and a de-

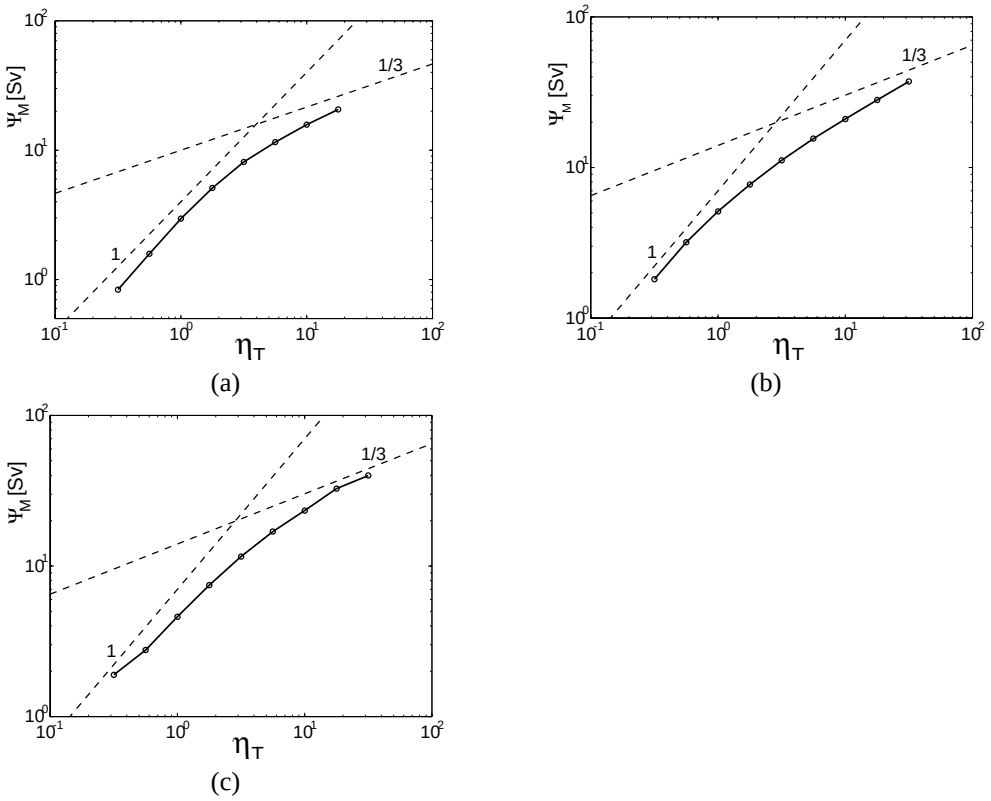

Figure 2.7: *(a) Maximum of meridional overturning streamfunction as a function of the strength of the buoyancy forcing η_T for the case with $A_H = 1.6 \cdot 10^7$ $m^2 s^{-1}$ without convective adjustment. (b) As (a), but for the case with $A_H = 1.6 \cdot 10^7$ $m^2 s^{-1}$ with convective adjustment. (c) As (a), but for the case with $A_H = 1.6 \cdot 10^5$ $m^2 s^{-1}$ and convective adjustment.*

pendence close to the classical relation for realistic forcing strength. It is therefore concluded, that the choice of $A_H = 1.6 \cdot 10^7$ $\mathrm{m^2 s^{-1}}$ in the standard case does indeed not influence the qualitative aspects of the steady large-scale circulation.

Chapter 3

Interdecadal variability under prescribed heat-flux forcing

The stability of purely thermally driven ocean flows in a single-hemispheric sector basin is investigated. Under restoring conditions for the temperature, the flow is stable. However, when forced with the associated heat flux, an interdecadal oscillatory time scale instability appears. This occurs as a Hopf bifurcation when the horizontal mixing coefficient of heat is decreased. The physical mechanism of the oscillation is described by analyzing the potential energy changes of the perturbation flow near the Hopf bifurcation. In the relatively slow phase of the oscillation, a temperature anomaly propagates westwards near the northern boundary on a background temperature gradient, thereby changing the perturbation zonal temperature gradient, with corresponding changes in meridional overturning. This is followed by a relatively fast phase in which the zonal overturning reacts to a change in sign of the perturbation meridional temperature gradient. The different responses of zonal and meridional overturning cause a phase difference between the effect of temperature and vertical velocity anomalies on the buoyancy work anomaly, the latter dominating the changes in potential energy. This phase difference eventually controls the time scale of the oscillation[*].

3.1 Introduction

Climate variability on decadal and interdecadal time scales has recently received a lot of attention. Indications for decadal to interdecadal variability have been found in many climate and climate proxy data, for example global surface air temperatures (Ghil and Vautard, 1991; Schlesinger and Ramankutty, 1994), variations in the formation rate of North Atlantic Deep Water (Roemmich and Wunsch, 1984) and ice core data (Hibler and Johnson, 1979). Knowledge of the patterns and amplitude of natural climate variability on these time scales is of crucial importance in the interpretation of climate change. The short length of the time series of SST and SLP (150 years at the most) causes strong uncertainties in reconstructions of patterns of interdecadal variability in these data.

[*]This chapter is based on the paper '*Instability of the thermohaline ocean circulation on interdecadal time scales*', by L. A. te Raa and H. A. Dijkstra, *J. Phys. Oceanography*, vol **32**, pp. 138-160, 2002

A nice overview of the data that have been analyzed since 1990 and the methods and terminology used can be found in Moron *et al.* (1998). In Deser and Blackmon (1993), the first empirical orthogonal function (EOF) of wintertime mean SST anomalies in the North Atlantic over the period 1900–1989 displays a basin-scale SST pattern with strongest positive anomalies in the Gulf Stream region. The time series of this EOF indicates that this region was colder than average over the period 1900–1940 and warmer over the remaining period. The second EOF is a dipole-like pattern with positive (negative) anomalies in the northern (southern) part of the basin with variability in the time series on decadal scales. Using more than 100 years of SST, SLP and wind data from the COADS dataset, Kushnir (1994) showed that SST, SLP and surface winds exhibit interdecadal variability, with a basin-scale SST pattern having maxima in the Labrador Sea and northeast of Bermuda. Moron *et al.* (1998) applied multi-channel singular spectrum analysis (MSSA) to a monthly time series (1901–1994) of SST anomaly fields to find a 13-year oscillation. Two maxima of opposite signs occur near Cape Hatteras and south of the Denmark Straits, with a peak-to-peak amplitude of about $0.5°$C. Recently, Delworth and Mann (2000) have identified surface temperature variability with a dominant time scale of 70 years with a pattern mostly concentrated in the North Atlantic.

The uncertainty in the patterns of observed variability and the lack of understanding of the physics of this type of variability have stimulated many model studies. The thermohaline ocean circulation is thought to play an important role in many of these studies. In the coupled GFDL model, interdecadal variability was found and analyzed by Delworth *et al.* (1993) and Delworth and Greatbatch (2000). The irregular oscillation has an average period of about 50 years and its pattern roughly corresponds to that found in observations by Kushnir (1994). The oscillation was hypothesized to be associated with density anomalies in the sinking region in the North Atlantic (with much smaller anomalies of the opposite sign in the broad rising region) and their coupling to anomalies in the circulation.

While it has been suggested that the Delworth *et al.* (1993) variability is a coupled ocean-atmosphere phenomenon (Weaver and Valcke, 1998), the study by Delworth and Greatbatch (2000) suggests that the oscillation is mainly caused by the low-frequency component of the atmospheric noise, combined with thermohaline feedbacks. However, decadal to interdecadal variability has also been found in many ocean-only model studies (Weaver *et al.*, 1993; Greatbatch and Zhang, 1995; Weaver and Sarachik, 1991a,b; Chen and Ghil, 1995). Greatbatch and Zhang (1995) find a regular oscillation with a period of 50 years in a single-hemispheric sector ocean model in which the flow is driven only by a time-independent heat flux. The SST anomaly pattern shows very good similarities to that in Delworth *et al.* (1993). Temperature anomalies are advected into the sinking region and change the strength of the overturning circulation with a certain phase lag between temperature and circulation anomalies. Also in other ocean-only model studies driven by a steady buoyancy flux, decadal to interdecadal variability has been found (Winton, 1996; Cai *et al.*, 1998; Huck *et al.*, 1999).

In models in which also the effect of salinity was taken into account by using mixed boundary conditions (Weaver *et al.*, 1993; Chen and Ghil, 1995; Yin and Sarachik, 1995), oscillations with periods between 10 and 50 years have also been found. In the proposed mechanism of these oscillations, a phase difference between density anomalies and changes in convection and overturning strength is involved (Yin, 1995). But despite all modeling efforts, the physical processes that cause this phase difference are still unclear. Winton (1996)

and Greatbatch and Peterson (1996) argue that viscous boundary-trapped waves are a key to interdecadal thermohaline oscillations. Instead, Huck *et al.* (1999) and Colin de Verdière and Huck (1999) suggest that a more general type of waves, with propagation speeds depending on the background stratification, is involved and that the phase difference is caused by both advection and adjustment.

Chen and Ghil (1995) show that the interdecadal oscillation likely arises as a critical parameter value is crossed, i.e. through a Hopf bifurcation. Following this idea, an impressive amount of work was done in a planetary geostrophic model by Huck *et al.* (1999) and Colin de Verdière and Huck (1999), who used the same set-up as Greatbatch and Zhang (1995). Indeed, they find that oscillations occur if the horizontal diffusivity is decreased below a certain value. Guided by the vertical structure of the anomaly fields, baroclinic instability is suggested as a cause of the oscillatory behavior. Different conceptual models have also been put forward to explain the oscillatory behavior and the processes controlling the period (Yin, 1995; Colin de Verdière and Huck, 1999). However, in these simple models the phase difference between the velocity and temperature fields is more or less imposed such that oscillations on interdecadal time scales occur.

Recently, it has become possible to compute directly three-dimensional steady flows of the thermohaline circulation in single-hemispheric models and to assess their linear stability. In this chapter, purely thermally driven flows are considered in the uncoupled ocean model THCM. Within this model, we show that steady states become unstable through a supercritical Hopf bifurcation as a critical value of the horizontal diffusivity is crossed (section 3.2). The physical mechanism of this oscillation is reconsidered by looking at the relevant terms in the perturbation potential energy balance (section 3.3). In the discussion (section 3.4), this physical mechanism is set in context with other mechanisms that have appeared in the literature.

3.2 Results

The results in this chapter have been computed with the THCM model. An increased vertical resolution near the surface was used, by stretching the grid in the z-direction through use of the mapping

$$z = \frac{\tanh(q_z \overline{z})}{\tanh(q_z)} \tag{3.1}$$

Here q_z is a stretching factor, the grid in $\overline{z}$ is equidistant and the grid in z is non-equidistant. A stretching factor $q_z = 2$ has been used in this chapter, which yielded a vertical resolution ranging from 41 m near the surface to 516 m near the bottom. The vertical length scale H_m has been adjusted correspondingly and has been taken $H_m = 41$ m. A horizontal eddy diffusivity $K_H = 1.5 \cdot 10^3$ m^{2}s^{-1} was taken as reference value. For convenience, the values of the eddy viscosities and eddy diffusivities used in this chapter are given in Table 3.1, together with their dimensionless counterparts.

A_H	=	$1.6 \cdot 10^7$	[m^{2}s^{-1}]	A_V	=	$1.0 \cdot 10^{-3}$	[m^{2}s^{-1}]
K_H	=	$1.5 \cdot 10^3$	[m^{2}s^{-1}]	K_V	=	$2.3 \cdot 10^{-4}$	[m^{2}s^{-1}]
E_H	=	$2.7 \cdot 10^{-3}$		E_V	=	$4.3 \cdot 10^{-7}$	
P_H	=	$2.3 \cdot 10^{-3}$		P_V	=	$9.2 \cdot 10^{-4}$	

Table 3.1: *Reference values of mixing parameters used in the numerical computations of chapter 3.*

3.2.1 The interdecadal oscillation

A branch of steady-state solutions under restoring boundary conditions is computed by increasing the parameter η_T, controlling the amplitude of the applied surface temperature (see equation 2.22), from 0 to its standard value $\eta_T = 10.0$. The steady state at $\eta_T = 10.0$ has a maximum meridional overturning of 20 Sv. The overturning streamfunction is plotted in Fig. 3.1a and shows the typical unicellular structure with sinking confined to the northernmost part of the domain. In Figs. 3.1c and e vector plots of the horizontal circulation for certain sections are shown, superposed on contour plots of the vertical velocity. The surface circulation is anti-cyclonic (Fig. 3.1c) with upward vertical velocities at the western part of the basin. A reversed flow occurs near the bottom (Fig. 3.1e), consistent with the overturning flow.

A section of temperature in a north-south vertical plane shows a 'thermocline' in the upper 1000 m, with slight static instabilities in the northern part of the domain (Fig. 3.1b). Surface temperatures show small advective departures (Fig. 3.1d) from the zonally uniform state, while at depth there is only very little variation (Fig. 3.1f). Note that the difference between the maximum and minimum temperature in the latter panel is only 0.7 degree.

The surface heat flux Q_{Td} of the steady state in Fig. 3.1 is shown in Fig. 3.2. The maximum amplitude of the surface heat flux is 45 Wm^{-2}, which is of the right order of magnitude for the North-Atlantic domain (Oberhuber, 1988). The heat flux is negative (positive) in the northern (southern) half of the basin with a slight signature of the western intensification of the ocean flow. The particular state in Fig. 3.1 is also a solution of the steady equations when the flow is forced by the prescribed flux Q_{Td}. In other words, this heat flux is needed to maintain the circulation and a surface temperature which closely matches the imposed temperature T_S.

If one considers the stability of this steady state under restoring boundary conditions (Q_T given by the restoring boundary condition in equation (2.6b)), such that temperature perturbations are considerably damped at the surface, it turns out that this state is linearly stable, because all eigenvalues have negative real part. The least damped oscillatory eigenmodes under restoring boundary conditions have centennial periods and will be investigated in chapter 5. One can also consider the stability of the steady state under the prescribed heat-flux forcing Q_{Td}. In this way, the temperature anomalies are not damped at the surface (Greatbatch and Zhang, 1995). Note that in this case, the temperature is determined up to an additive constant and hence a zero eigenvalue $\sigma = 0$ must appear in the spectrum. Under this forcing condition, the state in Fig. 3.1 is unstable to an eigenmode with a complex pair of eigenvalues $\sigma = 0.012 \pm 0.1966\, i$, which corresponds to an oscillation period

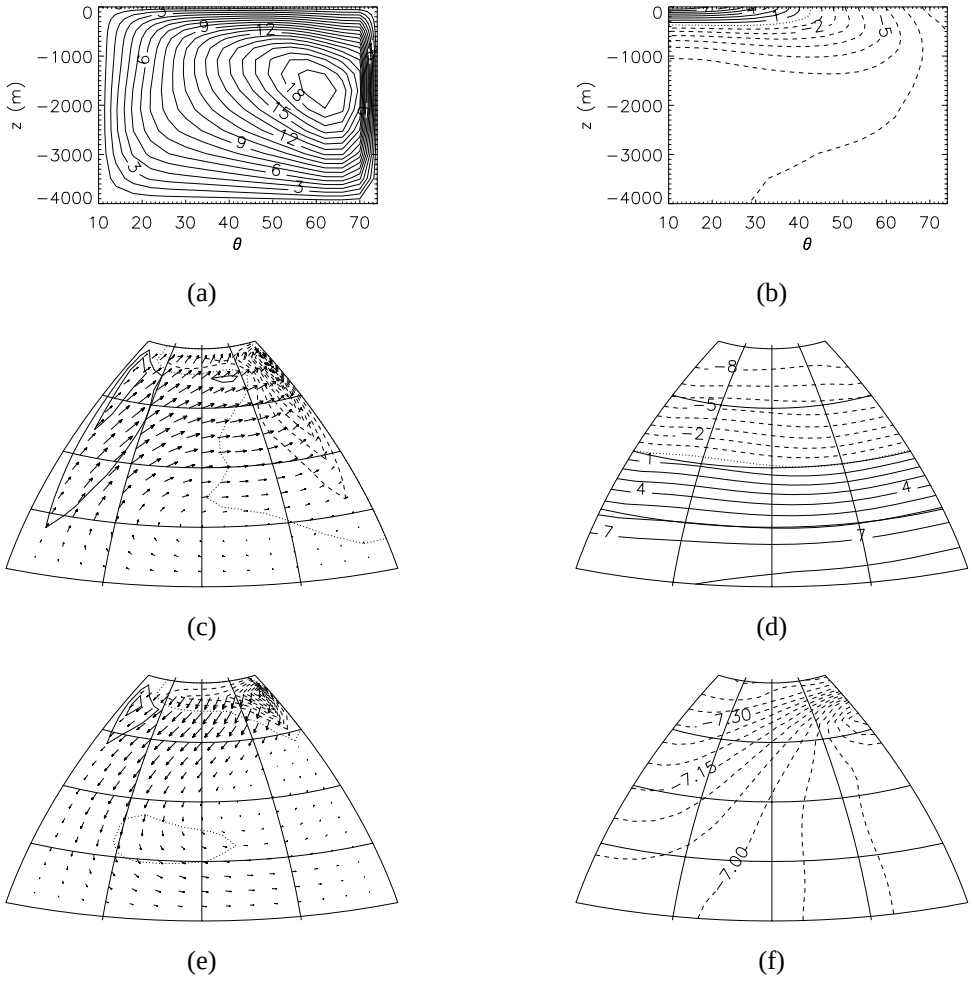

Figure 3.1: *Steady-state solution. (a) Meridional overturning streamfunction (in Sverdrups). (b) Temperature (dimensionless) for a north-south vertical plane through the middle of the basin ($\phi = 42°$W). The dimensional temperature T^* (in $^\circ$C) can be obtained from $T^* = 15.0 + \Delta T\, T$. (c) Velocity (dimensionless) near the surface (at 41 m depth). In this plot, vectors indicate the horizontal velocity, (u, v) and contours represent the dimensionless vertical velocity, w. Solid lines represent upwelling (flow out of the plane), dashed lines downwelling (flow into the plane). The maximum dimensional horizontal velocity is $1.7 \cdot 10^{-2}$ ms^{-1}, the maximum amplitude of the vertical velocity is $1.8 \cdot 10^{-6}$ ms^{-1} (downwelling). (d) Temperature near the surface. (e) Velocity at $z = -3200\, m$. Maxima are $5.5 \cdot 10^{-3}\, ms^{-1}$ for the horizontal and $2.1 \cdot 10^{-5}$ ms^{-1} (downwelling) for the vertical velocity. (f) Temperature at $z = -3200$ m.*

$\mathcal{P} = 2\pi r_0/(U\sigma_i) \approx 65$ years. The imaginary and real parts of the eigenvector $\mathbf{x} = \mathbf{x}_R + i\mathbf{x}_I$ corresponding to this oscillatory pair provide the time periodic disturbance structure $\mathbf{P}(t)$

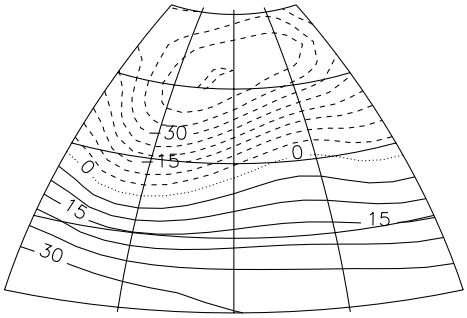

Figure 3.2: *Surface heat flux (in Wm^{-2}), diagnosed from the solution obtained under restoring boundary conditions from Fig. 3.1. Solid lines represent heat gain from the atmosphere, dashed lines heat loss to the atmosphere.*

with angular frequency σ_i and growth rate σ_r to which the steady state is unstable, i.e.

$$\mathbf{P}(t) = e^{\sigma_r t}\,[\mathbf{x}_R\ \cos(\sigma_i t) - \mathbf{x}_I\ \sin(\sigma_i t)] \tag{3.2}$$

The propagation of the perturbations can be followed by looking for example at $\mathbf{P}(\ \frac{-\pi}{2\sigma_i}) = \mathbf{x}_I$ and then at $\mathbf{P}(0) = \mathbf{x}_R$.

Pictures of typical patterns corresponding to $\mathbf{x}_I$ and $\mathbf{x}_R$ are shown in Figs. 3.3 and 3.4, respectively. Note that since these patterns are derived from eigenvectors, the absolute amplitude is arbitrary; only the relative amplitude of the fields within one eigenvector is fixed. To characterize the eigenmode, meridional overturning streamfunction, surface and deep velocities, and three slices of the temperature field are plotted. The mode is clearly not localized but has quite a global structure, although the anomalies reach their maximum amplitudes in the north and near the surface. At $t = -\pi/2\sigma_i$, the meridional overturning perturbation is positive, indicating a strengthening of the northward flow near the surface (Fig. 3.3a). There is anomalous upwelling in the northwest and anomalous downwelling in the northeast of the basin (Fig. 3.3c), with a similar pattern at the bottom of the domain (Fig. 3.3e). Near the surface there is a negative temperature anomaly in the northwestern corner, which extends down to the bottom due to 'convective mixing' (Figs. 3.3b, d and f). Otherwise, the temperature anomaly has quite a baroclinic character. A quarter of a period later, at $t = 0$, the meridional overturning is positive over almost the whole basin and the small oppositely rotating cell in the southern part of the domain that was present at $t = -\pi/2\sigma_i$ has disappeared (Fig. 3.4a). The vertical velocity perturbations have now switched location, with anomalous downwelling (upwelling) in the western (eastern) part of the domain (Figs. 3.4c, e). The temperature perturbation is now positive over most of the northern part of the basin, with a maximum in the northeast (Figs. 3.4b, d and f).

Clearly, there is propagation of both temperature and velocity anomalies. For later reference and for comparison with earlier work, the perturbation vertical velocities (Fig. 3.5) and temperature anomalies (Fig. 3.6) near the surface are plotted over half of the oscillation period. These fields are computed from the real and imaginary part of the eigenvector according to (3.2), where the exponential growth factor is not taken into account. The time

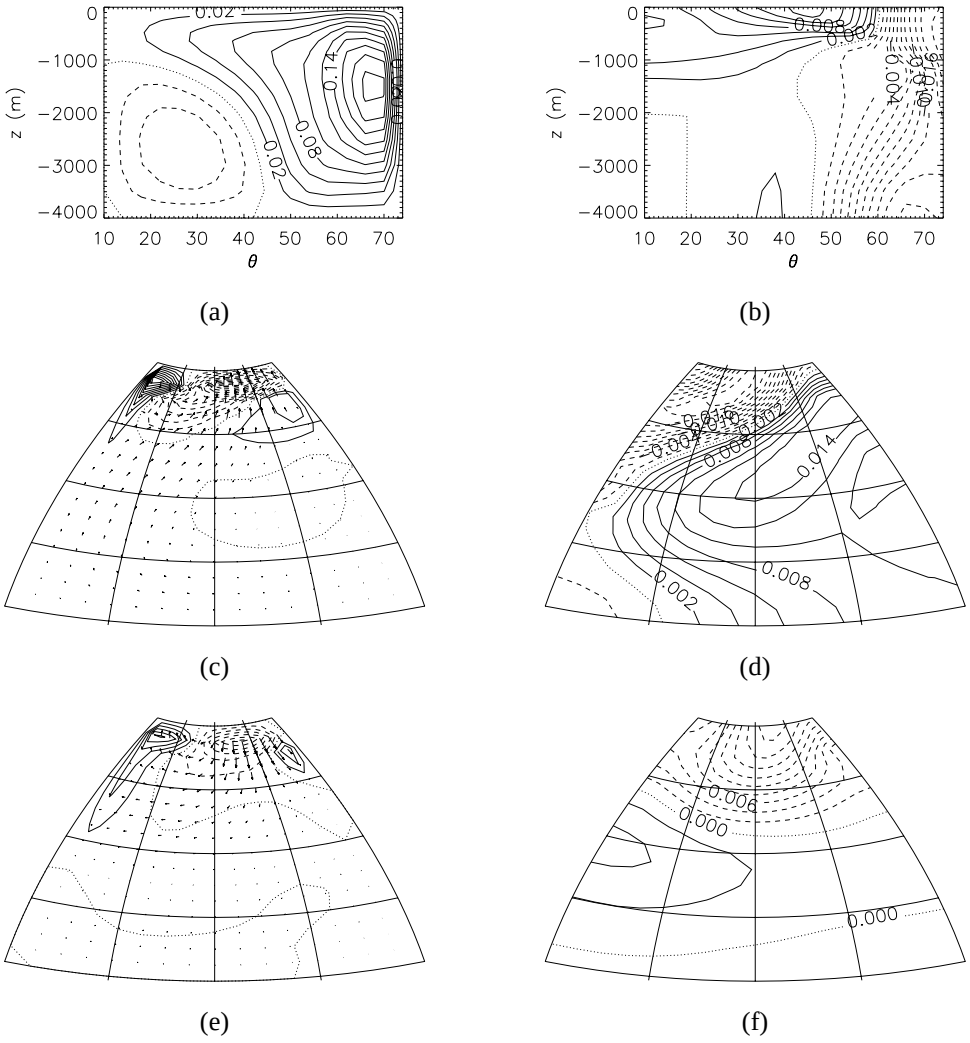

Figure 3.3: *Imaginary part of the eigenvector corresponding to the interdecadal mode ($\sigma_r = 0.0116$, $\sigma_i = 0.1966$). (a) Meridional overturning streamfunction. (b) Temperature for a north-south vertical plane through the middle of the basin. Solid lines represent positive values, dashed lines negative values. (c) Velocity at 41 m depth. (d) Temperature at 41 m depth. (e) Velocity at $z = -3200$ m. (f) Temperature at $z = -3200$ m. Note that the amplitude is arbitrary.*

scale in the figure caption is now dimensional; remember that the period of the oscillation is 65 years. Clearly, the vertical velocity anomalies have their largest amplitudes near the northern boundary and propagate westwards (Fig. 3.5). The positive temperature anomaly at the surface, present at $t = 0$, follows the same propagation as the vertical velocities near

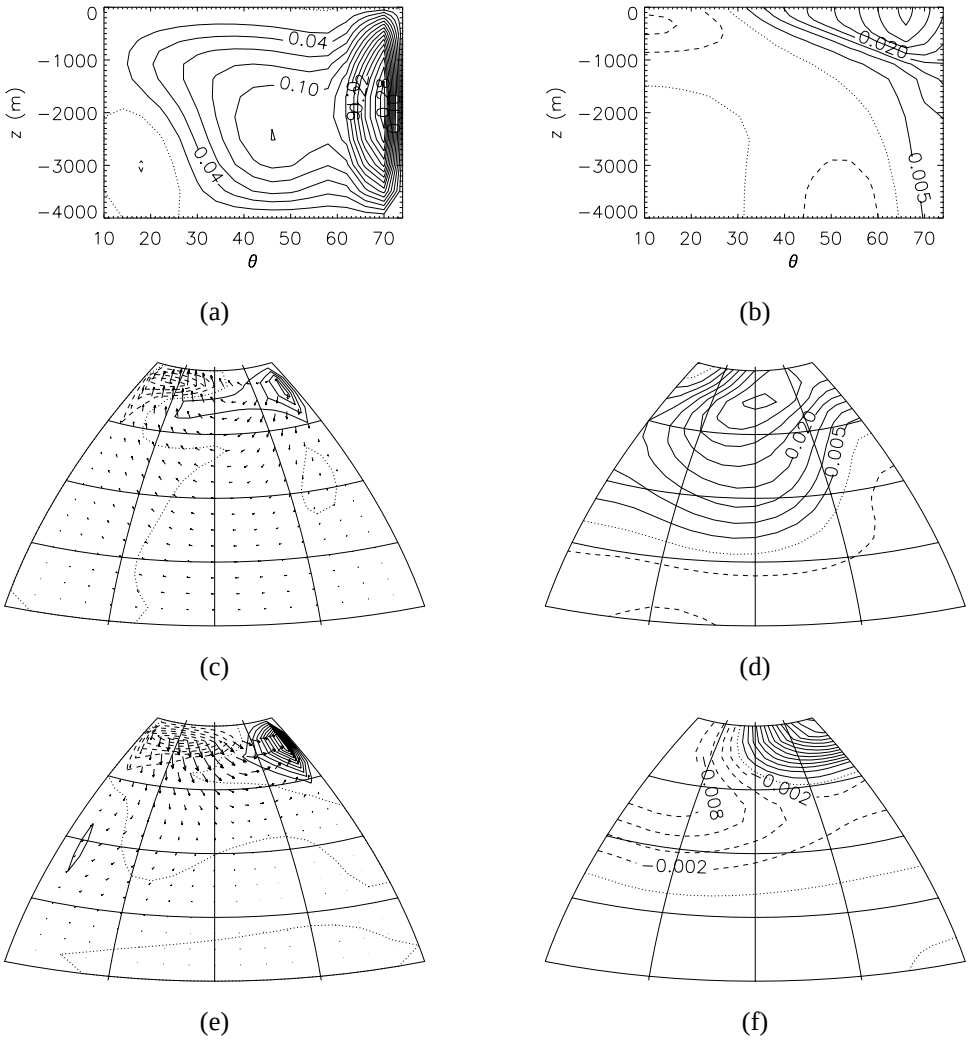

Figure 3.4: *Real part of the eigenvector corresponding to the interdecadal mode. (a) Meridional overturning streamfunction. (b) Temperature for a north-south vertical plane through the middle of the basin. (c) Velocity at* 41 *m depth. (d) Temperature at* 41 *m depth. (e) Velocity at* $z = -3200$ *m. (f) Temperature at* $z = -3200$ *m. Format is similar as in Fig. 3.3.*

the northern boundary (Fig. 3.6). Along the southern boundary, the anomalies are relatively weak and propagate eastwards.

The pattern and propagation behavior of this interdecadal eigenmode resemble those of the 50-year oscillation found by Greatbatch and Zhang (1995). Also Colin de Verdière and Huck (1999) have found an interdecadal oscillation with a period of about 30 years with sim-

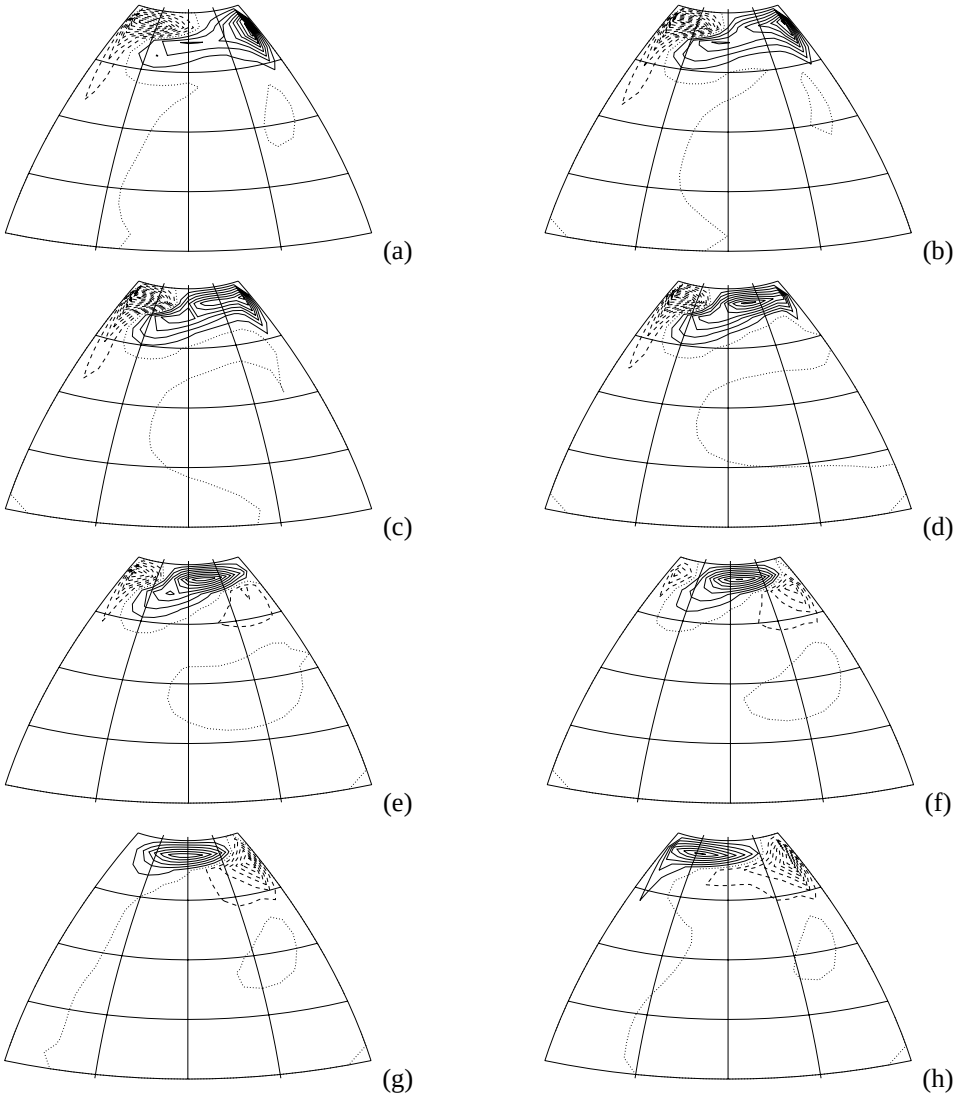

Figure 3.5: *Vertical velocity perturbations at* $z = -19$ *m at (a)* $t = 0$ *yr, (b)* $t = 4.1$ *yr, (c)* $t = 8.1$ *yr, (d)* $t = 12.2$ *yr, (e)* $t = 16.3$ *yr, (f)* $t = 20.3$ *yr, (g)* $t = 24.4$ *yr and (h)* $t = 28.4$ *yr. The plots are 1/16th period apart. Time* $t = 0$ *yr corresponds with the real part of the eigenvector (Fig. 3.4).*

ilar patterns in surface temperature and velocity anomalies. Apart from the western third of the domain, where their temperature anomalies are stationary, they find a westward propagation of temperature anomalies in the northern part of the domain. Huck *et al.* (1999) describe two types of interdecadal oscillations. The first type of oscillatory behavior is characterized by westward propagation of temperature anomalies in the northern part of the basin, while

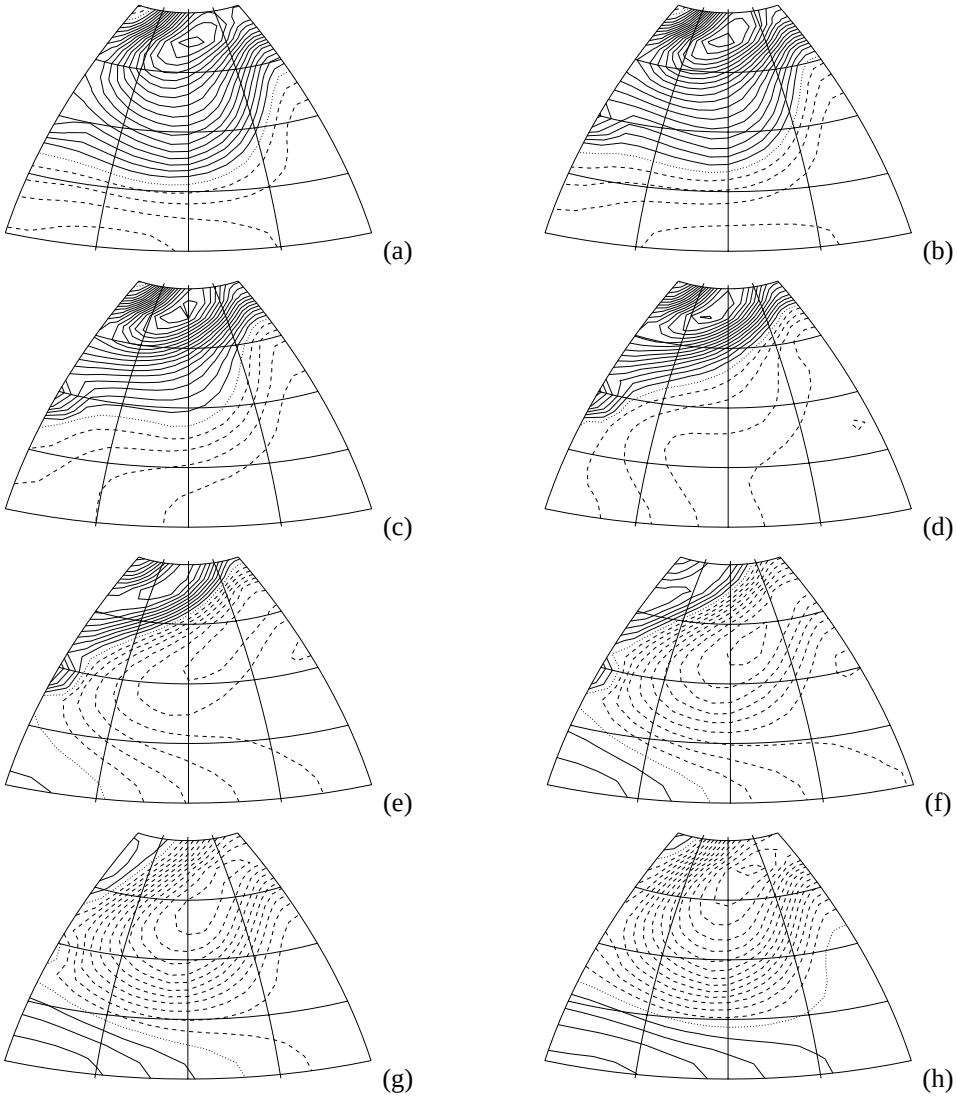

Figure 3.6: *Temperature perturbations at $z = -19$ m at (a) $t = 0$ yr, (b) $t = 4.1$ yr, (c) $t = 8.1$ yr, (d) $t = 12.2$ yr, (e) $t = 16.3$ yr, (f) $t = 20.3$ yr, (g) $t = 24.4$ yr and (h) $t = 28.4$ yr. The plots are 1/16th period apart.*

oscillations of the second type show stationary temperature anomalies in the northwest part of the domain. They argue that, depending on the structure of the prescribed fluxes and the magnitude of the diffusion, westward propagation is either stronger than advection by the mean eastward flow, leading to westward propagating anomalies, or that both effects more or less compensate each other, leading to near-stationary behavior. The interdecadal oscilla-

tion we find here seems to be of the first type, like the one found by Greatbatch and Zhang (1995) and Colin de Verdière and Huck (1999), as there is clear westward propagation in the northern part of the basin.

3.2.2 Regime diagram

The results in Chen and Ghil (1995) and Colin de Verdière and Huck (1999) clearly suggest that the unstable interdecadal mode can be stabilized by increasing the horizontal mixing coefficient of heat (K_H). To investigate the behavior of the growth rate and period with K_H, we have computed steady states under restoring conditions by using K_H as control parameter. For five different states, the surface heat flux was diagnosed and the stability of the steady state determined under prescribed flux conditions (as explained above). The growth rate and period corresponding to the interdecadal mode for the five different values of K_H are shown in Fig. 3.7. The growth rate crosses the zero-axis at $K_H = 1670\ \mathrm{m^2 s^{-1}}$. This indicates that a supercritical Hopf bifurcation occurs with decreasing K_H; the period at criticality is about 69 yr. For $K_H > 1670\ \mathrm{m^2 s^{-1}}$, the steady state is (linearly) stable, but for $K_H < 1670\ \mathrm{m^2 s^{-1}}$ it is unstable. The growth rate increases for smaller K_H and the period shortens slightly, being about 50 years at $K_H = 800\ \mathrm{m^2 s^{-1}}$.

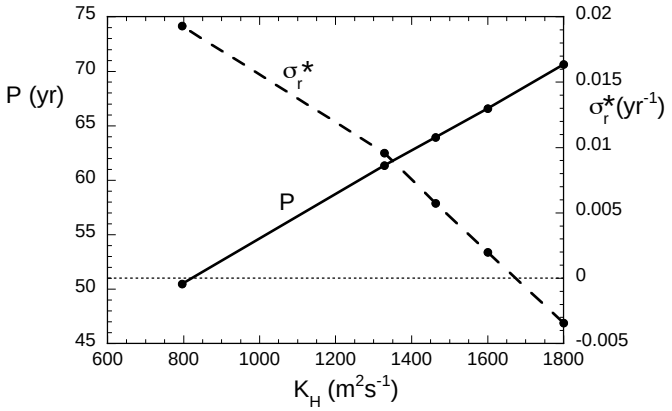

Figure 3.7: *Period (solid line) and growth rate (dashed line) as a function of the horizontal diffusivity K_H. The left vertical axis is for $\mathcal{P}$, the right vertical axis for σ_r^*.*

The location of the Hopf bifurcation defines the parameter value of K_H, at fixed K_V, bounding a steady flow regime and an oscillatory regime. By following the path of this Hopf bifurcation in another parameter, a regime diagram in a two-parameter plane is obtained. In the (K_V, K_H) parameter plane such a diagram (based on only a limited number of points) is plotted in Fig. 3.8. The regime below the curve marked with the open squares is the oscillatory regime. Slightly below this curve, periodic orbits of interdecadal period are expected. Increasing K_H stabilizes the interdecadal mode, while increasing K_V has a destabilizing effect. Changes in K_V have mainly an effect through changes of the steady-state overturning, which increases with increasing K_V. The point labeled with a diamond in Fig. 3.8 indicates

standard conditions and is located in the oscillatory regime. The period of the oscillation increases with decreasing K_V, but remains in the interdecadal range.

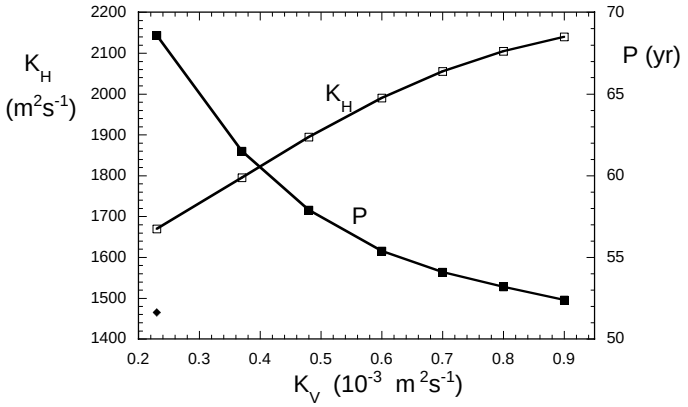

Figure 3.8: *Regime diagram in the (K_V-K_H) plane for the interdecadal oscillation under prescribed flux conditions. Open squares denote the values of K_H for which the Hopf bifurcation occurs. Below this curve, the steady state is unstable and oscillatory behavior is found; above this curve it is stable. The filled squares give the oscillation period at Hopf bifurcation. The point labeled with a diamond indicates the standard values of K_V and K_H.*

The use of convective adjustment is not essential for the occurrence of the oscillations. Convective adjustment decreases the critical K_H-value at Hopf bifurcation; without convective adjustment ($P_V^c = 0$) the critical K_H-value is about 1400 m^{2}s^{-1}. The destabilizing effect of convective adjustment corresponds to the destabilizing effect of K_V on the oscillation (note that convective adjustment corresponds to a local increase of K_V). Convective adjustment decreases the period, again in correspondence with the effect of K_V. Although the influence of bottom topography has not been considered explicitly here, it is expected that bottom topography stabilizes the interdecadal mode (Winton, 1997), since it also decreases the overturning.

The supercritical Hopf bifurcation is in correspondence with the results in Chen and Ghil (1995) and Colin de Verdière and Huck (1999). Huck *et al.* (1999) found that the critical K_H-value varied between 800 and 2500 m^{2}s^{-1}, depending on the model formulation and horizontal resolution used. They also found that convective adjustment was not essential for the oscillation to occur.

3.3 The physics of the interdecadal oscillation

There have been several attempts to describe the physical mechanism of this type of low-frequency (interdecadal) oscillations. To our opinion, to obtain a satisfactory description one has to separate growth of perturbations under unstable conditions from the physical mechanism which causes the oscillatory behavior.

3.3.1 Growth of perturbations

To understand why the interdecadal mode is unstable under a forcing with prescribed flux conditions, we must consider the growth of perturbations (below indicated by quantities with a tilde) on a particular steady state (below indicated by quantities with a bar). This is described by the equation for temperature perturbations

$$\frac{\partial \tilde{T}}{\partial t} + \bar{\boldsymbol{u}} \cdot \nabla \tilde{T} + \tilde{\boldsymbol{u}} \cdot \nabla \bar{T} + \tilde{\boldsymbol{u}} \cdot \nabla \tilde{T} = P_H \nabla_H \cdot \left(\nabla_H \tilde{T} \right) + P_V \frac{\partial}{\partial z} \left(\frac{\partial \tilde{T}}{\partial z} \right) + \tilde{Q}_T G(z) \quad (3.3)$$

where $\boldsymbol{u} = (u, v, w)^T$ and $\tilde{Q}_T$ is given by

$$\tilde{Q}_T = \begin{cases} -Bi\,\tilde{T} & \text{restoring} \\ 0 & \text{prescribed flux} \end{cases}$$

Multiplying by $\tilde{T}$, integrating over the flow domain and averaging over one oscillation period gives

$$\frac{1}{2} \overline{\frac{\partial <\tilde{T}^2>}{\partial t}} = -\overline{<\tilde{T}\,\tilde{\boldsymbol{u}} \cdot \nabla \bar{T}>} + \overline{<\tilde{T} \tilde{Q}_T G(z)>} - \overline{<\mathcal{D}_T>} \quad (3.4)$$

where $\mathcal{D}_T$ is the buoyancy dissipation, brackets $<\cdot>$ denote volume integration and a long bar denotes averaging over the period.

Note that $\overline{<\tilde{T}\,\boldsymbol{u} \cdot \nabla \tilde{T}>} = \overline{\frac{1}{2} <\boldsymbol{u} \cdot \nabla \tilde{T}^2>} = 0$ because of kinematic boundary conditions. This equation is essentially the volume-integrated equation for the available potential energy (Huang, 1998). Since $\overline{<\mathcal{D}_T>}$ is always positive definite, growth can only occur if the first term on the right-hand side is positive, i.e. if $\overline{<\tilde{T}\,\tilde{\boldsymbol{u}} \cdot \nabla \bar{T}>}$ is negative. The latter term is interpreted as the change of available potential energy due to interaction of the buoyancy perturbation and the anomalous buoyancy advection. The restoring boundary condition introduces an extra damping term $\overline{-<Bi\,\tilde{T}^2 G(z)>}$, which is absent under flux conditions.

The relative magnitudes of the terms in equation (3.4) under both restoring and flux conditions are given in Table 3.2. Upon a switch from restoring to flux conditions, the damping

	$\overline{-<\tilde{T}\,\tilde{\boldsymbol{u}} \cdot \nabla \bar{T}>}$	$\overline{<\tilde{T}\tilde{Q}_T G(z)>}$	$\overline{-<\mathcal{D}_T>}$	$\frac{1}{2}\overline{<\tilde{T}^2>}_t$
Restoring	0.73	-0.32	-1.0	-0.59
Flux	1.12	0.0	-1.0	0.12

Table 3.2: *Dimensionless terms in equation (3.4) under restoring and flux boundary conditions. Values are scaled with the absolute value of the dissipation.*

term from the restoring boundary condition disappears, but this alone is not enough to make $\partial \overline{<\tilde{T}^2>}/\partial t$ positive. Also the slight changes in the pattern of the eigenmode that occur upon a switch from restoring to flux conditions are important, as these cause an increase in the advective contribution, relative to the dissipation.

K_H (m^{2}s^{-1})	K_V (^{2}s^{-1})	$-\overline{<\tilde{T}\,\tilde{\boldsymbol{u}}\cdot\nabla\bar{T}>}$		$-\overline{<\mathcal{D}_T>}$		$\frac{1}{2}\overline{<\tilde{T}^2>_t}$
796.0	$2.3\cdot10^{-4}$	1.36	(0.82, 0.54)	-1.0	(-0.61, -0.39)	0.36
1460.0	$2.3\cdot10^{-4}$	1.12	(0.80, 0.32)	-1.0	(-0.81, -0.19)	0.12
1800.0	$2.3\cdot10^{-4}$	0.99	(0.75, 0.24)	-1.0	(-0.89, -0.11)	-0.01
K_H (m^{2}s^{-1})	K_V (m^{2}s^{-1})	$-\overline{<\tilde{T}\,\tilde{\boldsymbol{u}}\cdot\nabla\bar{T}>}$		$-\overline{<\mathcal{D}_T>}$		$\frac{1}{2}\overline{<\tilde{T}^2>_t}$
1460.0	$2.3\cdot10^{-4}$	1.12	(0.80, 0.32)	-1.0	(-0.81, -0.19)	0.12
1460.0	$3.7\cdot10^{-4}$	1.20	(0.87, 0.33)	-1.0	(-0.81, -0.19)	0.20
1460.0	$7.0\cdot10^{-4}$	1.66	(1.35, 0.31)	-1.0	(-0.75, -0.25)	0.66

Table 3.3: *Dimensionless terms in equation (3.4) for different values of K_H and K_V under prescribed flux conditions. Values are scaled with the absolute value of the total dissipation. The numbers between brackets in the third column are the values of the horizontal and vertical component of $-\overline{<\tilde{T}\,\tilde{\boldsymbol{u}}\cdot\nabla\bar{T}>}$, respectively and the numbers between brackets in the fourth column are the horizontal and vertical dissipation, respectively. The terms for standard values ($K_H = 1460\ m^2s^{-1}$, $K_V = 2.3\cdot10^{-4}\ m^2s^{-1}$) are given twice for convenience.*

The changes in growth rate with varying K_H and K_V (section 3.2.2) can also be understood by looking at the terms in equation (3.4). For several values of K_H and K_V the relative magnitudes of these terms are given in Table 3.3. With increasing K_H, advection becomes less important with respect to the total dissipation (Table 3.3), mainly due to a relative decrease in the vertical advection. Eventually, the growth rate for $K_H = 1800$ m^{2}s^{-1}, $K_V = 2.3\cdot10^{-4}$ m^{2}s^{-1} becomes negative, in correspondence with Fig. 3.7. If K_V is increased, the advection increases relative to the total dissipation. A larger vertical diffusivity causes a stronger circulation, resulting in a relatively larger contribution of the horizontal advective term (Table 3.3), which has a destabilizing effect.

The term $\overline{<\tilde{T}\,\tilde{\boldsymbol{u}}\cdot\nabla\bar{T}>}$ was considered in Colin de Verdière and Huck (1999) and used to demonstrate the growth of perturbations leading to the interdecadal oscillation in their model. While this approach and their conclusions are correct, there are two subtleties.

(i) Colin de Verdière and Huck (1999) consider as perturbation the difference between the equilibrated periodic orbit at supercritical conditions and a reference state. In this case, either this reference state and/or the time mean state may not satisfy exactly the steady equations, so that other production terms appear in (3.4). These terms will become larger as one is further away from critical conditions. In our approach here, this problem does not occur, because the underlying unstable steady state and the eigenvectors are available.

(ii) The production term $\overline{<\tilde{T}\,\tilde{\boldsymbol{u}}\cdot\nabla\bar{T}>}$ may explain growth of perturbations but, apart from its cumbersome interpretation, it is also not mechanistically selective. Every type of instability must have this term negative in the unstable regime.

Hence, it is important to distinguish between the growth of perturbations and the physical mechanism driving the oscillation. In understanding the mechanism, the crucial point is to

explain the phase difference between active fields in the oscillation (i.e. temperature and velocity fields). This will also indicate which physical processes determine the time scale of oscillation. In previous papers, this is recognized (Colin de Verdière and Huck, 1999), but a clear description of the physics of this phase difference has not been given.

3.3.2 Buoyancy work changes

As a means of analyzing what happens during the oscillation, the changes in potential energy along an oscillation cycle are considered. The balance for the dimensionless volume-integrated potential energy $\mathcal{U} = <-zT>$ is obtained directly from the temperature equation (2.5e) and becomes

$$\frac{d\mathcal{U}}{dt} = - <wT> + <z(P_V T_z)_z> + <z\, Q_T G(z)> \tag{3.5}$$

where the subscript z denotes differentiation to that variable. If one considers infinitesimal perturbations on a steady state, then the potential energy balance of the perturbations becomes

$$\frac{d\tilde{\mathcal{U}}}{dt} = -(<\bar{w}\tilde{T}> + <\tilde{w}\bar{T}>) + <z(P_V \tilde{T}_z)_z> \tag{3.6}$$

The first term on the right-hand side of (3.6) denotes the production (or destruction) of potential energy due to the effect of temperature perturbations on the mean flow, while the second term denotes the production (or destruction) of potential energy due to the effect of flow perturbations on the background stratification. The last term in (3.6) provides the change in potential energy due to changes in the stratification. The interpretation of $<\bar{w}\,\tilde{T}>$ is as follows: in a situation of steady-state downwelling ($\bar{w} < 0$) and a negative temperature perturbation ($\tilde{T} < 0$), relatively cold water is transported downwards, thereby decreasing the potential energy of the flow. Similar interpretations hold for the other terms (Huang, 1998). The first two terms on the right-hand side of (3.6) turn out to be dominant in the perturbation potential energy budget. The maximum value of the term $<z(P_V \tilde{T}_z)_z>$ is only 18 % of the maximum of $<\tilde{w}\bar{T}>$ and 14 % of the maximum of $<\bar{w}\tilde{T}>$.

The first two terms of the right-hand side in (3.6) are directly related to the mechanical energy balance of the flow. This balance can be obtained by multiplying the momentum equations by the velocity field and integrating over the domain, which gives

$$\varepsilon_R \frac{d\mathcal{E}}{dt} = <wT> - <\mathcal{D}_M> \tag{3.7}$$

where $\mathcal{E} = \frac{1}{2} <u^2 + v^2>$ is the volume-integrated kinetic energy of the flow and $\mathcal{D}_M$ is the dissipation of kinetic energy. Because the momentum equations are approximately diagnostic (and in our computations fully diagnostic, as we chose $\varepsilon_R = 0$), changes in the buoyancy work $<wT>$ induce changes in the kinetic energy, but these are instantaneously (with respect to the large time scale of the oscillation) balanced by dissipation. As there are no other production terms in (3.7), the changes in $<wT>$ are controlling the oscillatory behavior of the kinetic energy of the full three-dimensional flow.

In Fig. 3.9, the terms $<\bar{w}\tilde{T}>$ and $<\tilde{w}\bar{T}>$ are plotted during one oscillation cycle for the oscillation described in section 3.2.1 (with $K_H = 1460$ m^{2}s^{-1}). A phase difference exists

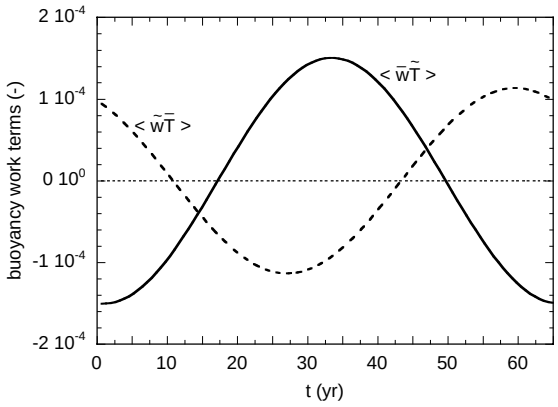

Figure 3.9: *Dimensionless terms* $<\bar{w}\tilde{T}>$ *(solid line) and* $<\tilde{w}\bar{T}>$ *(dashed line) as a function of time (in years) for one oscillation cycle.*

between both terms of the perturbation buoyancy work. About 26 years after $<\bar{w}\,\tilde{T}>$ has reached its minimum amplitude, $<\tilde{w}\bar{T}>$ is at a minimum, after which it takes about 6 years before $<\bar{w}\tilde{T}>$ reaches a maximum. Then the second half of the oscillation occurs in reversed order. The phase difference between these two fields drives the oscillatory behavior of the basin-integrated buoyancy work and hence through the coupling to the mechanical energy balance causes the oscillatory changes in the full three-dimensional flow.

The spatial patterns of $\bar{w}\tilde{T}$ and $\tilde{w}\bar{T}$ in a horizontal plane near the surface have been plotted for different phases of the oscillation in Figs. 3.10 and 3.11, respectively. The pattern of $\bar{w}\tilde{T}$ has a basin-wide structure, with the largest amplitudes near the northern boundary (Fig. 3.10), as the background vertical velocity is much larger there than in the rest of the basin. Temperature anomalies propagate in the northward and westward direction, which can be seen in the pattern of $\bar{w}\tilde{T}$. Near the northern boundary the anomalies extend to the bottom due to convection, but in the rest of the basin the signal has a baroclinic character. In contrast to the basin-scale patterns of $\bar{w}\tilde{T}$, the spatial pattern of $\tilde{w}\bar{T}$ (Fig. 3.11) seems to be confined to a band in the northern part of the basin, in which the vertical velocity anomalies propagate westwards. To establish the effect of the propagation of the w- and T-anomalies on the fields of $\bar{w}\tilde{T}$ and $\tilde{w}\bar{T}$ more clearly, Hovmöller diagrams of $\bar{w}\,\tilde{T}$ and $\tilde{w}\bar{T}$ are plotted along a line at the surface near the northern boundary (Fig. 3.12). Westward propagation of w-anomalies can be seen in the pattern of $\tilde{w}\bar{T}$ during the whole oscillation, while the propagation of T-anomalies occurs mainly between $t = 15$ yr and $t = 30$ yr and between $t = 45$ yr and $t = 60$ yr and is seen in $\bar{w}\tilde{T}$. Hence, to understand the phase difference between $<\bar{w}\,\tilde{T}>$ and $<\tilde{w}\bar{T}>$, we have to go back to the evolution of the temperature and vertical velocity anomalies (Fig. 3.5 and 3.6).

3.3.3 Origin of the phase difference

To explain how the propagation of the velocity and temperature perturbations induces the phase difference in the buoyancy work terms, we start with the situation at $t = 0$ yr (but

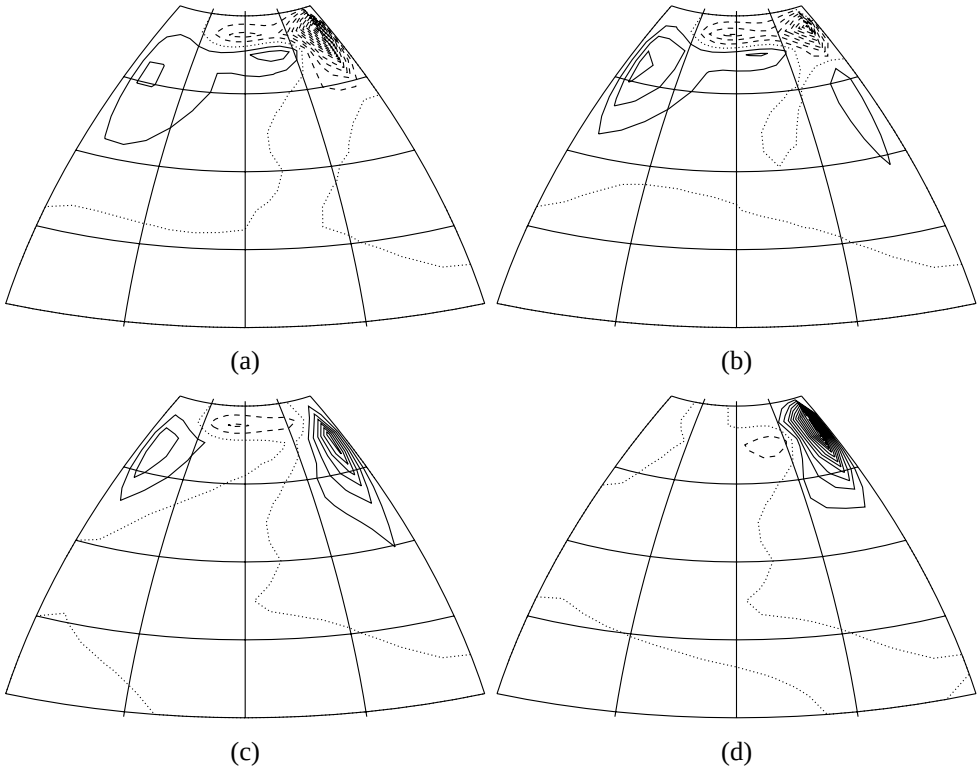

Figure 3.10: *Pattern of $\bar{w}\tilde{T}$ at a horizontal slice just below the surface (at $z = -19$ m) at (a) $t = 0$ yr, (b) $t = 8.1$ yr, (c) $t = 16.3$ yr and (d) $t = 24.4$ yr. The time interval between the plots is 1/8th period and the variables are normalized with the maximum value.*

we may take any point along the oscillation). At this stage, a positive temperature anomaly is present in the northern part of the basin (Fig. 3.6a) and propagates slowly westwards. In Fig. 3.13, the different advective terms in the perturbation temperature equation (3.3) are plotted along a zonal section near the northern boundary at the surface. The dominant advective terms, except near the eastern boundary, are given by

$$\frac{\partial \tilde{T}}{\partial t} \approx -\left(\tilde{v}\frac{\partial \bar{T}}{\partial \theta} + \frac{\bar{u}}{\cos\theta}\frac{\partial \tilde{T}}{\partial \phi} \right) \tag{3.8}$$

Using this balance, an estimate of the time scale of propagation can be derived (generalizing earlier work in Colin de Verdière and Huck (1999)) by using approximate analytic expressions for the perturbation meridional geostrophic velocity. This velocity can be expressed in terms of the zonal derivative of the temperature perturbation, as is derived in appendix B. The temperature perturbation in the north-central part of the basin satisfies to a reasonable approximation an exponential decrease, i.e.

$$\tilde{T}(\phi, \theta, z, t) = e^{\kappa z}\hat{T}(\phi, \theta, t) \tag{3.9}$$

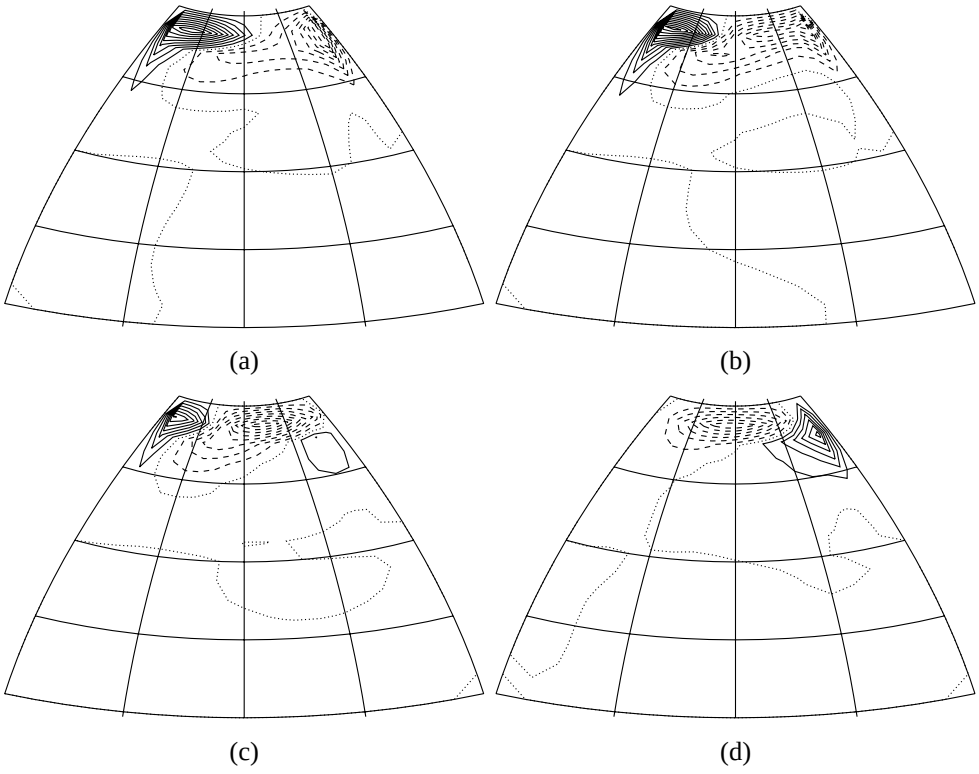

Figure 3.11: *Pattern of $\tilde{w}\bar{T}$ at a horizontal slice just below the surface (at $z = -19$ m) at (a) $t = 0$ yr, (b) $t = 8.1$ yr, (c) $t = 16.3$ yr and (d) $t = 24.4$ yr. Format as in Fig. 3.10.*

with κ a constant. Using this approximation, the integrals over depth in (B.3a) in appendix B can be evaluated exactly. This gives

$$\frac{\partial \hat{T}}{\partial t} - \frac{c}{\cos\theta}\frac{\partial \hat{T}}{\partial \phi} \approx 0 \tag{3.10}$$

where c is a phase speed of propagation of temperature anomalies ($c > 0$ indicates westward propagation), which at the surface is given by

$$c = -\left[\bar{u} + \hat{\alpha}\frac{Ra}{\sin\theta}\frac{\partial \bar{T}}{\partial \theta}\right] \tag{3.11}$$

where $\hat{\alpha} = 1/\kappa - 1/\kappa^2 + e^{-\kappa}/\kappa^2$. This phase speed is characteristic of the propagation of temperature anomalies on a background basic-state temperature (or potential vorticity) gradient. For example, a warm anomaly in a negative mean temperature gradient will induce northward (southward) perturbation velocities west (east) of the center of the anomaly. The perturbation velocities advect warm (cold) water northwards (southwards) west (east) of the initial anomaly, thereby moving the anomaly to the west (Colin de Verdière and Huck, 1999).

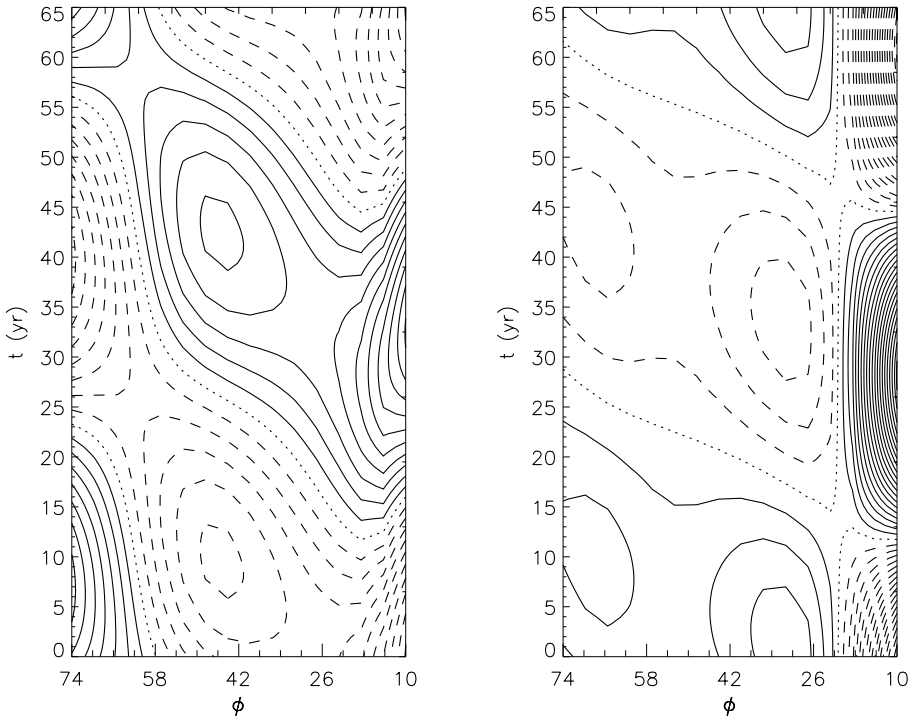

Figure 3.12: *Hovmöller diagram of (a) $\tilde{w}\bar{T}$ and (b) $\bar{w}\tilde{T}$ just below the surface (at $z = 19$ m depth) at $\theta = 68°N$. Both plots are normalized with their maximum values.*

We can use equation (3.11) to estimate the order of magnitude of the phase speed. As the phase speed is a relatively small difference between two large terms, we can only try to determine an estimate of the maximum speed in both eastward and westward direction. The anomalies reach their maximum amplitude in the northern part of the basin, so that the magnitude of $\bar{u}$ and $\partial\bar{T}/\partial\theta$ can be estimated by averaging over the horizontal area $[68°\text{W}, 16°\text{W}] \times [60°\text{N}, 72°\text{N}]$. Furthermore the anomalies are mostly confined to the upper 500 m. This yields estimates of $\bar{u} = 0.13$, $\partial\bar{T}/\partial\theta = -12$ at $z = -19$ m, and $\bar{u} = 0.06$, $\partial\bar{T}/\partial\theta = -10$ at $z = -557$ m, while averages over the upper 7 model layers (the upper 557 m) give $\bar{u} = 0.09$, $\partial\bar{T}/\partial\theta = -11$. Exponential fits of the temperature perturbation in the north-central part of the basin at $t = 0$ yr give $\hat{\alpha} = 0.25$ [at $(\phi, \theta) = (40°\text{W}, 72°\text{N})$] and $\hat{\alpha} = 0.21$ [at $(\phi, \theta) = (44°\text{W}, 72°\text{N})$]. Combination of these estimates yields that the dimensional phase speed can range between $c^* = 7 \cdot 10^{-3}$ ms^{-1} in westward direction and $c^* = 4 \cdot 10^{-3}$ ms^{-1}in eastward direction. With such phase speeds, a westward propagating temperature anomaly along the northern boundary needs at least 10 years to cross the basin from east to west. This results in oscillation periods on decadal or longer time scales.

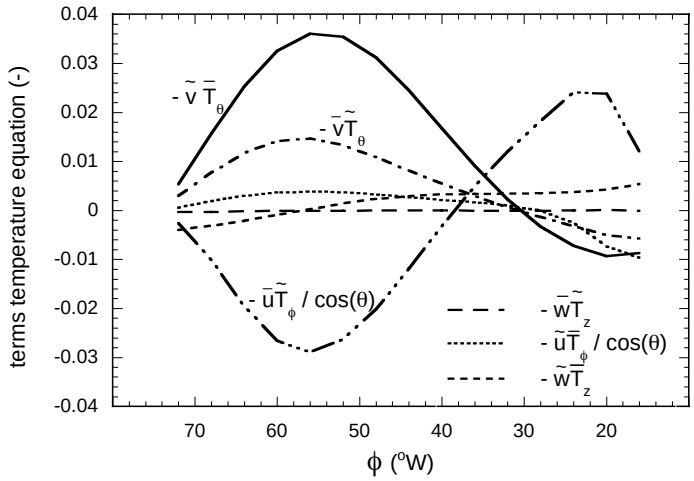

Figure 3.13: *Advective terms in the perturbation temperature equation as a function of longitude along the northern boundary ($\theta = 68^\circ$N) at $t = 0$ yr.*

Analogous to the meridional overturning streamfunction defined in equation (2.27), a dimensional zonal overturning streamfunction Ψ_Z can be defined as

$$\int_{\theta_S}^{\theta_N} u^* \, d\theta = -\frac{1}{r_0}\frac{\partial \Psi_Z}{\partial z^*}; \quad r_0 \int_{\theta_S}^{\theta_N} w^* \cos\theta = \frac{1}{r_0}\frac{\partial \Psi_Z}{\partial \theta} \tag{3.12}$$

In appendix B, expressions are derived for approximations to the meridional and zonal perturbation overturning streamfunctions $\tilde{\Psi}_M$ and $\tilde{\Psi}_Z$, respectively, in terms of the temperature anomalies, for example,

$$\tilde{\Psi}_M(\theta, z, t) = -\int_{-1}^{z} \left[\int_{\phi_W}^{\phi_E} \frac{Ra}{\sin\theta} f_\phi(\phi, \theta, z', t) d\phi \right] dz' \tag{3.13a}$$

$$f_\phi(\phi, \theta, z, t) = \int_{-1}^{z} \frac{\partial \tilde{T}}{\partial \phi} dz' - \int_{-1}^{0} \left(\int_{-1}^{z} \frac{\partial \tilde{T}}{\partial \phi} dz' \right) dz \tag{3.13b}$$

with a similar expression relating the zonal overturning perturbation to the average meridional perturbation temperature gradient (see (B.4) and (B.5) in appendix B). It is clear from equation (3.13) that the perturbation meridional overturning is directly related to the east-west perturbation temperature difference and similarly, that the perturbation zonal overturning is related to the north-south perturbation temperature difference. In Fig. 3.14a, the vertically averaged north-south perturbation temperature difference ΔT_{N-S} and the vertically averaged east-west perturbation temperature difference ΔT_{E-W} are plotted during one oscillation cycle. The spatially averaged meridional and zonal overturning anomalies $\tilde{\Psi}_{M,av}$ and $\tilde{\Psi}_{Z,av}$ are plotted in Fig. 3.14b during one oscillation cycle. During the slow propagation of the positive temperature anomaly westwards (say from $t = 0$ yr to $t = 15$ yr), ΔT_{N-S} hardly changes (Fig. 3.14a) and hence the zonal overturning perturbation remains negative (Fig. 3.14b). This

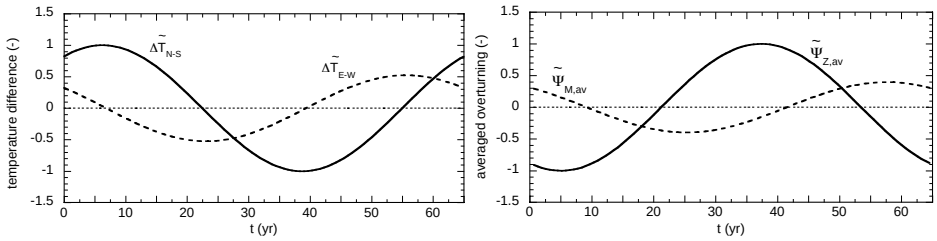

(a) (b)

Figure 3.14: *(a) Zonally averaged north-south temperature difference ΔT_{N-S} (solid line) and meridionally averaged east-west temperature difference ΔT_{E-W} (dotted line), both averaged over the upper 1525 m, as a function of time during one oscillation cycle. (b) Spatially averaged meridional overturning perturbation $\tilde{\Psi}_{M,av}$ (dashed line) and spatially averaged zonal overturning perturbation $\tilde{\Psi}_{Z,av}$ (solid line) as a function of time during one oscillation cycle. The amplitudes are scaled with the maximum values.*

can also be seen in Fig. 3.15, where the zonal overturning streamfunction is plotted for several phases during the oscillation.

On the other hand, during this time interval ΔT_{E-W} decreases rapidly (Fig. 3.14a). At this stage, the meridional overturning therefore decreases rapidly and changes from positive to negative around $t = 10$ yr, as can be seen in Fig. 3.14a and also in Fig. 3.16. This change in meridional overturning induces anomalous upwelling at the northern boundary of the domain compatible with the increase and westward propagation of vertical velocity anomalies (Figs. 3.5c and d). It also induces downwelling anomalies in the southern part of the basin. There, the evolution of the temperature anomalies is dominated by vertical exchange processes (Fig. 3.17), since the basic-state vertical temperature gradient is relatively large. Hence, through anomalous downwelling a positive temperature perturbation results in the south (Fig. 3.6f), which reduces the initially positive north-south perturbation temperature difference. The latter changes sign around $t = 22$ yr, causing the zonal overturning perturbation to become positive (Figs. 3.14b and 3.15g). The positive zonal overturning perturbation after $t = 22$ yr induces downwelling along the eastern boundary and upwelling in the northwest (Figs. 3.5g and h). This increases the vertically integrated east-west temperature difference (Fig. 3.14a) and the second half of the oscillation starts. Note that during the second half of the oscillation, a cold anomaly will lead to a positive zonal overturning anomaly, which causes upwelling of cold water in the west and downwelling of warm water in the east, again leading to westward propagation.

Now the processes controlling the phase difference between $<\bar{w}\tilde{T}>$ and $<\tilde{w}\bar{T}>$ can be explained. At $t = 0$ yr, $<\bar{w}\tilde{T}>$ is at a minimum (Fig. 3.9). The sign of $<\bar{w}\tilde{T}>$ turns out to be mainly determined by the surface temperature perturbation in the northeast, so that looking at the surface fields of both $\tilde{T}$ and the steady state shows that this term is dominated by steady-state downwelling of anomalously warm water, thus increasing the potential energy (both $<\bar{w}\tilde{T}>$ and $<\tilde{w}\bar{T}>$ appear with a minus sign in equation (3.6)). As the temperature anomaly propagates to the west, where the basic-state downwelling is weaker, $<\bar{w}\tilde{T}>$ increases. At the same time, $\tilde{T}$ in the northeast decreases through upwelling of cold water (which is a

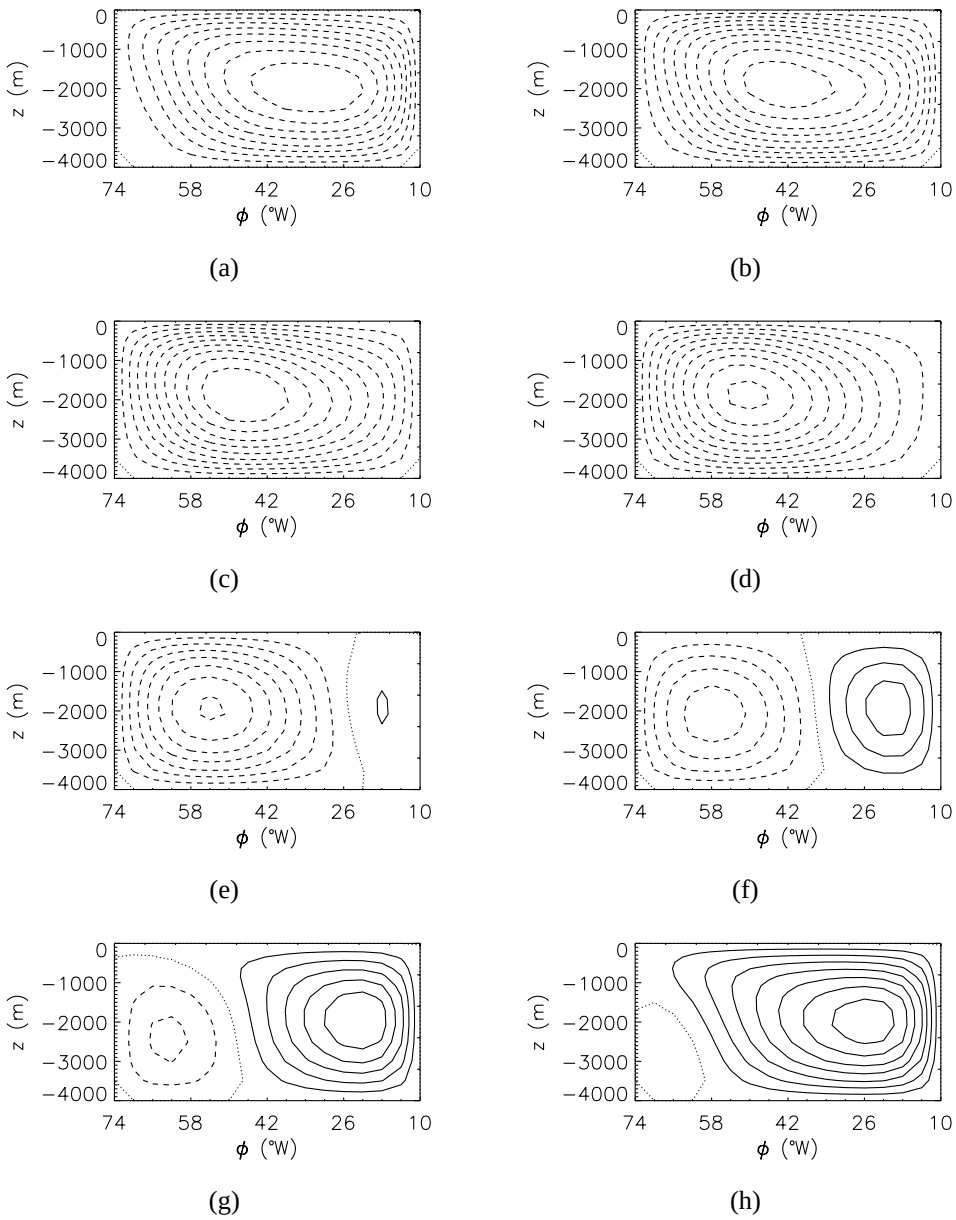

Figure 3.15: *Zonal overturning perturbations at (a)* $t = 0$ *yr, (b)* $t = 4.1$ *yr, (c)* $t = 8.1$ *yr, (d)* $t = 12.2$ *yr, (e)* $t = 16.3$ *yr, (f)* $t = 20.3$ *yr, (g)* $t = 24.4$ *yr and (h)* $t = 28.4$ *yr. The plots are 1/16th period apart.*

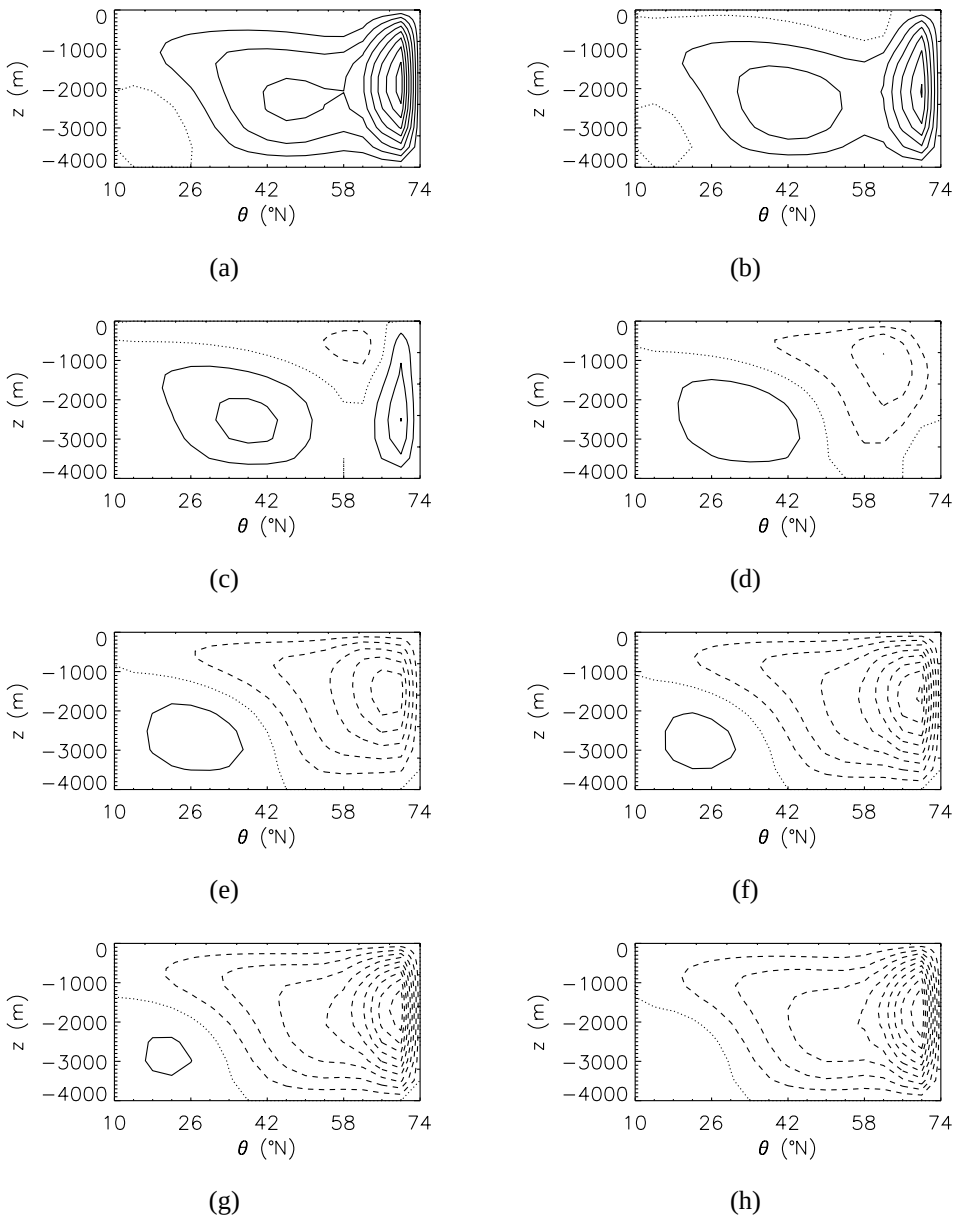

Figure 3.16: *Meridional overturning perturbations at (a)* $t = 0$ *yr, (b)* $t = 4.1$ *yr, (c)* $t = 8.1$ *yr, (d)* $t = 12.2$ *yr, (e)* $t = 16.3$ *yr, (f)* $t = 20.3$ *yr, (g)* $t = 24.4$ *yr and (h)* $t = 28.4$ *yr. The plots are 1/16th period apart.*

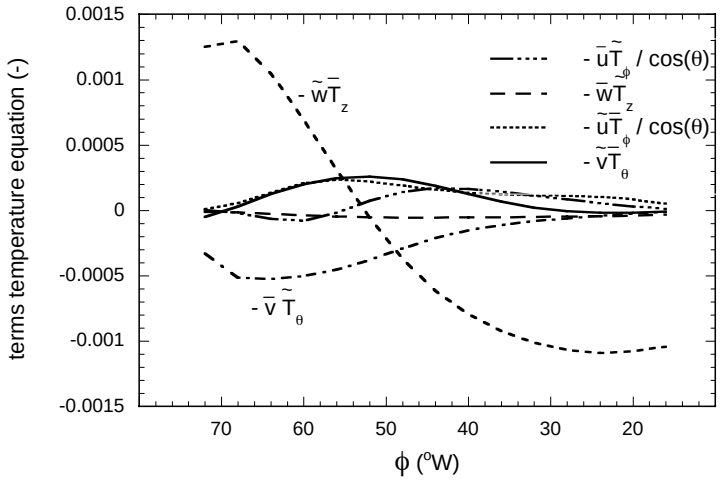

Figure 3.17: *Advective terms in the perturbation temperature equation as a function of longitude along the southern boundary ($\theta = 16^\circ N$) at $t = 0$ yr.*

reaction to the negative zonal overturning from the previous phase of the oscillation), so that $<\bar{w}\tilde{T}>$ increases even more and becomes positive after $t = 16$ yr. When the temperature perturbation in the whole northern part of the basin has become negative, $<\bar{w}\,\tilde{T}>$ reaches a maximum around $t = 33$ yr, so that downwelling of anomalously cold water causes a decrease of potential energy. The sign of the term $<\tilde{w}\,\bar{T}>$ is mainly determined along the northern boundary, so we see from Fig. 3.1 and Fig. 3.5 that, at $t = 0$ yr, the anomalous downwelling in the northwest in the region of cold steady-state temperatures causes $<\tilde{w}\,\bar{T}>$ to be positive. This term is therefore decreasing the potential energy. The upwelling which occurs along the northern boundary due to the rapid change in the meridional overturning causes $<\tilde{w}\bar{T}>$ to decrease and become negative around $t = 10$ yr. This upwelling has spread out along most of the northern boundary at about $t = 24$ yr, so that $<\tilde{w}\,\tilde{T}>$ reaches a minimum around $t = 27$ yr.

In summary, the phase difference between $<\bar{w}\tilde{T}>$ and $<\tilde{w}\bar{T}>$ thus comes from the phase difference between $\tilde{w}$ and $\tilde{T}$, which in turn originates from the westward propagation of the temperature anomalies and the interplay of changing zonal and meridional temperature gradients with subsequent responses of the zonal and meridional overturning (Fig. 3.18).

3.4 Summary and discussion

It has been shown that a steady state obtained under a prescribed heat flux will become unstable once the horizontal thermal diffusion is small enough. Note that the shape of the heat flux is not important for the destabilization process, because it does not affect the linear stability problem. Only the fact that damping of temperature anomalies is effectively zero is important. Obviously, this only holds at criticality and the shape of the heat flux will influence the periodic orbit arising from the instability in a way described by Huck *et al.* (1999).

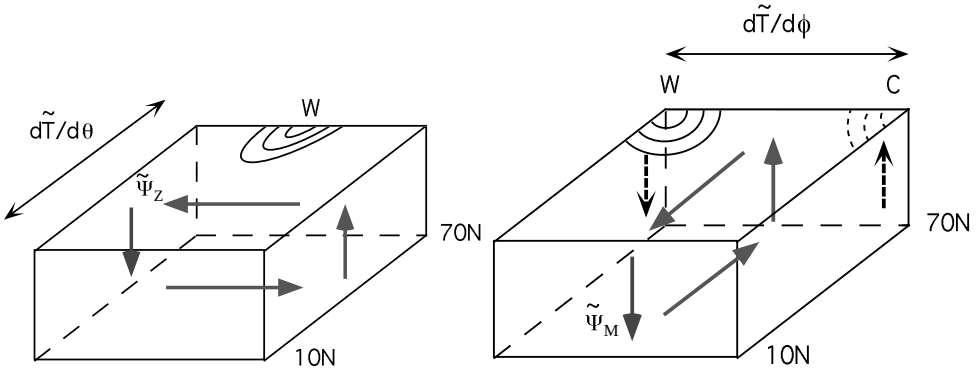

Figure 3.18: *Schematic diagram of the oscillation mechanism: a warm anomaly in the north-central part of the basin causes a positive meridional perturbation temperature gradient (a), which induces a negative zonal overturning perturbation. The anomalous upwelling and downwelling associated with this zonal overturning are consistent with westward propagation of the warm anomaly, while a cold anomaly appears in the east (b). Due to the westward propagation of the warm anomaly, the east-west temperature difference decreases and becomes negative, inducing a negative meridional overturning perturbation. The resulting upwelling and downwelling perturbations along the northern and southern boundary reduce the north-south perturbation temperature difference, causing the zonal overturning perturbation to change sign and the second half of the oscillation starts.*

The new element in this study is that the linear stability of these complex three-dimensional steady states has been computed and that it is demonstrated that the interdecadal mode arises through a supercritical Hopf bifurcation. A regime diagram in the (K_H, K_V) space shows that the stability characteristics change with these parameters, mainly through changes in the mean state, but that the time scale of the oscillatory mode remains interdecadal.

In correspondence with other studies, this shows that the interdecadal mode introduces a very robust preferred pattern in the buoyancy-driven ocean circulation. Winton (1997) shows that interdecadal thermohaline oscillations occurring in a model with a flat bottom under flux boundary conditions disappear when a bowl-shaped bottom topography is included. As bottom topography is expected to change the overturning, the results here suggest that the Hopf bifurcation is shifted in parameter space due to the effect of bottom topography. This is in agreement with the reappearance of the oscillation, under bottom topography, if the forcing strength is increased (Winton, 1997).

The oscillation also exists under restoring boundary conditions, but in this case it is stable. The large spatial scale of the SST-anomalies as seen in interdecadal variability may influence the atmospheric temperature, so that a restoring boundary condition with standard restoring coefficients imposes an unrealistically fast relaxation. Chen and Ghil (1996) coupled a simple ocean model to an energy-balance model of the atmosphere and showed that, at low frequencies, the ocean sees almost a constant heat flux. However, even if damping by the atmosphere is present, the existence of the interdecadal mode is not affected, but only its stability properties are changed.

Different ideas to explain the phase difference responsible for the oscillation have been proposed in the literature. In Greatbatch and Zhang (1995), it was suggested, but not analyzed further, that convective mixing is involved and that this, in combination with advective processes, leads to a phase difference between the temperature and velocity anomalies. Both the results in Huck *et al.* (1999) and our results clearly indicate that the oscillation still exists in the absence of convective mixing. This is also compatible with the mechanism described in the previous section. Although convective mixing may affect the phase difference between the two buoyancy production fields, it is not important for the existence of the oscillation. As convective mixing changes the vertical temperature gradient, it may reduce κ in equation (3.9). For $\kappa \gg 1$, the constant $\hat{\alpha}$ is approximately inversely proportional to κ. A reduction of κ in this case will lead to an increase in $\hat{\alpha}$ and hence a larger value of c. However, for values of $0 < \kappa < 1$, the effect of convective adjustment on the phase speed can be either way and it is not obvious how convective adjustment would affect the phase difference and the period of the oscillation.

In Winton (1996) and Greatbatch and Peterson (1996), viscous boundary-trapped waves which propagate as Kelvin waves are suggested to be responsible for the phase difference between velocity and temperature field. In the model here, the vertical velocity anomalies are indeed boundary trapped. From the analysis of Winton (1996) it follows that when the boundary-wave mechanism is dominant, the oscillation period should change significantly with the value of A_H (and scale with $A_H^{-1/2}$) when the steady state is fixed. In this case, the period should also be fairly insensitive to the buoyancy forcing Ra. We determined the linear stability of the steady state in Fig. 3.1 for different values of the parameters E_H and Ra, with the effect of changes in parameters only through the perturbation balances (the steady state remains the same). For $Ra = 0.5Ra_s, Ra = Ra_s$ and $Ra = 2Ra_s$, the dimensionless frequency σ_i is $0.14, 0.19$ and 0.22, respectively, where Ra_s is the standard value. This increase in frequency is expected from (23), but does not support the viscous boundary-wave mechanism. For $E_H = E_{Hs}, 2E_{Hs}$ and $5E_{Hs}$, we find frequencies of 0.19, 0.21 and 0.20, respectively, which indicates a weak dependence on E_H. While effects of boundary-wave propagation may still be present, these results suggest a dominant role for the propagation mechanism as suggested in section 3.3.

The mechanism proposed here is also fairly well in agreement with that suggested in Colin de Verdière and Huck (1999). Indeed, the propagation of temperature anomalies and the subsequent response of the flow is crucial. Here, we have given a detailed mechanistic view of how the response of the velocity field through both zonal and meridional overturning streamfunctions is related to the propagation of the temperature anomalies. Since only the buoyancy work terms monitor the actual changes in the mechanical energy balance and hence in the kinetic energy of the flow, it is not sufficient to show only the phase difference in the responses of the two streamfunctions (zonal and meridional), but one has to explain how the phase difference between the buoyancy work terms arises.

There is another argument to use an interpretation in terms of buoyancy work. In Colin de Verdière and Huck (1999), the instability has been referred to as baroclinic instability. Growth of perturbations in baroclinic instability indeed must be controlled by the same production term in the available potential energy balance as growth of perturbations in the instability leading to the interdecadal oscillation. However, one may ask how the phase difference between the density field and the velocity field arises in a classical case of baroclinic instability,

such as the Eady problem (Pedlosky, 1987). The change in potential energy of the perturbations is then given by

$$\frac{d\tilde{\mathcal{U}}}{dt} = <\bar{w}\tilde{\rho}> + <\tilde{w}\bar{\rho}> \tag{3.14}$$

where ρ is the density. For the dimensionless basic-state $\bar{u} = z+1, \bar{v} = \bar{w} = 0$ and $\bar{\rho} = y$, the first term on the right-hand side is identically zero. In quasi-geostrophic theory, the vertical velocity perturbations at first order in the Rossby number are given by

$$\tilde{w} = \varepsilon_R \mathcal{S}^{-1} \left(\frac{\partial \tilde{\rho}}{\partial t} + \tilde{\boldsymbol{u}} \cdot \nabla \bar{\rho} + \bar{\boldsymbol{u}} \cdot \nabla \tilde{\rho} \right) \tag{3.15}$$

where $\mathcal{S}$ is the Burger number (the square of the ratio of the length scale of the flow and the internal Rossby deformation radius), which is taken constant. Substituting the basic state, we find for the potential energy change of the perturbations

$$\frac{d\tilde{\mathcal{U}}}{dt} = \varepsilon_R \mathcal{S}^{-1} \left(<y\frac{\partial \tilde{\rho}}{\partial t}> + <y\tilde{v}> + <y(z+1)\frac{\partial \tilde{\rho}}{\partial x}> \right) \tag{3.16}$$

There exists a phase difference between these three terms, which is responsible for the oscillation. However, the basic-state upwelling is not involved in this phase difference since it is identically zero.

For the interdecadal instabilities, however, the existence of a basic state with a non-zero vertical velocity is crucial to the existence of the instability. Such a state also appears necessary in the three-layer model suggested in Colin de Verdière and Huck (1999) where long-time-scale instabilities occur. To our opinion, one could view this type of interdecadal instability as a 'generalized' baroclinic instability, but then many instabilities could be labeled with the same name. For example, also the overturning oscillations found in two-dimensional thermohaline models (Dijkstra and Molemaker, 1997), where the phase difference is determined by the terms $< wT >$ and $< wS >$, where S is the salinity, could then be called baroclinic instability. If one wishes to distinguish oscillations according to the processes leading to the phase difference, then we think the interdecadal instability falls in a separate class of thermohaline instabilities. In this way, the phase difference between the meridional and zonal overturning or that between the terms in the buoyancy work are mechanistically selective.

In this context, it would be interesting to investigate the origin of the phase difference driving the interdecadal oscillation found by Chen and Ghil (1995). If it is mainly determined by the temperature, while salinity plays only a minor role, the mechanism behind this oscillation is basically the same as the one we propose here. On the other hand, salinity can turn out to be the important factor in determining the phase difference of the oscillation. For example, the main phase difference could be between $<\bar{w}\,\tilde{S}>$ and $<\tilde{w}\bar{S}>$, or between one of these terms and either $<\bar{w}\tilde{T}>$ or $<\tilde{w}\bar{T}>$. In these latter cases, this oscillation would be different from the one we have found.

The results here motivate a different approach to analyze observations. A nice element of the results in this study is that the changes in the zonal and meridional overturning perturbations of the interdecadal mode can be related to changes in vertically integrated meridional

and zonal temperature differences, respectively (according to (3.13)). This motivates examination of the phase differences between east-west and north-south temperature differences over a long time in observations and CGCM simulations. Using these phase differences, a clear relationship between the interdecadal oscillations in this model and the variability found in observations might be established. In this way, the importance of instabilities of the thermohaline circulation in interdecadal climate variability can be assessed.

Chapter 4

Sensitivity of North-Atlantic multidecadal variability to freshwater-flux forcing

In this chapter, an explanation is proposed for the changes in the amplitude of multidecadal variability found in the GFDL climate model when different freshwater-flux fields in the flux correction procedure were considered. This explanation arises from a study of the stability of three-dimensional thermohaline flows in an idealized coupled ocean-atmosphere model. The shape of the freshwater flux affects the stability properties of the thermohaline flows, in particular the growth rates of an interdecadal mode. The physics of this change in growth rate is explained by analyzing the energy conversions in the flows. Under a stronger freshening of the northern North Atlantic, the interdecadal mode destabilizes, which can result in an increase of the amplitude of the multidecadal variability[*].

4.1 Introduction

The spatial patterns and temporal development associated with observed multidecadal variability can be simulated fairly well with coupled ocean-atmosphere GCMs (CGCMs, e.g. Delworth and Mann (2000)). Since these CGCMs represent a multitude of physical processes, each acting possibly on different spatial and temporal scales, it is difficult to extract understanding of a particular phenomenon (like multidecadal variability) from the output of these models. However, studies in which the sensitivity of the CGCM-results for the strength of certain effects was tested, have provided a wealth of information on the relevant processes. The suite of simulations presented in Delworth and Greatbatch (2000) convincingly shows that coupled feedbacks between the ocean and atmosphere are not involved in multidecadal variability. When the sole ocean component of the coupled model is forced by the annual-mean atmospheric fluxes of the coupled simulation, the multidecadal variability remains.

[*]This chapter is based on the paper '*Sensitivity of North-Atlantic multidecadal variability to freshwater-flux forcing*', by L. A. te Raa and H. A. Dijkstra (accepted for publication in *J. Climate*)

When the same ocean model is forced by the climatological fluxes, the variability disappears, which also disfavors any explanation of self-sustained ocean modes. The conclusion of Delworth and Greatbatch (2000), also based on other simulations, is that the multidecadal variability can be attributed to a damped mode in the ocean system, which is continuously excited by low-frequency atmospheric forcing. The heat flux is shown to be the most important component of this forcing.

The variability of the thermohaline overturning under a freshening of the northern North Atlantic is studied in another set of simulations with the same GFDL CGCM (Tziperman, 1997, 2000). By changing the restoring salinity field used in the flux correction procedure during the spin-up of the ocean component, different oceanic states are obtained as initial conditions for the integration of the coupled model. These different initial conditions represent changes in the ocean circulation due to some unknown external factor such as ice melting. When the northern North Atlantic is less saline, the overturning in the coupled model decreases. Simultaneously, it is found that the amplitude of the multidecadal oscillations in the model increases. Eventually, under strong restoring freshwater anomalies, the thermohaline circulation in the coupled model collapses.

The results in Delworth and Greatbatch (2000) suggest that the essential physics of the multidecadal variability can be understood from ocean-only models, possibly with only temperature as active buoyancy influencing variable. Indeed, interdecacal oscillations have been found in many idealized sector models, forced by only a surface heat flux (Chen and Ghil, 1995; Greatbatch and Zhang, 1995; Greatbatch and Peterson, 1996). From these studies, it was clear that a phase difference between changes in the overturning circulation and the resulting temperature differences is essential. Moreover, critical thresholds in dissipation (i.e. due to mixing of heat) also exist; when horizontal mixing of heat is too large, no interdecadal oscillations are found.

It was shown by Huck and Vallis (2001) and also in chapter 3 of this thesis that threshold behavior is associated with a Hopf bifurcation, which destabilizes a particular interdecadal mode in the flow, as had been suggested by Chen and Ghil (1995). The physical mechanism of growth and oscillation was described in chapter 3 from the patterns of the eigenvectors at the Hopf bifurcation. The oscillation mechanism is due to a phase-shifted response of the meridional and zonal overturning to westward propagating buoyancy anomalies, and consistent with the earlier descriptions by Huck *et al.* (1999).

The sensitivity of these interdecadal oscillations to the β-effect, the representation of convective adjustment, different thermal and momentum boundary conditions, coupling to the atmosphere and mesoscale variability has been investigated by Huck and co-workers (Huck *et al.*, 1999, 2001). From the results in chapter 3, it can be concluded that all the sensitivity results as in Huck *et al.* (2001) are more or less associated with a shift of this Hopf bifurcation in parameter space, but that the presence of the interdecadal mode is robust. Probably the interdecadal mode exists as a stable, but only slightly damped mode in a broad range of parameter space of CGCMs. It is known from simpler box models (Griffies and Tziperman, 1995; Rivin and Tziperman, 1997), that slightly damped modes can give pronounced variability at their internal oscillation time scale under atmospheric noise. Such a mechanism may also be active in CGCMs to excite the interdecadal mode.

With the knowledge of this interdecadal mode as a starting point, the specific aim in this chapter is to explain the change in amplitude of multidecadal variability in the simulations

A_H	=	$1.6 \cdot 10^7$	[m^{2}s^{-1}]	A_V	=	$1.0 \cdot 10^{-3}$	[m^{2}s^{-1}]
K_H	=	$1.0 \cdot 10^3$	[m^{2}s^{-1}]	K_V	=	$1.0 \cdot 10^{-4}$	[m^{2}s^{-1}]
E_H	=	$2.7 \cdot 10^{-3}$		E_V	=	$4.3 \cdot 10^{-7}$	
P_H	=	$1.6 \cdot 10^{-3}$		P_V	=	$4.0 \cdot 10^{-4}$	

Table 4.1: *Reference values of oceanic mixing parameters used in the numerical computations of chapter 4.*

in Tziperman (1997) and Tziperman (2000), in terms of changes in growth rate of an interdecadal mode. The coupled ocean-atmosphere model that is used consists of the THCM ocean model coupled to the atmospheric energy-balance model described in section 2.2.2. As the atmospheric model has no hydrological cycle, an additional boundary condition for salinity is needed for the ocean component of the model. A hybrid coupled model has been chosen for this study instead of a fully coupled model, so that the amplitude of the freshwater-flux forcing can be controlled in a transparent way. Steady-state solutions of this coupled ocean-atmosphere system are computed, together with their linear stability. Subsequently, the changes in the stability of interdecadal modes versus the freshwater-flux profiles are investigated. After describing the configuration of the coupled model in section 4.2, we show that an interdecadal mode exists as a stable mode in the coupled ocean-atmosphere system with temperature as the only buoyancy influencing variable (section 4.3). Stability changes under different freshwater-flux profiles are studied in section 4.3.3 and lead to an explanation of the changes in amplitude of the multidecadal variability as discussed in section 4.4.

4.2 Configuration and forcing of the coupled model

Throughout this chapter, the THCM coupled ocean-atmosphere model has been used. Solutions have been computed on a $16 \times 16 \times 17$ grid, of which 16 levels are ocean layers and the uppermost layer represents the atmosphere. No stretching was applied, so that the horizontal resolution was $4^\circ \times 4^\circ$ and the vertical resolution in the ocean 250 m. Reference values of the mixing parameters in the ocean model are given in Table 4.1.

An approximation for the solar insolation distribution $S_\odot$ is given in North (1975b) as

$$S_\odot(\theta) = 1.0 \; - \; 0.241 \, (3 \sin^2 \theta - 1.0) \tag{4.1}$$

The latitudinal profiles $D(\theta)$ of the atmospheric diffusivity and the planetary albedo α are chosen such that they resemble the profiles used by Fanning and Weaver (1996) and are given by

$$D(\theta) \;=\; 0.9 + 1.5 \, e^{-12\theta^2/\pi} \tag{4.2a}$$

$$\alpha(\theta) \;=\; 0.4 - 0.2 \cos 2\theta \tag{4.2b}$$

The freshwater-flux forcing was defined in equation (2.24). The influence of changes in freshwater input in the north can be studied by changing the parameter η_s in this equation. Profiles showing the latitudinal distribution of the solar insolation, the atmospheric diffusivity

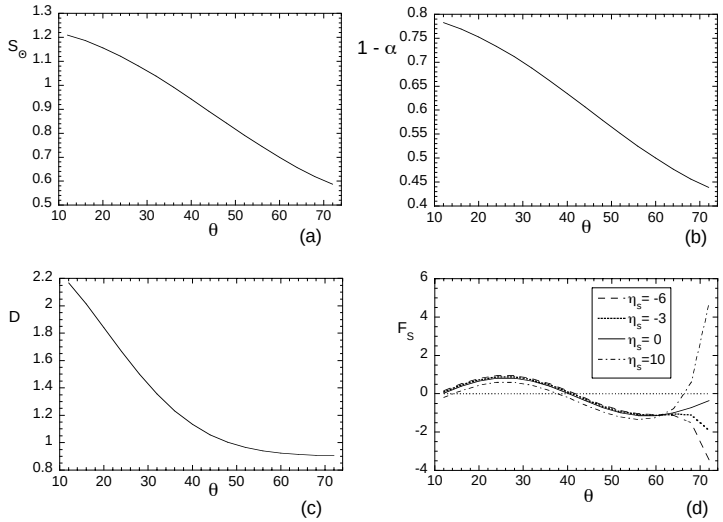

Figure 4.1: *Latitudinal profiles of (a) the distribution of the solar insolation $S_\odot(\theta)$, (b) the planetary co-albedo $1-\alpha(\theta)$, (c) the spatial distribution of the atmospheric diffusivity $D(\theta)$ and (d) the salt flux forcing $F_S(\theta)$. In the latter panel, the solid line is the standard forcing profile for $\eta_s = 0.0$, the dotted line is the profile for $\eta_s = -3.0$, the dashed line is for $\eta_s = -6.0$ and the dash-dotted line is for $\eta_s = 10.0$.*

and the co-albedo are shown in Fig. 4.1, together with the profile of the freshwater flux F_S for four values of the parameter η_s. For $\eta_s = 0$ the freshwater-flux profile crudely represents the observed freshwater flux, with evaporation south of about $40\,^\circ$N and precipitation at higher latitudes (compare to Fig. 1.5).

The wind speed was chosen as $U_a = 13.1$ ms^{-1}, such that the ocean-atmosphere exchange coefficient is 20 Wm^{-2}K^{-1}. The area-averaged atmospheric temperature is about $15°$C, close to the estimate of Budyko (1969) and North (1975b). The standard parameter values of the atmospheric model are listed in Table 4.2.

Σ_0	=	1360	[Wm^{-2}]	C_0	=	0.5	[-]
C_{po}	=	4200	[Jkg^{-1}K^{-1}]	H_m	=	250	[m]
ρ_a	=	1.25	[kg m^{-3}]	C_{pa}	=	1000	[Jkg^{-1}K^{-1}]
H_a	=	8400	[m]	U_a	=	13.1	[ms^{-1}]
C_H	=	$0.94\,C_E$	[-]	C_E	=	$1.3 \cdot 10^{-3}$	[-]
D_0	=	$1.0 \cdot 10^6$	[m^{2}s^{-1}]	μ	=	20.0	[Wm^{-2}K^{-1}]
A	=	200.0	[Wm^{-2}]	B	=	1.45	[Wm$^{-2\circ}$C^{-1}]

Table 4.2: *Reference values of the dimensional parameters used in the atmospheric model.*

4.3 Results

4.3.1 The interdecadal mode

The same approach as in the previous chapter is followed here, by computing first a branch of steady-state solutions of the coupled ocean-atmosphere model, using the magnitude of the solar constant Σ_0 as control parameter. At the standard value of Σ_0, the steady state has a maximum meridional overturning of 24.4 Sv (Fig. 4.2a). The overturning streamfunction shows the typical unicellular structure also found in the uncoupled model, with sinking confined to the northernmost part of the domain. The surface circulation is anti-cyclonic (Fig. 4.2c) with upward vertical velocities at the western part of the basin. A reversed flow occurs near the bottom (Fig. 4.2e), consistent with the overturning flow. A section of temperature in a north-south vertical plane shows a 'thermocline' in the upper 1000 m (Fig. 4.2b), with slight static instabilities in the northern part of the domain. Surface temperatures show some advective departures from the zonally uniform state (Fig. 4.2d), and the atmospheric temperature is almost zonally uniform with a north-south temperature gradient of about $20\ ^\circ$C (Fig. 4.2f).

For standard values of the parameters, the state in Fig. 4.2 is linearly stable. The least stable mode is associated with a complex pair of eigenvalues $\sigma = \sigma_r \pm \sigma_i\, i$, with dimensional growth rate $\sigma_r^* = -3.4 \cdot 10^{-3}$ yr^{-1} and oscillation period $\mathcal{P} = 2\pi/\sigma_i \approx 33$ years. Pictures of typical patterns corresponding to the imaginary and real parts of the eigenmode are shown in Figs. 4.3 and 4.4, respectively. To characterize the eigenmode, meridional overturning streamfunction, surface and deep velocities, the atmospheric temperature and two slices of the ocean temperature field are plotted.

The mode has quite a global structure, and the anomalies reach their maximum amplitude in the north and near the ocean surface. At $t = -\mathcal{P}/4$, the meridional overturning perturbation is negative in the northern part of the basin, indicating a local weakening of the northward surface flow at high latitudes (Fig. 4.3a). There is anomalous upwelling along the northern boundary and in the northeast of the domain and anomalous downwelling in the northwest of the basin (Fig. 4.3c), with a similar pattern at the bottom (Fig. 4.3e). Near the surface there is a positive temperature anomaly in the north (Fig. 4.3d), which extends almost down to the bottom (Fig. 4.3b). In the atmosphere, there is also a positive temperature anomaly (Fig. 4.3f), which has a similar structure as in the ocean.

A quarter of a period later, at $t = 0$, the meridional overturning anomaly has become negative over most of the basin (Fig. 4.4a). The positive vertical velocity anomaly that was present in the northeastern corner at $t = -\mathcal{P}/4$ has now propagated westward to the northwestern part of the basin, both near the surface and near the bottom (Figs. 4.4c, e). The positive temperature anomaly has also propagated westward (Fig. 4.4d) and has been followed by a negative anomaly, which is extending less deep (Fig. 4.4b). The atmospheric temperature perturbation has again a structure similar to that of the perturbation temperature at the ocean surface (Fig. 4.4f). Although the period of the eigenmode is shorter than in the uncoupled model in chapter 3, the patterns of the eigenmode and in particular the westward propagation of temperature anomalies, strongly resemble those of the interdecadal mode in the uncoupled model.

The growth rate and period of the interdecadal mode at the standard value of $D_0 =$

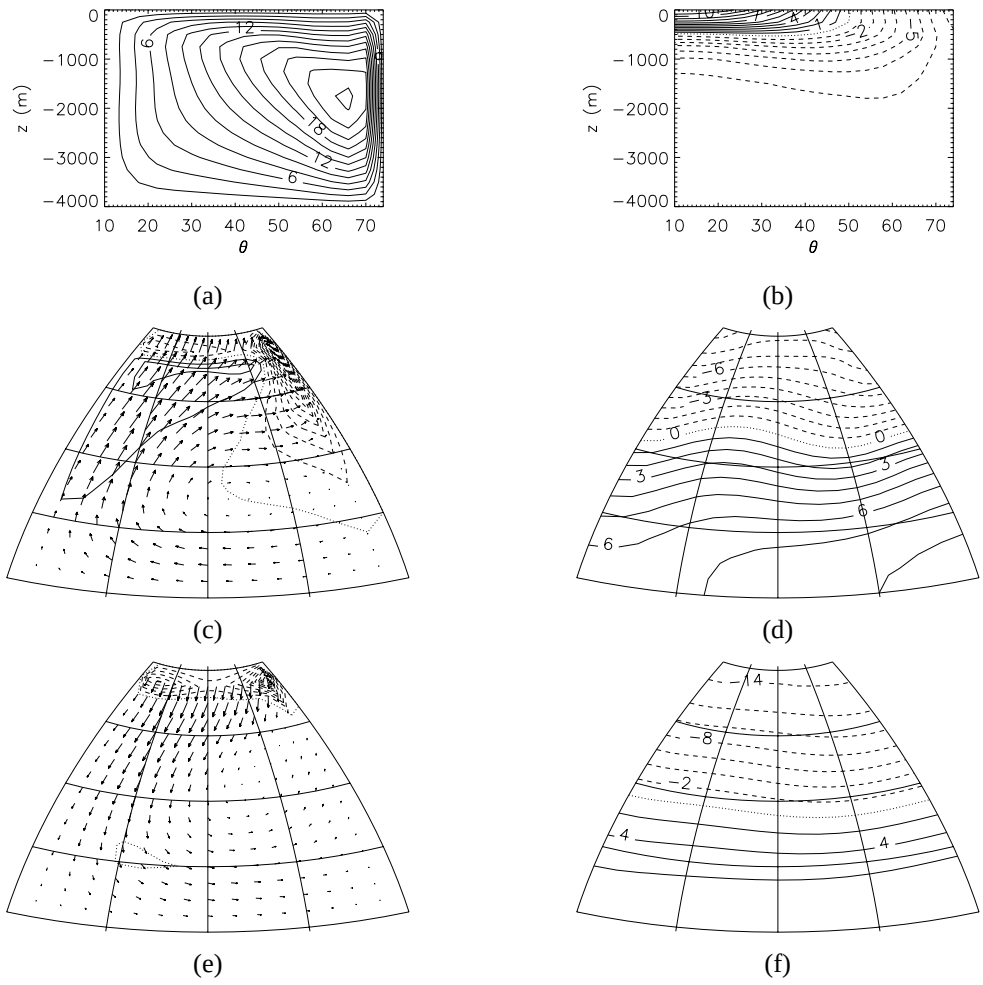

Figure 4.2: *Steady-state solution at standard values of the parameters. (a) Meridional overturning streamfunction (in Sverdrups). (b) Dimensionless temperature for a north-south vertical plane through the middle of the basin ($\phi = 42°$W). The dimensional temperature T^* (in $°$C) can be obtained from $T^* = 15.0 + \Delta T\, T$. (c) Velocity one level below the surface (at 250 m depth). In this plot, vectors indicate the horizontal velocity, (u, v) and contours represent the vertical velocity, w. Solid lines represent upwelling (flow out of the plane), dashed lines downwelling (flow into the plane). The maximum horizontal velocity is $1.6 \cdot 10^{-2}$ ms^{-1}, the maximum amplitude of the vertical velocity is $1.2 \cdot 10^{-5}$ ms^{-1} (downwelling). (d) Temperature near the surface. (e) Velocity at $z = -3500$ m. Maxima are $7.3 \cdot 10^{-3}$ ms^{-1} for the horizontal and $1.1 \cdot 10^{-5}$ ms^{-1} (downwelling) for the vertical velocity. (f) Atmospheric temperature. The dimensional atmospheric temperature T_a^* can be obtained from $T_a^* = 15.0 + \Delta T\, T_a$.*

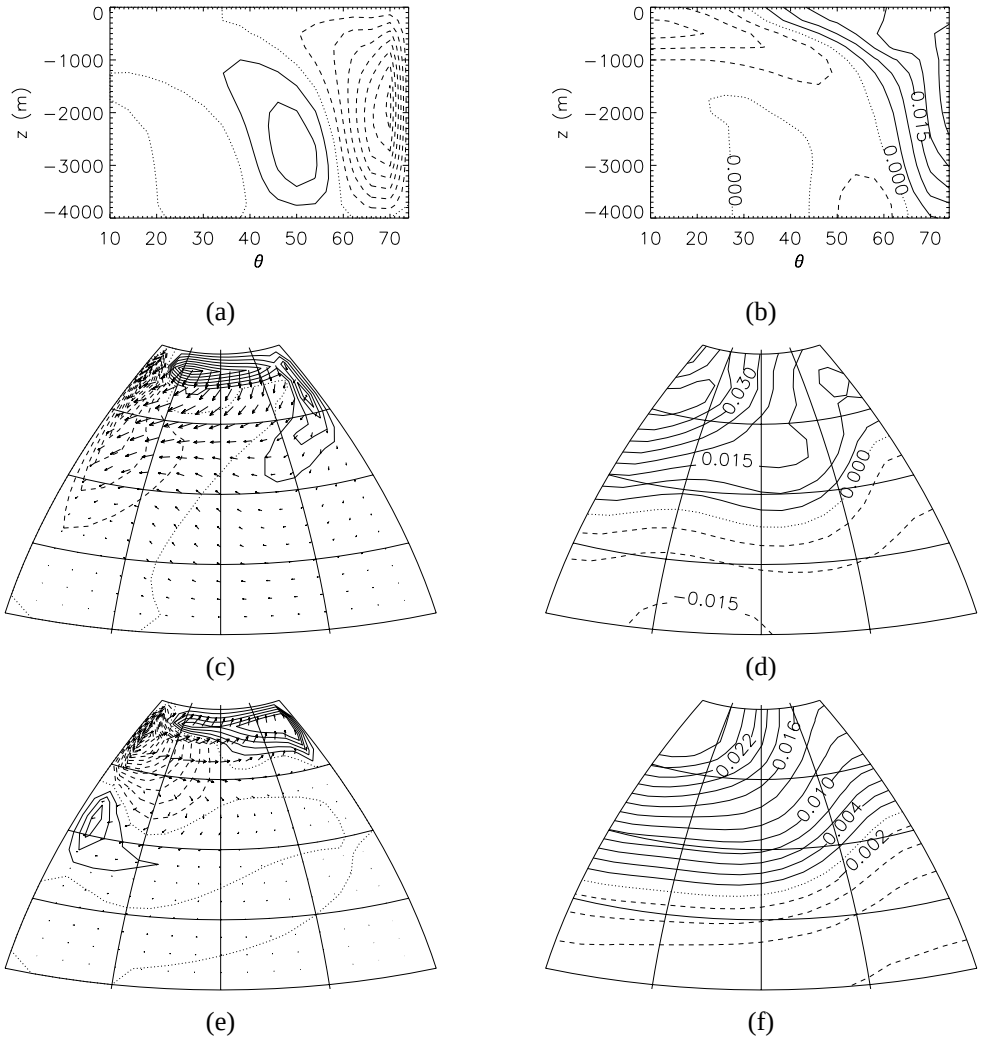

Figure 4.3: *Imaginary part of the eigenvector corresponding to the interdecadal mode (with period* $\mathcal{P} = 33$ *yr and growth rate* $\sigma_r^* = -3.4 \cdot 10^{-3}$ *yr*$^{-1}$*). (a) Meridional overturning streamfunction. (b) Temperature for a north-south vertical plane through the middle of the basin. (c) Velocity at* 250 *m depth. (d) Temperature at* 250 *m depth. (e) Velocity at* $z = -3500$ *m. (f) Atmospheric temperature. Note that the amplitude is arbitrary.*

10^6 m^{2}s^{-1} are plotted as the rightmost point in Fig. 4.5. For decreasing atmospheric diffusivity D_0, the period (Fig. 4.5) decreases, in accordance with the results found by Chen and Ghil (1996). The growth rate increases with decreasing D_0, but does not become positive, even when D_0 is decreased over an order of magnitude. Decreasing K_H from its standard

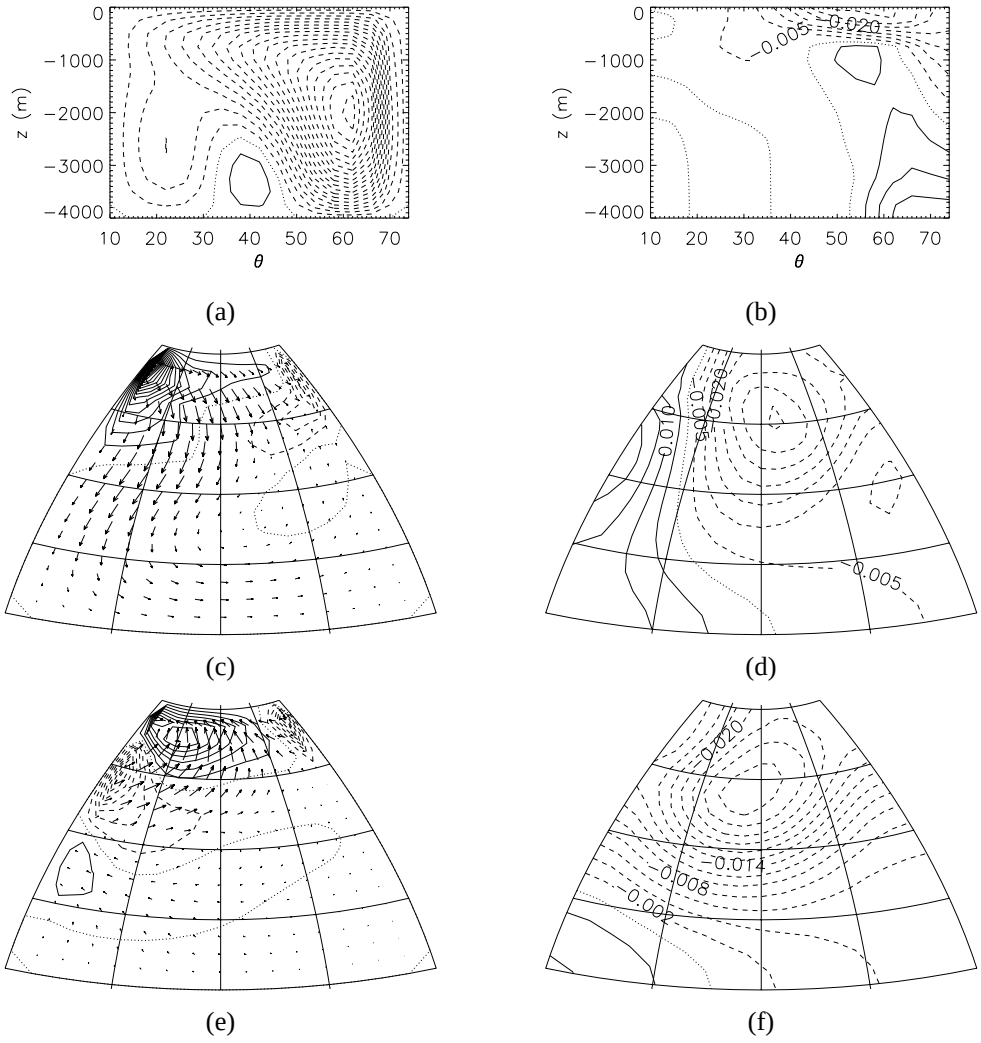

Figure 4.4: *Real part of the eigenvector corresponding to the interdecadal mode. (a) Meridional overturning streamfunction. (b) Temperature for a north-south vertical plane through the middle of the basin. (c) Velocity at* 250 *m depth. (d) Temperature at* 250 *m depth. (e) Velocity at* $z = -3500$ *m. (f) Atmospheric temperature. Format is similar as in Fig. 4.3.*

value $K_H = 1000$ m^{2}s^{-1} to 600 m^{2}s^{-1} hardly affected the growth rate of the interdecadal mode and it remained negative. The growth rate of the mode will also be influenced by the coupling coefficient μ between ocean and atmosphere, but in order to keep a realistic steady state, the coupling coefficient μ can only be chosen within a limited range.

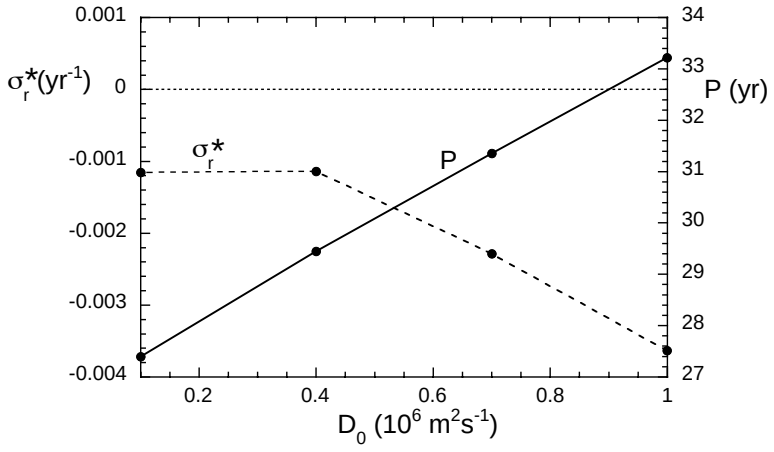

Figure 4.5: *Growth rate (dashed line) and period (solid line) as a function of the atmospheric diffusivity D_0. The left vertical axis is for σ_r^*, the right vertical axis for $\mathcal{P}$.*

4.3.2 Mechanisms of growth and oscillation

Although the interdecadal mode is decaying for the parameter range considered in the coupled ocean-atmosphere model, its physics is the same as that of the unstable mode in chapter 3. In the latter mode, the westward propagation of temperature anomalies causes a phase difference between the anomalous zonal and meridional temperature gradients with corresponding changes in perturbation meridional and zonal overturning. These phase differences show up in the phase difference between the terms in the potential energy balance of the perturbations.

In the case where temperature is the only buoyancy variable, the balance for the volume-integrated potential energy in the ocean $\mathcal{U} = <-zT>$ was given in equation (3.5) in chapter 3. In the coupled ocean-atmosphere case considered here, the potential energy balance of the perturbations can be written as

$$\frac{d\tilde{\mathcal{U}}}{dt} = - <\bar{w}\tilde{T}> - <\tilde{w}\bar{T}> -\mathcal{D} - \mathcal{A} \tag{4.3}$$

The first term on the right hand side of (4.3) denotes the production (or destruction) of potential energy due to the effect of temperature perturbations on the mean flow, while the second term denotes the production (or destruction) of potential energy due to the effect of flow perturbations on the background stratification. The term $\mathcal{D}$ provides the change in potential energy due to changes in the stratification as a result of diffusive processes, and the term

$$\mathcal{A} = \frac{\mu\, r_0}{\rho_0 C_{po} H_m U} <z(\tilde{T}_a - \tilde{T})G(z)>$$

represents the change in potential energy due to ocean-atmosphere interactions.

The terms $-<\bar{w}\tilde{T}>$, $-<\tilde{w}\bar{T}>$ and $-\mathcal{A}$ are plotted in Fig. 4.6 during one oscillation period of the interdecadal mode shown in Figs. 4.3 and 4.4. About 12 years after $-<\bar{w}\,\tilde{T}>$ has reached its minimum amplitude, $-<\tilde{w}\bar{T}>$ is at a minimum, after which it takes about

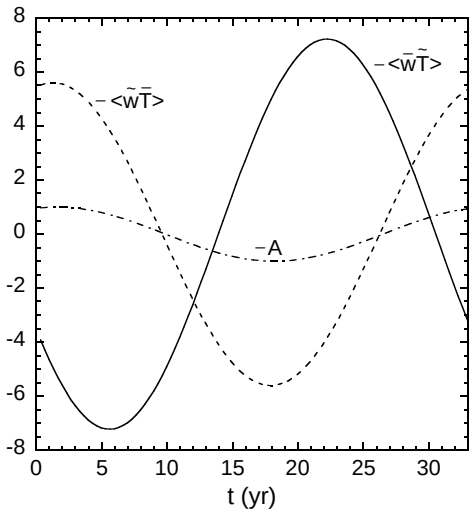

Figure 4.6: *Dimensionless terms* $-<\bar{w}\tilde{T}>$ *(solid line),* $-<\tilde{w}\bar{T}>$ *(dashed line) and* $-\mathcal{A}$ *(dash-dotted line) as a function of time for one oscillation cycle. The terms are scaled with the maximum amplitude of* $\mathcal{A}$*.*

4 years before $-<\bar{w}\tilde{T}>$ reaches a maximum, after which the second half of the oscillation starts. The phase difference between both terms of the perturbation buoyancy work is the same as in the uncoupled ocean model of chapter 3. This confirms that the interdecadal mode in the coupled ocean-atmosphere model is an internal ocean mode, of which the mechanism is described in chapter 3. The influence of the atmospheric field on this phase difference is relatively small.

The period of the interdecadal mode in the coupled model is shorter than in the uncoupled ocean model, because of slight differences in the steady-state solutions of the two models. In chapter 3 an estimate of the phase speed of the propagating temperature anomalies was derived (see equation (3.11)). The surface circulation is somewhat stronger in the coupled model than in the uncoupled one, which would lead to slower propagating temperature anomalies according to equation (3.11). However, the meridional basic-state temperature gradient is much stronger (more negative) in the coupled model than in the uncoupled one, which can be seen by comparing Fig. 4.2d of this chapter and Fig. 3.1d of chapter 3. The net effect is that the westward propagation speed of the temperature anomalies in the coupled model is larger than in the uncoupled one and that the interdecadal oscillation has a shorter period.

In the ocean-only model in chapter 3, the interdecadal mode is damped under restoring conditions and it is a growing mode under prescribed flux conditions, whereas in the coupled model used here it is always damped. This can be understood from the equation for the evolution of infinitesimally small temperature perturbations

$$\frac{\partial \tilde{T}}{\partial t} + \bar{\boldsymbol{u}} \cdot \nabla \tilde{T} + \tilde{\boldsymbol{u}} \cdot \nabla \bar{T} = \nabla_H \cdot \left(P_H \nabla_H \tilde{T} \right) + \frac{\partial}{\partial z} \left(P_V \frac{\partial \tilde{T}}{\partial z} \right) + \tilde{Q}_T G(z) \qquad (4.4)$$

Growth or decay of oceanic temperature anomalies can be determined by considering the behavior of the energy functional $E_T = \frac{1}{2} <\overline{\tilde{T}^2}>$, where the long bar denotes averaging over one period. The evolution equation for E_T can be determined by multiplying equation (4.4) by $\tilde{T}$, averaging over one oscillation period and integrating over the domain, which yields

$$\frac{1}{2}\frac{\partial <\overline{\tilde{T}^2}>}{\partial t} = - <\overline{\tilde{T}\,\tilde{\boldsymbol{u}}\cdot\nabla\bar{T}}> + <\overline{\tilde{T}\tilde{Q}_T G(z)}> - \mathcal{D}_T \tag{4.5}$$

where $\mathcal{D}_T$ is the volume-integrated buoyancy dissipation. As in the uncoupled model of chapter 3, in the right hand side a term $<\overline{\tilde{T}\tilde{Q}_T G(z)}>$ appears, which is in the coupled case given by

$$<\overline{\tilde{T}\tilde{Q}_T G(z)}> = \frac{r_0}{\rho_0 C_{po} H_m U} <\overline{\tilde{T}\tilde{Q}^*_{oa} G(z)}> \tag{4.6a}$$

$$= -\frac{\mu r_0}{\rho_0 C_{po} H_m U} <\overline{\tilde{T}(\tilde{T}-\tilde{T}_a) G(z)}> \tag{4.6b}$$

and hence related to the atmospheric temperature anomaly. This term can be rewritten using the equation for the atmospheric temperature anomalies

$$\frac{\partial \tilde{T}_a}{\partial t} = \hat{D}_0 \nabla_H \cdot (D(\theta)\nabla_H \tilde{T}_a) - B\,R\,\tilde{T}_a + \mu\,R\,(\tilde{T}-\tilde{T}_a) \tag{4.7}$$

where the notations $\hat{D}_0 = D_0/(U r_0)$ and $R = r_0/(\rho_a H_a C_{pa} U)$, introduced in chapter 2, have been used again. Multiplying by $\tilde{T}_a$, averaging over one oscillation period and integrating over the atmospheric domain gives

$$\frac{1}{2}\frac{\partial <\overline{\tilde{T}_a^2}>}{\partial t} = -\mathcal{D}_{atm} - B\,R <\overline{\tilde{T}_a^2}> + \mu\,R <\overline{\tilde{T}_a(\tilde{T}-\tilde{T}_a)}> \tag{4.8a}$$

$$\mathcal{D}_{atm} = \hat{D}_0 <\overline{D(\theta)|\nabla_H \tilde{T}_a|^2}> \tag{4.8b}$$

where Green's theorem was used to obtain (4.8b). Because of the small thermal inertia of the atmosphere, the left-hand side of (4.8a) is approximately zero, yielding

$$0 = \mu\,R <(\overline{\tilde{T}\tilde{T}_a})> - (\mu + B)\,R <\overline{\tilde{T}_a^2}> - \mathcal{D}_{atm} \tag{4.9}$$

As both the atmospheric dissipation $-\mathcal{D}_{atm}$ and the term $-(\mu+B) <\overline{\tilde{T}_a^2}>$ are negative definite, the term $\mu <(\overline{\tilde{T}\tilde{T}_a})>$ has to be positive definite. In other words, because atmospheric temperature anomalies hardly grow or decay, the stabilizing effect of the atmospheric dissipation and of the term $-(\mu+B) <\overline{\tilde{T}_a^2}>$ on the atmospheric temperature anomalies has to be compensated by a destabilizing effect of the term $\mu <(\overline{\tilde{T}\tilde{T}_a})>$. Using equations (4.6) and (4.9), we find

$$<\overline{\tilde{T}\tilde{Q}^*_{oa} G(z)}> = -\mu <\overline{\tilde{T}^2 G(z)}> + \mu <\overline{\tilde{T}\tilde{T}_a G(z)}> \tag{4.10a}$$

$$= -\mu <\overline{\tilde{T}^2 G(z)}> + (\mu+B) <\overline{\tilde{T}_a^2}> + \mathcal{D}_{atm}/R \tag{4.10b}$$

In an ocean-only model forced by either a restoring boundary condition or a prescribed heat flux, we would have

$$< \overline{\tilde{T}\tilde{Q}^*_{oa}G(z)} > \quad = \quad \begin{cases} -\mu < \overline{\tilde{T}^2 G(z)} > & \text{restoring} \\ 0 & \text{prescribed flux} \end{cases}$$

Coupling to the atmosphere thus has a direct damping effect on oceanic temperature anomalies (the first term on the right-hand side of (4.10b)), which is also present in the restoring case for an ocean-only model. On the other hand, there is also an indirect destabilizing effect due to the reaction of the atmospheric temperature anomalies and atmospheric dissipation on the oceanic temperature anomaly (the last two terms on the right-hand side of equation (4.10b)). We computed the terms on the right-hand side of equation (4.10b) and in all cases considered here, the absolute value of $-\mu < \overline{\tilde{T}^2 G(z)} >$ is larger than $(\mu + B) < \overline{\tilde{T}_a^2} > + \mathcal{D}_{atm}/R$. This yields that the term $< \overline{\tilde{T}\tilde{Q}^*_{oa}G(z)} >$ is negative, which means that the net effect of the atmospheric coupling is to damp the interdecadal mode. Oceanic temperature anomalies are damped more strongly in the coupled model than in an ocean-only model under prescribed flux conditions, but, due to the destabilizing effect of the reacting atmospheric temperature, this damping is less strong than in an ocean-only model under restoring boundary conditions.

4.3.3 Impact of the shape of the freshwater-flux forcing

Having established the relation between the interdecadal mode in the coupled model and the one in chapter 3, we now turn to the effect of salinity. Starting from the parameter values at the left point of Fig. 4.5, i.e. $D_0 = 1.0 \cdot 10^5$ m^{2}s^{-1}, the strength of the freshwater flux is increased from zero to $F_0 = 4.5 \cdot 10^{-7}$ ms^{-1} for a value $\eta_s = 0$ in the freshwater-flux profile.

With only a slight decrease from 25.0 Sv to 24.5 Sv, the maximum meridional overturning hardly reacts to this increase in freshwater forcing. The surface salinity and density fields for $F_0 = 4.5 \cdot 10^{-7}$ ms^{-1} are plotted in Fig. 4.7a and b, respectively. The surface temperature

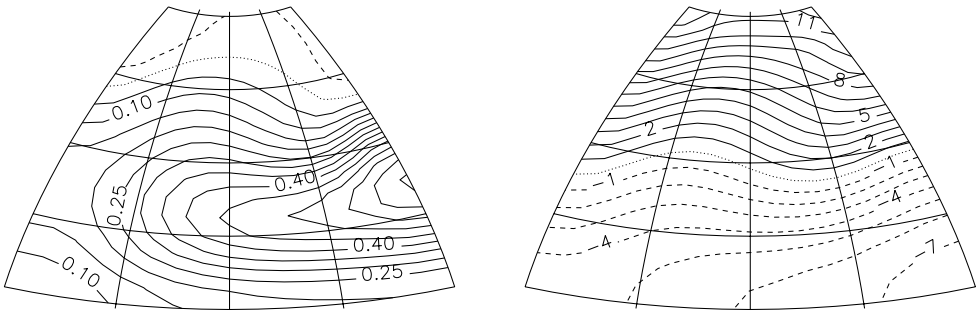

(a) (b)

Figure 4.7: *(a) Steady-state (dimensionless) salinity field at* 250 *m depth for freshwater-flux amplitude* $F_0 = 4.5 \cdot 10^{-7}$ *ms*$^{-1}$*. The dimensional salinity* S^* *can be obtained from* $S^* = S_0 + \Delta S\, S$*. (b) Dimensionless density field at* 250 *m depth.*

field is not shown, as it is fairly similar to the field shown in Fig. 4.2d. North of about $60\,^{\circ}$N the salinity is about 34.95, it increases towards a maximum value of 35.65 at the eastern boundary around $30\,^{\circ}$N and then decreases again towards the southern boundary. Comparison of Figs. 4.2d and 4.7b shows that the salinity has only a marginal effect on the density field (Note that the temperature in Fig. 4.2d is equal to minus the density, so that it can indeed be compared to Fig. 4.7b).

The dimensional growth rate and period of the interdecadal mode have been computed for increasing values of F_0 and are plotted in Fig. 4.8. The growth rate decreases with increasing

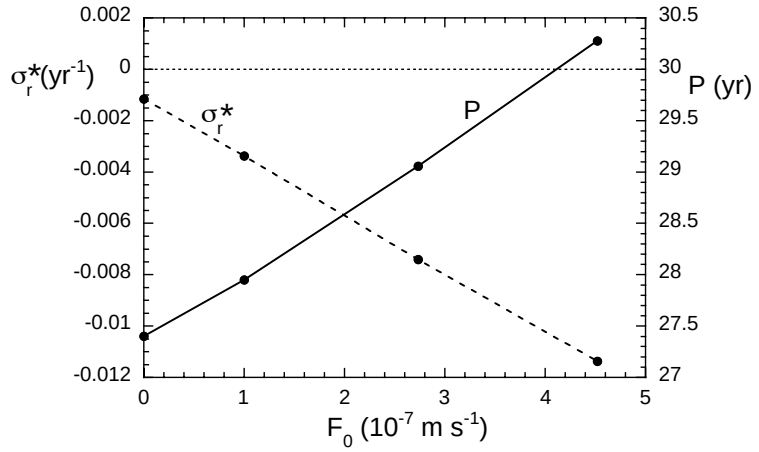

Figure 4.8: *Growth rate (dashed line) and period (solid line) as a function of F_0 for $D_0 = 1.0 \cdot 10^5$ $m^2 s^{-1}$. The left vertical axis is for σ_r^*, the right vertical axis for $\mathcal{P}$.*

strength of the freshwater flux, while the period of the oscillation increases slightly. The spatial patterns of salinity of the imaginary and real parts of the mode for $F_0 = 4.5 \cdot 10^{-7}$ ms^{-1} are plotted in Fig. 4.9a and b, respectively, with the corresponding temperature patterns in Fig. 4.9c and d. The temperature and salinity fields of the eigenvector have a rather similar spatial structure. At $t = -\mathcal{P}/4$, there is a positive salinity anomaly in the north-central part of the basin (Fig. 4.9a), while there is also a positive temperature anomaly in the northern part of the basin (Fig. 4.9c). The salinity anomaly propagates westward and southward (Fig. 4.9b) and is followed by a negative salinity anomaly a quarter of a period later, at $t = 0$. At that time the positive temperature anomaly has also propagated westward (Fig. 4.9d), and the temperature in the eastern half of the basin is already negative. A comparison of the relative amplitudes of the salinity and temperature fields in Fig. 4.9 shows that the density of this eigenmode is dominated by temperature. Freshwater-flux forcing with $\eta_s = 0$ has thus no significant influence on the steady state nor on the spatial structure of the interdecadal mode, but it has a substantial effect on the growth rate of this mode.

Next, for $F_0 = 4.5 \cdot 10^{-7}$ ms^{-1}, the shape of the profile of F_S is changed (see Fig. 4.1) by varying the parameter η_s in equation (2.24). On an increase of η_s to $\eta_s = 10$, i.e. extra evaporation north of about $65\,^{\circ}$N, the overturning increases to about 27.9 Sv. On the other hand, the overturning decreases with about 1 Sv to 23.4 Sv if η_s is decreased to $\eta_s = -6$.

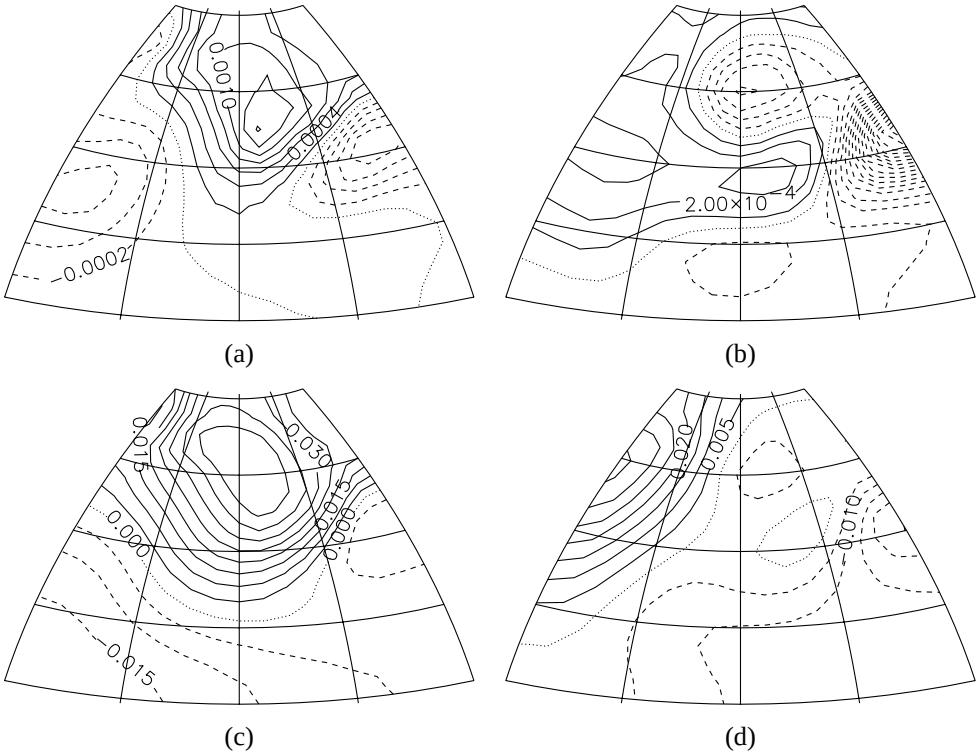

Figure 4.9: *(a) Spatial pattern of the salinity field of the imaginary part of the eigenvector at 250 m depth for* $F_0 = 4.5 \cdot 10^{-7}$ *ms*$^{-1}$*. (b) Spatial pattern of the salinity field of the real part of the eigenvector at 250 m depth. (c) as (a), but for the temperature field. (d) As (b), but for the temperature field.*

An increase in η_s, which corresponds to strong evaporation in the north, causes stronger damping of the interdecadal mode (Fig. 4.10). However, if η_s is decreased, the growth rate of this mode increases and crosses the zero-axis at about $\eta_s = -2.5$, with a critical period of about 32 yr (Fig. 4.10). This indicates that freshwater input in the north, which leads to a decreased meridional overturning, is able to destabilize the flow.

To understand the effects of the strength (F_0) and the shape (η_s) of the freshwater-flux forcing on the growth rate of the interdecadal mode, again energy arguments are used. The growth of density perturbations, due to both salinity and temperature perturbations, can be considered by monitoring the behavior of the energy functional $E = \frac{1}{2} < \overline{\tilde{\rho}^2} >$, which is a more general form of E_T. The time-derivative of E can be determined using

$$\frac{1}{2}\frac{d}{dt} < \overline{\tilde{\rho}^2} > = \left\langle \overline{\tilde{\rho}\frac{\partial \tilde{\rho}}{\partial t}} \right\rangle = \left\langle \overline{\tilde{\rho}\left(\lambda \frac{\partial \tilde{S}}{\partial t} - \frac{\partial \tilde{T}}{\partial t}\right)} \right\rangle \tag{4.11}$$

Using equations (2.5e) and (2.5f), this becomes

$$\frac{dE}{dt} = P_A + D_H + D_V + P_B \tag{4.12}$$

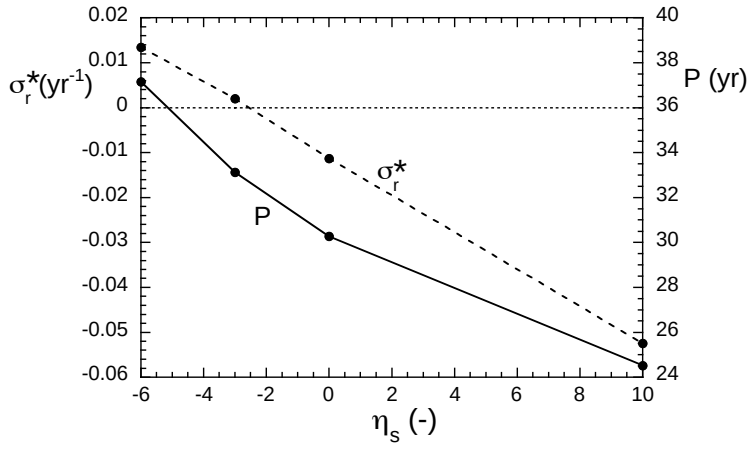

Figure 4.10: *Growth rate (dashed line) and period (solid line) as a function of the change in the freshwater-flux profile η_s. The left vertical axis is for σ_r^*, the right vertical axis for $\mathcal{P}$.*

with

$$P_A = -<\overline{\tilde{\rho}\,\tilde{\boldsymbol{u}}\cdot\nabla\bar{\rho}}> \tag{4.13a}$$

$$D_H = P_H\,<\overline{\tilde{\rho}\,\nabla_H^2\tilde{\rho}}> \tag{4.13b}$$

$$D_V = <\overline{\tilde{\rho}\,\frac{\partial}{\partial z}\left(P_V\frac{\partial\tilde{\rho}}{\partial z}\right)}> \tag{4.13c}$$

$$P_B = -\frac{\mu r_0}{\rho_0 C_{po} H_m U}\,<\overline{\tilde{\rho}\,(\tilde{T}_a-\tilde{T})\,G(z)}> \tag{4.13d}$$

which is the more general form of equation (4.5). As the total dissipation $D_H + D_V$ is negative definite, growth can only occur if P_A or P_B is positive. The latter of these two is interpreted as the change of available potential energy due to ocean-atmosphere interaction. The interpretation of P_A is slightly more complicated. Basically, this term represents the change of available potential energy due to feedback of the anomalous buoyancy advection on the density perturbation. Suppose, for instance, that both $\tilde{\boldsymbol{u}}\cdot\nabla\bar{\rho}$ and $\tilde{\rho}$ are positive, then the density decreases (as $\partial\tilde{\rho}/\partial t \sim -\tilde{\boldsymbol{u}}\cdot\nabla\bar{\rho} < 0$) at a location of anomalously light water ($\tilde{\rho} < 0$). This positive feedback tends to increase the energy functional E, corresponding to a destabilization of the flow.

The anomalous buoyancy advection can be split into anomalous advection of the background temperature field and anomalous advection of the salinity field, so that

$$P_A = P_A^T + P_A^S = -<\overline{\tilde{\rho}\,\tilde{\boldsymbol{u}}\cdot\nabla(-\bar{T})}> - <\overline{\tilde{\rho}\,\tilde{\boldsymbol{u}}\cdot\lambda\nabla\bar{S}}>$$

Usually, the salt advection feedback P_A^S is considered to be a positive feedback, and the temperature advection feedback P_A^T a negative one (e.g. Stommel (1961); Welander (1986)). In this classical interpretation, both feedbacks are thought of as a causal chain of processes in the two-dimensional plane of the meridional overturning. For instance, a negative salinity

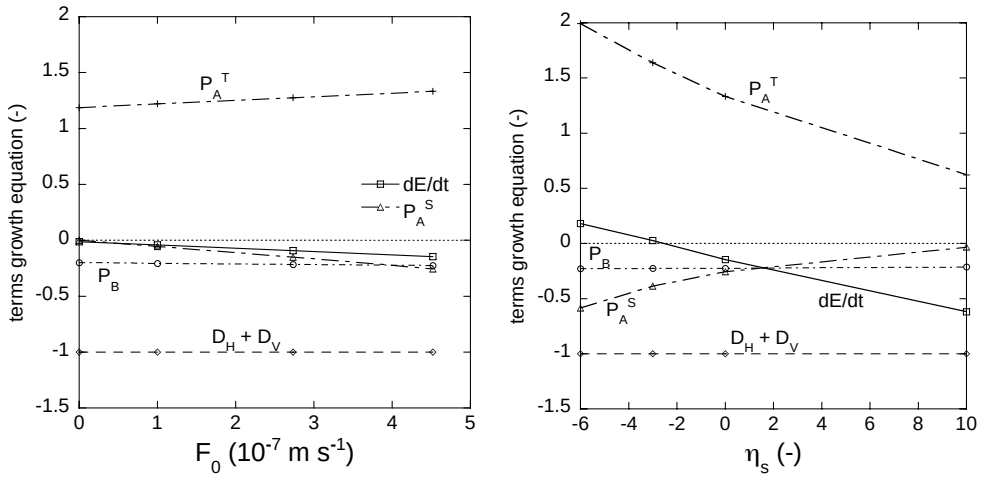

Figure 4.11: *(a) Terms in equation (4.12) as a function of F_0. All terms have been scaled with the absolute value of $(D_H + D_V)$. (b) As in (a), but as a function of η_s.*

anomaly in the north reduces the meridional overturning, causing less northward advection of salty surface water, thereby intensifying the original salinity anomaly.

The relative magnitudes of the terms in equation (4.12) are plotted as a function of F_0 in Fig. 4.11a for $\eta_s = 0$. The three-dimensional nature of the interdecadal mode appears to be essential in determining the stability properties of the mode, as P_A^T is positive and P_A^S negative (Fig. 4.11a). If F_0 is increased, the decrease in P_A^S (relative to the total dissipation) is stronger than the increase in P_A^T (relative to the total dissipation), so that dE/dt becomes more negative. In other words, due to increased anomalous advection of background salinity, the positive feedback between the anomalous advection of the background density field and the density perturbation is decreased, so that the available potential energy decreases and the flow is stabilized.

If η_s is decreased below -2.5, the destabilizing effect of the temperature feedback becomes stronger than the stabilizing effect of the other terms (Fig. 4.11b). In this case, the increased freshwater input in the north causes an anomalous circulation in such a way that there is a strong positive feedback of the anomalous advection of the background temperature field on the density perturbation. This makes dE/dt positive and causes the growth of the interdecadal mode.

4.4 Summary and discussion

Within an idealized coupled ocean-atmosphere model in which temperature is the only active buoyancy influencing variable, it has been explicitly shown that a robust interdecadal mode exists. The processes controlling the physical mechanism of the oscillation are the same as in the ocean-only situation considered in chapter 3. Westward propagating temperature

anomalies near the northern boundary cause changes in the perturbation zonal temperature gradient, with corresponding changes in the meridional overturning. These, in turn, lead to changes in the meridional perturbation temperature gradient, with a corresponding reaction of the zonal overturning.

With the physical mechanism of the interdecadal mode well-understood, we concentrated in this chapter on a systematic investigation of the stability of this mode in the context of a coupled ocean-atmosphere model. First, the situation in which temperature is the only active buoyancy influencing variable was considered. The real new element of this work, with respect to studies that have appeared in the literature, is that as a next step, the effect of salinity on the growth rate of the interdecadal mode was investigated.

In all investigated parameter regimes for the coupled model without salinity, the growth rate of the interdecadal mode is negative. Even for small values of D_0, the damping influence of the atmosphere remains strong enough to keep the steady state stable. An energy analysis, in which the norm of temperature perturbations was used as energy functional, showed that the stabilizing effect of the atmosphere consists of two parts. There is a direct damping effect on oceanic temperature anomalies, as in the restoring case for ocean-only models. However, this damping effect is partly neutralized, because in the coupled model the atmospheric temperature can react to changes in the ocean. This makes that in the coupled model the interdecadal mode is damped less than in an ocean-only model under restoring conditions, but it is damped more than in an ocean-only model forced by a prescribed heat flux.

The inclusion of salinity in the buoyancy field affects mainly the growth rate of the interdecadal mode, but not its mechanism. Under a standard freshwater-flux forcing, the salinity field hardly influences the steady-state overturning, but it decreases the energy transfer from the steady circulation to the interdecadal mode. In particular, the three-dimensional salt advection feedback has a stabilizing effect on the flow, as it weakens the positive feedback between the anomalous advection of the background density and the density perturbation.

Within the framework sketched above, many other model results can be synthesized. The existence of a stable interdecadal mode is consistent with the interpretation of the CGCM results in Delworth and Greatbatch (2000). In their model, variability at multidecadal time scales disappears when the ocean-only model is forced with the climatological atmospheric fluxes. Hence, the variability is excited by the atmospheric noise through mechanisms which have been described in Griffies and Tziperman (1995) within a simple box model. Note however, that the interdecadal mode is not represented in the box-model of Griffies and Tziperman (1995), as the dynamics of this mode is essentially three-dimensional.

However, one has to be cautious with the interpretation of results of transient computations in terms of stability of internal modes. If interdecadal variability is found in a numerical time integration, this does not necessarily mean that an unstable interdecadal mode is present, as there is often numerical noise in a time integration. Although usually rather weak, this noise level might already be enough to excite a marginally stable interdecadal mode.

Huck *et al.* (2001) find a limited regime of sustained interdecadal oscillations at small vertical mixing coefficient $K_V = 5 \cdot 10^{-5}$ m^{2}s^{-1} when they use a constant albedo, but with variable albedo (as used here) they find sustained oscillations for all values of the exchange coefficient. Apparently, in the work of Huck *et al.* (2001), the interdecadal mode is damped less than in our results. A possible reason could be that the presence of numerical noise excites the marginally stable interdecadal mode in the results of Huck *et al.* (2001). Another

possibility is that the lower value of A_H used by Huck *et al.* (2001) results in less damping of the interdecadal mode.

The sensitivity of the growth rate of the interdecadal mode to the freshwater-flux profile has indicated that slight changes in the mean state can already destabilize the flow. The self-sustained interdecadal variability in the coupled ocean-atmosphere model of Chen and Ghil (1996) is another example of how easily the interdecadal mode can be excited by a slight change in the mean state, even without salinity. In their study, the shortwave radiative flux into the ocean (the first term in our equation (2.14)) has been ignored. In this way, the area-averaged sea surface temperature in their model is equal to the averaged atmospheric temperature, yielding a different steady state, with likely different stability properties.

In ocean-only models in which temperature is the only active buoyancy component, self-sustained interdecadal variability has often been found. In these models, the flow is easily destabilized (Greatbatch and Zhang (1995); Huck *et al.* (1999); chapter 3 of this thesis) because of the lack of atmospheric damping. For these models the position in parameter space of the Hopf bifurcation, separating the regime of steady and oscillatory behavior of the flow, is crucial for the occurrence of interdecadal variability. Changing parameters will shift the position of this bifurcation, and the flow may change from oscillatory to steady. However, even if the flow is stable, the addition of noise in this type of models will easily excite the variability again.

Many studies of interdecadal variability have been done with models forced by mixed boundary conditions. However, both the stability and variability of these models are known to be extremely sensitive to parameters and model configuration (Weaver and Sarachik, 1991b). This sensitivity likely explains the host of different results, types of oscillations and periods found in these models (e.g. Chen and Ghil (1995); Weaver and Sarachik (1991a,b)). One of the potential causes of these problems is the use of convective adjustment, which has been shown to introduce artificial limit points and Hopf bifurcations (Vellinga, 1998). Our preliminary analysis has indicated that the problems with these artificial bifurcations are much less pronounced if the ocean model is coupled to an energy-balance atmospheric model, with additional prescribed freshwater fluxes, because the surface temperature is then free to adjust. We think therefore that it is best not to use models with mixed boundary conditions for the investigation of phenomena like interdecadal variability, but to use —at least— a hybrid coupled model as was used here.

This study shows the relevance of idealized models for understanding complex problems like the stability and variability of the North-Atlantic Ocean circulation. Whereas models with a high degree of complexity are used to simulate observed phenomena and point towards important processes or sensitivities involved, idealized models are needed to identify precise causes and physical mechanisms. In this way, the central point of this study was to explain the increase in amplitude of the multidecadal variability in the GFDL-CGCM found by Tziperman (2000), when the northern North Atlantic was made less saline. Again using an energy analysis, we have shown that changing the shape of the freshwater-flux forcing has a significant effect on the energy transfer to the interdecadal mode. Increased freshwater input in the north causes an anomalous circulation such that the positive feedback of the anomalous advection of the background temperature field on the density perturbation is strengthened. If the freshwater input in the north is strong enough, this feedback will overcome the combined damping effects of dissipation, atmospheric coupling and advection of

the background salinity field. The tendency of the energy functional $<\tilde{\rho}^{\,2}>$ will then become positive, causing growth of the interdecadal mode. In the CGCM of Tziperman (2000), there is weak multidecadal variability under standard freshwater-flux forcing, as the marginally damped interdecadal mode is excited by noise. When the northern North Atlantic is made less saline, the positive feedback of the anomalous advection of the background temperature field on the density perturbation causes growth of the interdecadal mode, resulting in an increased amplitude of the multidecadal variability.

Chapter 5

Modes of internal thermohaline variability in a single-hemispheric ocean basin

In this chapter, it is investigated which internal modes of variability of the thermohaline ocean circulation can most easily extract energy from the mean flow in an idealized single-hemispheric ocean basin. Relevant for the large-scale low-frequency variability of the flows are two kinds of oscillatory modes. The modes in one of these classes, which have interdecadal time scales, are the truly three-dimensional interdecadal modes which have been investigated in chapter 3, while modes in the other class have a multicentennial time scale. The latter modes are shown to persist as internal modes of variability of two-dimensional flows and are therefore related to overturning (or loop) oscillations. The physical mechanism of propagation of the multicentennial modes is described and the relevance of the internal modes is investigated through analysis of stochastically forced transient flows[*].

5.1 Introduction

The thermohaline ocean circulation varies on many time scales, ranging from decades to much longer, as far as we can tell from instrumental and paleoclimatic data (National Research Council, 1995). There exist but few continuous instrumental records with any spatial resolution and useful accuracy on these time scales, most of them in the North-Atlantic Ocean. Fairly long SST data sets exist, such as COADS (Da Silva *et al.*, 1994), from which near-surface patterns of variability on interannual to decadal time scales have been determined (Deser and Blackmon, 1993; Kushnir, 1994). Much less information is available about variability of the ocean circulation at deeper levels. Nonetheless, changes in water mass characteristics associated with, for instance, changes in convective activity have been observed (Dickson and Brown, 1994; Schlösser *et al.*, 1991).

[*]This chapter is based on the paper '*Modes of internal thermohaline variability in a single-hemispheric ocean basin*', by L. A. te Raa and H. A. Dijkstra (submitted to *J. Mar. Res.*)

The instrumental record is too short to give any observational indications for climate variability at time scales longer than a couple of decades. Evidence for longer-term variability must therefore come from proxy data. Ice and sediment cores, tree rings and other (e.g. biological) data have yielded substantial evidence of variability at centennial time scales (Stocker and Mysak, 1992; McDermott *et al.*, 2001).

The thermohaline ocean circulation is thought to play an important role in the variability on interdecadal as well as centennial time scales (Broecker *et al.*, 1985; Stocker and Mysak, 1992; Sarachik *et al.*, 1996). Many different models, varying in complexity from simple box models to global coupled ocean-atmosphere models, have been used to investigate variability of the climate and that of the thermohaline circulation in particular (section 1.3). As was also mentioned in the previous chapter, the GFDL climate model has had a prominent role in this type of studies. Many studies with idealized models have for instance been done to try to explain the multidecadal variability found by Delworth *et al.* (1993) in a 600-yr long simulation with the global coupled GFDL model.

Two different ideas have resulted from the variety of mechanisms proposed to explain the multidecadal variability found by Delworth *et al.* (1993). One is that the mode responsible for the multidecadal variability in the GFDL model is a westward propagating temperature signal, which is associated with anomalies in the overturning circulation. In its simplest form, this mode is found as a sustained oscillation in models in which the heat flux is prescribed, and no salinity field is active (Greatbatch and Zhang, 1995; Huck *et al.*, 1999). This is the mode found in chapters 3 and 4 as an instability of the three-dimensional circulation. The physical mechanism of propagation of this mode was shown to be essentially three-dimensional (chapter 3). A completely different theory is that this mode is governed by basically two-dimensional ocean processes. Its simplest form is derived from a four-box model (Griffies and Tziperman, 1995; Rivin and Tziperman, 1997) and its physics has been described in more detail by Sirkes and Tziperman (2001). It is associated with the positive and negative advection feedbacks of salt and heat, respectively, which have a phase difference because of the flow response. As there are so little observations in the deeper ocean, it cannot be decided on the basis of observations which of these explanations is correct.

In the coupled GFDL-model results of Delworth *et al.* (1993), there is also variability on longer (centennial) time scales, for example in the amplitude of the multidecadal variability, but the 600-yr run is too short to examine this in more detail. However, variability at centennial time scales has been found in several other numerical modeling studies (Mikolajewicz and Maier-Reimer, 1990; Weaver *et al.*, 1993; Winton and Sarachik, 1993). The variability in these studies can be interpreted in terms of the loop oscillation described by Welander (1986). A salinity anomaly causes weakening or strengthening of the overturning through an advective feedback. The period of this oscillation is therefore related to the overturning time scale.

So far, only the three-dimensional interdecadal mode of chapter 3 has been identified as an internal oscillatory eigenmode of the thermohaline circulation in the context of a single-hemispheric basin. The question whether also other (two-dimensional) interdecadal modes, or modes with longer time scales, can be found as internal modes of the thermohaline circulation, asks for a systematic study of the preferred modes of variability of the thermohaline circulation. In this chapter, these modes are investigated for single-hemispheric basin flows in the ocean-only case. The relevant oscillatory eigenmodes following from the linear stability

analysis are considered in section 5.2. Apart from the interdecadal mode, described already in chapter 3, another class of modes is found, which has centennial periods and which can easily extract energy from the mean flow. The physical mechanism of these centennial modes is considered in section 5.3. In section 5.4, transient flows are considered to study how these modes affect the total circulation. A framework for understanding internal thermohaline variability on interdecadal and centennial time scales is sketched in the discussion in section 5.5.

5.2 Linear stability of 3D thermohaline flows

The studies in this chapter have been carried out with the THCM ocean-only model in the standard configuration described in section 2.4. The equidistant grid was used, with a vertical resolution of 250 m. The horizontal eddy diffusivity was set to $K_H = 1000\,\mathrm{m^2 s^{-1}}$. Standard values of the mixing parameters used in this chapter are given in Table 5.1.

A_H	=	$1.6 \cdot 10^7$	[m^{2}s^{-1}]	A_V	=	$1.0 \cdot 10^{-3}$	[m^{2}s^{-1}]
K_H	=	$1.0 \cdot 10^3$	[m^{2}s^{-1}]	K_V	=	$2.3 \cdot 10^{-4}$	[m^{2}s^{-1}]
E_H	=	$2.7 \cdot 10^{-3}$		E_V	=	$4.3 \cdot 10^{-7}$	
P_H	=	$1.6 \cdot 10^{-3}$		P_V	=	$9.2 \cdot 10^{-4}$	

Table 5.1: *Reference values of mixing parameters used in the numerical computations of chapter 5.*

A branch of steady-state solutions under restoring boundary conditions for temperature has again been computed by increasing the parameter η_T, controlling the amplitude of the applied surface temperature (see equation 2.22), from 0 to its standard value $\eta_T = 10.0$. The steady state at $\eta_T = 10.0$, which is rather similar to the steady state of the reference solution in chapter 3, has a maximum meridional overturning of 22.5 Sv. Plots of the meridional overturning, two slices of the velocity field and three slices of the density field of this steady state are shown in Fig. 5.1. The meridional overturning consists of one cell with sinking confined to the northernmost part of the domain. The surface circulation is anti-cyclonic (Fig. 5.1c) with upward vertical velocities at the western part of the basin. A reversed flow occurs at 1500 m (Fig. 5.1e) and also near the bottom (not shown), consistent with the overturning circulation. A section of density in a north-south vertical plane shows a 'pycnocline' in the upper 1000 m, with only slight static instabilities in the northern part of the domain (Fig. 5.1b). Surface density patterns show small advective departures (Fig. 5.1d) from the zonally uniform state, while at 1500 m the density has a maximum in the northeastern part of the basin (Fig. 5.1f).

The linear stability of this steady state under different boundary conditions was considered by computing the 8 most unstable or least damped eigenmodes for three cases (see Table 5.2). In case F (prescribed heat flux conditions) the surface heat flux perturbation is zero, whereas in case R (restoring boundary condition) the surface temperature perturbation is zero. Case M is the same as case R, apart from the fact that salinity perturbations are now also allowed. Note that in all three cases, the steady-state salinity field has the constant value $S = S_0$. To make the connection with the results in chapter 3, we first consider the stability

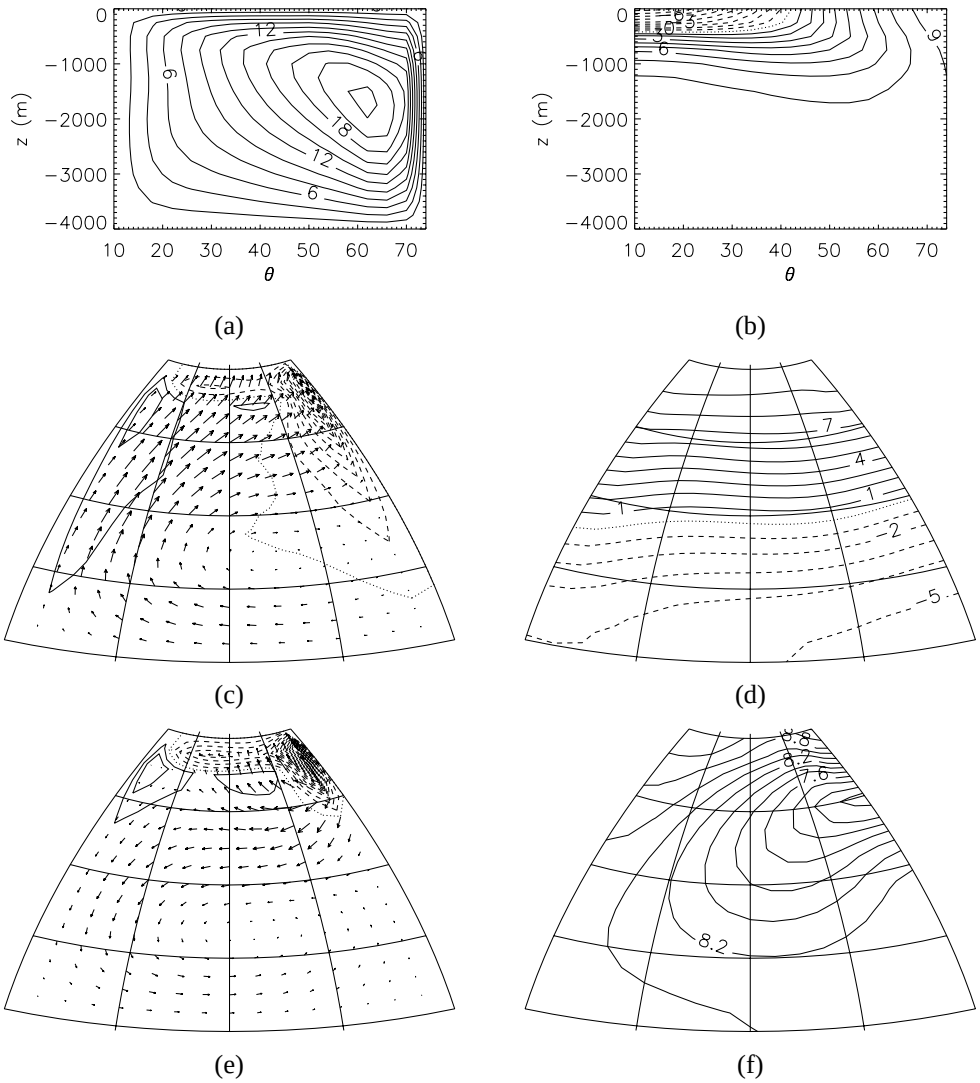

Figure 5.1: *Steady-state solution. (a) Meridional overturning streamfunction (in Sverdrups). (b) Density (dimensionless) for a north-south vertical plane through the middle of the basin ($\phi = 42°W$). The dimensional density can be obtained from $\rho^* = \rho_0(1 + \alpha_T \Delta T \rho)$. (c) Velocity (dimensionless) near the surface (at 250 m depth). The maximum dimensional horizontal velocity is $2.0 \cdot 10^{-2}$ ms^{-1}, the maximum amplitude of the vertical velocity is $1.1 \cdot 10^{-5}$ ms^{-1} (downwelling). (d) Density near the surface. (e) Velocity at $z = -1500$ m. Maxima are $4.9 \cdot 10^{-3}$ ms^{-1} for the horizontal and $3.6 \cdot 10^{-5}$ ms^{-1} (downwelling) for the vertical velocity. (f) Density at $z = -1500$ m.*

analysis of the steady state shown in Fig. 5.1 under prescribed heat-flux forcing (case F).

Case	Stability analysis	Mode	Growth rate (yr^{-1})	Period (yr)
F	prescribed flux	$\mathcal{M}_I$	0.024	54
		$\mathcal{C}_1$	-0.023	456
R	restoring	$\mathcal{C}_1$	-0.025	347
M	mixed	$\mathcal{C}_2$	-0.017	396
		$\mathcal{C}_1$	-0.025	347

Table 5.2: *Different cases considered in the linear stability analysis.*

5.2.1 Prescribed heat-flux forcing

The surface heat flux Q_{Td} of the steady state shown in Fig. 5.1 is diagnosed and then prescribed as a boundary condition instead of the restoring boundary condition in (2.6a). By construction, the steady-state solution in Fig. 5.1 is also a solution under the prescribed heat flux Q_{Td}. The steady state turns out to be unstable, as the two eigenmodes with largest real part form a complex pair of eigenvalues $\sigma = \sigma_r \pm i\sigma_i$ with positive growth rate $\sigma_r = 0.049$, corresponding to a dimensional growth rate $\sigma_r^* = 0.024$ yr^{-1}. The mode, which we label mode $\mathcal{M}_I$, has a period $\mathcal{P} = 2\pi r_0/(U\sigma_i) = 54$ yr, which is in the interdecadal range. To characterize the eigenmode, the meridional overturning streamfunction, two slices of the buoyancy field and the surface velocity field are plotted. Pictures of typical patterns corresponding to the imaginary and real parts of the eigenvector of mode $\mathcal{M}_I$ are shown in Fig. 5.2.

At $t = -\pi/2\sigma_i$, the meridional overturning perturbation is negative in most of the basin, indicating a weakening of the northward surface flow (Fig. 5.2a). Near the surface, there is a positive density anomaly in the southeastern part of the basin (Figs. 5.2c and e), but in the northwestern corner the density anomaly is negative and extends to the bottom due to convective mixing. There is anomalous upwelling along most of the northern boundary (Fig. 5.2g), consistent with the overturning anomaly. A quarter of a period later, at $t = 0$, the negative meridional overturning anomaly has extended southward (Fig. 5.2b). The positive buoyancy anomaly has propagated northward and westward (Figs. 5.2d and f) and extends down to the bottom along the northern boundary. There is anomalous upwelling in the northwestern and anomalous downwelling in the northeastern corner of the basin (Fig. 5.2h), giving rise to a cyclonic surface circulation. This mode is the same mode as the interdecadal mode described in detail in chapter 3, which can be seen by comparing the patterns of the mode in Fig. 5.2 to those in Figs. 3.3 and 3.4. The only differences between the configuration used in this chapter and the one in chapter 3 are the vertical grid (which was non-equidistant in chapter 3) and the value of K_H. From Fig. 3.7 it can be seen that the period of the interdecadal mode in the case of a non-equidistant grid for $K_H = 1000$ m^{2}s^{-1} is about 55 yr (compared to 54 yr here), showing that the vertical stretching of the grid hardly influences the mode. In chapter 3 the westward propagation of buoyancy (temperature) anomalies was shown to be a key element in this oscillation, causing a phase difference between the anomalous zonal and

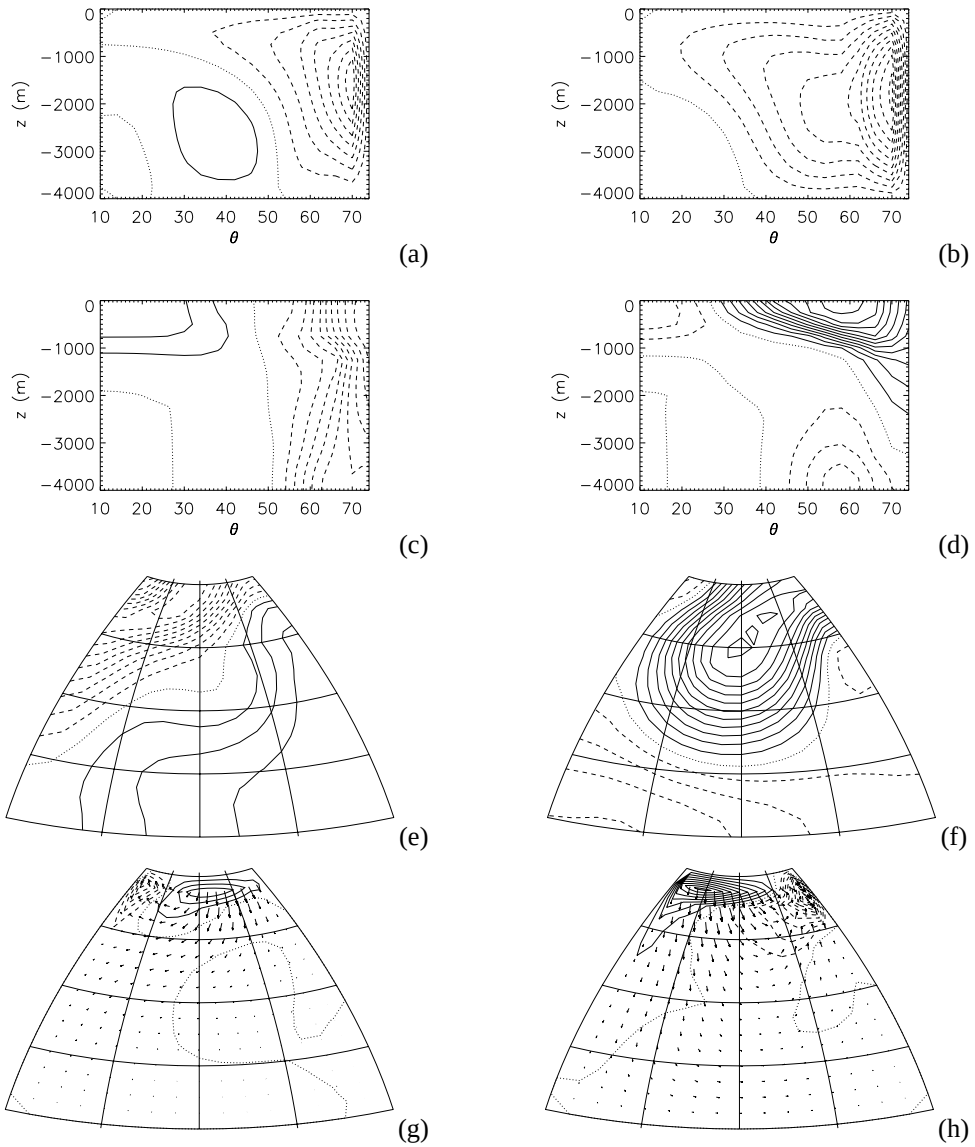

Figure 5.2: *Imaginary and real parts of the eigenvector corresponding to the interdecadal mode $\mathcal{M}_I$ under prescribed flux boundary conditions. The left panels show the imaginary part of the eigenvector, the right panels the real part. (a) and (b) Meridional overturning streamfunction. (c) and (d) Density at $\phi = 42°$W. (e) and (f) Density at 250 m depth. (g) and (h) Velocity at 250 m depth. Note that the amplitude is arbitrary.*

meridional buoyancy gradients, which in turn gives a phase-lagged response of the meridional and zonal overturning perturbations. This mode is therefore an essentially three-dimensional phenomenon.

The next eigenmodes in the spectrum are a damped real mode, which is not of interest for the present study, and another oscillatory mode with dimensional growth rate $\sigma_r^* = -0.023$ yr^{-1} and a centennial period $\mathcal{P} = 456$ yr. The imaginary and real parts of this mode, which was labeled $\mathcal{C}_1$, are shown in Fig. 5.3. Plotted are the meridional and zonal overturning and the zonally and meridionally averaged density field. At $t = -\pi/2\sigma_i$, the meridional overturning anomaly is positive in most of the basin (Fig. 5.3a), thereby strengthening the overturning. Near the surface and along the northern boundary there is a very weak cell that rotates in opposite direction. The zonal overturning anomaly is positive (Fig. 5.3c), indicating anomalous westward flow near the surface and anomalous eastward flow in the deep ocean. Near the surface, there is a large positive density anomaly in most of the basin (Fig. 5.3e and g). The negative density anomaly that can be seen around 1500 m depth in the zonally averaged density field (Fig. 5.3e) has a maximum near the eastern boundary (Fig. 5.3g).

A quarter of a period later, at $t = 0$, the positive meridional overturning anomaly has shifted northward and has been followed by a negative anomaly in the southern part of the basin (Fig. 5.3b). Below 1000 m, there is a strong negative zonal overturning anomaly, but in the upper 1000 m it is very weak (Fig. 5.3d). Anomalously dense water is found in the deep southern part of the basin and in the upper 1500 m of the northern part of the basin (Fig. 5.3f). Again, the density anomalies have largest amplitudes near the eastern boundary (Fig. 5.3h).

Although this mode is damped in the present configuration, its presence shows that the thermohaline circulation is in principle capable of generating internal variability on centennial time scales as well, as damped modes might be excited by stochastic components in the forcing (Griffies and Tziperman, 1995). Before investigating the physical mechanism of mode $\mathcal{C}_1$ in more detail in section 5.3, we turn to the results of the linear stability analysis under restoring boundary conditions for temperature.

5.2.2 Restoring boundary conditions

The stability analysis was repeated while using a restoring boundary condition (case R in Table 5.2), with Q_T given by the restoring condition in equation (2.6a). In this case all eigenvalues have negative real parts, so that the steady state is stable. The least damped oscillatory eigenmode is a mode with growth rate $\sigma_r^* = -0.025$ yr^{-1} and period $\mathcal{P} = 347$ yr (Table 5.2). The velocity and density patterns of this mode are quite similar to those of mode $\mathcal{C}_1$, which were shown in Fig. 5.3, and we conclude that this must be the same mode. There are some modifications near the surface due to the different boundary condition, which also cause the period to be a bit shorter in case R than in case F. The interdecadal mode was not found within the first 8 eigenmodes. This is in correspondence with the fact that a restoring boundary condition for temperature damps the interdecadal mode considerably, as explained in chapter 3.

The effect of the presence of salinity perturbations on the steady state of Fig. 5.1 was studied by performing a second linear stability analysis under restoring boundary conditions, but now with $\lambda = 7.6$, that is, a coefficient $\alpha_S = 7.6 \cdot 10^{-4}$ in the equation of state (case

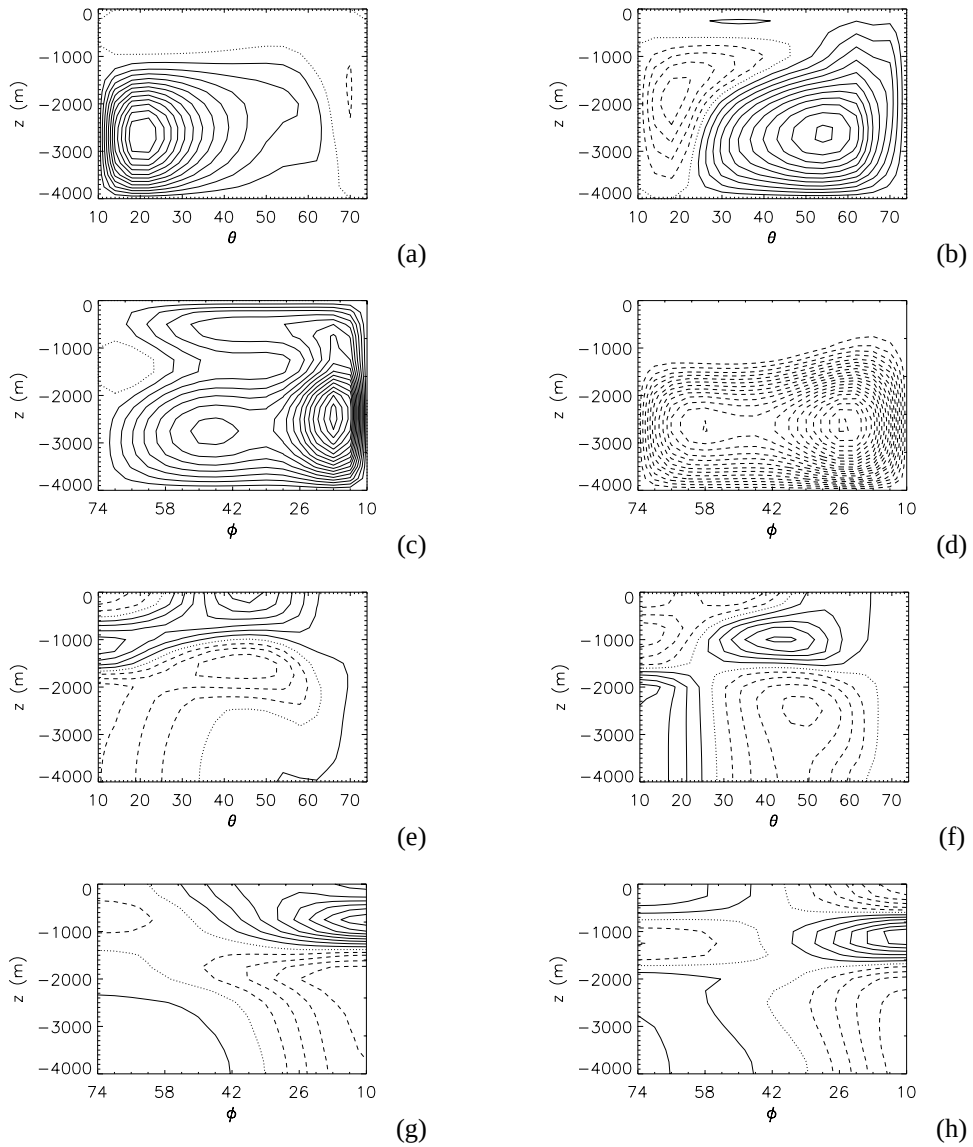

Figure 5.3: *Imaginary (left) and real (right) parts of the eigenvector corresponding to centennial mode $\mathcal{C}_1$. (a) and (b) Meridional overturning streamfunction. (c) and (d) Zonal overturning streamfunction. (e) and (f) Zonally averaged density. (g) and (h) Meridionally averaged density.*

M in Table 5.2). In other words, we allow for perturbations on the constant steady-state salinity field, so that density perturbations can be caused by both temperature and salinity perturbations. Again, all eigenvalues have negative real parts, but this time two oscillatory

eigenmodes are found (Table 5.2). One of them is mode $\mathcal{C}_1$, with the same growth rate and period as in case R. The second oscillatory mode, which was labeled $\mathcal{C}_2$, has also a period in the centennial range ($\mathcal{P} = 396$ yr) and has a growth rate $\sigma_r^* = -0.017$ yr^{-1}. The main difference between mode $\mathcal{C}_1$ and $\mathcal{C}_2$ is that density perturbations in mode $\mathcal{C}_2$ are determined by both temperature and salinity, whereas they are determined by temperature only in mode $\mathcal{C}_1$.

The imaginary and real parts of mode $\mathcal{C}_2$ are shown in Fig. 5.4. To characterize this mode, the meridional overturning, the zonally and meridionally averaged density field and the zonally averaged temperature and salinity field are plotted. At $t = -\pi/2\sigma_i$, there is a strong positive meridional overturning anomaly in most of the basin (Fig. 5.4a), except in the southern part, where there is a weak negative anomaly near the surface. The negative density anomaly near the surface in the zonally averaged density field (Fig. 5.4c) is mainly due to the negative salinity anomaly (Fig. 5.4g), while the positive density anomaly around 1500 m depth (Fig. 5.4c) is mainly caused by a cold anomaly (Fig. 5.4e). The amplitudes of the density anomalies have a maximum at the eastern boundary (Fig. 5.4i). At $t = 0$, the negative overturning anomaly has extended and occupies the whole basin (Fig. 5.4b), thereby weakening the overturning circulation. The density anomalies have moved downwards (Fig. 5.4d), which is again a combined effect of temperature (Fig. 5.4f) and salinity (Fig. 5.4h). Also in this phase of the oscillation, the maximum amplitudes of the density anomalies occur at the eastern boundary (Fig. 5.4j).

A comparison of the patterns of the modes $\mathcal{C}_1$ and $\mathcal{C}_2$ shows that there are many similarities. Near the surface, the salinity anomalies play a substantial role in the density perturbations and consequently the surface density perturbations are more negative in mode $\mathcal{C}_2$ than in $\mathcal{C}_1$. This induces a more complex surface structure of the meridional overturning in mode $\mathcal{C}_2$. However, the zones of maximum amplitude in the meridional overturning and spatial patterns of the meridionally averaged density are similar for both modes.

5.3 Physics of the centennial modes

Centennial variability found in previous studies (Mikolajewicz and Maier-Reimer, 1990; Winton and Sarachik, 1993), in which (mainly) salinity anomalies are advected around the meridional overturning loop, has mostly been linked to the loop oscillation of Welander (1986). Clearly, advection of salinity anomalies can not play a role in the centennial mode $\mathcal{C}_1$, in which density anomalies are determined by temperature only. Nevertheless, a related mechanism must be at work here: temperature anomalies cause flow perturbations, resulting in advection of heat which consequently changes the temperature anomalies. The feedback between temperature (or density) and flow perturbations involves the full three-dimensional temperature and velocity fields. This feedback can be made more transparent by considering also the meridional and zonal overturning perturbations, in addition to the velocity fields. Assuming that, to first order, the thermal wind balance holds for the perturbation flow, the zonal and meridional velocity perturbations $\tilde{u}$ and $\tilde{v}$ are related to the meridional and zonal perturbation density gradients through

$$\frac{\partial \tilde{u}}{\partial z} = \frac{Ra}{\sin\theta}\frac{\partial \tilde{\rho}}{\partial \theta}\,; \quad \frac{\partial \tilde{v}}{\partial z} = -\frac{Ra}{\sin\theta\cos\theta}\frac{\partial \tilde{\rho}}{\partial \phi} \tag{5.1}$$

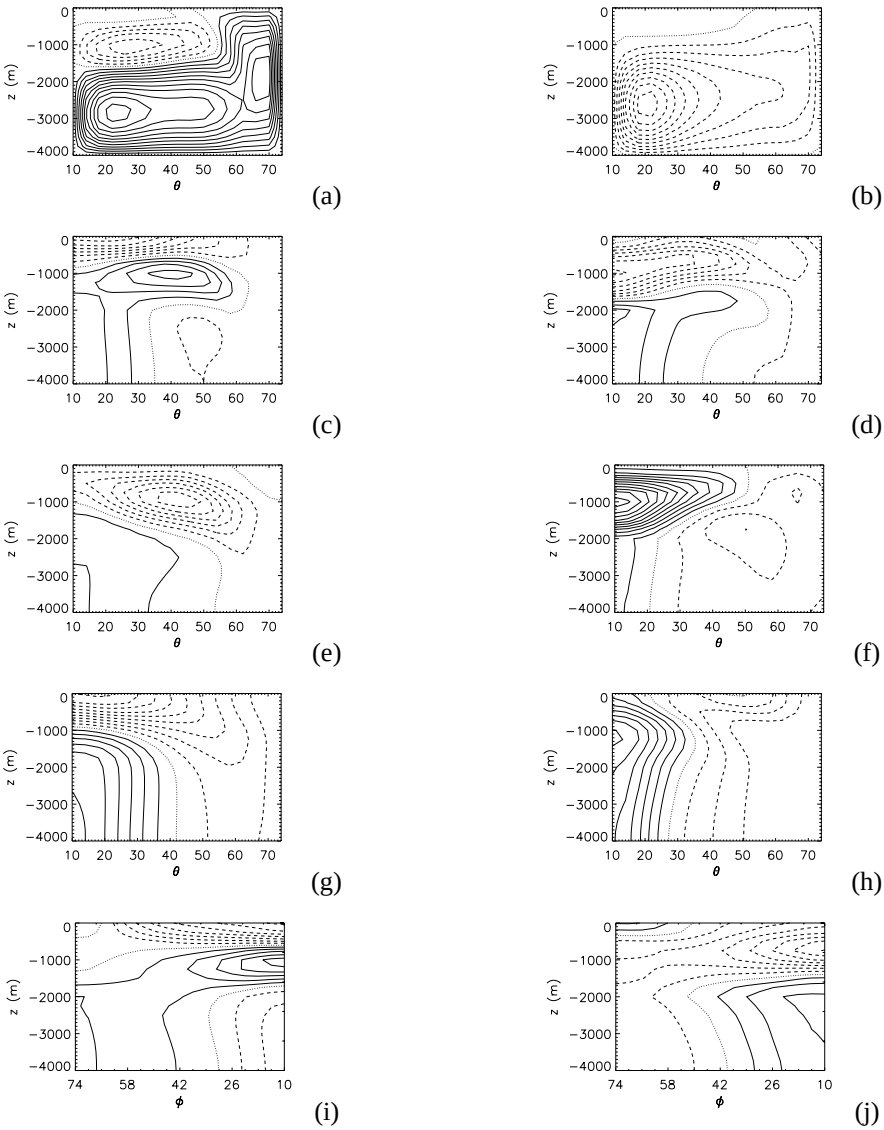

Figure 5.4: *Imaginary (left) and real (right) parts of the eigenvector corresponding to centennial mode $\mathcal{C}_2$ (computed with $\lambda = 7.6$). (a) and (b) Meridional overturning streamfunction. (c) and (d) Zonally averaged density. (e) and (f) Zonally averaged temperature. (g) and (h) Zonally averaged salinity. (i) and (j) Meridionally averaged density.*

The propagation features of mode $\mathcal{C}_1$ can then be explained as follows. At $t = -\pi/2\sigma_i$, there is a negative density perturbation in the center and in the southeastern part of the basin, with anomalously dense water near the surface in the northeast (Figs. 5.3e and g). The neg-

ative density anomaly in the deep southern part of the ocean (Fig. 5.3e) is advected upward by the steady-state meridional overturning (Fig. 5.3f). Effects of the downward advection of density anomalies by the steady-state circulation can be seen near the eastern boundary as well (Fig. 5.3h). On the other hand, density anomalies also induce an anomalous circulation, which then advects the steady-state density field. Namely, in the upper 1000 m and below 2000 m, the (zonally averaged) meridional perturbation density gradient is positive (Fig. 5.3e), so that the anomalous zonal velocity increases towards the surface, which corresponds with the anomalous zonal overturning (Fig. 5.3c). Also, the (meridionally averaged) zonal perturbation density gradient is positive in the upper 1500 m and negative below this depth, which causes the anomalous meridional velocity to increase with z below about 1500 m, resulting in the positive meridional overturning perturbation shown in Fig. 5.3a. This meridional overturning perturbation advects relatively light water downwards between about $30°$N and $60°$N, leading to a negative density anomaly in the deep ocean north of about $30\,°$N (Fig. 5.3f).

In turn, the changes in perturbation density affect the anomalous flow. For instance, the meridional perturbation density gradient has become negative below about 1500 m at $t = 0$, causing the anomalous zonal velocity to decrease with z. This gives a negative zonal overturning anomaly below 1500 m (Fig. 5.3d). The positive zonal perturbation density gradient between about 800 m and 1800 m depth (Fig. 5.3h) leads to an anomalous meridional velocity which decreases with z and this is reflected in the negative meridional overturning cell which develops in the southern part of the basin (Fig. 5.3b). Now, the anomalous meridional overturning at $t = 0$ creates a positive density anomaly in the center of the basin due to anomalous upwelling of relatively dense steady-state water (the opposite of Fig. 5.3e). On the other hand, the steady-state meridional overturning advects the anomalous density field, which can for instance be seen in the movement of density anomalies near the surface and the eastern boundary. Together, these effects yield an anomalous density field which is the opposite of that in Figs. 5.3e and g, after which the second half of the oscillation occurs. The propagation of the anomalies in mode $\mathcal{C}_2$ can be explained in a similar way. As it is slightly more complicated, because both temperature and salinity anomalies play a role, we will not explain mode $\mathcal{C}_2$ in detail here.

From the description above, it appears that advection of density anomalies by the large-scale overturning circulation is important for the existence of the centennial modes. However, flow perturbations also advect the steady-state density field and the fact that the circulation is three-dimensional makes the situation even more complex. Although the advection of steady-state density by the anomalous circulation plays a role as well, the time scale of the oscillation will certainly be related to the overturning time scale of the steady state. This time scale, say τ_{ov}, can be estimated as the total volume of the basin divided by the maximum meridional overturning. For the steady state here, the overturning time scale is $\tau_{ov} = 200$ yr, which is less than the oscillation periods (347 yr and 456 yr), but of the right order of magnitude. A similar type of mode was also found in two-dimensional situations in which there is flow in the meridional/vertical plane only (Dijkstra and Molemaker, 1997). Winton and Sarachik (1993) found centennial loop oscillations in both 2D- and 3D-frictional geostrophic models. Therefore the question arises if there is any connection between the centennial modes $\mathcal{C}_1$ and $\mathcal{C}_2$ and modes in the 2D-situation.

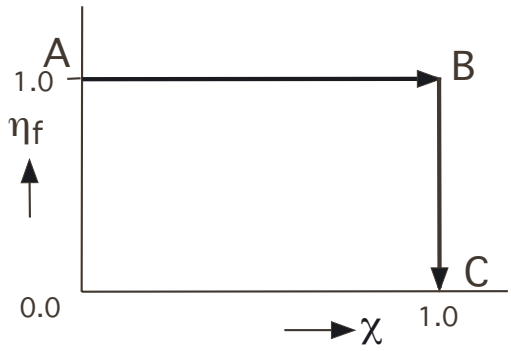

Figure 5.5: *Path in the parameter plane set by χ and η_f along which the steady state and the mode $\mathcal{C}_1$ are followed.*

To investigate this, we follow both modes along a path in parameter space, making a continuous connection between the 3D-situation considered so far and a quasi-2D case, in which there is no rotation and, as a consequence, no circulation in the zonal direction. Two different paths are chosen, to allow for the inclusion of a case with a non-zero freshwater-flux forcing as well. Mode $\mathcal{C}_1$ is followed along a path as sketched in Fig. 5.5. Starting from the situation with restoring boundary conditions, first the boundary conditions on all side boundaries are changed continuously from no-slip to slip conditions, by changing the parameter χ in (2.7) from 0 to 1. Next, the rotation rate is decreased to zero by changing the parameter η_f in (2.5a) and (2.5b) to zero. As in the final situation the forcing is zonally independent, the resulting steady flow has no zonal structure. Along this path a control parameter ζ is defined as $\zeta = \chi + (1 - \eta_f)$, such that $\zeta = 0.0$ in the standard case (point A in Fig. 5.5), $\zeta = 1.0$ for the situation with full rotation and slip boundary conditions (point B in Fig. 5.5) and $\zeta = 2.0$ in the rotationless quasi-2D case (point C in Fig. 5.5). Along this path, the steady states change considerably and for selected locations along the path, stability analyses were performed under restoring boundary conditions with $\lambda = 0$.

The growth rate and period of mode $\mathcal{C}_1$ are shown in Figs. 5.6a and b as a function of ζ, and the overturning time scale τ_{ov} is plotted in Fig. 5.6c as a measure of the change in steady-state overturning along the path taken. The growth rate remains negative along the path, but increases just before $\zeta = 2$. The oscillation period remains around 350 yr, except for a sharp increase just before $\zeta = 2$. These sudden changes in growth rate and oscillation period are related to the increased overturning time scale at $\zeta = 2.0$, which reflects the change from a geostrophic to a frictional balance in the steady-state solutions. As advection by the steady-state flow is an important factor in the mechanism of the centennial modes, a longer overturning time will increase the oscillation period. The slower overturning circulation is also responsible for the sudden increase in growth rate in Fig. 5.6a.

It is remarkable that the mode $\mathcal{C}_1$ is connected to an oscillatory mode in the two-dimensional situation with a period $\mathcal{P} = 1650$ yr. The steady-state patterns of the meridional overturning and the density field in the rotationless case (point C in Fig. 5.5) are plotted in Fig. 5.7a and b, respectively. The imaginary and real parts of the meridional overturning and a slice of the density field of this 2D-mode are shown in Fig. 5.7c-f. At $t = -\pi/2\sigma_i$, the

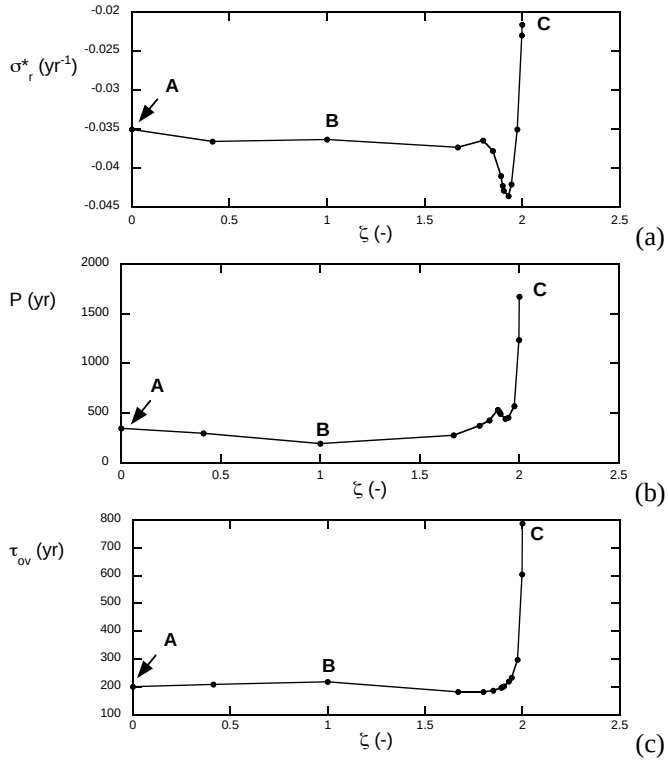

Figure 5.6: *(a) Growth rate (in yr^{-1}) of centennial mode $\mathcal{C}_1$ as a function of the control parameter ζ. (b) Period in years as a function of ζ. (c) Overturning time scale τ_{ov} in years as a function of ζ. The dots indicate values of ζ for which a linear stability analysis was performed.*

center of a light anomaly is located at about 1000 m depth at the southern boundary, with anomalously dense water near the bottom in the southern corner of the basin (Fig. 5.7e). The steady-state overturning advects the anomalously light surface water (Fig. 5.7d) northward and this light water is then convected downwards. The deep dense anomaly near the southern boundary (Fig. 5.7e) is also advected upwards by the steady-state overturning circulation.

On the other hand, at $t = -\pi/2\sigma_i$, there is a positive perturbation density gradient in the upper 1000 m, which drives (instantaneously) a northward flow in this layer (Fig. 5.7c). In the middle of the basin, the perturbation density gradient is negative, causing southward flow. The anomalously dense water below 2000 m in the south causes anomalous downwelling in this part of the basin. The density perturbations in Fig. 5.7e thus result almost instantaneously in meridional overturning perturbations shown in Fig. 5.7c. This anomalous circulation advects light southern surface water (Fig. 5.7b) to the north, where it will spread downwards. On the other hand, relatively dense water will be advected southward and upwards, creating a dense anomaly in the center and near the surface at $t = 0$ (Fig. 5.7f). Therefore, the anomalous advection of the steady-state density field also creates a phase-lagged response in the perturbation density field. The perturbation density field at $t = 0$ then causes (instanta-

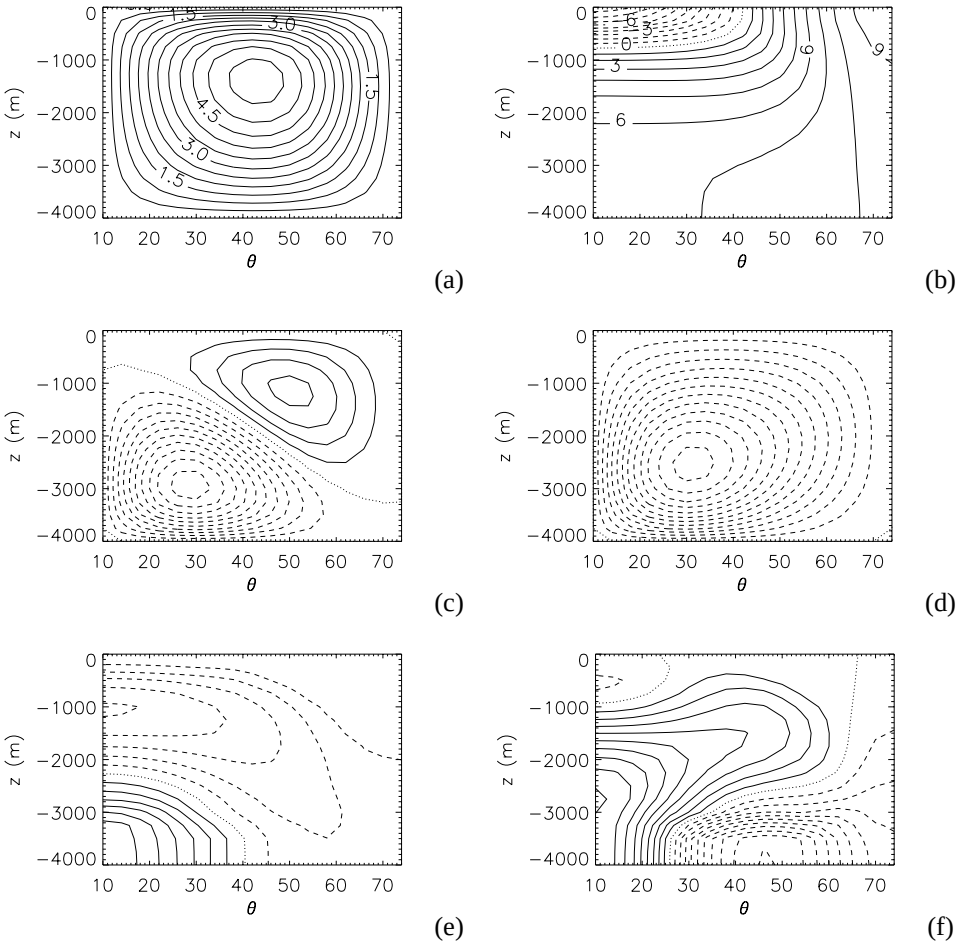

Figure 5.7: *Steady-state meridional overturning (a) and density at $\phi = 42^\circ$W (b) for the two-dimensional case (point C in Fig. 5.6). Imaginary and real parts of the eigenvector corresponding to the 2D-mode with period $\mathcal{P} = 1670$ yr. (c) Imaginary part of the meridional overturning streamfunction. (d) Real part of the meridional overturning streamfunction. (e) Imaginary part of the density at $\phi = 42^\circ$W. (f) Real part of the density at $\phi = 42^\circ$W.*

neously) southward flow in the upper 2500 m and downwelling along the southern boundary (Fig. 5.7d).

In this quasi two-dimensional case, density perturbations seem to be advected mainly around the overturning loop by the steady-state circulation, with a minor effect of the anomalous advection of the steady-state density field. If this is indeed the case, the oscillation time scale is set by steady-state advection of anomalous density. This is investigated by consider-

ing the linearized equation for temperature perturbations (as in this case $\rho = -T$)

$$\frac{\partial \tilde{T}}{\partial t} + \mu_1 \tilde{\boldsymbol{u}} \cdot \nabla \bar{T} + \mu_2 \bar{\boldsymbol{u}} \cdot \nabla \tilde{T} = P_H \nabla_H \cdot \left(\nabla_H \tilde{T} \right) + P_V \frac{\partial}{\partial z} \left(\frac{\partial \tilde{T}}{\partial z} \right) \tag{5.2}$$

Here perturbation fields are indicated by quantities with a tilde and the steady-state fields by quantities with a bar, and μ_1 and μ_2 are dimensionless parameters introduced to control the amplitude of both advection terms. In the standard case, $\mu_1 = \mu_2 = 1.0$. By repeating the stability analysis in the rotationless case (point C in Fig. 5.5) for a few lower values of μ_1 and μ_2 while keeping the steady state fixed, it was investigated which of the two advection terms controls the period of the mode. Decreasing μ_1 does not affect the period, but the latter increases strongly with a decrease in μ_2 (Fig. 5.8a and b). This confirms that the period in

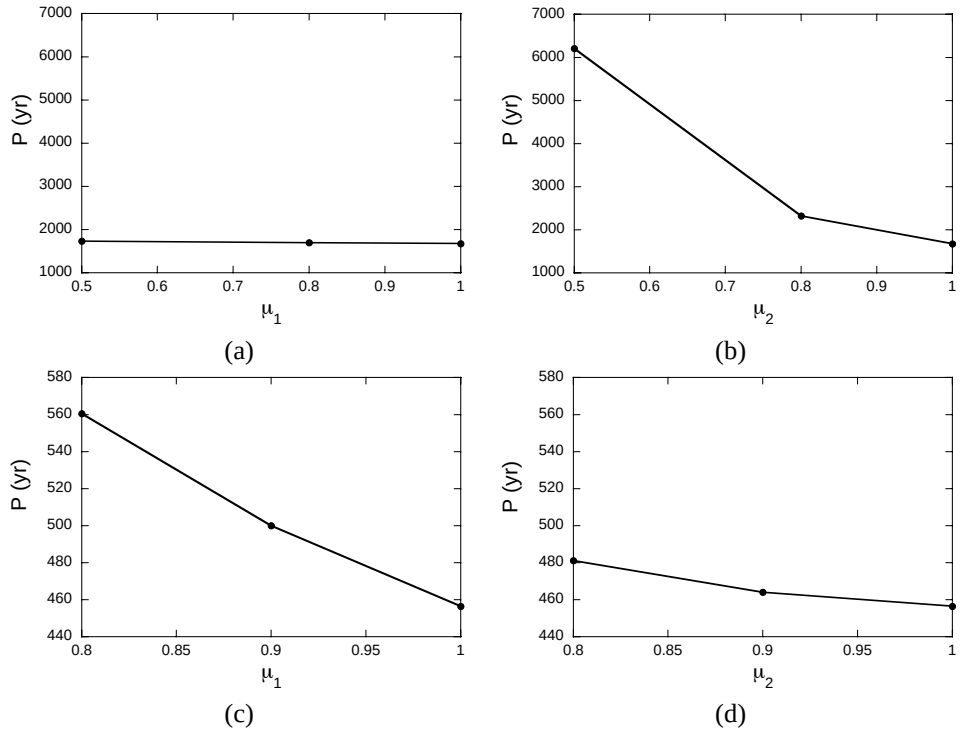

Figure 5.8: *Period of the two-dimensional mode shown in Fig.5.7c-f as a function of (a) μ_1 and (b) μ_2. Period of the three-dimensional mode $\mathcal{C}_1$ shown in Fig. 5.3 under prescribed flux conditions as a function of (c) μ_1 and (d) μ_2.*

the 2D case is set by the advection of density anomalies around the steady-state overturning loop.

A similar analysis was done for mode $\mathcal{C}_1$ in the three-dimensional case, by repeating the stability analysis of case F with different values for μ_1 and μ_2. The period of mode $\mathcal{C}_1$ increases not only on a decrease in μ_2, but also, and even more strongly, on a decrease in

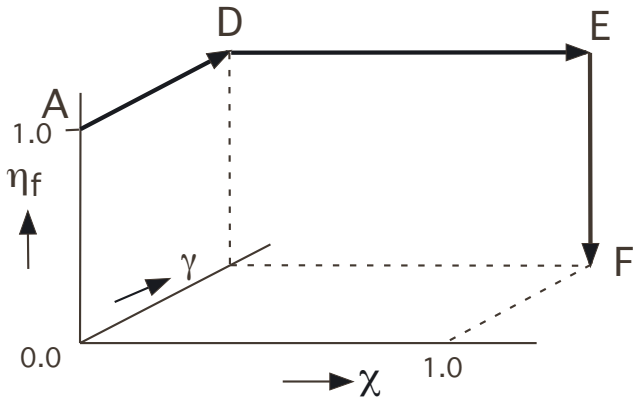

Figure 5.9: *Path in the parameter plane set by χ, η_f and γ along which the steady state and mode $\mathcal{C}_2$ are followed.*

μ_1 (Fig. 5.8c and d). The oscillation time scale of the three-dimensional centennial mode is thus set by the rather complex interplay of advection of density anomalies by the (three-dimensional) steady circulation and the anomalous advection of the steady-state density field.

As salinity perturbations are involved in mode $\mathcal{C}_2$, the path in parameter space along which this mode was followed, is chosen such that it includes the case with mixed boundary conditions (Fig. 5.9), with a nonzero steady salinity field. In this way also the salt advection feedback due to the anomalous advection of the background salinity field is taken into account. First, the freshwater-flux forcing is increased up to $\gamma = 0.12$, which corresponds to a freshwater-flux amplitude $F_0 = 4.8 \cdot 10^{-7}$ ms^{-1} and next the boundary conditions on the side boundaries are changed to slip conditions. For this case, the rotation rate is then decreased to zero. A control parameter ξ is chosen such that the points A, D, E and F in Fig. 5.9 correspond to $\xi = 0$ (no-slip, full rotation), $\xi = 1$ (no-slip, mixed boundary conditions for T and S and full rotation), $\xi = 2$ (slip, mixed boundary conditions for T and S, full rotation) and $\xi = 3$ (slip, mixed boundary conditions for T and S, no rotation), respectively. All along this path, mode $\mathcal{C}_2$ can be followed (Fig. 5.10). The increase in freshwater-flux forcing and the change to slip boundary conditions both have a slight stabilizing effect on the mode, whereas the growth rate increases again towards the rotationless case (Fig. 5.10a). The period is not strongly affected by the change in boundary conditions or the increase in freshwater-flux forcing, but increases sharply from about $\mathcal{P} = 400$ yr to about $\mathcal{P} = 1000$ yr just before $\xi = 3$. This increase, as well as the increase in growth rate around $\xi = 2.9$, corresponds again to a change in overturning time scale (Fig. 5.10c). The fact that mode $\mathcal{C}_2$ can be followed to the 2D mixed boundary condition case establishes the link between the 3D centennial oscillations found here and the 2D overturning oscillations, as found in Dijkstra and Molemaker (1997).

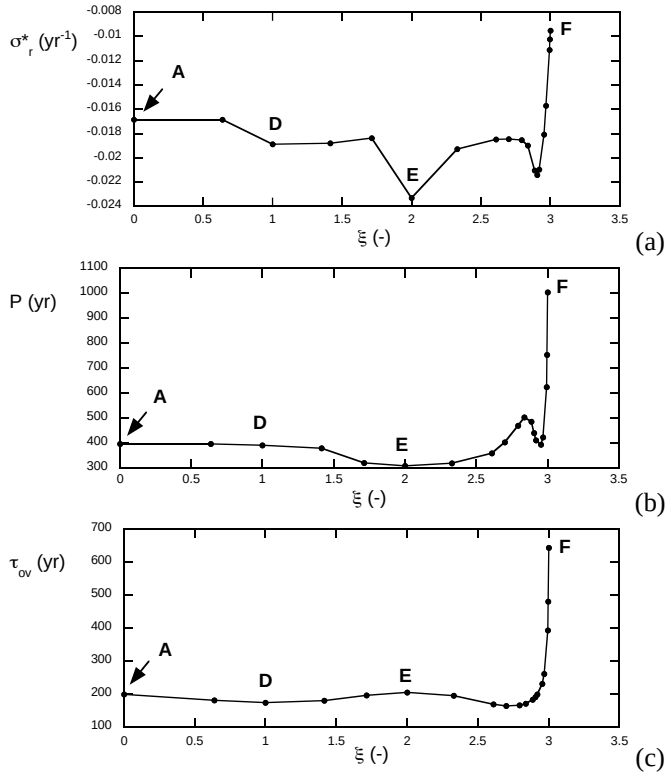

Figure 5.10: *(a) Growth rate (in yr^{-1}) of centennial mode $\mathcal{C}_2$ as a function of the control parameter ξ. (b) Period in years as a function of ξ. (c) Overturning time scale in years as a function of ξ. The dots indicate values of ξ for which a stability analysis was performed.*

5.4 Transient flows

Whereas the linear stability analysis used so far is a very useful technique for classifying internal modes of variability, transient flow computations are needed to study the finite-amplitude behavior of the flow. A long time integration under a prescribed heat-flux forcing was performed, with a steady-state solution (obtained with continuation methods) as initial condition. A stochastic component is added to the diagnosed heat flux, as is explained below in more detail. The steady-state solution used for the initialization is a slightly modified version of the steady state shown in Fig. 5.1, as we increased the horizontal diffusivity to $K_H = 1800$ m^{2}s^{-1}. In chapter 3, it was shown that the interdecadal mode destabilizes under prescribed heat-flux forcing through a Hopf bifurcation, if K_H is decreased below a certain critical value. The value of $K_H = 1800$ m^{2}s^{-1} was chosen in order to obtain a linearly stable steady state. Also, the grid was stretched in the z-direction to increase the vertical resolution near the surface, yielding a vertical resolution ranging from 41 m near the surface to 516 m near the bottom. The typical vertical scale H_m over which the function $G(z)$ in

equations (2.5e) and (2.5f) varies, is adjusted to 41 m. Apart from K_H and H_m, all other parameters remain unchanged. A steady-state solution was then obtained by continuation of the parameter η_T in (2.6) to its standard value $\eta_T = 10.0$. It closely resembles the state shown in Fig. 5.1, but the maximum meridional overturning transport is now 18.6 Sv. A linear stability analysis was performed to check that this steady state is indeed stable when forced with the diagnosed heat flux (without any stochastic component added). The least damped mode is the interdecadal mode $\mathcal{M}_I$, which has in this case a growth rate of $-3.4 \cdot 10^{-3}$ yr^{-1} and a period of 71 yr. The second oscillatory mode is the centennial mode $\mathcal{C}_1$, with a growth rate of -0.031 yr^{-1} and a period of 492 yr.

The stochastic part Q_{Ts} of the heat-flux forcing is chosen as a linear combination of a few sinusoids, in order to account for random temporal but spatially coherent features, and is given by

$$Q_{Ts} = \sum_{i=1}^{3}\sum_{j=1}^{3} \hat{A}(t) \sin\left[i\pi\left(\frac{\phi-\phi_W}{\phi_E-\phi_W}\right)+\xi_1\right] \sin\left[j\pi\left(\frac{\theta-\theta_S}{\theta_N-\theta_S}\right)+\xi_2\right] \qquad (5.3)$$

Here $\hat{A}$ is a random amplitude, varying between -1.5 and 1.5, and ξ_1 and ξ_2 are random (time-dependent) phases. Only three wavenumbers are used, such that only large-scale anomalies are generated. As THCM is an implicit model, a time step of 0.4 yr can be used. The random coefficients are changed every time step, which implies a decorrelation time less than 0.4 yr. With the steady state described above as an initial condition, the implicit model was integrated forward in time for 12,000 years. The resulting time series of the maximum meridional overturning shows clear interdecadal variability (Fig. 5.11a). This is also visible as a pronounced peak in the spectrum (Fig. 5.11b) around frequency $f = 0.014$ yr^{-1}, which corresponds to a period of 71 yr. There seem to be variations on longer time scales in the time series as well (Fig. 5.11a), but they do not show up as distinct peaks in the spectrum.

In order to find the patterns of variability, the meridional overturning and a slice of the temperature field at $z = -41$ m are sampled every 6 years over the last 6000 years of the integration period. The number of degrees of freedom is reduced by performing a standard Principal Component Analysis (PCA) on both fields (Preisendorfer, 1988). The resulting 20 leading principal components, which account for 100% of the variance in the case of the meridional overturning (and 98.4% of the variance in case of the near-surface temperature), are the input for an MSSA analysis (Plaut and Vautard, 1994); a window length of 900 yr is taken. The basic principles of the MSSA technique are explained in appendix C. For the meridional overturning, several statistical modes with interdecadal periods are found, of which the most dominant mode explains 42% of the total variance within the 900-year window. This mode lies well above the 97.5% confidence interval of the Monte Carlo significance test of Allen and Robertson (1996). It has a period of 69 yr, which corresponds very well to the period at the peak in the Fourier spectrum. The most dominant mode for the near-surface temperature explains only 8% of the total variance within the 900-year window, but it has also a period of 69 yr. Snapshots of the reconstructed components of the most dominant statistical modes of the meridional overturning and the temperature at $z = -41$ m at $t = 564$ yr and $t = 582$ yr (a quarter of a period apart) are shown in Fig. 5.12a and b. At $t = 564$ yr, the meridional overturning perturbation is weakly negative, and there is a positive temperature anomaly in the northwestern part of the basin. A quarter of a period later, at $t = 582$ yr, the meridional

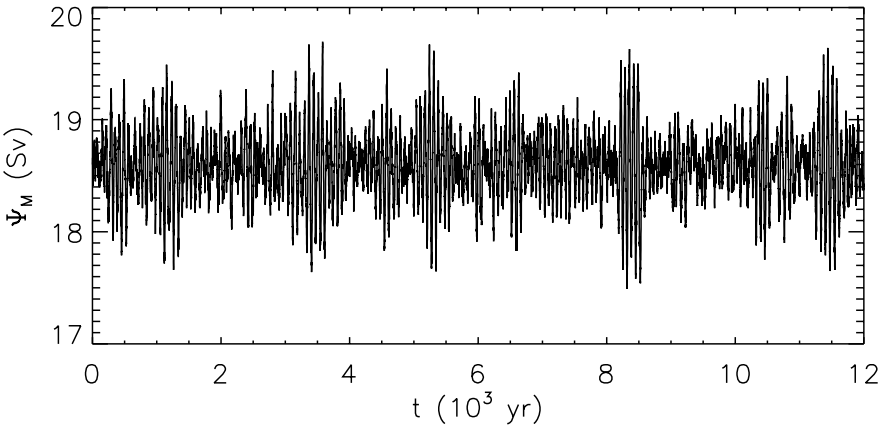

(a)

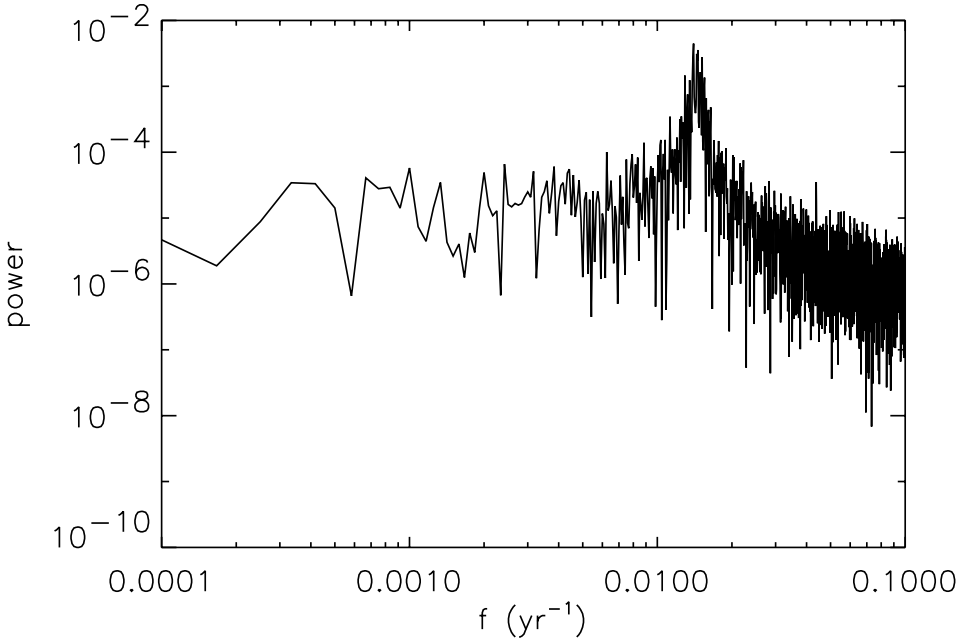

(b)

Figure 5.11: *(a) Time series of the maximum meridional overturning (in Sv). (b) Fourier spectrum of the time series shown in (a).*

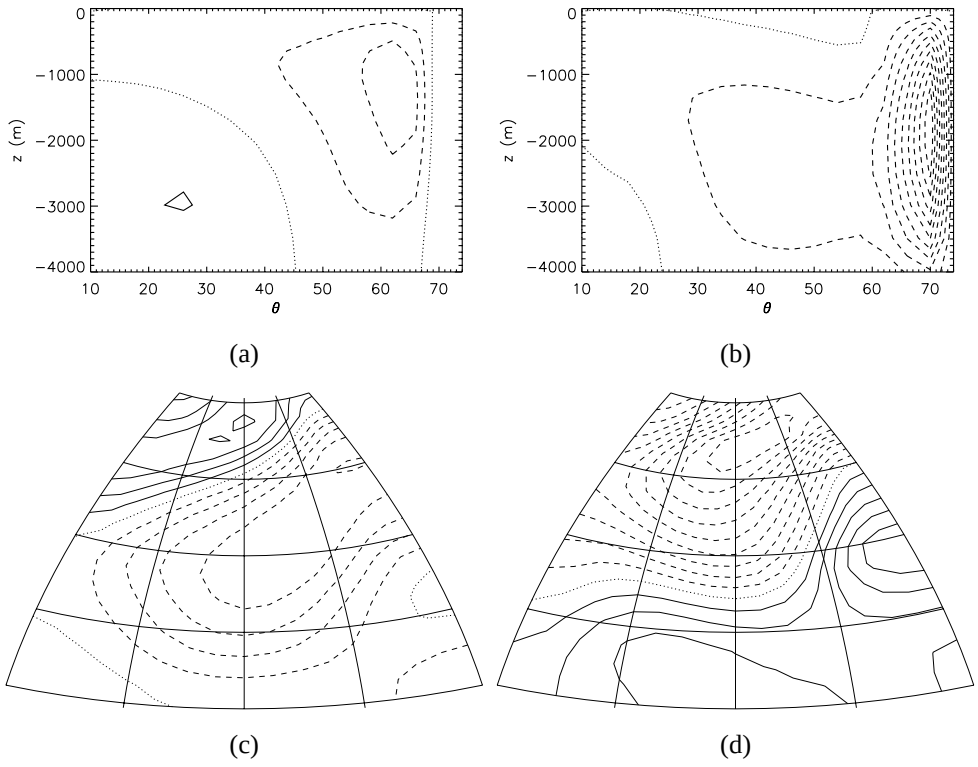

Figure 5.12: *Reconstructed component of meridional overturning at (a)* $t = 564$ *yr and (b)* $t = 582$ *yr, and temperature at* $z = -41$ *m at (c)* $t = 564$ *yr and (d)* $t = 582$ *yr.*

overturning perturbation has become more negative. The positive temperature perturbation has propagated westward and has been followed by a negative temperature anomaly. Both the patterns and the period of these statistical modes strongly resemble those of mode $\mathcal{M}_I$ that was found with the linear stability analysis (Fig. 5.2a and b, note that in this case $\rho = -T$). The time series in Fig. 5.11a clearly shows that the amplitude of the interdecadal variability is modified on time scales ranging from centuries to millennia, but none of the patterns from the MSSA analysis corresponding to oscillations with centennial periods is statistically significant, according to the test of Allen and Robertson (1996).

5.5 Summary and discussion

In this chapter, it was shown that, when the linear stability of the large-scale steady thermohaline circulation in a single-hemispheric basin is considered, only two classes of normal modes are found: interdecadal and centennial modes. To our knowledge, this is the first time that also centennial modes have been shown explicitly to exist as eigenmodes of this system. Main characteristics of an interdecadal mode are the westward propagation of temperature

anomalies on the steady-state temperature field (Huck *et al.* (1999), see also chapter 3 of this thesis) and the resulting phase-lagged response of the zonal and meridional overturning, which make it a truly three-dimensional phenomenon. The growth rate of the interdecadal mode is sensitive to the type of surface boundary conditions, but its existence and period are not (chapter 3). For similar values of all other parameters, the circulation was found to be stable under restoring conditions (case R), but unstable to the interdecadal mode under prescribed flux conditions (case F).

Focus of this chapter was on the physics of the second class of modes with centennial oscillation periods; actually, two different centennial modes were found. Both centennial modes are related to the overturning or loop oscillations, as advection of density anomalies by the steady-state overturning is essential for their mechanism. For mode $\mathcal{C}_1$, the density perturbation is completely determined by temperature, even if salinity perturbations are allowed, whereas for mode $\mathcal{C}_2$, both temperature and salinity determine the density. The latter mode was also found in a stability analysis under mixed boundary conditions (case M). It was shown that the oscillation period is mainly determined by the overturning time scale of the steady-state flow. The fact that the centennial modes have equivalent modes in two-dimensional, rotationless situations (as demonstrated in section 5.3) suggests that the oscillation mechanism can be understood from an essentially two-dimensional situation. Although propagation characteristics are of course different in the three-dimensional version of the mode, these changes are not essential for the existence of the mode. The latter does, for example, not hold for the interdecadal mode, which is absent in a two-dimensional situation.

The transient flow results in section 5.4 clearly showed that even when the interdecadal mode is stable, it can be excited under stochastic forcing. Longer-term variability was found as well, and although it is very likely due to the presence of the centennial modes, these modes could not be extracted as statistically significant modes.

Based on the propagation characteristics of both classes of modes, it is clear that only centennial modes can be represented in the four-box model as introduced in Griffies and Tziperman (1995). The time scale of this box-model oscillation is basically set by the ventilation time of the sinking box, which can vary from tens to hundreds of years (Sirkes and Tziperman, 2001). We have run the same box model for several sets of model parameters, and could easily find oscillation periods of 200 yr instead of 50 yr, by varying the depth of the upper boxes. Therefore, we think that the interdecadal mode in the box model of Griffies and Tziperman (1995) is actually a loop oscillation like the centennial modes described here, but with a period that has shifted to the interdecadal range due to the choice of box model parameters.

The 530 yr-oscillation found by Sirkes and Tziperman (2001) in a global model forced by mixed boundary conditions shows features of a mainly two-dimensional mechanism, related to advection of temperature and salinity anomalies around the overturning loop. Whereas the authors argue that this oscillation might be related to interdecadal variability, which would then be driven by a two-dimensional mechanism as in Griffies and Tziperman (1995), we think that it is much more likely that Sirkes and Tziperman (2001) have found a centennial mode in their model. In the present study, we have found only one type of interdecadal modes, and both the time scale and the propagation characteristics of the oscillation found by Sirkes and Tziperman (2001) are not compatible with that of this 3D interdecadal mode. On the other hand, they compare very well with the properties of the centennial modes $\mathcal{C}_1$ or $\mathcal{C}_2$.

Centennial variability related to loop oscillations has also been found in the global LSG model under stochastic forcing (Mikolajewicz and Maier-Reimer, 1990) and in a stochastically forced zonally averaged double-hemispheric model (Mysak and Stocker, 1993). The patterns associated with this variability also show propagation of buoyancy anomalies over a 'loop' determined by the underlying steady state. Can the centennial modes serve as a 'building block' to explain the variability found in these models? One could argue that centennial modes as found here are less relevant to these models, because the centennial modes are damped rather strongly. However, the study of Winton and Sarachik (1993) shows that centennial oscillations are rather sensitive to the pattern of the freshwater-flux forcing. In addition, the friction in these models is substantially lower than that used here. These effects may modify the stability properties of the centennial modes considerably and make them highly relevant to explain low-frequency variability of the global thermohaline ocean circulation.

To summarize, the following framework for the interpretation of internal thermohaline variability in the single-hemispheric case appears. At interdecadal time scales, variability is generated by a three-dimensional interdecadal mode that can either lead to self-sustained oscillations, or to variability that is excited by noise. This variability will be modulated on the overturning time scale if centennial modes are able to gain energy, either through their interaction with the underlying steady state or through nonlinear interactions with the interdecadal mode.

Chapter 6

Identification of the mechanism of interdecadal variability

In this chapter, interdecadal variability of thermally driven flows in an idealized, single-hemispheric ocean basin is followed along a path in the modeling hierarchy, using transient flow computations with the GFDL MOM model. The variability in the simplest case, that of viscous, purely thermally driven flows in an ocean basin with a box-shaped geometry, is shown to be caused by the interdecadal mode described in chapter 3. The westward propagation of temperature anomalies and the phase difference between the anomalous zonal and meridional overturning of this interdecadal mode are used as characteristics to identify the physical mechanism of the variability. In this way, the variability can be followed towards a less viscous regime in which also the effects of continental geometry and bottom topography are included. It is shown that the physical mechanism underlying this variability undergoes no qualitative changes[*].

6.1 Introduction

In chapters 3 to 5, North Atlantic interdecadal variability in a single-hemispheric sector basin has been studied extensively with the THCM model. It was shown that interdecadal variability in the idealized case of relatively viscous flows in an ocean basin with a box-shaped geometry is caused by an internal oscillatory mode of the system. This mode is characterized by a westward propagating temperature anomaly, which causes a phase difference between the zonal and meridional temperature gradients and correspondingly between the meridional and zonal overturning streamfunctions (section 3.3). The study in chapter 3 forms the first part in a modeling strategy aimed at understanding interdecadal variability in observations and CGCM simulations of climate. By restricting the study to the idealized limiting case of thermally driven single-hemispheric basin flows, the physical mechanism underlying the variability could be understood in detail. In chapters 3 to 5, the interdecadal mode was shown

[*]This chapter is based on the paper '*Identification of the mechanism of interdecadal variability in the North-Atlantic Ocean*', by L. A. te Raa, J. Gerrits and H. A. Dijkstra (submitted to *J. Phys. Oceanography*)

to be a robust feature of the viscous flow in a single-hemispheric ocean basin. This supports the hypothesis that this mode is playing an important role in interdecadal variability in more complex and more realistic model simulations. The next step is to investigate if characteristics of this mechanism can indeed be identified in a hierarchy of models of increasing complexity. The study in this chapter is the first part of the considerable task of trying to follow the interdecadal mode through the complete model hierarchy towards fully coupled ocean-atmosphere-sea-ice models.

The most realistic case considered in this chapter is that of the flow in a single-hemispheric basin with continental geometry and bottom topography, forced by a prescribed heat flux. The horizontal eddy viscosity in this most realistic case has a value that is commonly used in coarse-resolution models, which is a hundred times lower than the value used in the previous chapters. As was mentioned in chapter 2, steady-state solutions computed with the THCM model on a horizontal resolution of $4^\circ \times 4^\circ$ with a horizontal eddy viscosity of $1.6 \cdot 10^5$ m^{2}s^{-1} turn out to be dominated by wiggles resulting from an unresolved coastal boundary layer. The MOM model is much less sensitive to the effects of such unresolved boundary layers. Therefore, in this chapter numerical time integrations are performed with the Modular Ocean Model (MOM). The starting point for the study in this chapter is the idealized high-viscosity case considered in chapter 3. First, for this configuration the variability in MOM is shown to originate from the interdecadal mode found in THCM. Next, the horizontal eddy viscosity is decreased to $A_H = 1.6 \cdot 10^5$ m^{2}s^{-1}, and continental geometry is included. For this configuration, the effect of wind forcing is also considered. Finally, for the purely thermally driven case also bottom topography is included.

Within the relatively simple context of a single-hemispheric ocean-only model, interdecadal variability has been found in many studies, in which many different model configurations were used. Some studies used a box-shaped geometry —no continents and no bottom topography— (Greatbatch and Zhang, 1995; Chen and Ghil, 1995; Greatbatch and Peterson, 1996; Winton, 1996; Huck *et al.*, 2001), in others continental geometry was included in a flat-bottomed basin (Weaver *et al.*, 1994), or an idealized bottom topography was used (Winton, 1997; Huck *et al.*, 2001). The variability in the study of Weaver *et al.* (1994) was hardly influenced by wind forcing. In contrast, the interdecadal mode in the study of Huck *et al.* (2001) was suppressed by a strong wind forcing, while for climatological wind stress forcing the amplitude of the variability was enhanced and the period decreased with respect to the case without wind forcing. The period of the purely thermally driven interdecadal oscillations found by Chen and Ghil (1995) also decreases when wind stress forcing is included, and the amplitude increases slightly.

Although the behavior of the variability in some of these studies seems to be the same, different physical mechanisms were proposed as explanations for the modeled variability: changes in local heat storage (Greatbatch and Zhang, 1995), propagating viscous boundary waves (Greatbatch and Peterson, 1996; Winton, 1996, 1997), convective changes in the Labrador Sea (Weaver *et al.*, 1994), or potential vorticity waves (Huck *et al.*, 2001). In this chapter, it is shown that it is possible to identify the mechanism of interdecadal variability in more complex flows by using the characteristic features of the physical mechanism that was identified in the idealized limiting case of chapter 3. In this way, the results presented here provide a framework within which also other model results can be interpreted. This might help answer the question whether the variability found in various studies in the literature is

caused by many different mechanisms, or by merely one or two. In the latter case, many of the differences in periods and spatial patterns of the modeled variability are quantitative differences, which are due to the different models that have been used. The rest of this chapter is set up as follows. In section 6.2, the correspondence between the variability in MOM and in THCM for the idealized standard configuration is investigated. The interdecadal variability is followed towards a less viscous regime in section 6.3. The effects of a more realistic geometry and the influence of wind forcing are investigated in section 6.4, after which the results are summarized and discussed in section 6.5.

6.2 Interdecadal variability in MOM

All results in this chapter have been computed with version 3.1 of the MOM model (Pacanowski and Griffies, 1998), of which a short description was given in chapter 2. In the standard case, continental geometry and bottom topography are not included and the basin is 4000 m deep everywhere. The horizontal resolution is $4^\circ \times 4^\circ$ and there are 16 non-equally distributed vertical levels, with a layer thickness ranging from 50 m for the upper four layers to 583 m for the lowest layer. In a few simulations, a higher resolution has been used, with either $2^\circ \times 2^\circ$ or $1^\circ \times 1^\circ$ in the horizontal direction and 24 layers in the vertical.

The flow is forced either by a restoring boundary condition for temperature (equation (2.4b)) or a prescribed heat flux, the latter being diagnosed from a spin-up simulation under the restoring boundary condition. The restoring temperature T_S^* is given by equation (2.22). The dimensionless parameter η_T in this equation is set to $\eta_T = 10.0$ for all simulations in this chapter, resulting in a dimensional meridional temperature difference of $20°$C over the basin. The time scale τ_T on which surface temperatures are restored to the prescribed temperature T_S^* is taken to be 30 days. This time scale, which is shorter than that used in chapters 3 and 5, has been chosen in order to obtain a realistic amplitude of the surface heat flux. The horizontal diffusivity of heat is taken $K_H = 700$ m^{2}s^{-1}. For this value, the flow is expected to be unstable to the interdecadal mode. In unstably stratified regions, the vertical eddy diffusivity is increased to $K_V^c = 10^2$ m^{2}s^{-1}. The other parameters are taken as in chapter 3, and the standard values of the parameters in MOM are given in Table 6.1. The asynchronous integration technique of Bryan (1984) is used, and timesteps of

2Ω	=	$1.4 \cdot 10^{-4}$	[s^{-1}]	r_0	=	$6.4 \cdot 10^6$	[m]
D	=	$4.0 \cdot 10^3$	[m]	g	=	9.8	[ms^{-2}]
ρ_0	=	$1.0 \cdot 10^3$	[kg m^{-3}]	τ_T	=	30	[days]
T_0	=	15.0	[°C]	α_T	=	$1.0 \cdot 10^{-4}$	[K^{-1}]
A_H	=	$1.6 \cdot 10^7$	[m^{2}s^{-1}]	A_V	=	$1.0 \cdot 10^{-3}$	[m^{2}s^{-1}]
K_H	=	700.0	[m^{2}s^{-1}]	K_V	=	$2.3 \cdot 10^{-4}$	[m^{2}s^{-1}]
F_0	=	0.0	[ms^{-1}]	τ_0	=	0.0	[Nm^{-2}]
K_V^c	=	$1.0 \cdot 10^2$	[m^{2}s^{-1}]	ΔT	=	1.0	[°C]

Table 6.1: *Reference values of parameters used in the numerical computations with MOM in chapter 6.*

$\Delta t_E = \Delta t_I = 0.0625$ hr and $\Delta t_T = 1$ day are taken for the barotropic part, the baroclinic part and the tracers, respectively. Several test simulations showed that the results were not influenced by the use of this asynchronous integration technique. In all cases, the computations are initialized from the zero solution for velocity and temperature, while salinity is kept constant throughout. At the lateral boundaries, no-slip conditions are used.

The simulations that have been done are summarized in Table 6.2. Simulation 1 is the standard run for the idealized model configuration also used in chapter 3. It is repeated at a higher resolution in simulation 2. Simulations 3, 4 and 5 deal with the decrease of the horizontal viscosity towards $A_H = 1.6 \cdot 10^5$ m^{2}s^{-1}, and in simulations 6, 7 and 8 continental geometry is added. In simulation 9, the influence of wind stress forcing is investigated. Finally, the effect of the addition of bottom topography is considered in simulations 10 and 11.

Sim.	A_H (m^2/s)	K_H (m^2/s)	Res.	Cont.	Topo.	Wind	Ψ_M (Sv)	$\mathcal{P}$ (yr)
1.	$1.6 \cdot 10^7$	700	$4^\circ \times 4^\circ \times$ L16	No	No	No	21	45
2.	$1.6 \cdot 10^7$	700	$2^\circ \times 2^\circ \times$ L24	No	No	No	21	45
3.	$1.6 \cdot 10^6$	1000	$4^\circ \times 4^\circ \times$ L16	No	No	No	20	58
4.	$1.6 \cdot 10^6$	700	$4^\circ \times 4^\circ \times$ L16	No	No	No	21	$54 + 106$
5.	$1.6 \cdot 10^5$	700	$4^\circ \times 4^\circ \times$ L16	No	No	No	26	$48 + 95$
6.	$1.6 \cdot 10^7$	700	$4^\circ \times 4^\circ \times$ L16	Yes	No	No	16	–
7.	$1.6 \cdot 10^5$	700	$4^\circ \times 4^\circ \times$ L16	Yes	No	No	29	73
8.	$1.6 \cdot 10^5$	700	$2^\circ \times 2^\circ \times$ L24	Yes	No	No	24	44
9.	$1.6 \cdot 10^5$	700	$4^\circ \times 4^\circ \times$ L16	Yes	No	Yes	25	$57 + 120$
10.	$1.6 \cdot 10^5$	700	$2^\circ \times 2^\circ \times$ L24	Yes	Yes	Yes	20	–
11.	$1.6 \cdot 10^5$	350	$1^\circ \times 1^\circ \times$ L24	Yes	Yes	No	17	22

Table 6.2: *Summary of the simulations done with MOM. Column 1 gives the simulation number mentioned in the text, column 2 and column 3 the values of A_H and K_H, respectively. The resolution is given in column 4 (the vertical resolution is indicated by the number of layers, i.e. L16 means 16 layers in the vertical). Column 5 and column 6 indicate whether or not continental geometry and bottom topography were included, respectively, and column 7 whether or not wind forcing was included. Column 8 gives the maximum meridional overturning after a statistically stationary state had been reached at the end of the spin-up. Column 9 gives the period of the oscillation found after the switch to prescribed heat-flux forcing. In all simulations, a spin-up (usually 3000 years) under restoring boundary conditions was performed, after which the heat flux was diagnosed. The model was then integrated (for another 1000 to 6000 years) under this prescribed heat-flux forcing.*

The model is first integrated forward in time for 3000 years in the standard configuration under the restoring boundary condition until a steady state has been reached (simulation 1). The meridional overturning at $t = 3000$ yr is plotted in Fig. 6.1a and consists of one clockwise cell with a maximum amplitude of about 21 Sv. The temperature and velocity fields in the upper layer at this time are plotted in Figs. 6.1b and 6.1c, respectively. The near-surface

temperature is almost zonally uniform, with a meridional temperature difference of about $19°$C. The near-surface velocity field is anti-cyclonic, with upwelling in the southwestern part of the basin and downwelling in the northeast. This steady state is in close correspondence with the steady state obtained with the THCM-model in the standard case of chapter 3 (Fig. 3.1).

Next, the heat flux through the surface at $t = 3000$ yr is diagnosed and then prescribed as a boundary condition instead of the restoring condition, and the model is integrated for another 3000 yr under this prescribed heat-flux forcing. A time series of the meridional overturning under prescribed heat-flux forcing is plotted in Fig. 6.1d for the point in the basin where the overturning was maximum at the end of the spin-up (in the rest of this chapter, this will simply be called the maximum meridional overturning). About 1000 yr after the switch to prescribed heat-flux forcing, an interdecadal oscillation with a period of 45 yr becomes visible in the meridional overturning. The oscillation finally equilibrates with an amplitude of about 5 Sv. When the simulation was repeated at a resolution of $2° \times 2°$ in the horizontal and 24 levels in the vertical, the same results were obtained (simulation 2 in Table 6.2). Therefore, only the results of simulation 1 are described in the following.

Snapshots of the temperature anomalies just below the surface during one oscillation cycle are shown in Fig. 6.2. A large-scale cold anomaly located in the north-central part of the basin at $t = 5677.5$ yr propagates westward along the northern boundary and is followed by a warm anomaly in the northeastern corner of the basin between $t = 5692.5$ yr and $t = 5700$ yr. This warm anomaly is first propagating westward at a latitude of about $50\,°$N and propagates then in northwestern direction, after which a cold anomaly forms again at the eastern boundary. Cyclonic propagation of weak anomalies can be seen along the southern and eastern boundaries.

The spatial patterns and propagation characteristics of these temperature anomalies strongly resemble those of the interdecadal mode described in chapter 3. Also the period of the oscillation found here is in accordance with the results of chapter 3. Although in THCM, K_H was only decreased to 800 m^{2}s^{-1}, the period behaved rather linearly with K_H (Fig. 3.7). A linear extrapolation to $K_H = 700$ m^{2}s^{-1} of the period shown in Fig. 3.7 yields a period of 48 yr of the interdecadal oscillation in THCM, which corresponds well with the period of the finite-amplitude oscillation in MOM. It should be pointed out however, that there is a fundamental difference between the (infinitesimally small) perturbations acting on a steady state, which were used to describe the oscillation mechanism in the previous chapters, and the finite-amplitude anomalies with respect to the time-mean state that are used here. If nonlinearities are small, these two will not differ very much, but in a highly nonlinear regime these differences might become more pronounced.

The fact that the westward propagation of temperature anomalies, which is one of the 'fingerprints' characterizing the interdecadal mode, is also found in the oscillation in MOM, already suggests that the latter is indeed caused by the internal mode described in chapter 3. This is confirmed by plots of the zonally averaged anomalous north-south temperature difference ΔT_{N-S} and meridionally averaged anomalous east-west temperature difference ΔT_{E-W} (Fig. 6.3a) and of the spatially averaged meridional and zonal overturning anomalies (Fig. 6.3b) for the last part of the simulation. The meridionally averaged east-west temperature difference leads the zonally averaged north-south temperature difference by about 12 yr, which is about a quarter to one-third of an oscillation period. For the interdecadal

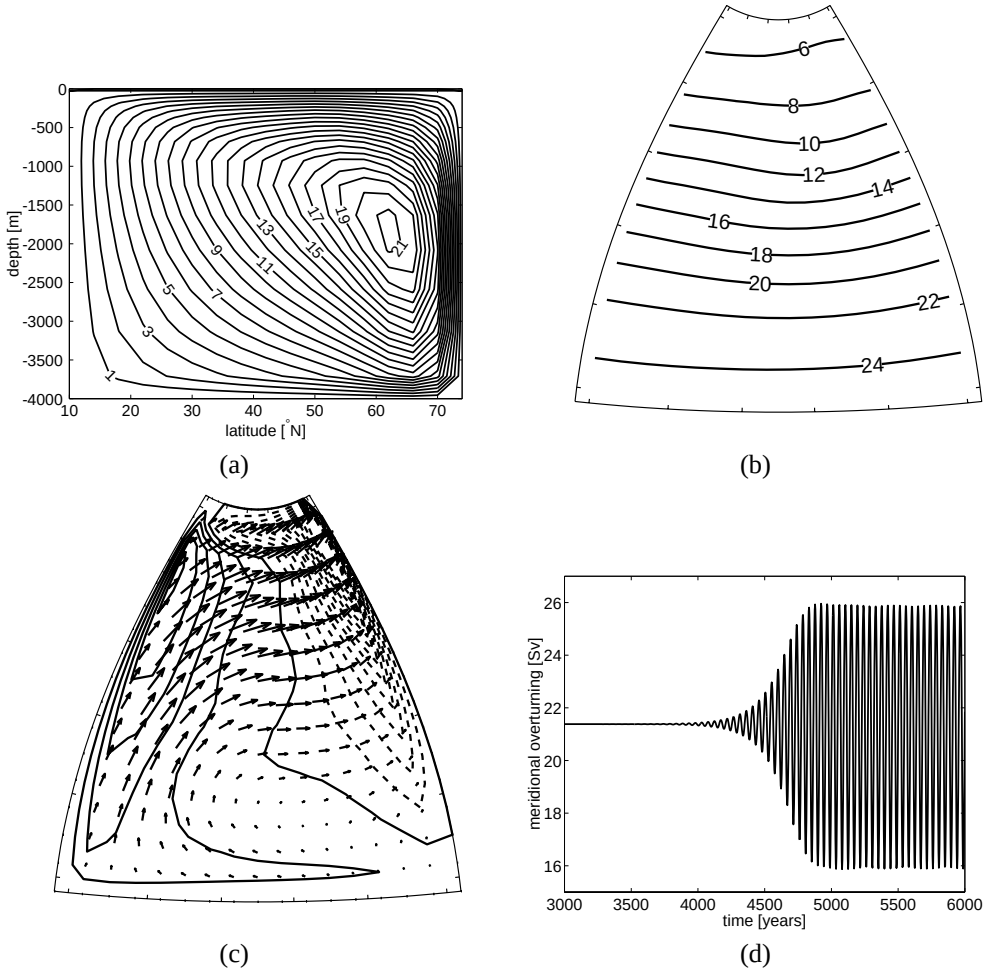

Figure 6.1: *(a) Meridional overturning (in Sverdrups) at the end of the* 3000*-yr spin-up for the standard case (simulation 1). (b) Upper-layer temperature field at the end of the* 3000*-yr spin-up. (c) Upper-layer velocity field at the end of the spin-up. Vectors indicate the horizontal velocity and contours represent the vertical velocity. Solid contour lines represent upwelling (flow out of the plane), dashed lines downwelling (flow into the plane). (d) Time series of meridional overturning under the prescribed heat flux diagnosed instantaneously at* $t = 3000$ *yr. The time series is plotted for the point where the meridional overturning at* $t = 3000$ *yr is at a maximum.*

mode described in chapter 3, this phase difference is about one-third of an oscillation period. The spatially averaged meridional overturning, which is at a maximum when ΔT_{E-W} is maximum, lags the spatially averaged zonal overturning by about 13 yr.

Finally, it was shown in chapter 3 that the interdecadal mode can be described in terms of the phase difference between the two buoyancy work terms of the linearized potential

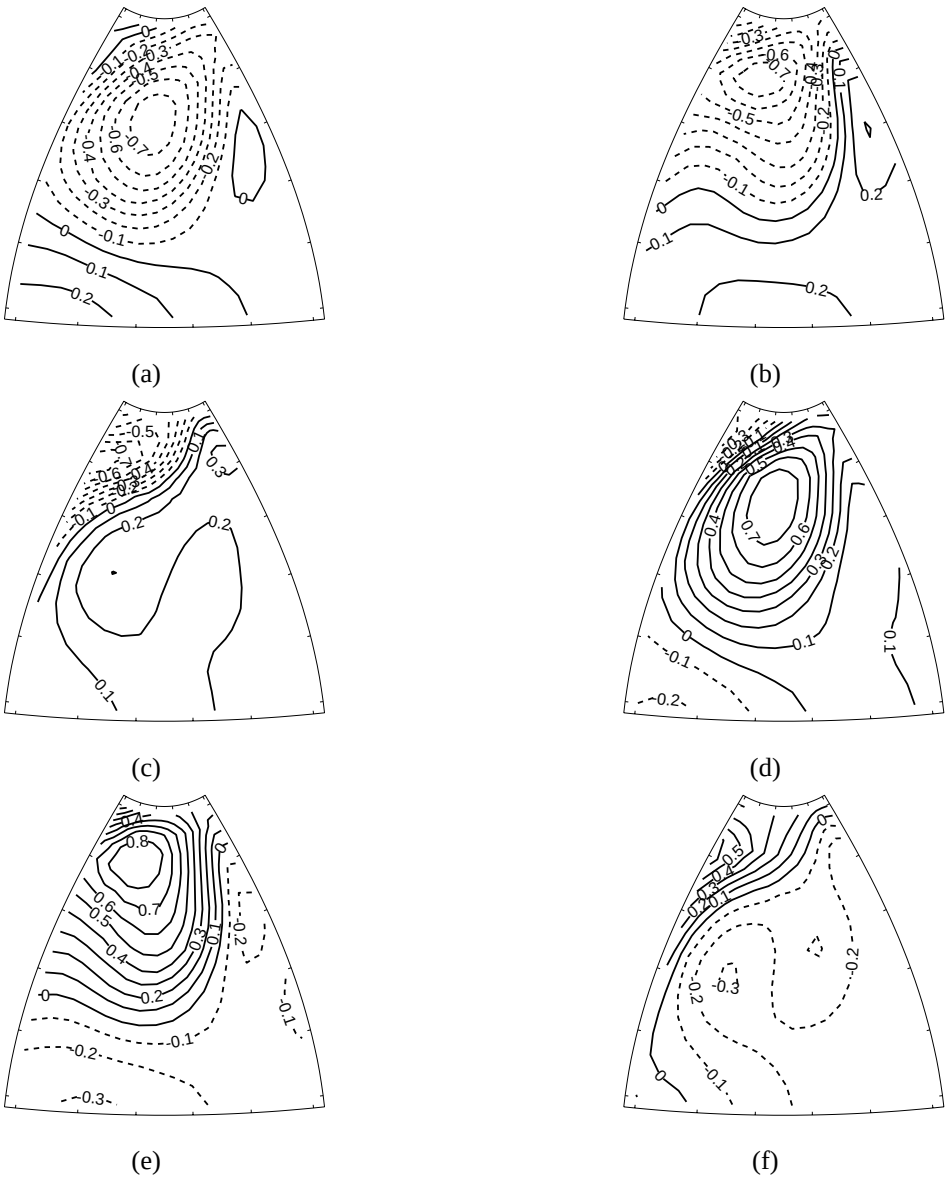

Figure 6.2: *Snapshots of the temperature anomaly with respect to an average over the last four oscillation periods at six times during one oscillation cycle for simulation 1, at (a)* $t = 5677.5$ *yr, (b)* $t = 5685$ *yr, (c)* $t = 5692.5$ *yr, (d)* $t = 5700$ *yr, (e)* $t = 5707.5$ *yr and (f)* $t = 5715$ *yr.*

energy balance for the perturbations (equation (3.6)). For the finite amplitude oscillation found here, the dimensional volume-integrated potential energy $\mathcal{U}$ is defined as $<\rho g z>$, where the asterisk denoting dimensional variables has been omitted, and the potential energy

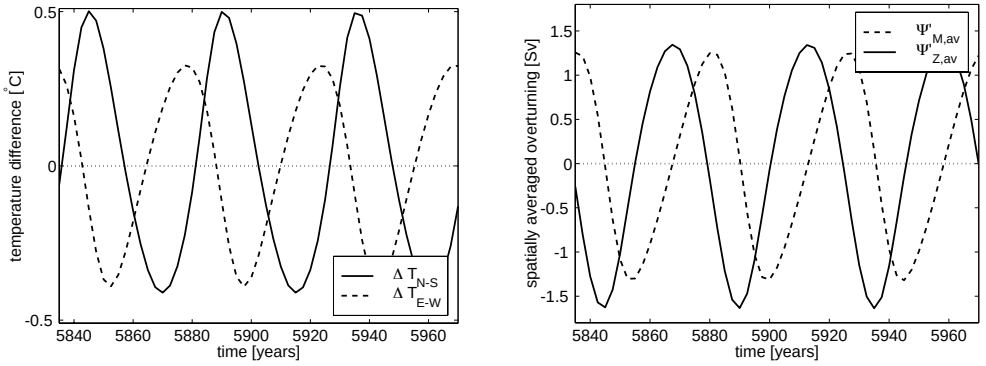

(a) (b)

Figure 6.3: *(a) Zonally averaged anomalous north-south temperature difference ΔT_{N-S} (solid line) and meridionally averaged anomalous east-west temperature difference ΔT_{E-W} (dashed line), averaged over the upper 1438 m, during the last part of the integration for simulation 1. (b) Time series of the spatially averaged meridional overturning anomaly (dashed line) and the spatially averaged zonal overturning anomaly (solid line).*

balance is given by

$$\frac{d\mathcal{U}}{dt} = g < w\rho > + \mathcal{D}_\rho + \mathcal{S} \tag{6.1}$$

where $\mathcal{D}_\rho$ denotes the change in potential energy due to changes in the stratification caused by vertical diffusion and convection. The term $\mathcal{S}$ is a source term indicating changes in potential energy due to the surface heat flux. All variables can be decomposed into a period-averaged part and the deviation from this average, for instance $T = \bar{T} + T'$ for the temperature. In this chapter, quantities with a bar are period-averaged quantities and primed quantities are deviations from this average. The potential energy balance for the anomalies can then be written as

$$\frac{d\mathcal{U}'}{dt} = g < \bar{w}\rho' > + g < w'\bar{\rho} > + g < w'\rho' > + \mathcal{D}'_\rho + g < \bar{w}\bar{\rho} > \tag{6.2}$$

The temporal variation of the terms in (6.2) is shown in Fig. 6.4. In Fig. 6.4a, the buoyancy work terms $g < \bar{w}\rho' >$, $g < w'\bar{\rho} >$ and $g < w'\rho' >$ are plotted as a function of time during three oscillation cycles. The nonlinear contribution of $g < w'\rho' >$ to the total buoyancy work is relatively small (Fig. 6.4a), so that the oscillation in the total buoyancy work is still dominated by the phase difference between $g < \bar{w}\rho' >$ and $g < w'\bar{\rho} >$. This was also the case for the interdecadal mode in chapter 3 (compare to Fig. 3.9). In Fig. 6.4b, the sum of the three buoyancy work terms, the tendency in potential energy and the sum of the other terms, $\mathcal{D}'_\rho + g < \bar{w}\bar{\rho} >$, are shown. The latter term is not calculated directly, but only as the residue of the tendency in potential energy and the term $g\,(< \bar{w}\rho' > + < w'\bar{\rho} > + < w'\rho' >)$, because convective adjustment makes the term $\mathcal{D}'_\rho$ rather complex. Although there is now also a nonlinear contribution of convective adjustment in $\mathcal{D}'_\rho$ that was not present in the studies in

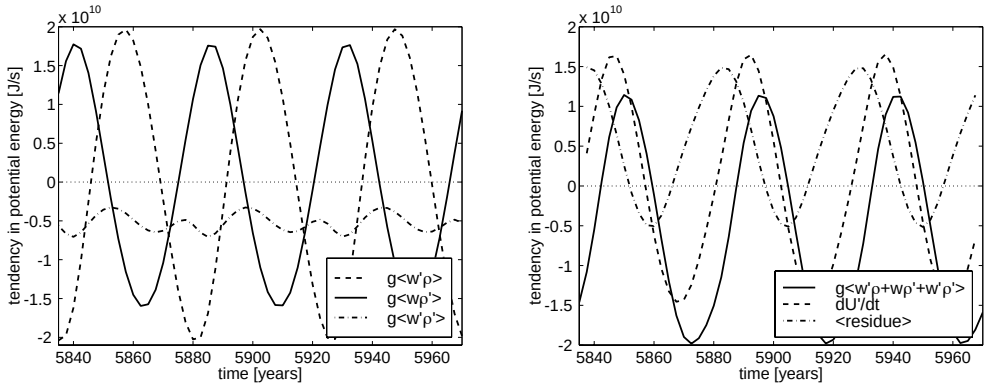

Figure 6.4: *Terms in the potential energy equation as a function of time for simulation 1. (a) Buoyancy work terms* $g < w'\bar{\rho} >$ *(dashed line),* $g < \bar{w}\rho' >$ *(solid line) and* $g < w'\rho' >$ *(dash-dotted line). (b) Sum of the buoyancy work terms* $g\,(< \bar{w}\rho' > + < w'\bar{\rho} > + < w'\rho' >)$ *(solid line), total change in potential energy* $d\mathcal{U}'/dt$ *(dashed line) and the residue* $d\mathcal{U}'/dt - g\,(< \bar{w}\rho' > + < w'\bar{\rho} > + < w'\rho' >)$ *(dashed-dotted line).*

the previous chapters, it is still the buoyancy work that determines the oscillatory behavior of the potential energy (Fig. 6.4b), just as was found in the THCM results.

All important features that characterized the interdecadal mode of chapter 3, namely the westward propagation of temperature anomalies in the north, the phase difference between zonal and meridional overturning and the phase difference between the linear buoyancy work terms, are thus also found in the nonlinear oscillation in MOM. Therefore, we can conclude that this interdecadal oscillation is caused by the interdecadal mode which was identified in THCM in chapter 3. Now that the physical mechanism of the variability found in MOM has been identified, the robustness of this variability against a decrease in horizontal viscosity is considered next.

6.3 Effects of horizontal eddy viscosity

In simulations 3, 4 and 5, the effect of a decrease in horizontal eddy viscosity on the interdecadal variability is studied. Decreasing A_H is expected to result in more complex flow behavior, which might hamper the interpretation of its variability considerably. However, in chapter 3, it was shown that increasing the horizontal diffusivity has a stabilizing effect on the flow, as this decreases the growth rate of the interdecadal mode. An increase in horizontal diffusivity is therefore expected to yield less complex behavior. A path in parameter space along which numerical time integrations were performed was chosen such that the model behavior was expected to change only gradually along this path (Fig. 6.5) and possible changes in interdecadal variability could be seen most clearly. Therefore, in simulation 3, the horizontal eddy viscosity was decreased to $A_H = 1.6 \cdot 10^6$ m^{2}s^{-1}, while at the same time the horizontal eddy diffusivity was increased to $K_H = 1000$ m^{2}s^{-1}. In simulation 4, K_H was

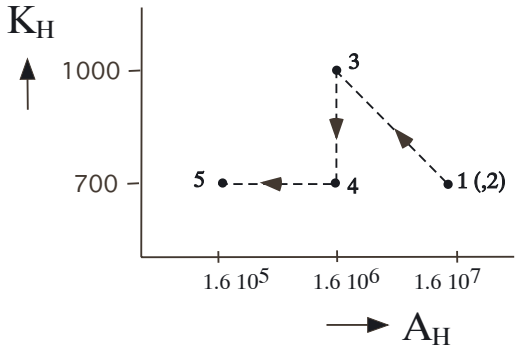

Figure 6.5: *Path in the A_H-K_H-parameter plane that was followed for simulations 1 to 5. Dots indicate the points for which the time integrations were performed.*

decreased again to its standard value $K_H = 700$ m^{2}s^{-1}, and in simulation 5, A_H was further decreased to $A_H = 1.6 \cdot 10^5$ m^{2}s^{-1} (Fig. 6.5).

The maximum meridional overturning after the spin-up under restoring boundary conditions decreases to 20 Sv for simulation 3 and the flow is concentrated more to the western boundary than in the standard case (not shown). A spectrum of the maximum meridional overturning of the last 500 years of the integration under prescribed heat flux conditions is shown in Fig. 6.6a. Interdecadal oscillations with a period of 58 yr show up as a clear peak in the spectrum. For comparison, the spectrum of the standard case is plotted in Fig. 6.6b. The peak around $\mathcal{P} = 45$ yr in Fig. 6.6b represents the interdecadal oscillation described in the previous section. The other peaks in Figs. 6.6a and b are higher harmonics of the interdecadal oscillation that are excited by nonlinear interactions. These peaks contain only little energy relative to the interdecadal peak, and the higher harmonics are therefore not seen in the time series of the meridional overturning (Fig. 6.1d).

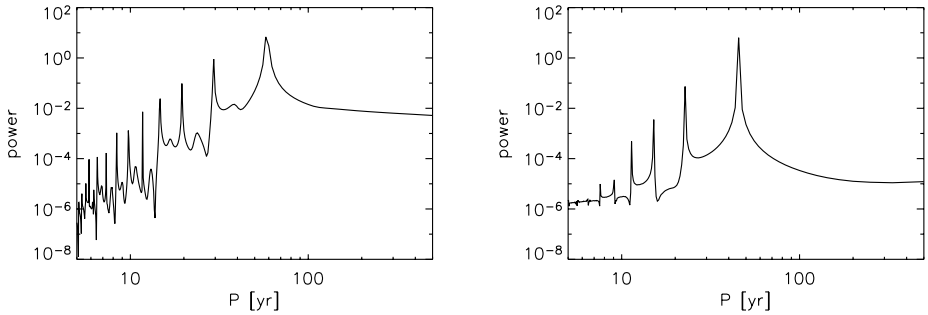

Figure 6.6: *(a) Fourier spectrum of a 500-yr time series of the maximum meridional overturning after the switch to flux boundary conditions, for simulation 3 ($A_H = 1.6 \cdot 10^6$ m^2s^{-1} and $K_H = 1000$ m^2s^{-1}). (b) As in (a), but for the standard case (simulation 1).*

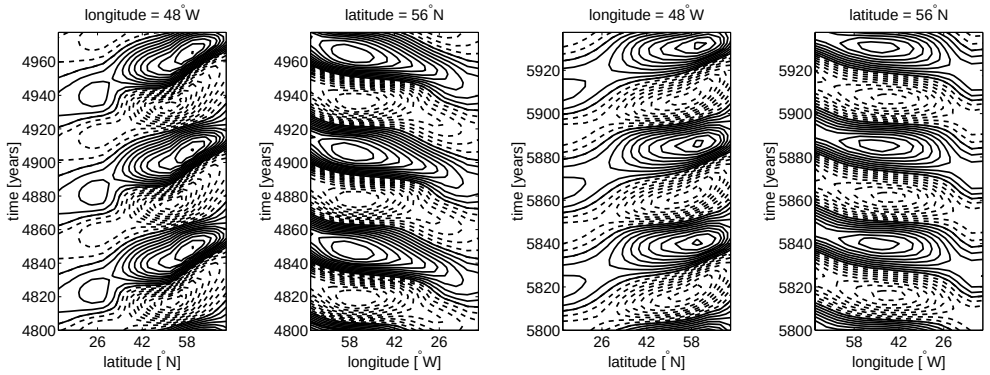

Figure 6.7: *(a) Hovmöller diagram of the upper-layer temperature anomalies for simulation 3 along $\phi = 48°$W. The anomalies are plotted during 176 yr, which corresponds to three oscillation periods ($\mathcal{P} = 58$ yr). (b) As (a), but along $\theta = 56°$N. (c) Hovmöller diagram of the upper-layer temperature anomalies for simulation 1 along $\phi = 48°$W. The anomalies are plotted during 135 yr, which corresponds to three oscillation periods ($\mathcal{P} = 45$ yr). (d) As (c), but along $\theta = 56°$N.*

In Fig. 6.7a and b, Hovmöller diagrams of the upper-layer temperature anomalies along $\phi = 48°$W and along $\theta = 56°$N are plotted to illustrate the propagation of the anomalies. In Fig. 6.7c and d, Hovmöller diagrams along the same sections are plotted for the standard case (simulation 1) for comparison. Both the propagation in westward and in northward direction remain qualitatively unchanged.

The fact that the propagation of temperature anomalies remains largely intact indicates already that the interdecadal variability in simulation 3 is caused by the interdecadal mode described in the previous chapters and that the characteristics of this mode do not change strongly with the parameters varied. This is confirmed by Fig. 6.8, which shows the phase difference between ΔT_{N-S} and ΔT_{E-W} and the phase difference between the spatially averaged meridional and zonal overturning anomalies. About 5 years after ΔT_{N-S} has reached a maximum, ΔT_{E-W} reaches its minimum value (Fig. 6.8a). The minimum in ΔT_{N-S} occurs at the same time as the maximum in ΔT_{E-W}. The spatially averaged zonal overturning anomaly leads the spatially averaged meridional overturning anomaly by 10 to 20 years (Fig. 6.8b). A qualitatively similar phase difference was found in the standard case (compare to Fig. 6.3b) and in chapter 3. The zonal overturning anomaly is still quite well in anti-phase with ΔT_{N-S}, but the meridional overturning anomaly is somewhat out of phase with ΔT_{E-W}. This causes a decreased level of correspondence of the phase difference between ΔT_{N-S} and ΔT_{E-W} compared to the standard case. Relatively small changes in the stratification as well as the circulation can already cause these mismatches. However, there is a strong qualitative agreement, showing that the basic mechanism of the interdecadal oscillation remains unchanged.

Next, the horizontal diffusivity is decreased to its standard value $K_H = 700$ m^{2}s^{-1} in simulation 4, after which A_H is further decreased to $A_H = 1.6 \cdot 10^5$ m^{2}s^{-1} in simulation 5 (Fig. 6.5). In both simulations, two dominant oscillation periods appear (see Table 6.2). A

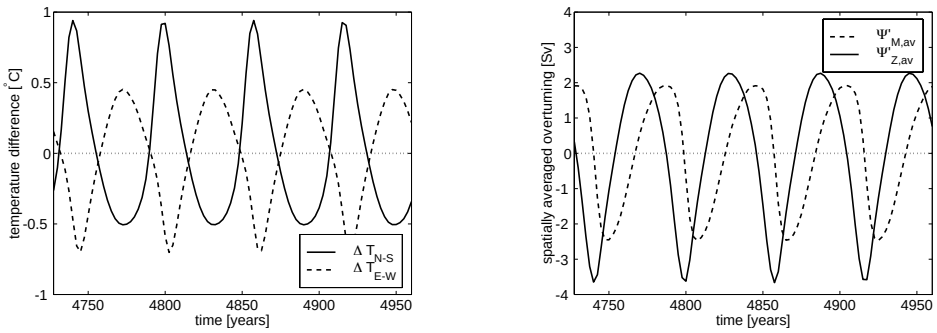

Figure 6.8: *Phase differences for simulation 3 ($A_H = 1.6 \cdot 10^6$ m^2s^{-1} and $K_H = 1000$ m^2s^{-1}). (a) Time series of the zonally averaged anomalous north-south temperature difference ΔT_{N-S} (solid line) and meridionally averaged anomalous east-west temperature difference ΔT_{E-W} (dashed line), both averaged over the upper 1438 m, during the last part of the integration under flux boundary conditions. (b) Time series of the spatially averaged meridional overturning anomaly (dashed line) and the spatially averaged zonal overturning anomaly (solid line).*

spectrum of the maximum meridional overturning for simulation 5 is shown in Fig. 6.9a. Most energy is contained in the spectral peak at the interdecadal period ($\mathcal{P} = 48$ yr). However, there is also a spectral peak around the double period, at about $\mathcal{P} = 95$ yr. The peak at $\mathcal{P} = 32$ yr is one of the higher harmonics of this low-frequency peak. From a dynamical systems point of view, the appearance of a peak at the double period in the spectrum after A_H has been decreased, indicates that a period-doubling bifurcation point has been passed. A two-dimensional projection of a phase trajectory, constructed by plotting the maximum meridional overturning in simulation 5 at a certain time t_1 against the maximum meridional

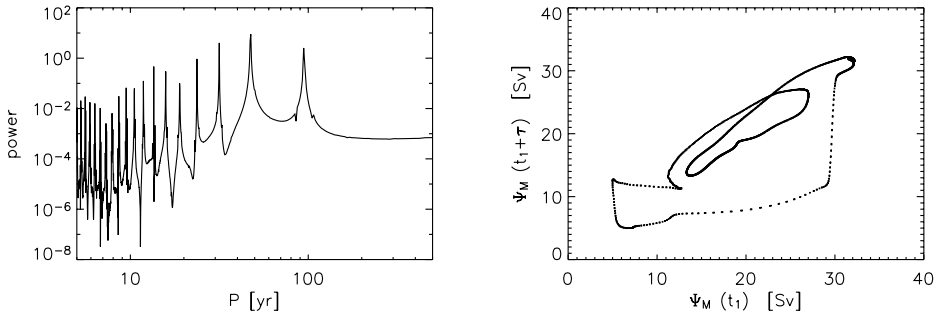

Figure 6.9: *(a) Fourier spectrum of a 5500-yr time series of the maximum meridional overturning for simulation 5 ($A_H = 1.6 \cdot 10^5$ m^2s^{-1} and $K_H = 700$ m^2s^{-1}). (b) Phase trajectory of maximum meridional overturning at a certain time plotted versus the overturning 2.5 years earlier, for simulation 5.*

overturning at time $t_1 + \tau$, with a phase lag $\tau = 2.5$ yr, is shown in Fig. 6.9b. The projection of the phase trajectory needs two loops to return to its original position in phase space, indicating the presence of a period-doubling bifurcation.

The flow behavior in simulation 5, which has become more complex due to the period-doubling bifurcation, is analyzed by applying an MSSA analysis (appendix C) to the upper-layer temperature field. To this end, the model output was sampled every 2 years for a 1000-yr period after the oscillation had equilibrated. The number of degrees of freedom was first reduced by performing a Principal Component Analysis (PCA). The resulting 20 leading principal components (PCs), which account for 100% of the variance, are the input for the MSSA analysis, for which a window length of 150 yr is taken. The most dominant statistical mode is an interdecadal mode with a period of 47 yr, which explains 59.4% of the variance within the 150-yr window. Next in the spectrum of statistical eigenmodes is a mode with $\mathcal{P} = 94$ yr, followed by higher harmonics with periods of 31.5 yr, 23.6 yr, and 15.7 yr.

Snapshots of the reconstructed component of the most dominant statistical mode (RC pair 1–2) are shown in Fig. 6.10 for six times during one oscillation period of 47 yr. The description is started at $t = 4048$ yr, when a cold anomaly occupies most of the basin south of $60°$N (Fig. 6.10a). This anomaly, which is strongest near the western boundary, slowly propagates northward (Figs. 6.10b, c and d). A warm anomaly has formed in the southeastern part of the basin at $t = 4056$ yr, which in turn propagates westward between $t = 4056$ yr and $t = 4072$ yr (Figs. 6.10b, c and d). During the second half of the oscillation the warm anomaly propagates northward along the western boundary (Figs. 6.10e, f) and a new cold anomaly forms and propagates to the west. When compared to the temperature anomalies at higher values of A_H (see Fig. 6.2), the westward propagation occurs now at lower latitudes, and the northward propagation is more confined to the region near the western boundary. The lower horizontal eddy viscosity results in a narrower mean-state western boundary current. At the same time, the zonal velocity in the northern part of the basin has increased. For instance, the upper-layer zonal velocity at the end of the spin-up, averaged over the northern half of the basin, has increased from 0.011 ms^{-1} in simulation 1 to 0.018 ms^{-1} in simulation 5. The westward propagation of anomalies has therefore shifted to lower latitudes. The northward propagation of temperature anomalies, which is caused by advection by the mean velocity field, is consequently concentrated more to the western boundary.

These propagation characteristics can be seen more clearly in Hovmöller diagrams of the upper-layer temperature of RC pair 1–2 along sections at $\phi = 48\,°$W and $\theta = 56°$N (Fig. 6.11). Northward propagation is strongest between $15\,°$N and $45°$N and most of the westward propagation occurs between $10°$W and $50°$W. Although the details of the propagation of temperature anomalies change with decreasing A_H, the main propagation direction remains northwestward.

To investigate if the statistical interdecadal mode is characterized by the same phase differences as the internal (dynamical) interdecadal mode, the temperature was averaged over the upper 1438 m, after which a PCA analysis was performed on this vertically averaged temperature field. Again the 20 leading PCs (accounting for 99.9% of the variance) were used as input for the MSSA analysis. The interdecadal mode with $\mathcal{P} = 47$ yr explained 55% of the variance within the 150-yr window. From the RCs of this mode, the zonally averaged meridional temperature difference ΔT_{N-S} and the meridionally averaged zonal temperature difference ΔT_{E-W} were computed (Fig. 6.12a). About 3 yr after ΔT_{N-S} has reached a

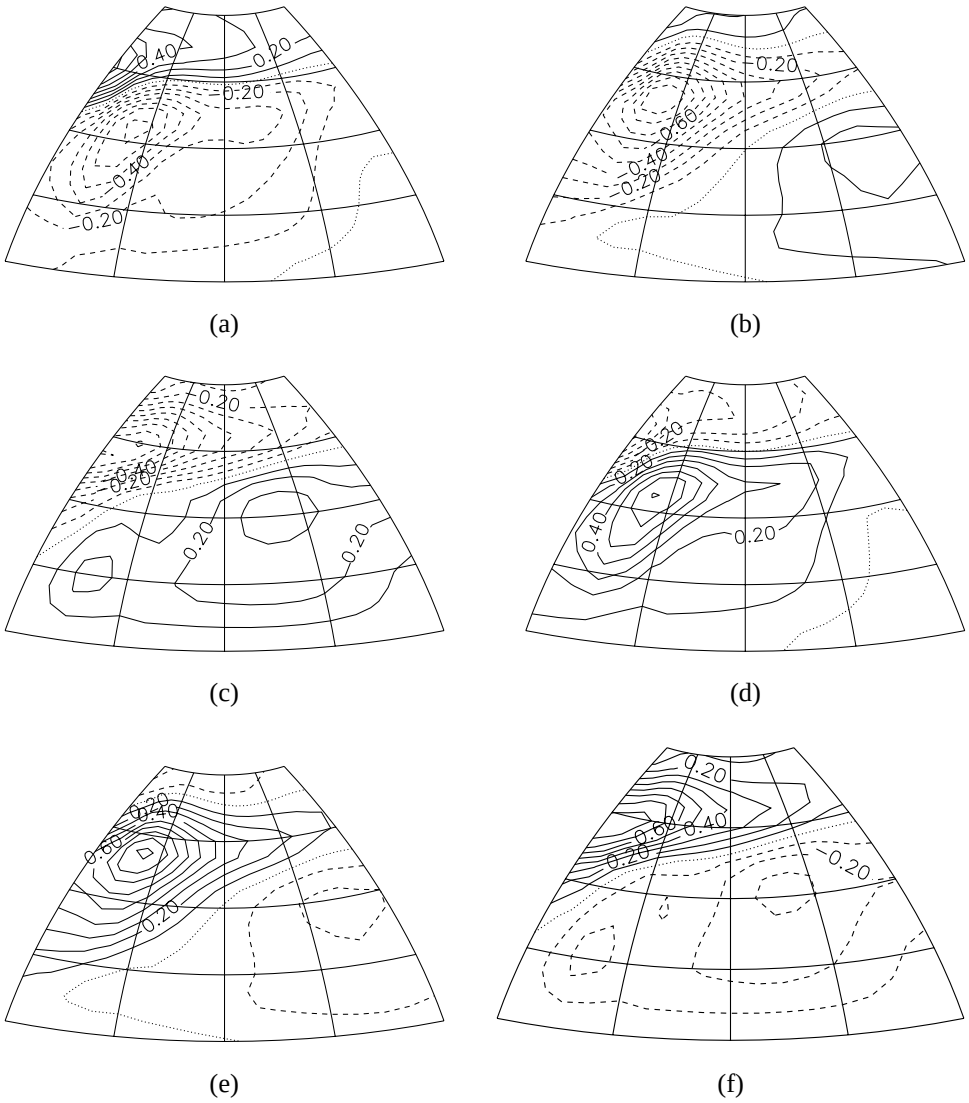

Figure 6.10: *Reconstructed component of the most dominant statistical mode of the upper-layer temperature (RC pair 1–2) for simulation 5 at six times during one oscillation cycle ($\mathcal{P} = 47$ yr). Snapshots are shown for (a) $t = 4048$ yr, (b) $t = 4056$ yr, (c) $t = 4064$ yr, (d) $t = 4072$ yr, (e) $t = 4080$ yr and (f) $t = 4088$ yr. The plots are scaled with the maximum value of 2.8°C.*

maximum, ΔT_{E-W} is at a minimum.

The phase difference between the spatially averaged meridional and zonal overturning perturbations was computed by performing MSSA analysis on both the meridional and the

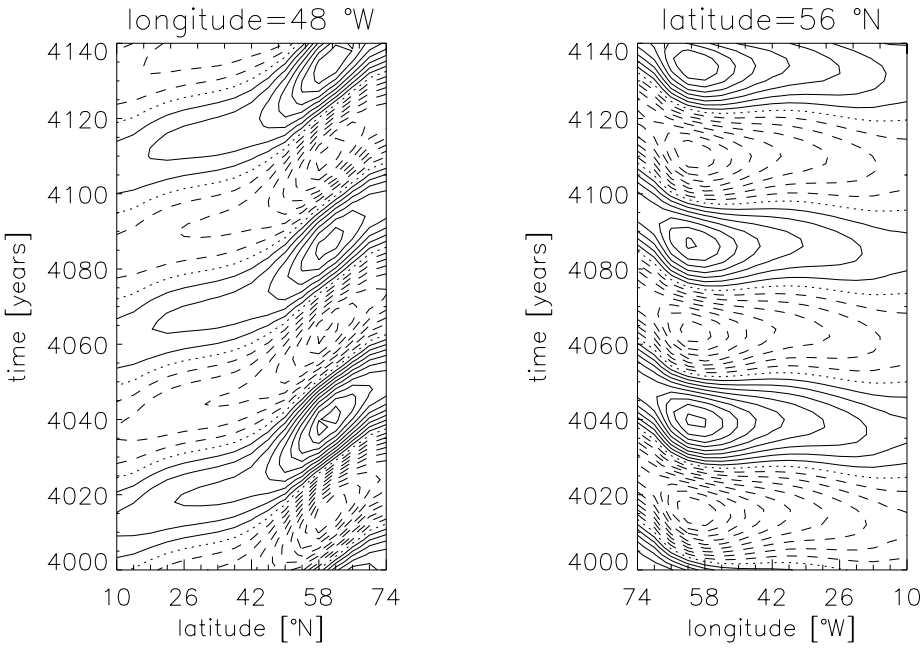

Figure 6.11: *(a) Hovmöller diagram of RC pair 1–2 of the upper-layer temperature along* $\phi = 48°$ *W. The maximum value is* $1.4°$*C. (b) As (a), but along* $\theta = 56°$*N and with a maximum value of* $2.4°$*C.*

zonal overturning streamfunctions. Again a PCA analysis was performed first on both fields, and the 20 leading EOFs, accounting for 100% of the variance in both the meridional and the zonal overturning, were used in the MSSA analysis. For both fields, the most dominant statistical mode was the interdecadal mode with $\mathcal{P} = 47$ yr, explaining 50% of the variance in the 150-yr window for the meridional overturning (and 60% in case of the zonal overturning). The reconstructed components of these most dominant statistical modes of meridional and zonal overturning were averaged spatially and the resulting time series are plotted in Fig. 6.12b. The spatially averaged zonal overturning leads the spatially averaged meridional overturning by about 10 yr, which is qualitatively the same phase difference as was found in the standard case in simulation 1 (see Fig. 6.3). The spatially averaged zonal overturning is in anti-phase with ΔT_{N-S}, as was also found in the standard case with high A_H. The spatially averaged meridional overturning is not exactly in phase with ΔT_{E-W}, but lags by about 5 years. However, the typical phase differences between the meridional and zonal overturning and between the zonal and meridional temperature gradients, which characterize the interdecadal oscillation in the standard case, are still present for $A_H = 1.6 \cdot 10^5$ m^{2}s^{-1}.

The interdecadal mode identified in THCM could also be characterized by the phase difference between the two buoyancy work terms dominating the linearized potential energy equation for the perturbations. In Fig. 6.4 it was shown that nonlinearities play also a (small)

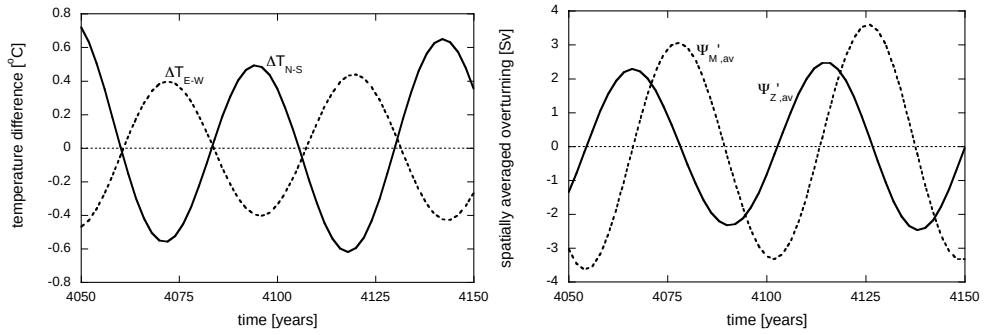

(a) (b)

Figure 6.12: *(a) Zonally averaged north-south temperature difference ΔT_{N-S} (solid line) and meridionally averaged east-west temperature difference ΔT_{E-W} (dashed line), both averaged over the upper 1438 m, of RC pair 1–2. (b) Spatially averaged meridional overturning (dashed line) and spatially averaged zonal overturning (solid line) of RC pair 1–2.*

role in the potential energy budget of the interdecadal oscillation in MOM, but that changes in potential energy were still mainly determined by the total buoyancy work $g(<\bar{w}\rho'> + <w'\bar{\rho}> + <w'\rho'>)$. In Fig. 6.13, the tendency in potential energy, the total buoyancy work term and the residual term representing potential energy changes due to dissipation and convection are plotted for simulations 3 and 5. Changes in potential energy are no longer

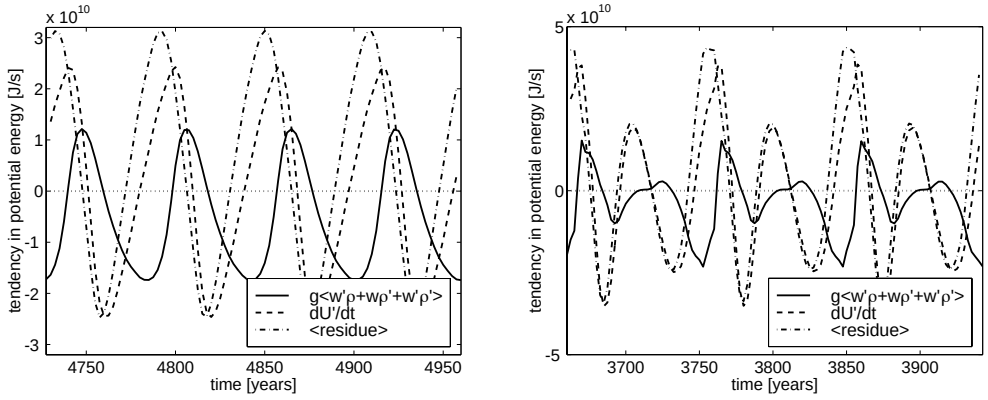

(a) (b)

Figure 6.13: *(a) Terms in the perturbation potential energy equation for simulation 3. Plotted are the sum of the buoyancy work terms $g\,(<\bar{w}\rho'> + <w'\bar{\rho}> + <w'\rho'>)$ (solid line), the total change in potential energy $d\mathcal{U}'/dt$ (dashed line) and the residue $d\mathcal{U}'/dt - g\,(<\bar{w}\rho'> + <w'\bar{\rho}> + <w'\rho'>)$ (dashed-dotted line). (b) As (a), but for simulation 5.*

dominated by the total buoyancy work, but, especially in simulation 5, by the residual term.

The rather good correspondence of the propagation characteristics and the phase differences between the spatially averaged meridional and zonal overturning, as well as the phase

difference between ΔT_{N-S} and ΔT_{E-W} for simulations 1, 3, 4 and 5, has revealed that the interdecadal variability in all four cases is most likely caused by the same mechanism. This excludes the possibility that Fig. 6.13 and Fig. 6.4 do not correspond due to a change in the physical mechanism driving the interdecadal variability in simulations 1 and 5. Therefore, it is concluded that the dominating effect of buoyancy work changes on changes in potential energy is not a useful characteristic of the interdecadal mode. This is probably caused by the fundamental difference between the (infinitesimally small) perturbations acting on a steady state, which were used to describe the oscillation mechanism in the previous chapters, and the finite-amplitude anomalies with respect to the time-mean state that are used here.

6.4 Effects of continental geometry, wind and bottom topography

So far, the basin had a flat bottom and was bounded by lines of constant longitude and latitude. The effect of continental geometry on the interdecadal variability is now investigated by adding a 'realistic' North-Atlantic continental geometry, while the bottom is kept flat. This was done for the case with $A_H = 1.6 \cdot 10^7$ m^{2}s^{-1} in simulation 6 and for $A_H = 1.6 \cdot 10^5$ m^{2}s^{-1} in simulations 7 and 8 (see Table 6.2). In simulation 6 ($A_H = 1.6 \cdot 10^7$ m^{2}s^{-1}), no oscillations were found after the switch to flux boundary conditions and the system remained in a steady state. Continental geometry thus stabilizes the flow with respect to a situation with a box-shaped geometry.

The steady state obtained at the end of the spin-up under restoring boundary conditions for simulation 7 ($A_H = 1.6 \cdot 10^5$ m^{2}s^{-1}) has a maximum meridional overturning of 29 Sv. The velocity and temperature fields in the upper layer at the end of the spin-up are shown in Fig. 6.14. The horizontal circulation is directed to the main sinking area in the north-eastern corner of the basin (Fig. 6.14a). The northward heat transport by this western boundary current causes small departures from the zonally uniform state in the upper-layer temperature (Fig. 6.14b). After the switch to flux boundary conditions, the system is integrated for another 1000 years and an interdecadal oscillation with a period of 73 yr is excited. When this simulation is repeated with a horizontal resolution of $2^\circ \times 2^\circ$ and 24 vertical layers (simulation 8), the maximum meridional overturning at the end of the spin-up is 24 Sv. Under prescribed heat-flux conditions, the interdecadal oscillation is found again, but its period has decreased to 44 yr. The considerable changes in maximum overturning and in the oscillation period show the strong effect of the unresolved continental boundary layers (although it must be noted that the shape of the basin is also changed slightly when the resolution is increased). However, as the qualitative features of the oscillation are the same at both resolutions, in the following only the results of the coarse-resolution run (simulation 7) are described.

The period-doubling, which was present in the case without continental geometry and with $A_H = 1.6 \cdot 10^5$ m^{2}s^{-1} (simulation 5), has disappeared in simulation 7. This indicates that continental geometry has a stabilizing effect on the periodic orbit. Snapshots of the upper-layer temperature anomaly during one oscillation cycle are shown in Fig. 6.15. The large-scale warm anomaly located in the southeastern part of the basin at $t = 3712.5$ yr (Fig. 6.15a) propagates in northwestern direction and is followed by a cold anomaly around $t = 3750$ yr (Fig. 6.15d), which also propagates to the northwest. In Fig. 6.16a, the spatially

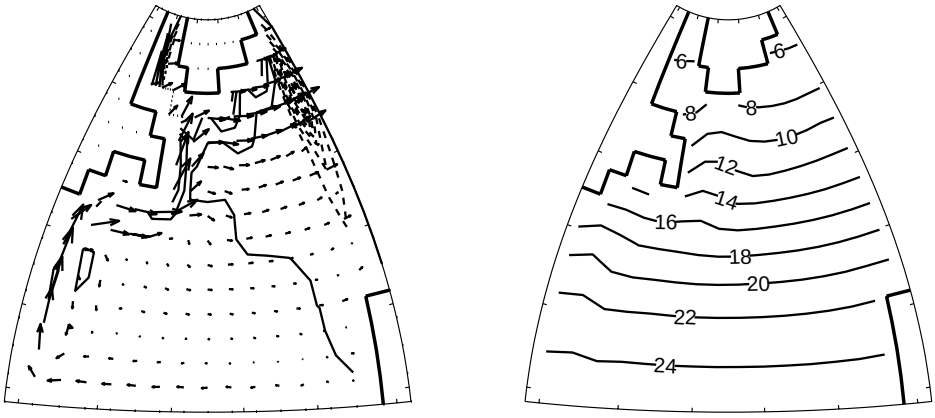

Figure 6.14: *(a) Upper-layer velocity field at the end of the spin-up for simulation 7. (b) Upper-layer temperature field at the end of the spin-up. In these plots longitude (from* 74° *W to* 10° *W) is plotted on the horizontal axis and latitude (from* 10° *N to* 74° *N) on the vertical axis. The continental boundaries are indicated by bold lines.*

averaged meridional and zonal overturning anomalies are plotted as a function of time. The spatially averaged zonal overturning anomaly leads the spatially averaged meridional overturning anomaly by 10 to 20 years. In the cases without continental geometry, the phase difference between meridional and zonal overturning could be related to a phase difference between anomalous zonal and meridional temperature differences in the upper 1500 m of the ocean. The latter phase difference could therefore serve as a characteristic of the interdecadal mode. However, when continental geometry is included, the definition of ΔT_{N-S} and ΔT_{E-W} is no longer straightforward. The temperature difference ΔT_{N-S} could in the case with continental geometry be defined by subtracting the average temperature in a box at low latitudes from the average temperature in a box at high latitudes (after averaging over a certain depth). However, several tests showed that the resulting phase difference between ΔT_{N-S} and ΔT_{E-W} is very sensitive to the choice of the location of the boxes. It is therefore difficult to use the phase difference between ΔT_{N-S} and ΔT_{E-W} as a characteristic feature of the interdecadal oscillation when continental geometry is included.

Next, in simulation 9, also wind forcing is included with a pattern according to the analytical formula of Bryan (1987) given in equation (2.25), and a standard amplitude $\tau_0 = 0.1$ Nm^{-2}. At the end of the spin-up, a steady state with a maximum meridional overturning of 25 Sv has been reached. After the switch to prescribed heat-flux conditions, the integration was continued for another 1000 years. The spectrum of the maximum meridional overturning of the last 500 years of the integration under prescribed flux conditions shows spectral peaks around $\mathcal{P} = 57$ yr and $\mathcal{P} = 120$ yr (not shown). The latter shows that wind forcing has a destabilizing effect on the flow, in accordance with the results obtained by Huck *et al.* (2001) under climatological wind-stress forcing. The spatially averaged meridio-

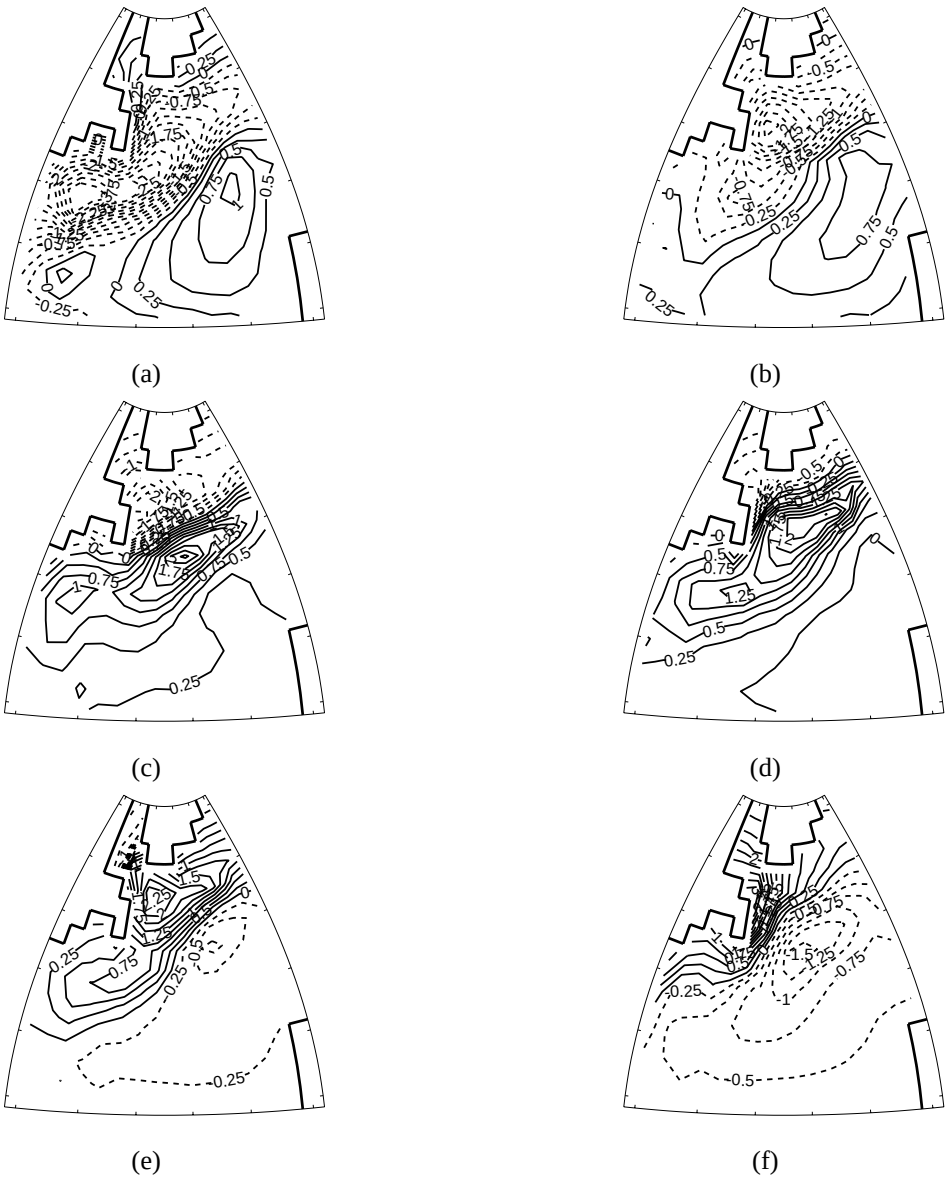

Figure 6.15: *Snapshots of the upper-layer temperature anomaly at six phases during one oscillation cycle for the case with continental geometry, a flat bottom and* $A_H = 1.6 \cdot 10^5 m^2 s^{-1}$ *(simulation 7,* $\mathcal{P} = 73$ *yr). Snapshots are shown for (a)* $t = 3712.5$ *yr, (b)* $t = 3725$ *yr, (c)* $t = 3737.5$ *yr, (d)* $t = 3750$ *yr, (e)* $t = 3762.5$ *yr and (f)* $t = 3775$ *yr. In these plots longitude (from* $74^\circ W$ *to* $10^\circ W$*) is plotted on the horizontal axis and latitude (from* $10^\circ N$ *to* $74^\circ N$*) on the vertical axis.*

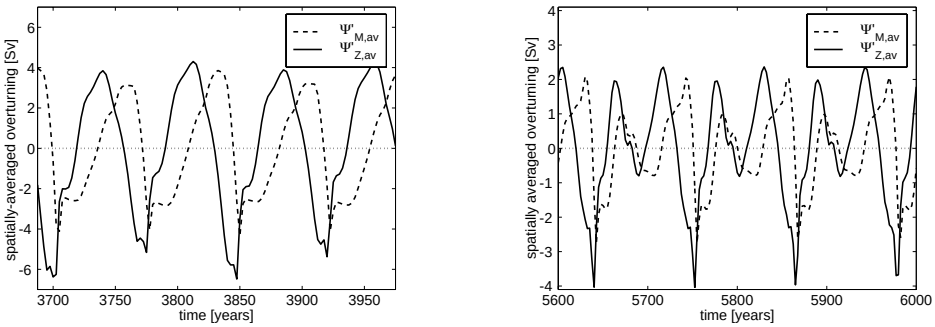

Figure 6.16: *(a) Time series of the spatially averaged meridional overturning anomaly (dashed line) and the spatially averaged zonal overturning anomaly (solid line) during the last part of the simulation under flux boundary conditions for simulation 7. (b) As (a), but for simulation 9.*

nal and zonal overturning anomalies for simulation 9 are plotted in Fig. 6.16b as a function of time. The spatially averaged zonal overturning anomaly is still leading the spatially averaged meridional overturning anomaly, indicating that the inclusion of wind-stress forcing has not qualitatively changed the physical mechanism underlying the interdecadal variability.

Finally, the effect of bottom topography on the variability was investigated by adding a 'realistic' bathymetry. However, when simulation 9 was repeated with a configuration in which bottom topography was included, a numerical mode related to the (too) coarse representation of the bathymetry emerged. This simulation was therefore repeated on a grid with a horizontal resolution of $2^\circ \times 2^\circ$ and 24 vertical layers (simulation 10 in Table 6.2). The statistical equilibrium at the end of the spin-up, which has a maximum meridional overturning of 20 Sv, turned out to be stable under prescribed heat-flux conditions. This shows the stabilizing effect of bottom topography on the flow. Unfortunately, on a decrease of the horizontal diffusivity to $K_H = 350$ m^{2}s^{-1}, the numerical mode returned. Therefore, a simulation was performed using a resolution of $1^\circ \times 1^\circ$, with 24 vertical layers and $K_H = 350$ m^{2}s^{-1}. With this resolution, also variability with a higher frequency was resolved. A test showed that in this case the asynchronous integration did no longer give correct results. As the use of synchronous integration would increase the required computing time considerably, the wind forcing was turned off, so that the asynchronous integration technique could still be applied. Simulation 11 was thus performed with a horizontal resolution of $1^\circ \times 1^\circ$ and with $K_H = 350$ m^{2}s^{-1} (see Table 6.2). The meridional overturning and the upper-layer temperature of the statistical equilibrium reached at the end of the spin-up are shown in Fig. 6.17. The maximum meridional overturning is about 17 Sv, with sinking around $60\,^\circ$N. The meridional heat transport by the western boundary current causes zonal asymmetries in the upper-layer temperature field, especially in the northern part of the basin (Fig. 6.17b). After the switch to prescribed heat-flux boundary conditions, an oscillation with a 22-yr period develops. Snapshots of the upper-layer temperature anomalies during one oscillation cycle are shown in Fig. 6.18. The cold anomaly starting in the southeastern part of the basin at $t = 4032.5$ yr (Fig. 6.18a) propagates to the northwest and is followed by a warm anomaly at $t = 4043$ yr

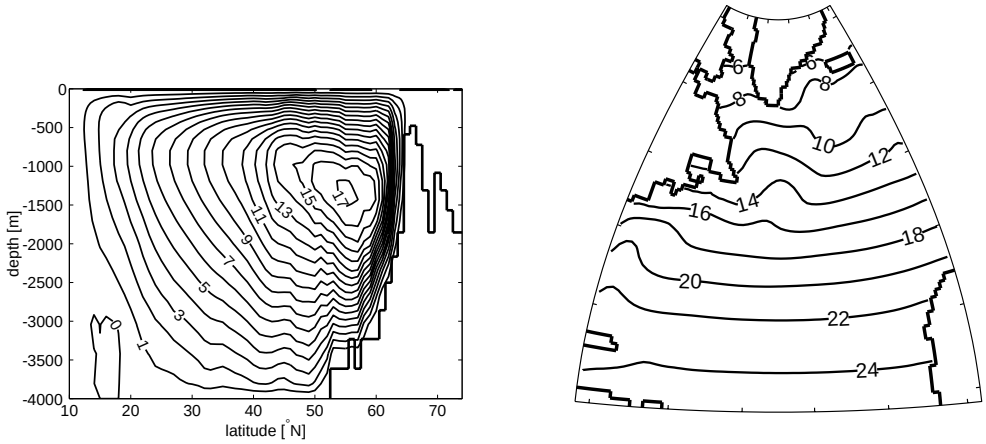

(a) (b)

Figure 6.17: *(a) Meridional overturning (in Sverdrups) at the end of the spin-up for simulation 11. (b) Upper-layer temperature field at the end of the spin-up. Longitude (from* $74^\circ W$ *to* $10^\circ W$*) is plotted on the horizontal axis and latitude (from* $10^\circ N$ *to* $74^\circ N$*) on the vertical axis.*

(Fig. 6.18d).

The spatially averaged meridional and zonal overturning are plotted as a function of time in Fig. 6.19. The spatially averaged zonal overturning is still leading the spatially averaged meridional overturning. The 22-yr oscillation found in the case with $K_H = 350$ m^{2}s^{-1} and bottom topography has the same qualitative features as the interdecadal oscillation in the case with continental geometry but a flat bottom and $K_H = 700$ m^{2}s^{-1}, indicating that the underlying physical mechanism has remained the same.

6.5 Summary and discussion

In this chapter, the interdecadal variability in a thermally driven single-hemispheric basin in the MOM model was shown to be caused by the interdecadal mode described in chapter 3. The identification was made using typical features characterizing this mode, namely the westward propagation of temperature anomalies, the resulting phase difference between meridional and zonal temperature differences and the corresponding phase difference between the zonal and meridional overturning anomalies. In chapter 3, it was already shown that the interdecadal mode is robust for changes in K_H and K_V, but the fact that it has been identified in two independent models confirms the robustness of this mode.

The main point of the study in this chapter was to show that the interdecadal mode can be followed from the idealized case of highly viscous flow in a basin with a simple geometry towards a more realistic situation, using the characteristics defined in the idealized case. In a series of simulations, the horizontal eddy viscosity was decreased by two orders of magnitude to a value commonly used in coarse-resolution ocean models ($A_H = 1.6 \cdot 10^5$ m^{2}s^{-1}). Next, a 'realistic' North-Atlantic continental geometry was added and finally also bottom topography

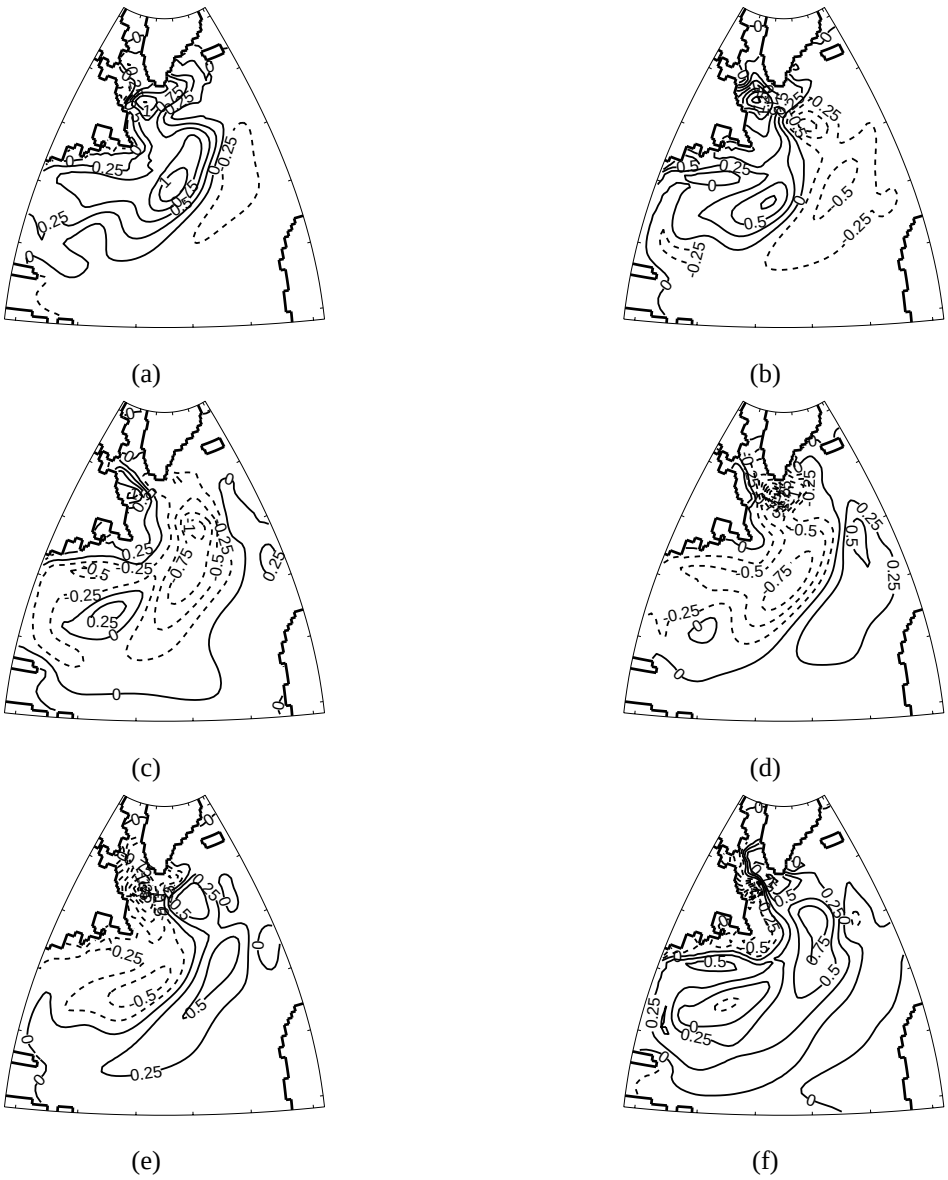

Figure 6.18: *Snapshots of the upper-layer temperature anomaly at six phases during one oscillation cycle for the case with continental geometry, bottom topography and* $A_H = 1.6 \cdot 10^5 m^2 s^{-1}$ *(simulation 11,* $\mathcal{P} = 22$ *yr). Snapshots are shown for (a)* $t = 4032.5$ *yr, (b)* $t = 4036$ *yr, (c)* $t = 4039.5$ *yr, (d)* $t = 4043$ *yr, (e)* $t = 4046.5$ *yr and (f)* $t = 4050$ *yr. In these plots longitude (from* $74^\circ W$ *to* $10^\circ W$*) is plotted on the horizontal axis and latitude (from* $10^\circ N$ *to* $74^\circ N$*) on the vertical axis.*

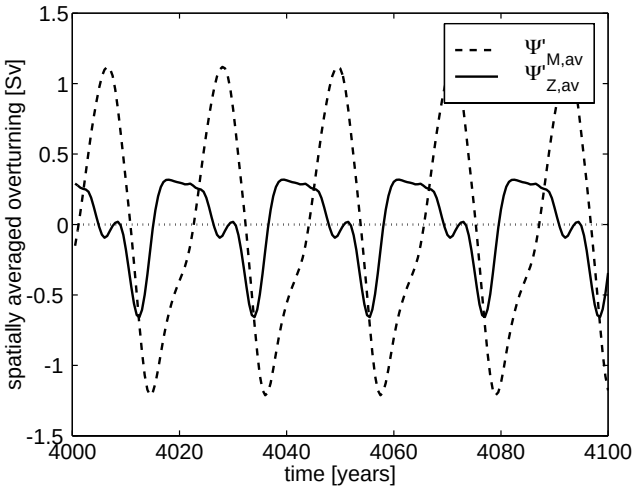

Figure 6.19: *Time series of spatially averaged meridional overturning (dashed line) and spatially averaged zonal overturning (solid line) during the last part of the simulation under flux boundary conditions for simulation 11.*

was included. Along this path, the main propagation direction of temperature anomalies remains (north)westward and the phase difference between meridional and zonal overturning anomalies remains such that the zonal overturning leads the meridional overturning. This work is the first part of a path that might finally allow for the identification of the physical mechanism underlying the interdecadal variability in CGCM simulations and observations.

Another approach for understanding interdecadal variability in CGCMs would be to follow the variability, starting from a CGCM simulation, along a path towards a simple model configuration. The advantage of such an approach is that one can start with the realistic variability. However, as the variability at this starting point is not yet understood, characteristics cannot be defined, which makes it extremely hard to follow the variability down in the modeling hierarchy. As period and spatial patterns of the variability are likely to change when different models or model configurations are considered, there is no way to check whether the physical mechanism driving the variability is still the same.

In the approach followed here, both the choice of the proper characteristics in the idealized case and the identification of these characteristics in more complex cases is of great importance. There is no single objective way to choose the characteristics identifying the oscillation mechanism. However, a characteristic should be a feature that is central to the mechanism and thus to the existence of the oscillation. For example, the mechanism described in chapter 3 would not work if there was no propagation of temperature anomalies. Also, the phase difference between the meridional and zonal temperature differences ΔT_{N-S} and ΔT_{E-W} characterizes the interdecadal mode in a basin without continental geometry. However, the identification of this characteristic phase difference is difficult when continental geometry is included as it is not yet clear how ΔT_{N-S} and ΔT_{E-W} should be defined in that case. It is therefore important to have more than one characteristic to describe a mecha-

nism. When variability is followed along a certain path and only one characteristic changes, this might point towards the fact that the characteristic was not well-chosen. On the other hand, as soon as the mechanism identified in the idealized case is no longer controlling the modeled variability, all of the characteristics are likely to change.

The fact that the physical mechanism of the interdecadal mode has been identified in several steps of the model hierarchy, shows not only that this mode is a robust feature, but also that the method of identifying certain features characterizing the mechanism can be a fruitful approach in understanding variability in various model configurations. The results presented here provide a framework within which results from other model studies can be interpreted. With westward propagation of temperature anomalies and a phase difference between the meridional and zonal overturning as characteristics that identify the physical mechanism of the interdecadal mode, it can be investigated if the interdecadal variability found in other model studies can be attributed to this mode.

Northwestward propagating temperature anomalies are clearly present in the interdecadal oscillation found by Greatbatch and Zhang (1995) in a planetary geostrophic model. As in their results zonal overturning anomalies are not shown, it cannot be checked if the phase relation between meridional and zonal overturning anomalies is the same as for the interdecadal mode described here. However, in the oscillation of Greatbatch and Zhang (1995), the maximum meridional overturning occurs when there is a negative sea-surface temperature anomaly in the northwestern corner of the basin and a positive anomaly in the north-central part of the basin. The same phase relation between meridional overturning and surface temperature anomalies is found here (see Figs. 6.10d and 6.12b around $t = 4075$ yr).

Westward propagating temperature anomalies also characterize the interdecadal oscillations found by Huck and co-workers in a series of studies (Colin de Verdière and Huck, 1999; Huck *et al.*, 1999; Huck and Vallis, 2001; Huck *et al.*, 2001). Using a tangent linear model of their planetary geostrophic model, Huck and Vallis (2001) show that these oscillations arise from an internal mode of the system. From the results in Huck *et al.* (1999) and Colin de Verdière and Huck (1999), it can be clearly seen that there is a similar phase relation between meridional overturning and sea-surface temperature anomalies as in the interdecadal mode described here.

Density anomalies that propagate westward are also present in the oscillations found by Greatbatch and Peterson (1996). The maximum meridional overturning in those oscillations was shown to lag a temperature difference ΔT_{SN}, defined as the temperature averaged over the region north of 35°N subtracted from the temperature averaged over the region south of 35°N, by about one-third oscillation period (Greatbatch and Peterson, 1996). Taking into account that the temperature difference ΔT_{N-S} used here will be approximately in anti-phase with ΔT_{SN}, comparison to Figs. 6.12a and b shows that the phase relation found by Greatbatch and Peterson (1996) is in accordance with our results. Although an important characteristic of the physical mechanism of the interdecadal mode described here, namely the phase difference between the meridional and zonal overturning anomalies, cannot be investigated for the studies mentioned above, we hypothesize that the interdecadal variability in this thesis and the interdecadal variability found by Greatbatch and Zhang (1995), Greatbatch and Peterson (1996), as well as the interdecadal oscillations in the simulations of Huck and co-workers (e.g. Huck *et al.* (1999, 2001)), are all caused by the same internal mode of the system.

The interdecadal variability found by Chen and Ghil (1995) under mixed boundary conditions, as well as in a purely thermally driven flow, is associated with density anomalies in the northwestern part of the basin, which move anti-cyclonically. This variability might also be caused by the interdecadal mode described here, but as no surface temperature or density anomaly patterns, nor any phase relations are shown in the paper of Chen and Ghil (1995), this cannot be decided yet. There are some indications of northwestward propagation of sea-surface temperature anomalies in the 22-yr oscillation of Weaver *et al.* (1994), but the anomalies are mainly confined to the northwestern corner of the basin and the Labrador Sea, in contrast with the basin-scale pattern of the anomalies found here. Closer investigation would be needed to find out whether the physical mechanism underlying the interdecadal oscillation of Weaver *et al.* (1994) is the same as that of the interdecadal mode described here, or completely different.

Only the first steps along a path towards a realistic simulation of interdecadal variability have been taken in this study. However, the northwestward propagating patterns of the interdecadal oscillation described here resemble the anomalies of dynamic topography (which are related to density anomalies) of the variability in the coupled simulation of Delworth *et al.* (1993) fairly well. Moreover, when the meridional overturning in Delworth *et al.* (1993) is at a maximum, the dynamic topography anomaly pattern corresponds to a density pattern with a positive density anomaly in the northwestern corner of the basin and a negative anomaly in the south-western part of the basin. The relation between sea-surface temperature (and thus density) anomalies and meridional overturning anomalies of the interdecadal oscillation described here is similar. These correspondences suggest that also the interdecadal variability in Delworth *et al.* (1993) can be explained by the thermally driven interdecadal mode described here.

The spatial pattern of the surface temperature anomalies associated with the interdecadal oscillation found here show some resemblance with the SST anomaly patterns of variability observed by Kushnir (1994). Some signs of northwestward propagation can also be seen in the observed anomaly patterns (Delworth and Mann (2000), see also Fig. 1.2 in chapter 1), but this is not very clear. The phase difference between the meridional and zonal overturning anomalies, which was a clear characteristic in the case of the modeled variability, cannot be determined for the observations. Therefore, the question whether the interdecadal mode is also contributing to the observed multidecadal variability cannot be answered yet. The interdecadal mode will have to be followed further up in the model hierarchy towards fully coupled ocean-atmosphere-sea-ice GCMs. Only in a careful investigation of the spatial patterns and propagation characteristics of the variability along such a path in the model hierarchy, the relation between the interdecadal mode described here and the multidecadal variability in CGCMs and observations might be clarified.

Chapter 7

Summary and synthesis

The main objective of this thesis was to investigate the internal variability of the North-Atlantic thermohaline ocean circulation on interdecadal to centennial time scales in a systematic way. This work is motivated by the current uncertainty about the role of internal thermohaline variability in North-Atlantic climate variability. Internal variability of the thermohaline circulation has been proposed as a possible cause of climate variability at interdecadal and centennial time scales. The possibility of such internal variability has been investigated in many numerical modeling studies, with models varying from very simple box models to highly complex CGCMs. However, there is still no agreement about the dominant periods and associated spatial patterns of the variability, nor about the physical mechanisms driving it. Both the time scale and the spatial characteristics of the observed variability have been simulated rather well with the coupled GFDL model (Delworth and Mann, 2000). However, due to the complexity of CGCMs like the GFDL model, the physical mechanism of the variability is hard to understand from such a simulation. On the other hand, many mechanisms have been proposed based on studies with simpler models, but it is unclear how they can be connected to the variability in CGCMs and observations. The main problem seems to be the lack of an interpretation framework within which the results from numerical modeling studies can be related to each other and to observations.

The studies presented in this thesis are part of an approach in which is tried to establish such an interpretation framework. In this approach, the variability is studied in a hierarchy of models, using techniques from dynamical systems theory. Steady-state solutions of the three-dimensional thermohaline flows are computed, and their linear stability is determined. From a dynamical systems point of view, the variability of the flow is to a large extent determined by the unstable or weakly stable oscillatory eigenmodes of a system. Focus in the approach taken here is on understanding the physical mechanisms of the oscillatory eigenmodes in an idealized case and identifying characteristics that belong to these mechanisms. In subsequent steps, it is investigated if eigenmodes of more complex cases can be related to those in the idealized limiting case. In addition, it will have to be shown that the temporal and spatial variability of the total flow, as obtained by transient-flow computations, can be (partly) attributed to the internal modes of the system. The ultimate goal of this approach is to understand variability in complex state-of-the-art CGCMs and observations. In this thesis,

several steps within this approach have been taken.

In chapter 3, the internal variability in the idealized limiting case of single-hemispheric thermally driven flows in a high-viscosity regime has been studied. It was shown that, under prescribed heat-flux conditions, the flow is unstable to an oscillatory eigenmode with an interdecadal period. The physical mechanism of this mode was investigated in detail for conditions close to the stability boundary. It was demonstrated that the westward propagation of temperature anomalies causes a phase difference between the zonal and meridional overturning anomalies, which leads to new temperature anomalies, consistent with the propagating anomaly patterns.

In chapter 4, this interdecadal mode was followed towards a more complex model configuration, by taking two steps along a path up in the model hierarchy. In the first step, the ocean model was coupled to an energy-balance model for the atmosphere, which did not contain a hydrological cycle. The least damped mode, which had again an interdecadal period, was shown to have the same mechanism as the interdecadal mode studied in chapter 3. In the next step, a prescribed freshwater-flux forcing was added and the effects of the transport of salt on the mechanism and stability properties of the interdecadal mode were investigated. Whereas the physical mechanism is not affected by the inclusion of salinity, the stability properties of the mode were shown to be rather sensitive to the shape of the freshwater-flux forcing. A strengthening of the freshwater input in the northern North Atlantic destabilizes the flow. In this way, the results presented in this chapter provided an explanation for the increase in multidecadal variability that was found in the coupled GFDL model when the freshwater input in the northern North Atlantic was (artificially) increased (Tziperman, 2000).

Chapter 5 focussed on a systematic investigation of what kind of oscillatory modes exist in the uncoupled ocean model apart from the interdecadal mode. It was found that a second type of modes exists, with centennial periods. Advection of density anomalies by the meridional overturning is essential for the mechanism of these modes, and the oscillation period is mainly determined by the overturning time scale of the steady-state flow. For all parameter settings investigated, the centennial modes were damped. Transient-flow computations showed that, even when the steady state is stable, variability at many time scales can be excited under a stochastic forcing. The variability at interdecadal time scales was shown to be caused by the interdecadal mode described in chapter 3.

In chapter 6, a second path up in the model hierarchy is followed, towards a less viscous regime in which also the effects of continental geometry and bottom topography are included. To this end, transient-flow computations with the MOM model have been performed. The starting point is again the viscous thermally driven flow in the idealized-basin configuration. By considering characteristic features of the physical mechanism of the interdecadal mode in the idealized case, the variability in MOM could be related to the interdecadal mode described in chapter 3. No qualitative changes occurred when the variability was followed up in the model hierarchy.

The interdecadal variability as observed in the instrumental record and in proxy records is most likely the result of a multitude of physical processes. On the basis of the results presented in this thesis, the hypothesis can be put forward that the period of the interdecadal variability in observations and CGCM simulations of climate is mainly determined by the interdecadal mode described here. Although many other processes influence the variability

quantitatively, it is the physical mechanism described in chapter 3 that mainly sets the time scale of the variability. In order to test this hypothesis, the interdecadal variability will have to be followed up in the modeling hierarchy to the level of fully coupled GCMs. To this end, the internal modes of more complex models should be computed and transient-flow computations will have to be performed. The steps in the modeling hierarchy that were taken in chapters 4 and 6 of this thesis indicate that the interdecadal mode identified in chapter 3 is a robust feature of the single-hemispheric thermohaline circulation. Important steps in the modeling hierarchy that need to be investigated in future work are, for instance, the extension to a global model and the coupling to a sea-ice model and a full (dynamical) atmospheric model.

Recently, it has become possible to compute steady-state solutions and the linear stability of a global ocean model with full continental geometry and bottom topography. A model version in which the global ocean model has been coupled to an energy-balance model for the atmosphere has also been developed recently (Weijer *et al.*, 2003). With this model the robustness of the interdecadal mode in a global context can be studied. Moreover, also a systematic investigation of the internal modes of the thermohaline circulation in a global ocean model is now within reach. So far, only a linear stability analysis of the uncoupled global model under restoring boundary conditions for temperature and salinity has been performed (Weijer and Dijkstra, 2003). The steady state was found to be stable and the least damped oscillatory eigenmodes had millennial time scales. These modes are associated with advection of buoyancy anomalies around the global overturning loop. No oscillatory modes with shorter periods were found within the first 7 eigenvectors. The physical mechanism of the interdecadal mode described in this thesis does not depend on the structure of the steady-state solution near the southern boundary of the single-hemispheric basin. Therefore, it is expected that a similar interdecadal mode also exists in a global ocean model, with westward propagating temperature anomalies in the North-Atlantic Ocean and probably small amplitudes outside the North Atlantic. The fact that no interdecadal modes were found in the study of Weijer and Dijkstra (2003) is most likely due to the use of restoring boundary conditions for both temperature and salinity in their linear stability analysis. It is expected that a North-Atlantic interdecadal mode will be found in a linear stability analysis under prescribed fluxes of heat and freshwater, or in a stability analysis of the coupled model.

It is not so clear a priori if a similar interdecadal mode can exist in the North-Pacific Ocean. The steady-state zonal velocity in the North Pacific is likely to be different from that in the North Atlantic. According to the estimate given in chapter 3, this might result in a different propagation speed of the temperature (or buoyancy) anomalies, which would lead to a different oscillation period. The larger zonal extent of the Pacific basin suggests a longer time scale of the variability. Even if an internal mode like the North-Atlantic interdecadal mode exists in the North Pacific, its time scale is therefore likely to be different. In the South Atlantic and South Pacific the situation is quite different, due to the presence of the ACC, and no modes with a mechanism like the North-Atlantic interdecadal mode are expected.

Both the centennial modes in the single-hemispheric basin and the millennial modes of Weijer and Dijkstra (2003) in the global model seem to be related to the advection of buoyancy anomalies around the overturning loop. These millennial modes might therefore be the global equivalent of the centennial modes found in the single-hemispheric basin. Their much longer period in the global model could then be the result of the much longer overturning

time scale. On the other hand, the centennial and millennial modes might belong to separate classes of modes. In this case, the centennial modes are most likely related to the overturning cell in one ocean basin, which would explain why their period is much shorter than that of the millennial modes. The fact that no centennial modes were found by Weijer and Dijkstra (2003) might then point towards an increased damping of the centennial modes and would have to be investigated further.

The THCM model is currently also being extended with a thermodynamic sea-ice model, which will allow for a study of the robustness of the interdecadal mode in the presence of sea-ice. However, several numerical modeling studies have suggested that also a truly coupled internal mode of the ocean-sea-ice system exists, which has a decadal to interdecadal period (Yang and Neelin, 1993; Zhang *et al.*, 1995). A physical mechanism for such an oscillation was proposed by Yang and Neelin (1993), on the basis of numerical simulations with a zonally averaged ocean model, coupled to a thermodynamic sea-ice model. The mechanism involves a feedback between the melting (freezing) of sea-ice and weakening (strengthening) of the thermohaline circulation. The reduced (increased) northward heat transport by the overturning circulation causes in turn again growth (melting) of sea-ice. The introduction of a second internal mode with an interdecadal time scale might give rise to complex time-dependent behavior.

A mechanism for a coupled ocean-atmosphere mode with an interdecadal time scale has been suggested by Timmermann *et al.* (1998), to explain the variability with a time scale of 35 yr that was found in a study with the coupled ECHAM3/LSG model. The proposed physical mechanism is rather complex and involves coupled ocean-atmosphere interactions in the North Atlantic. The atmospheric response to an SST anomaly in the North Atlantic causes anomalous freshwater fluxes and Ekman transports, which lead to sea-surface salinity anomalies. These influence convection and the strength of the overturning circulation. The induced changes in meridional heat transport lead to SST anomalies of the opposite sign. Unfortunately, for a truly coupled ocean-atmosphere mode, an idealized limiting model configuration in which the mechanism can be understood in detail might be hard to find. However, it might be necessary to define characteristics that can be used to identify the above-mentioned mechanism in other CGCM simulations. Only in this way it can be investigated if such a coupled ocean-atmosphere mode indeed exists, and whether it interacts with other interdecadal modes.

In chapter 6, it was shown that the inclusion of wind forcing did not change the mechanism of the interdecadal variability significantly. However, on the coarse resolution used in this thesis, the wind-driven ocean circulation can only be represented very crudely. For a proper representation of the (mean) North-Atlantic wind-driven ocean circulation, the Gulf Stream should be a narrow current that separates from the North-American coast near Cape Hatteras. A correct Gulf Stream separation can be obtained in eddy-resolving GCMs, which use a typical horizontal resolution of $1/10^\circ$ or less and correspondingly low values of the horizontal eddy viscosity (Smith *et al.*, 2000; Hurlburt and Hogan, 2000; Chassignet and Garraffo, 2001). At such resolutions, the steady-state velocity field and, correspondingly, also the northward heat transport in the western boundary current region will differ considerably from those obtained in the coarse-resolution studies described in this thesis. In a study at a higher resolution, the inclusion of the wind-driven circulation might therefore have significant effects on the interdecadal mode. Moreover, also the wind-driven circulation

itself can generate low-frequency variability. In a hierarchy of intermediate-complexity models, ranging from barotropic quasi-geostrophic to baroclinic shallow-water models, a robust internal mode (the so-called gyre mode) has been identified (Nauw and Dijkstra, 2001; Simonnet and Dijkstra, 2002). In models in which stratification was represented, this gyre mode has a decadal period. A linear stability analysis of the full three-dimensional wind-driven and thermohaline ocean circulation at sufficient resolution is still out of reach. With the current GCMs it is not yet possible to perform transient-flow computations that, on one hand, can be run long enough for the detection of interdecadal (thermohaline) variability and, on the other hand, can be performed on a resolution that is high enough to capture low-frequency wind-driven variability. The true connection of the wind-driven and thermohaline ocean variability, which can only be studied in a high-resolution context, remains a challenge for future research.

In summary, it was shown in this thesis that the internal variability of the thermohaline ocean circulation can be investigated systematically by using techniques from numerical bifurcation theory. Within an idealized context of a single-hemispheric ocean basin, both interdecadal and centennial modes were shown to exist. By analyzing the patterns of the eigenmodes, transparent physical mechanisms of these oscillations could be constructed. The variability in a hierarchy of single-hemispheric basin models could be related to the interdecadal eigenmode, by using characteristics associated with the physical mechanism of the mode. It is expected that a systematic investigation of the internal modes of variability of the global thermohaline circulation can be performed in the near future. In this way, the combined use of dynamical systems theory and transient-flow computations in a hierarchy of models will provide an interpretation framework for understanding internal thermohaline variability. Such a framework will contribute to our understanding of the observed climate variability on interdecadal and longer time scales.

Appendix

A Dynamical systems theory

Many introductory textbooks about dynamical systems theory and its applications are available (Wiggins, 1990; Kuznetsov, 1995; Nayfeh and Balachandran, 1995). A short overview of some of the basic ingredients of this approach is given here. This appendix is largely based on Dijkstra *et al.* (1999).

The evolution of a scalar function $x(t)$ can in general be described by the one-dimensional dynamical system

$$\frac{dx}{dt} = f(x, \mu, t) \tag{A.1}$$

where f is a smooth (sufficiently differentiable) function and μ a parameter. The dynamical system is called autonomous if f does not depend explicitly on t. A solution of an autonomous dynamical system is a fixed point if

$$f(\bar{x}, \bar{\mu}) = 0 \tag{A.2}$$

A fixed point is also called a stationary solution or steady state.

In the analysis of the linear stability of a particular fixed point $(\bar{x}, \bar{\mu})$, infinitesimally small perturbations $\tilde{x}$ of the steady state are considered, i.e.

$$x = \bar{x} + \tilde{x} \tag{A.3}$$

Linearization of (A.1) around $\bar{x}$ by substituting (A.3) and omitting higher-order terms gives

$$\frac{dx}{dt} = \frac{\partial f(\bar{x}, \bar{\mu})}{\partial x}\tilde{x} \tag{A.4}$$

Substitution of solutions of the form $\tilde{x}(t) = e^{\sigma t}\hat{x}$ leads to an eigenvalue problem for the complex growth factor $\sigma = \sigma_r + i\sigma_i$

$$\sigma\hat{x} = \frac{\partial f(\bar{x}, \bar{\mu})}{\partial x}\hat{x} \tag{A.5}$$

A bifurcation point is a specific value of μ for which $\partial f(\bar{x}, \bar{\mu})/\partial x = 0$, so that the stationary solution is neutrally stable with respect to the perturbation $\hat{x}$. In general, a bifurcation point indicates a qualitative change in the behavior of the solution, as the stability and/or the number of solutions changes when the bifurcation point is crossed.

In the simplest type of bifurcations, the codimension-one bifurcations, only one parameter is involved. An example of such a simple bifurcation occurs in the one-dimensional autonomous dynamical system

$$\frac{dx}{dt} = f(x,\mu) = \mu x - x^3 \tag{A.6}$$

For $\mu < 0$, there is only one stationary state (or fixed point) $\bar{x} = 0$ as a solution of $f(\bar{x},\mu) = 0$. For $\mu > 0$, three fixed points exist, i.e. $\bar{x} = 0$, $\bar{x} = \sqrt{\mu}$ and $\bar{x} = -\sqrt{\mu}$, and hence the number of fixed points changes as μ crosses zero. The latter two solutions are symmetry-related, because $f(-x,\mu) = -f(x,\mu)$.

Substituting (A.3) into (A.6) and linearizing around $\bar{x}$ leads to

$$\frac{d\tilde{x}}{dt} = (\mu - 3\bar{x}^2)\tilde{x} \tag{A.7}$$

Hence, the growth of the perturbations is determined by the sign of the eigenvalues σ of the 'Jacobian' $\partial f/\partial x = \mu - 3\bar{x}^2$. For $\bar{x} = 0$, it follows that $\sigma = \mu$, indicating that $\bar{x} = 0$ is stable for $\mu < 0$ but unstable for $\mu > 0$. For both additional fixed points existing at $\mu > 0$, it follows that $\sigma = -2\mu$, showing that these are both stable.

The bifurcation diagram of the system (A.6) is shown in Fig. A.1a as a graph of $\bar{x}$ versus μ, where the branches of stable fixed points are indicated by solid lines and the unstable states by dashed lines. At $\mu = 0$, the system undergoes a qualitative change, since the number of fixed points changes from one to three. The corresponding bifurcation is called a pitchfork bifurcation. Two other bifurcation diagrams, those for the saddle node bifurcation and the transcritical bifurcation are shown in Figs. A.1b and c, respectively, and the simplest one-dimensional systems (as in equation (A.6)) that exhibit these bifurcations are provided in the figure caption.

Whereas in the previous bifurcations, the number of fixed points or the stability of a certain fixed point changes as a parameter is varied, it is also possible that the character of the solution changes from stationary to oscillatory as a single parameter is changed. An example of a simple dynamical system undergoing such a transition is the two-dimensional autonomous system given by

$$\frac{dx}{dt} = \mu x - \omega y - x(x^2 + y^2) \tag{A.8a}$$

$$\frac{dy}{dt} = \mu y + \omega x - y(x^2 + y^2) \tag{A.8b}$$

By the transformation $x = r\cos\theta$ and $y = r\sin\theta$, (A.8) transfers into

$$\frac{dr}{dt} = \mu r - r^3 \tag{A.9a}$$

$$\frac{d\theta}{dt} = \omega \tag{A.9b}$$

Comparing (A.9a) with (A.6), it can be seen that a pitchfork bifurcation occurs at $\mu = 0$ in the (r,μ)-plane. For $\mu < 0$, only one stable fixed point exists, which corresponds to a stationary solution of the original equations (A.8). However, for $\mu > 0$ the stable nontrivial

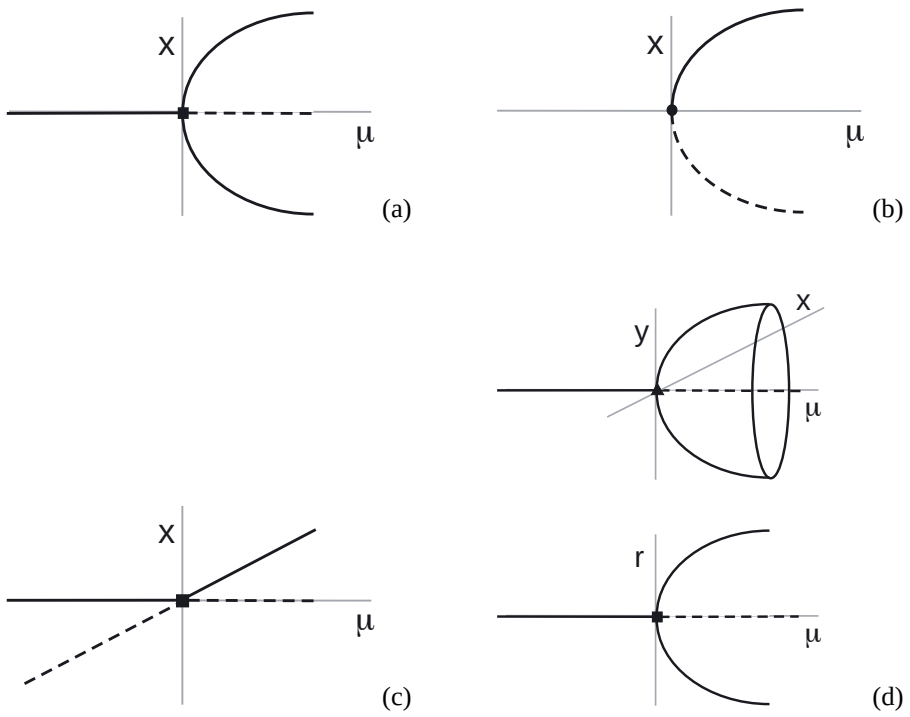

Figure A.1: *Overview of the codimension-one bifurcations and the simplest dynamical system exhibiting this bifurcation. The convention is to mark pitchfork and transcritical bifurcations with a filled square, saddle node bifurcations by a filled circle and Hopf bifurcations with a filled triangle. (a) Pitchfork bifurcation,* $dx/dt = \mu\, x - x^3$*. (b) Saddle node bifurcation,* $dx/dt = \mu - x^2$*; this bifurcation is also referred to as a limit point. (c) Transcritical bifurcation,* $dx/dt = \mu\, x - x^2$*. (d) Hopf bifurcation,* $dx/dt = \mu\, x - \omega\, y - x(x^2 + y^2)$*;* $dy/dt = \mu\, y + \omega\, x - y(x^2 + y^2)$*.*

fixed points of (A.9a) now correspond to a periodic solution of the original equations (A.8) with a frequency ω, according to (A.9b). The bifurcation diagram for this case is shown in Fig. A.1d. For $\mu < 0$ only one stable stationary state exists, but for $\mu > 0$ this state becomes unstable and a stable periodic solutions appears. At $\mu = 0$ the system undergoes a qualitative change, and the bifurcation is called a Hopf bifurcation.

The examples above illustrate that multiple steady states can occur due to a pitchfork, transcritical or saddle node bifurcation, whereas a Hopf bifurcation may introduce temporal variability in the system. More complicated bifurcations may arise when more than one parameter in the system is changed. For example, codimension-two bifurcations may arise through a intersection of paths of codimension-one bifurcations as a second parameter is varied. Complicated behavior is usually found, when parameters are increased to values far above criticality and different routes from regular to chaotic behavior have been identified (Nayfeh and Balachandran, 1995).

B Diagnostic momentum equations

Since the momentum equations are linear when inertia is neglected, approximate expressions of the perturbation geostrophic velocities can be obtained in terms of temperature (or more general buoyancy) perturbations. Consider the set of diagnostic equations for the perturbation velocities, i.e.

$$-\tilde{v}\sin\theta = -\frac{1}{\cos\theta}\frac{\partial\tilde{p}}{\partial\phi} + E_H L_u(\tilde{u},\tilde{v}) + E_V\frac{\partial^2\tilde{u}}{\partial z^2} \tag{B.1a}$$

$$\tilde{u}\sin\theta = -\frac{\partial\tilde{p}}{\partial\theta} + E_H L_v(\tilde{u},\tilde{v}) + E_V\frac{\partial^2\tilde{v}}{\partial z^2} \tag{B.1b}$$

$$\frac{\partial\tilde{p}}{\partial z} = Ra\,\tilde{T} \tag{B.1c}$$

$$0 = \frac{\partial\tilde{w}}{\partial z} + \frac{1}{\cos\theta}\left(\frac{\partial\tilde{u}}{\partial\phi} + \frac{\partial(\tilde{v}\cos\theta)}{\partial\theta}\right) \tag{B.1d}$$

where $L_u(\tilde{u},\tilde{v})$ and $L_v(\tilde{u},\tilde{v})$ are linear operators denoting horizontal friction. Integration over the total depth shows that, since wind forcing is absent, the vertically averaged pressure is constant. Hence, the pressure can be determined explicitly from the temperature fields, with the result

$$\tilde{p} = Ra\left[\int_{-1}^{z}\tilde{T}dz' - \int_{-1}^{0}(\int_{-1}^{z}\tilde{T}dz')\,dz\right] \tag{B.2}$$

Using this expression and neglecting friction, one obtains from the geostrophic relations that

$$\tilde{v} = \frac{Ra}{\sin\theta\cos\theta}\left[\int_{-1}^{z}\frac{\partial\tilde{T}}{\partial\phi}dz' - \int_{-1}^{0}(\int_{-1}^{z}\frac{\partial\tilde{T}}{\partial\phi}dz')\,dz\right] \tag{B.3a}$$

$$\tilde{u} = \frac{-Ra}{\sin\theta}\left[\int_{-1}^{z}\frac{\partial\tilde{T}}{\partial\theta}dz' - \int_{-1}^{0}(\int_{-1}^{z}\frac{\partial\tilde{T}}{\partial\theta}dz')\,dz\right] \tag{B.3b}$$

With these expressions and the definition of the perturbation meridional and zonal overturning streamfunctions, expressions can be derived for $\tilde{\Psi}_M$ and $\tilde{\Psi}_Z$ in terms of the temperature anomalies, namely

$$\tilde{\Psi}_M(\theta,z,t) = -\int_{-1}^{z}\left[\int_{\phi_W}^{\phi_E}\frac{Ra}{\sin\theta}\,f_\phi(\phi,\theta,z',t)d\phi\right]dz' \tag{B.4a}$$

$$f_\phi(\phi,\theta,z,t) = \int_{-1}^{z}\frac{\partial\tilde{T}}{\partial\phi}dz' - \int_{-1}^{0}(\int_{-1}^{z}\frac{\partial\tilde{T}}{\partial\phi}dz')\,dz \tag{B.4b}$$

and

$$\tilde{\Psi}_Z(\phi,z,t) = \int_{-1}^{z}\left[\int_{\theta_S}^{\theta_N}\frac{Ra}{\sin\theta}\,f_\theta(\phi,\theta,z',t)d\theta\right]dz' \tag{B.5a}$$

$$f_\theta(\phi,\theta,z,t) = \int_{-1}^{z}\frac{\partial\tilde{T}}{\partial\theta}dz' - \int_{-1}^{0}(\int_{-1}^{z}\frac{\partial\tilde{T}}{\partial\theta}dz')\,dz \tag{B.5b}$$

C Multi-channel Singular Spectrum Analysis

A Multi-channel Singular Spectrum Analysis (MSSA) is used to determine propagating patterns that are optimal in representing the variance (Plaut and Vautard, 1994). The aim of using MSSA is to identify coherent space-time patterns, given a regularly sampled archive of maps. MSSA is mathematically equivalent to extended EOF analysis (EEOF) (Weare and Nasstrom, 1982), but in MSSA focus is on the temporal structure of the variability, whereas in EEOF the spatial variability is emphasized.

The essentials of the technique are summarized here, and some of the terminology used in this thesis is introduced. Let a dataset $\mathbf{X}$ consist of a multi-channel time series $\mathbf{X}_{l,i}$, $l = 1, ..., L$; $i = 1, ..., N$, where l represents the channel number and i time. Index l may represent a point number on a specific grid or a principle component (PC) if the data are pre-filtered with principle component analysis (PCA). We assume that $\mathbf{X}$ has zero mean and is stationary. By making M lagged copies of $\mathbf{X}$, the state vector at time i is given by

$$(\mathbf{X}_{1,i+1}, \mathbf{X}_{1,i+2}, ..., \mathbf{X}_{1,i+M}, \mathbf{X}_{2,i+1}, ..., \mathbf{X}_{2,i+M}, ..., \mathbf{X}_{L,i+1}, ..., \mathbf{X}_{L,i+M}) \tag{C.1}$$

where M is the window length. The cross-variance matrix T for a chosen window length M has a block-Toeplitz form in which each block $\mathsf{T}_{ll'}$ is the lag covariance matrix (with maximum lag M) between channel l and l'. The $L \times M$ real eigenvalues λ_k of the symmetric matrix T are sorted in decreasing order where an eigenvector (referred to as a ST-EOF) $\mathbf{E}^k$ is associated with the k-th eigenvalue λ_k. The $\mathbf{E}^k$ are M-long time sequences of vectors, describing space-time patterns of decreasing importance as their order k increases. A space-time principle component (referred to as ST-PC) a^k can be computed by projecting $\mathbf{X}$ onto $\mathbf{E}^k$; λ_k is the variance in a^k. In this way, the MSSA expansion of the original data series is given by

$$\mathbf{X}_{l,i+j} = \sum_{k=1}^{L \times M} a_i^k \mathbf{E}_{lj}^k, j = 1, ..., M \tag{C.2}$$

PCA (Preisendorfer, 1988) and single-channel singular spectrum analysis (SSA, Vautard and Ghil (1989); Vautard *et al.* (1992)) are particular cases of MSSA: PCA can be derived from MSSA with $M = 1$, and SSA with $L = 1$.

When two consecutive eigenvalues are nearly equal and the two corresponding ST-EOFs, as well as the associated ST-PCs, are in quadrature, an oscillation is present in the data. The dominant period of this oscillation is given by that of the ST-PCs and the spatial pattern is that of the ST-EOFs (Plaut and Vautard, 1994). The sum of the right-hand side of equation (C.2), restricted to one or several terms, describes the part of the signal behaving as the corresponding ST-EOFs. The components constructed in this way are called reconstructed components (RCs). In this way, the part of the signal involved with an oscillation can be isolated. The original signal is exactly the sum of all RCs.

Bibliography

Allen, M. R. and Robertson, A. W. (1996). Distinguishing modulated oscillations from coloured noise in multivariate datasets. *Climate Dynamics*, **12**, 775 – 784.

Berger, A. (1978). Long-term variations of daily insolation and Quaternary climatic changes. *J. Atmos. Sciences*, **35**, 2362–2367.

Bradley, R. S. (1999). *Paleoclimatology: Reconstructing Climates of the Quaternary*. Academic Press, New York, U.S.A.

Broecker, W. S. (1991). The Great Ocean Conveyor. *Oceanography*, **4**, 79–89.

Broecker, W. S., Peteet, D. M., and Rind, D. (1985). Does the ocean-atmosphere system have more than one stable mode of operation? *Nature*, **315**, 21–26.

Bryan, F. (1987). Parameter sensitivity of primitive equation ocean general circulation models. *J. Phys. Oceanography*, **17**, 970–985.

Bryan, K. (1984). Accelerating the convergence to equilibrium of ocean-climate models. *J. Phys. Oceanography*, **14**, 666–673.

Bryan, K. and Cox, M. (1967). A numerical investigation of the oceanic general circulation. *Tellus*, **19**, 54–80.

Bryden, H. L., Griffiths, M. J., Lavin, A. M., Millard, R. C., Parilla, G., and Smethie, W. M. (1996). Decadal changes in water mass characteristics at 24°N in the subtropical North Atlantic Ocean. *J. Climate*, **9**, 3162–3186.

Budyko, M. I. (1969). The effect of solar radiation variations on the climate of the earth. *Tellus*, **21**, 611–619.

Cai, W., Greatbatch, R. J., and Zhang, S. (1998). Interdecadal variability in an ocean model driven by a small, zonal redistribution of the surface buoyancy flux. *J. Phys. Oceanography*, **25**, 1998–2010.

Capotondi, A. (2000). Oceanic wave dynamics and interdecadal variability in a climate system model. *J. Geophysical Res.*, **105**, 1017–1036.

Chassignet, E. P. and Garraffo, Z. D. (2001). Viscosity parameterization and the Gulf Stream separation. In P. Muller and D. Henderson, editors, *From Stirring to mixing in a stratified ocean*, Proceedings 'Aha Huliko'a Hawaiian winter workshop. Univ. of Hawaii, pages 37–41.

Chen, F. and Ghil, M. (1995). Interdecadal variability of the thermohaline circulation and high-latitude surface fluxes. *J. Phys. Oceanography*, **22**, 161–167.

Chen, F. and Ghil, M. (1996). Interdecadal variability in a hybrid coupled ocean-atmosphere model. *J. Phys. Oceanography*, **26**, 1561–1578.

Colin de Verdière, A. (1988). Buoyancy driven planetary flows. *J. Mar. Res.*, **46**, 215–265.

Colin de Verdière, A. and Huck, T. (1999). Baroclinic instability: an oceanic wavemaker for interdecadal variability. *J. Phys. Oceanography*, **29**, 893–910.

Cox, M. (1984). A primitive equation, three dimensional model of the ocean. Technical Report 1, GFDL Ocean group.

Da Silva, A. M., Young, C. C., and Levitus, S. (1994). Atlas of surface marine data 1994, volume 1: Algorithms and procedures. Technical Report 6, NOAA.

Delworth, T. L. and Greatbatch, R. J. (2000). Multidecadal thermohaline circulation variability driven by atmospheric surface flux forcing. *J. Climate*, **13**, 1481–1495.

Delworth, T. L. and Mann, M. E. (2000). Observed and simulated multidecadal variability in the Northern Hemisphere. *Climate Dynamics*, **16**, 661–676.

Delworth, T. L., Manabe, S., and Stouffer, R. J. (1993). Interdecadal variations of the thermohaline circulation in a coupled ocean-atmosphere model. *J. Climate*, **6**, 1993–2011.

Deser, C. and Blackmon, M. L. (1993). Surface climate variations over the North Atlantic Ocean during winter: 1900-1989. *J. Climate*, **6**, 1743–1753.

Dickson, R. and Brown, J. (1994). The production of North Atlantic Deep Water. *J. Geophysical Res.*, **99**, 12,319–12,341.

Dijkstra, H. A. (2000). *Nonlinear Physical Oceanography*. Kluwer Academic Publishers, Dordrecht, The Netherlands. 480 pp.

Dijkstra, H. A. and Molemaker, M. J. (1997). Symmetry breaking and overturning oscillations in thermohaline-driven flows. *J. Fluid Mech.*, **331**, 195–232.

Dijkstra, H. A., Schmeits, M. J., and Katsman, C. A. (1999). Internal variability of the North-Atlantic wind-driven ocean circulation. *Surveys in Geophysics*, **20**, 463–503.

Dijkstra, H. A., Öksüzŏglu, H., Wubs, F. W., and Botta, E. F. F. (2001). A fully implicit model of the three-dimensional thermohaline ocean circulation. *Journal of Computational Physics*, **173**, 685–715.

Fanning, A. F. and Weaver, A. J. (1996). An atmospheric energy-moisture balance model: climatology, interpentadal climate change, and coupling to an ocean general circulation model. *J. Geophysical Res.*, **101**, 15,111–15,128.

Fisher, D. A. (1982). Carbon-14 production compared to oxygen isotope records from Cape Century, Greenland and Devon Island, Canada. *Clim. Change*, **4**, 419–426.

Ghil, M. (2002). Natural climate variability. In T. E. Munn, M. MacCracken, and J. Perry, editors, *Encyclopedia of global environmental change*, volume 1. J. Wiley and Sons.

Ghil, M. and Vautard, R. (1991). Interdecadal oscillations and the warming trend in global temperature time series. *Nature*, **350**, 324–327.

Golub, G. H. and Van Loan, C. F. (1983). *Matrix Computations*. The Johns Hopkins University Press, Baltimore, MD, U.S.A.

Gordon, A. L. (1986). Interocean exchange of thermocline water. *J. Geophysical Res.*, **91**, 5037–5046.

Greatbatch, R. J. and Peterson, K. A. (1996). Interdecadal variability and oceanic thermohaline adjustment. *J. Geophysical Res.*, **101**, 20,467–20,482.

Greatbatch, R. J. and Zhang, S. (1995). An interdecadal oscillation in an idealized ocean basin forced by constant heat flux. *J. Climate*, **8**, 82–91.

Griffies, S. M. and Tziperman, E. (1995). A linear thermohaline oscillator driven by stochastic atmospheric forcing. *J. Climate*, **8**, 2440–2453.

Grove, J. M. (1988). *The Little Ice Age*. Methuen, London, U.K.

Guckenheimer, J. and Holmes, P. (1983). *Nonlinear oscillations, Dynamical systems and Bifurcations of Vector Fields*. Springer Verlag, Berlin-Heidelberg, Germany.

Haney, R. L. (1971). Surface thermal boundary conditions for ocean circulation models. *J. Phys. Oceanography*, **4**, 241–248.

Hasselmann, K. (1976). Stochastic climate models. I: Theory. *Tellus*, **28**, 473–485.

Hibler, W. D. and Johnson, S. J. (1979). The 20-yr cycle in Greenland ice core records. *Nature*, **280**, 481–483.

Huang, R. X. (1998). Mixing and available potential energy in a boussinesq ocean. *J. Phys. Oceanography*, **28**, 669–678.

Huck, T. and Vallis, G. K. (2001). Linear stability analysis of the three-dimensional thermally-driven ocean circulation: application to interdecadal oscillations. *Tellus*, **53A**, 526–545.

Huck, T., Colin de Verdière, A., and Weaver, A. J. (1999). Interdecadal variability of the thermohaline circulation in box-ocean models forced by fixed surface fluxes. *J. Phys. Oceanography*, **29**, 865–892.

Huck, T., Vallis, G. K., and Colin de Verdière, A. (2001). On the robustness of interdecadal modes of the thermohaline circulation. *J. Climate*, **14**, 940–963.

Hurlburt, H. E. and Hogan, P. J. (2000). Impact of $1/8^\circ$ to $1/64^\circ$ resolution on Gulf Stream model-data comparisons in basin-scale subtropical Atlantic Ocean models. *Dyn. Atmos. Oceans*, **32**, 283–329.

Imbrie, J. and Imbrie, J. Z. (1980). Modeling the climatic response to orbital variations. *Science*, **207**, 943–953.

IPCC (2001). *Climate change 2001: The scientific basis. Contribution of working group I to the third assessment report of the Intergovernmental Panel on Climate Change [Houghton, J. T. and Ding, Y. and Griggs, D. J. and Noguer, M. and van der Linden, P. J. and Dai, X. and Maskell, K. and Johnson, C. A. (eds.)]*. Cambridge University Press, Cambridge, United Kingdom and New York, NY, U.S.A.

Johns, W. E., Shay, T. J., Bane, J. M., and Watts, D. R. (1995). Gulf Stream structure, transport and recirculation near 68°W. *J. Geophysical Res.*, **100**, 817–838.

Joyce, T. M. and Robbins, P. (1996). The long-term hydrographic record at Bermuda. *J. Climate*, **9**, 3122–3131.

Kaplan, A., Cane, M. A., Kushnir, Y., Clement, A. C., and Blumenthal, M. B. (1998). Analyses of global sea surface temperature 1856-1991. *J. Geophysical Res.*, **103**, 18567–18589.

Keller, H. B. (1977). Numerical solution of bifurcation and nonlinear eigenvalue problems. In P. H. Rabinowitz, editor, *Applications of Bifurcation Theory*. Academic Press, New York, U.S.A.

Kushnir, Y. (1994). Interdecadal variations in North Atlantic sea surface temperature and associated atmospheric conditions. *J. Phys. Oceanography*, **7**, 141–157.

Kuznetsov, Y. A. (1995). *Elements of Applied Bifurcation Theory*. Springer Verlag, New York, U.S.A.

Lean, J. and Rind, D. (1998). Climate forcing by changing solar radiation. *J. Climate*, **11**, 3069–3094.

Levitus, S., Antonov, J. I., Boyer, T. P., and Stephens, C. (2000). Warming of the world ocean. *Science*, **287**, 2225–2229.

Mann, M. E., Park, J., and Bradley, R. S. (1995). Global interdecadal and century-scale oscillations during the past five centuries. *Nature*, **378**, 266–270.

McDermott, F., Mattey, D. P., and Hawkesworth, C. (2001). Centennial-scale Holocene climate variability revealed by a high-resolution δ^{18}O record from SW Ireland. *Science*, **294**, 1328–1331.

Mikolajewicz, U. and Maier-Reimer, E. (1990). Internal secular variability in an ocean general circulation model. *Climate Dynamics*, **4**, 145–156.

Moron, V., Vautard, R., and Ghil, M. (1998). Trends, interdecadal and interannual oscillations in global sea-surface temperature. *Climate Dynamics*, **14**, 545–569.

Mysak, L. A. and Stocker, T. F. (1993). Century-scale variability in a randomly forced, two-dimensional thermohaline ocean circulation model. *Climate Dynamics*, **8**, 103–116.

National Research Council (1995). *Natural Climate Variability on Decade-to-Century Time Scales [Martinson, D. G. and Bryan, K. and Ghil, M. and Hall, M. M. and Karl, T. R. and Sarachik, E. S. and Sorooshian, S. and Talley, L. D. (eds)]*. National Academy Press, Washington, DC, U.S.A.

Nauw, J. J. and Dijkstra, H. A. (2001). The origin of low-frequency variability of double-gyre wind-driven flows. *J. Mar. Res.*, **59**, 567–597.

Nayfeh, A. H. and Balachandran, B. (1995). *Applied Nonlinear Dynamics*. John Wiley, New York, U.S.A.

North, G. R. (1975a). Analytical solution to a simple climate model with diffusive heat transport. *J. Atmos. Sciences*, **32**, 1301–1307.

North, G. R. (1975b). Theory of energy balance climate models. *J. Atmos. Sciences*, **32**, 2033–2043.

Oberhuber, J. M. (1988). *The Budget of Heat, Buoyancy and Turbulent Kinetic Energy at the Surface of the Global Ocean*. Max Planck Institute für Meteorologie Hamburg report nr. 15, Hamburg, Germany.

Osborn, T. (1997). Thermohaline oscillations in the LSG OGCM: propagating anomalies and sensitivity to parameterizations. *J. Phys. Oceanography*, **25**, 2046–2064.

Pacanowski, R. C. and Griffies, S. M. (1998). Mom 3.0 manual. Available from http://www.gfdl.gov/∼smg/MOM/web/guide_parent/guide_parent.html.

Pedlosky, J. (1987). *Geophysical Fluid Dynamics*. Springer-Verlag, New York, U.S.A.

Peixoto, J. P. and Oort, A. H. (1992). *Physics of Climate*. AIP Press.

Pierce, D. W., Barnett, T. P., and Mikolajewicz, U. (1995). Competing roles of heat and freshwater flux in forcing thermohaline oscillations. *J. Phys. Oceanography*, **25**, 2046–2064.

Plaut, G. and Vautard, R. (1994). Spells of low-frequency oscillations and weather regimes in the northern hemisphere. *J. Atmos. Sciences*, **51**, 210–236.

Plaut, G., Ghil, M., and Vautard, R. (1995). Interannual and interdecadal variability in 335 years of Central England Temperature. *Science*, **268**, 710–713.

Preisendorfer, R. W. (1988). *Principal Component Analysis in Meteorology and Oceanography*. Elsevier Publishers, Amsterdam, The Netherlands.

Rivin, I. and Tziperman, E. (1997). Linear versus self-sustained interdecadal thermohaline variability in a coupled box model. *J. Phys. Oceanography*, **27**, 1216–1232.

Roemmich, D. H. and Wunsch, C. (1984). Apparent changes in the climatic state of the deep North Atlantic Ocean. *Nature*, **307**, 447–450.

Samelson, R. M. and Vallis, G. K. (1997). Large-scale circulation with small diapycnal diffusion: the two-thermocline limit. *J. Mar. Res.*, **55**, 223–275.

Sarachik, E. S., Winton, M., and Yin, F. L. (1996). Mechanisms for decadal-to-centennial climate variability. In D. L. T. Anderson and J. Willebrand, editors, *Decadal climate variability, Dynamics and predictability*, pages 157–210. Springer.

Schlesinger, M. E. and Ramankutty, N. (1994). An oscillation in the global climate system of period 65-70 years. *Nature*, **367**, 723–726.

Schlösser, P., Bonisch, G., Rhein, M., and Bayer, R. (1991). Reduction of deep water formation in the Greenland Sea during the 1980s: evidence from tracer data. *Science*, **251**, 1054–1056.

Schmitz, W. J. (1995). On the interbasin-scale thermohaline circulation. *Rev. Geophys.*, **33**, 151–173.

Simonnet, E. and Dijkstra, H. A. (2002). Spontaneous generation of low-frequency modes of variability in the wind-driven ocean circulation. *J. Phys. Oceanography*, **32**, 1747–1762.

Sirkes, Z. and Tziperman, E. (2001). Identifying a damped oscillatory thermohaline mode in a general circulation model using an adjoint model. *J. Phys. Oceanography*, **31**, 2297–2306.

Sleijpen, G. L. G. and Van der Vorst, H. A. (1996). A Jacobi-Davidson iteration method for linear eigenvalue problems. *SIAM J. Matrix Anal. Appl.*, **17**, 410–425.

Smith, R. D., Maltrud, M. E., Bryan, F. O., and Hecht, M. W. (2000). Numerical simulations of the North Atlantic Ocean at $1/10^\circ$. *J. Phys. Oceanography*, **30**, 1532–1561.

Stocker, T. F. and Mysak, L. A. (1992). Climatic fluctuations on the century time scale: a review of high-resolution proxy data and possible mechanisms. *Clim. Change*, **20**, 227–250.

Stommel, H. (1961). Thermohaline convection with two stable regimes of flow. *Tellus*, **2**, 244–230.

Stuiver, M. (1980). Solar variability and climatic change during the current millennium. *Nature*, **286**, 868–871.

Sutton, R. T. and Allen, M. R. (1997). Decadal predictability of North Atlantic sea surface temperature and climate. *Nature*, **388**, 563–567.

Sy, A., Rhein, M., Lazier, J. N. R., Koltermann, K. P., Meincke, J., Putzka, A., and Bersch, M. (1997). Surprisingly rapid spreading of newly formed intermediate waters across the North Atlantic Ocean. *Nature*, **388**, 563–567.

Timmermann, A., Latif, M., Voss, R., and Grötzner, A. (1998). Northern hemisphere interdecadal variability; a coupled air-sea mode. *J. Climate*, **11**, 1906–1931.

Tourre, Y., Rajagopalan, B., and Kushnir, Y. (1999). Dominant patterns of climate variability in the Atlantic over the last 136 years. *J. Climate*, **12**, 2285–2299.

Tziperman, E. (1997). Inherently unstable climate behaviour due to weak thermohaline ocean circulation. *Nature*, **386**, 592–595.

Tziperman, E. (2000). Proximity of the present-day thermohaline circulation to an instability threshold. *J. Phys. Oceanography*, **30**, 90–104.

Vallis, G. K. (2000). Large-scale circulation and production of stratification: effects of wind, geometry, and diffusion. *J. Phys. Oceanography*, **30**, 933–954.

Van Dorsselaer, J. J. (1997). Computing eigenvalues occurring in continuation methods with the Jacobi-Davidson QZ method. *J. Comp. Physics*, **138**, 714–733.

Vautard, R. and Ghil, M. (1989). Singular spectrum analysis in nonlinear dynamics with applications to paleoclimatic time series. *Physica D*, **35**, 395–424.

Vautard, R., Yiou, P., and Ghil, M. (1992). Singular spectrum analysis: A toolkit for short, noisy chaotic signals. *Physica D*, **58**, 95–126.

Vellinga, M. (1998). Multiple equilibria of the thermohaline circulation as a side effect of convective adjustment. *J. Phys. Oceanography*, **28**, 305–319.

Weare, B. C. and Nasstrom, J. N. (1982). Examples of extended empirical orthogonal function analyses. *Monthly Weather Review*, **110**, 481–485.

Weaver, A. J. and Sarachik, E. S. (1991a). Evidence for decadal variability in an ocean general circulation model: an advective mechanism. *Atmosphere-Ocean*, **29**, 197–231.

Weaver, A. J. and Sarachik, E. S. (1991b). The role of mixed boundary conditions in numerical models of the ocean's climate. *J. Phys. Oceanography*, **21**, 1470–1493.

Weaver, A. J. and Valcke, S. (1998). On the variability of the thermohaline circulation in the GFDL coupled model. *J. Climate*, **11**, 759–767.

Weaver, A. J., Marotzke, J., Cummings, P. F., and Sarachik, E. S. (1993). Stability and variability of the thermohaline circulation. *J. Phys. Oceanography*, **23**, 39–60.

Weaver, A. J., Aura, S., and Myers, P. G. (1994). Interdecadal variability in an idealized model of the North Atlantic. *J. Geophysical Res.*, **99**, 12,423 – 12,441.

Weijer, W. and Dijkstra, H. A. (2001). A bifurcation study of the three-dimensional thermohaline ocean circulation: the double hemispheric case. *J. Mar. Res.*, **59**, 599–631.

Weijer, W. and Dijkstra, H. A. (2003). Multiple oscillatory modes of the global ocean circulation. *Submitted to J. Phys. Oceanography*.

Weijer, W., Dijkstra, H. A., Öksüzŏglu, H., Wubs, F. W., and de Niet, A. C. (2003). A fully-implicit model of the global ocean circulation. *Submitted to J. Comp. Phys.*

Welander, P. (1971). The thermocline problem. *Phil. Trans. Roy. Soc. London*, **A270**, 415–421.

Welander, P. (1982). A simple heat-salt oscillator. *Dyn. Atmos. Oceans*, **6**, 233–242.

Welander, P. (1986). Thermohaline effects in the ocean circulation and related simple models. In J. Willebrand and D. L. T. Anderson, editors, *Large scale transport processes in Oceans and Atmosphere*, pages 163–200. D. Reidel.

Wiggins, S. (1990). *Introduction to Applied Nonlinear Dynamical Systems and Chaos*. Springer-Verlag, Heidelberg-Berlin, Germany.

Winton, M. (1996). The role of horizontal boundaries in parameter sensitivity and decadal-scale variability of coarse-resolution ocean general circulation models. *J. Phys. Oceanography*, **26**, 289–304.

Winton, M. (1997). The damping effect of bottom topography on internal decadal-scale oscillations of the thermohaline circulation. *J. Phys. Oceanography*, **27**, 203–208.

Winton, M. and Sarachik, E. S. (1993). Thermohaline oscillations induced by strong steady salinity forcing of ocean general circulation models. *J. Phys. Oceanography*, **23**, 1389–1410.

Wright, D. G. and Stocker, T. F. (1992). Sensitivities of a a zonally averaged global ocean circulation model. *J. Geophysical Res.*, **97**, 12707–12730.

Yang, J. and Neelin, J. D. (1993). Sea-ice interaction with the thermohaline circulation. *Geophys. Res. Letters*, **20**, 217–220.

Yin, F. L. (1995). A mechanistic model of ocean interdecadal thermohaline oscillations. *J. Phys. Oceanography*, **25**, 3239–3246.

Yin, F. L. and Sarachik, E. S. (1994). An efficient convective adjustment scheme for ocean general circulation models. *J. Phys. Oceanography*, **24**, 1425–1430.

Yin, F. L. and Sarachik, E. S. (1995). Interdecadal thermohaline oscillations in a sector ocean general circulation model: advective and convective processes. *J. Phys. Oceanography*, **25**, 2465–2484.

Zhang, S., Lin, C. A., and Greatbatch, R. J. (1995). A decadal oscillation due to the coupling between an ocean circulation model and a thermodynamic sea-ice model. *J. Mar. Res.*, **53**, 79–106.

Samenvatting

Klimaatvariabiliteit en de oceaan

Ons dagelijks leven wordt in grote mate beïnvloed door het klimaat, hoewel we ons daar vaak niet van bewust zijn. De wereldwijde landbouwproductie en de hoogte van de zeespiegel zijn bijvoorbeeld sterk afhankelijk van het klimaat. Veranderingen in het klimaat zullen daarom naast ecologische ook grote economische en sociale gevolgen hebben. Zowel de wetenschappelijke als de politieke belangstelling voor het klimaat is de laatste tijd sterk toegenomen door de bezorgdheid over klimaatveranderingen, die door de mens veroorzaakt worden.

Toekomstige klimaatveranderingen zullen het gevolg zijn van het gecombineerde effect van door de mens veroorzaakte veranderingen en natuurlijke schommelingen in het klimaat (natuurlijke klimaatvariabiliteit). Een voorbeeld van een natuurlijke schommeling in het klimaat is het El Niño verschijnsel, waarbij iedere 3 tot 4 jaar het water in de Stille Oceaan nabij de evenaar ongewoon warm wordt, terwijl tegelijkertijd het weer op talloze plaatsen drastisch verandert. Om klimaatveranderingen in de komende eeuw nauwkeurig te kunnen voorspellen, is het van groot belang goed te begrijpen waardoor de natuurlijke schommelingen in het klimaat met een tijdsduur van enkele decennia of langer worden veroorzaakt.

Van grote invloed op het klimaat zijn de oceanen, onder andere doordat ze grote hoeveelheden warmte opnemen en deze via de stromingen naar andere gebieden transporteren. Zo komt een aanzienlijk deel van al het warmtetransport van de evenaar naar de polen voor rekening van de oceanen. Kenmerkend is dat veranderingen in het grootschalige (mondiale) stromingspatroon in de oceaan plaatsvinden op tijdschalen van enkele maanden tot duizenden jaren. Dit soort veranderingen speelt waarschijnlijk dan ook een grote rol in klimaatvariabiliteit over decennia en langer.

De grootschalige oceaancirculatie

De grootschalige oceaancirculatie wordt veroorzaakt door de wind aan het zeeoppervlak en door verschillen in de zwaarte van het zeewater. Deze zogenaamde dichtheidsverschillen zijn het gevolg van verschillen in temperatuur en zoutgehalte van het zeewater: hoe kouder en hoe zouter het water, des te zwaarder het is. De verschillen in temperatuur ontstaan doordat de oceaan nabij de evenaar veel sterker verwarmd wordt dan op hoge breedtegraden. Verschillen in zoutgehalte ontstaan vooral doordat de neerslag (die zoet water aan de oceaan toevoegt) en de verdamping (die het achterblijvende water zouter maakt) niet overal gelijk zijn. Het stromingspatroon dat wordt veroorzaakt door de verschillen in temperatuur en zoutgehalte

wordt de *thermohaliene circulatie* genoemd.

Een schets van de oceaanstromingen aan het oppervlak, die het gevolg zijn van zowel de windgedreven als de thermohaliene circulatie, is te zien in Fig. 1.3 op pagina 6. Kenmerkend voor de circulatie aan het oppervlak zijn de grote wervelstructuren over de hele breedte van de oceaan, die zowel op het noordelijk als het zuidelijk halfrond te vinden zijn. In de Noord-Atlantische Oceaan zijn er twee van dit soort wervelstructuren, waarbij de zuidelijke de grootste is, met daartussen een sterke oostwaartse stroming, de Golfstroom. Deze stroming transporteert warm water richting noord-west Europa en zorgt daarmee voor een relatief mild klimaat in onze streken.

Het beeld dat in Fig. 1.3 geschetst wordt is echter niet compleet, want ook het water in de diepzee is in beweging. De totale oceaancirculatie wordt schematisch weergegeven in Fig. 1.6 op pagina 8. In deze figuur, waarin de wereldkaart zodanig is opgedeeld dat de oceanen zo min mogelijk vervormd zijn, geven de donkere pijlen schematisch de gemiddelde oppervlaktestroming weer en de lichtere pijlen de gemiddelde stroming in de diepzee. In de Noord-Atlantische Oceaan wordt het warme en zoute oppervlaktewater dat via de Golfstroom naar het noorden stroomt, sterk afgekoeld. Als gevolg hiervan wordt het water erg zwaar. Het vermengt zich met dieper gelegen water en zinkt langzaam naar de diepzee. Daar stroomt het vervolgens traag naar het zuiden, om uiteindelijk de Indische Oceaan en de Stille Oceaan te bereiken. Het water warmt heel langzaam op en komt dan weer omhoog, waarna het via de oppervlaktecirculatie terugstroomt naar de Noord-Atlantische Oceaan. Het water is vele honderden tot duizenden jaren onderweg, voordat het weer bij dezelfde plaats terugkomt.

Deze globale circulatie wordt wel beschreven als een soort oceanische transportband, waarmee warmte en zout over grote afstanden worden vervoerd. Hoewel de oppervlaktestromingen in Fig. 1.6 ook door de wind worden aangedreven, kan Fig. 1.6 min of meer gezien worden als een schematische weergave van de thermohaliene circulatie. Deze wordt ook wel *omwentelingscirculatie* genoemd, omdat het water als het ware omgewenteld wordt in de oceaan.

Interne variabiliteit van de thermohaliene circulatie

De stromingen die te zien zijn in Fig. 1.6, zijn gemiddelde stromingen. De werkelijke stromingen veranderen voortdurend een beetje van sterkte en richting. Dit kan het gevolg zijn van veranderingen in de aandrijvende factoren. De oceaancirculatie kan echter ook spontaan variëren, dus zonder dat er veranderingen optreden in de wind en de uitwisseling van warmte en zoet water tussen oceaan en atmosfeer. Een dergelijke (regelmatige) fluctuatie noemt men een *interne oscillatie*.

In het dagelijks leven zijn veel voorbeelden van interne oscillaties te vinden. Een schommel waar kort een duwtje tegenaan gegeven wordt, zal daarna een tijd uit zichzelf heen en weer blijven schommelen zonder dat iemand hem heen en weer hoeft te bewegen. Een schommel is een voorbeeld van een gedempte oscillatie, dat wil zeggen dat de beweging na verloop van tijd zal ‘uitdempen’ en de schommel weer stil komt te hangen. Een ander voorbeeld is een vlag, die bij een matige bries strak staat, maar die plotseling begint te wapperen wanneer het wat harder gaat waaien. Bij een bepaalde windsterkte treedt ook hier een interne oscillatie op. Dit ook na te bootsen door langs een dun papiertje te blazen. Bij zacht blazen beweegt het papiertje niet, maar door steeds harder te blazen, zal het papiertje ineens gaan flapperen.

Een belangrijk kenmerk van een oscillatie is de periode, de tijdsduur van één slingering. Interne oscillaties van de windgedreven circulatie hebben periodes van maanden tot jaren. Interne oscillaties van de thermohaliene circulatie, waarbij ook de trage stromingen in de diepzee zich moeten aanpassen, hebben periodes van tientallen tot honderden of zelfs duizenden jaren. De variaties die optreden als gevolg van één of meerdere interne oscillaties, noemt men *interne variabiliteit*. Voor het begrijpen van klimaatvariabiliteit op tijdschalen van tientallen jaren en langer is onderzoek naar interne variabiliteit van de thermohaliene circulatie van groot belang.

Metingen en simulaties

Metingen op diverse plaatsen in de oceaan van onder andere temperatuur en stroomsnelheid wijzen erop, dat de grootschalige oceaancirculatie inderdaad varieert op tijdschalen van zo'n 30 tot 50 jaar (variaties zoals deze, met een tijdsduur van enkele decennia, worden *interdecadale* variabiliteit genoemd). Grote gebieden in de Noord-Atlantische Oceaan worden gedurende zo'n periode afwisselend warmer en kouder dan normaal. Metingen zijn echter schaars en en geven onvoldoende inzicht om de oorzaken van de variabiliteit te begrijpen.

Bij het bestuderen van de oceaancirculatie maken oceanografen daarom veelvuldig gebruik van computermodellen waarmee de oceaancirculatie gesimuleerd wordt. Met uitgebreide en complexe computermodellen kunnen zowel de gemiddelde stromingspatronen als de variabiliteit redelijk goed gesimuleerd worden. Het probleem is echter, dat deze modellen zo ingewikkeld zijn, dat het zeer moeilijk is om de gesimuleerde variabiliteit te begrijpen. We komen niet veel verder dan de constatering dat de gesimuleerde variabiliteit samenhangt met een wisselwerking tussen de dichtheid (en dus de temperatuur en het zoutgehalte) van het zeewater en de stromingen. Een dergelijke wisselwerking betekent dat door een verandering in dichtheid de thermohaliene circulatie verandert. Hierdoor zal vervolgens het transport van warmte en zout veranderen, wat op zijn beurt weer zorgt voor dichtheidsveranderingen, enzovoort. Om op den duur uitspraken te kunnen doen over de huidige of de toekomstige variabiliteit van de thermohaliene circulatie, is een meer gedetailleerde verklaring van deze verschijnselen nodig, waarmee beter begrepen kan worden waardoor de tijdschaal en structuur van de variabiliteit worden bepaald.

Daarom worden ook vaak simulaties gedaan met modellen waarin de oceaan op een vereenvoudigde manier is weergegeven en waarin de variabiliteit daardoor beter te begrijpen is. Een veel gebruikte vereenvoudiging bij het bestuderen van interne variabiliteit van de thermohaliene circulatie is, dat de wind aan het zeeoppervlak buiten beschouwing wordt gelaten. Dit kan, omdat variaties in de windgedreven circulatie op veel kortere tijdschalen plaatsvinden. Ook worden vaak alleen de stromingen berekend in de Noord-Atlantische Oceaan, omdat dit vanwege het zinken van zwaarder water een belangrijk gebied voor de thermohaliene circulatie is. Bovendien wordt de oceaan in zo'n vereenvoudigd model vaak begrensd door rechte randen. Er mag verwacht worden dat de precieze vorm van de continenten het kwalitatieve gedrag van grootschalige stromingen niet erg beïnvloedt. Op grond van simulaties met dit soort geïdealiseerde modellen zijn diverse verklaringen geopperd voor de interne variabiliteit van de thermohaliene circulatie. Deze modellen hebben echter ook een nadeel. Juist door de vereenvoudigde weergave van de oceaan in zulk soort modellen, is het verband tussen de resultaten van deze modelsimulaties en de gemeten variabiliteit vaak zeer onduidelijk.

Dit proefschrift

In dit proefschrift wordt de interne variabiliteit van de thermohaliene circulatie in de Noord-Atlantische Oceaan op een systematische manier bestudeerd. Hiertoe zijn berekeningen en simulaties met twee computermodellen gedaan. Deze modellen verschillen van elkaar in de methode die gebruikt wordt om de stromingen uit te rekenen. De gebruikelijke methode is om voor een bepaald tijdstip de stromingen, temperaturen en zoutgehaltes uit te rekenen en vervolgens deze berekeningen in een zogenaamde *numerieke tijdsintegratie* voor zeer veel opeenvolgende tijdstippen te herhalen. Dit wordt gedaan voor een vaste keuze van parameters (gegevens die nodig zijn voor de berekening, zoals de sterkte van de zwaartekracht en de sterkte van menging van koud en warm water). Van sommige parameters, zoals de sterkte van de zwaartekracht, is de waarde zeer precies bekend, maar van andere, bijvoorbeeld de sterkte van de menging, is de waarde erg onzeker. De stromingen worden daarom vaak uitgerekend voor diverse parameterwaardes. Daarvoor moeten wel elke keer alle berekeningen van de numerieke tijdsintegratie worden herhaald.

Voor het onderzoek beschreven in dit proefschrift is echter voornamelijk gebruik gemaakt van een model, waarin een geheel andere methode wordt toegepast. Deze methode is gebaseerd op wiskundige technieken uit de zogenaamde *dynamische systeemtheorie*. In het onderzoek naar de variabiliteit van de thermohaliene circulatie is deze methode vrijwel nieuw. In deze aanpak worden eerst de stationaire (tijdsonafhankelijke) stromingen, temperaturen en zoutgehaltes berekend voor een bepaalde keuze van parameters. Uit deze berekening kan vervolgens vrij eenvoudig het stationaire stromingspatroon voor een andere keuze van parameters bepaald worden. Op deze manier wordt dus het tijdsonafhankelijke gedrag voor een groot aantal parameterwaardes berekend.

Hierna wordt berekend of zeer kleine verstoringen van het stationaire stromingspatroon zullen uitdempen, of dat deze juist groter zullen worden. Voor het onderzoek in dit proefschrift zijn met name fluctuerende verstoringen van belang, omdat die kunnen uitgroeien tot een interne oscillatie van het stromingspatroon. In de dynamische systeemaanpak wordt echter niet het tijdsafhankelijke proces uitgerekend waarin de verstoringen uitgroeien tot een interne oscillatie van het stromingspatroon. Er wordt alleen bepaald hoe deze specifieke verstoringen (die *interne modi* worden genoemd) eruit zien, of ze zullen groeien dan wel uitdempen en wat —in het geval van een oscillerende verstoring— hun periode is.

De dynamische systeemaanpak heeft twee belangrijke voordelen. Ten eerste kan hiermee interne variabiliteit op een systematische manier onderzocht worden. Niet alleen de stationaire stroming, maar ook de interne modi kunnen namelijk relatief eenvoudig uitgerekend worden voor verschillende parameterwaardes. Voor sommige parameterwaardes zullen de interne modi groeien, bij andere waardes zijn ze gedempt. Dit wordt duidelijk in het voorbeeld van de vlag: als het niet te hard waait, dempen verstoringen snel uit en staat de vlag strak, maar bij harde wind gaan kleine fluctuerende verstoringen groeien en gaat de vlag wapperen. Kwalitatieve veranderingen in het gedrag van de stromingen (wel of geen wapperende vlag) kunnen zo goed in kaart gebracht worden. Ten tweede kan interne variabiliteit met de dynamische systeemaanpak beter begrepen worden. Naar verwachting zullen de snelst groeiende interne modi een dominante bijdrage leveren aan de interne variabiliteit. Met behulp van de dynamische systeemanalyse kunnen deze interne modi in detail bestudeerd worden. Om het volledige, tijdsafhankelijke gedrag van de stromingen te begrijpen, kunnen vervolgens nume-

rieke tijdsintegraties worden gedaan. In dit proefschrift is daarom een combinatie gebruikt van dynamische systeemanalyse en numerieke tijdsintegraties.

In de beide modellen die in dit proefschrift zijn toegepast, is als uitgangssituatie een sterk vereenvoudigd model van de Noord-Atlantische Oceaan gebruikt. Hierin wordt de oceaan begrensd door rechte randen, is de bodem vlak en kunnen alleen temperatuurverschillen stroming veroorzaken. Eerst worden de belangrijkste interne modi in deze geïdealiseerde situatie bestudeerd. Vervolgens wordt bekeken welke kwalitatieve veranderingen optreden in de interne modi, wanneer elementen zoals het effect van neerslag en verdamping worden toegevoegd. Daarna wordt de interne variabiliteit, die met behulp van numerieke tijdsintegraties voor de uitgangssituatie wordt gevonden, gerelateerd aan één van de eerder gevonden interne modi. Tenslotte wordt een verband gelegd tussen deze interne variabiliteit en de variabiliteit in een meer realistische situatie. In hoofdstuk 2 worden de gebruikte computermodellen en methodes behandeld. In de hoofdstukken 3 tot en met 6 worden de berekeningen en simulaties beschreven, die met deze twee modellen gedaan zijn.

Resultaten

In hoofdstuk 3 wordt aangetoond dat, in de vereenvoudigde modelcontext die als uitgangssituatie is gebruikt, een interne mode bestaat met een periode van ongeveer 65 jaar. Deze interdecadale mode wordt gekenmerkt door grote gebieden in het noordelijke deel van het oceaanbekken, waar de temperatuur afwisselend hoger en lager is dan bij de stationaire stroming. Gedurende een oscillatieperiode bewegen deze gebieden in westelijke richting, waarbij in het oosten nieuwe gebieden van abnormaal warm of koud water ontstaan. Tegelijkertijd wordt de omwentelingscirculatie afwisselend sterker en zwakker. Een tweede kenmerk van deze interdecadale mode is, dat de stroming in oost-westrichting steeds eerder verandert dan de stroming in noord-zuidrichting. In hoofdstuk 3 wordt aan de hand van deze kenmerken een precieze verklaring gegeven van de mode. De periode wordt bepaald door de tijd die de gebieden met abnormaal warm of abnormaal koud water nodig hebben om de overkant van de oceaan te bereiken.

In hoofdstuk 4 wordt onder andere het effect van neerslag en verdamping aan het zeeoppervlak toegevoegd aan het model. De stromingen worden nu niet meer alleen door verschillen in temperatuur veroorzaakt, maar ook door verschillen in zoutgehalte, zodat er sprake is van een echte thermohaliene circulatie. De in hoofdstuk 3 beschreven interdecadale mode blijkt ook in dit geval te kunnen bestaan. Hoewel de periode is afgenomen tot ongeveer 30 jaar, is de fysische verklaring van de mode vrijwel hetzelfde als in de situatie zonder zoutverschillen. Dit geeft aan dat temperatuurverschillen voor deze mode veel belangrijker zijn dan verschillen in zoutgehalte. De snelheid waarmee de mode kan groeien of uitdempen, blijkt sterk af te hangen van de precieze locaties waar neerslag en verdamping optreden. Deze resultaten bieden mogelijk ook een verklaring voor de in een studie met een veel complexer model (Tziperman, 1997) gevonden relatie tussen de sterkte van interdecadale variabiliteit en het patroon van neerslag en verdamping.

Een tweede type interne mode, met een periode van zo'n 400 jaar, wordt beschreven in hoofdstuk 5. Kenmerkend voor deze mode zijn gebieden met abnormaal licht en zwaar water, die met de omwentelingscirculatie mee lijken te bewegen. Deze mode bestaat zowel in de context van stromingen die alleen door temperatuurverschillen veroorzaakt worden, als

voor thermohaliene stromingen en is als volgt te verklaren. Als het oppervlaktewater in het noorden (door een toevallige verstoring) kouder en dus zwaarder is dan normaal, dan zal dit water gemakkelijker zinken en zal de omwentelingscirculatie sneller gaan lopen. Echter, als gevolg van de de sterkere circulatie zal er nu ook meer warm oppervlaktewater naar het noorden getransporteerd worden. Enige tijd later zal het water in het noorden daardoor juist weer extra warm en dus lichter worden. Het extra koude water dat zich eerst in het noorden bevond, is ondertussen door de omwentelingscirculatie meegevoerd naar de diepzee en naar het zuiden. Nu treedt de omgekeerde serie gebeurtenissen op: de omwentelingscirculatie wordt zwakker, er is minder noordwaarts warmtetransport en het oppervlaktewater in het noorden wordt weer kouder. Dit staat in de literatuur bekend als een 'omwentelingsoscillatie'. In de hier gebruikte modelcontext dempt deze interne mode uit. Ook gedempte modi kunnen echter belangrijk zijn. Wanneer er namelijk voortdurend (kleine) verstoringen zijn, kan ook een gedempte oscillatie blijven bestaan. Dit is bijvoorbeeld ook het geval bij de schommel: hoewel de slingering van de schommel gedempt is, zal de schommel toch heen en weer blijven slingeren zolang er regelmatig een duwtje tegenaan gegeven wordt.

In hoofdstuk 6 worden de resultaten van een serie numerieke tijdsintegraties beschreven. Eerst wordt aangetoond, dat de in hoofdstuk 3 beschreven interne mode inderdaad interdecadale variabiliteit tot gevolg heeft. Vervolgens wordt het model in verscheidene stappen ingewikkelder gemaakt door, onder andere, continenten en een meer realistische vorm van de oceaanbodem toe te voegen. Hierdoor wordt de structuur van de interne variabiliteit complexer. Aan de hand van de eerder gedefinieerde kenmerken van de interdecadale mode, kan echter worden vastgesteld dat ook de variabiliteit in de meer realistische modelcontext door deze interdecadale mode wordt veroorzaakt.

Besluit

In het onderzoek dat beschreven is in dit proefschrift, is de interne variabiliteit van de thermohaliene oceaancirculatie in de Noord-Atlantische Oceaan bestudeerd met behulp van een combinatie van dynamische systeemanalyses en numerieke tijdsintegraties. De gevolgde aanpak biedt de mogelijkheid om op een systematische manier tot een overzicht te komen van interne oscillaties van de thermohaliene circulatie. Ook de meest realistische situatie die in dit proefschrift is bestudeerd, is nog steeds een vereenvoudigde weergave van de grootschalige oceaancirculatie. De resultaten in dit proefschrift geven dan ook alleen kwalitatieve informatie over de variabiliteit van de thermohaliene circulatie.

Naar alle waarschijnlijkheid zal de gemeten variabiliteit het gevolg zijn van een combinatie van processen. Wel kan echter de hypothese geopperd worden, dat de interdecadale mode die in dit proefschrift beschreven wordt, de tijdschaal bepaalt van de interdecadale variabiliteit in metingen en in simulaties met complexe modellen. Om een dergelijke hypothese te testen, is nog veel onderzoek nodig. De verwachting is, dat in de nabije toekomst ook de interne modi van de globale oceaancirculatie kunnen worden bepaald. Deze belangrijke stap is nodig voor het leggen van het verband tussen de resultaten in dit proefschrift en de gemeten (interdecadale) variabiliteit. Tevens zal uit een dergelijk vervolgonderzoek moeten blijken, of de gedempte 400-jaar mode een rol speelt in de interne variabiliteit van de thermohaliene circulatie op tijdschalen van enkele eeuwen.

Tenslotte heeft de benadering van interne variabiliteit van de thermohaliene circulatie via

de interne modi het begin opgeleverd van een kader, waarbinnen de resultaten van numerieke tijdsintegraties van vele andere studies geïnterpreteerd kunnen worden. Dit is essentieel voor het verkrijgen van een beter begrip van de interne variabiliteit van de thermohaliene circulatie en van groot belang voor het onderzoek naar eventuele toekomstige klimaatveranderingen.

Dankwoord

Met veel plezier heb ik gewerkt aan mijn promotieonderzoek, waarvan dit proefschrift het resultaat is. Ik had dit onderzoek niet kunnen doen zonder de directe en indirecte bijdragen van velen. Ik wil graag van de gelegenheid gebruik maken om hen te bedanken.

Allereerst wil ik mijn beide promotoren, Henk Dijkstra en Will de Ruijter, bedanken. Henk was als directe begeleider nauw betrokken bij mijn onderzoek. Zijn aanstekelijke enthousiasme werkte altijd bijzonder motiverend. Ook heb ik veel geleerd van zijn fysisch inzicht, zijn grenzeloze optimisme en zijn gevoel voor de grote lijn. Will de Ruijter was meestal wat meer op de achtergrond aanwezig, maar wel altijd geïnteresseerd in de resultaten van het onderzoek. Zijn heldere en constructieve commentaar op mijn proefschrift heb ik erg gewaardeerd.

Het was erg leuk om de afgelopen vier jaar mijn kamer op het IMAU te kunnen delen met Janine Nauw. Veel, heel veel extra theepauzes hebben we gehouden, maar minstens zo vaak bespraken we samen onze nieuwste resultaten of probeerden we een 'basic oceanography'-probleem te begrijpen. En dankzij Janine's karakteristieke uitspraken viel er altijd veel te lachen (wat niet onopgemerkt bleef). Janine, heel erg bedankt voor alle theepauzes, de wetenschappelijke en niet-wetenschappelijke gesprekken, maar bovenal voor je humor en je vriendschap.

De samenwerking met Jeroen Gerrits tijdens het laatste halfjaar was niet alleen één van de leukste gedeeltes van het onderzoek, maar leidde ook in korte tijd tot een hoofdstuk van dit proefschrift en een artikel. Jeroen deed niet alleen (overdag, 's avonds en in het weekend) de simulaties die nodig waren, maar maakte ook het grootste deel van de figuren van ons gezamenlijke werk, die hij bovendien telkens geduldig opnieuw maakte als ik weer eens van gedachten veranderde. Jeroen, bedankt voor de prettige samenwerking en het vele werk dat je gedaan hebt.

Ik wil ook graag alle andere collega's op het IMAU bedanken voor het scheppen van een stimulerende, maar ook ontspannen werksfeer. Discussies met Wilbert Weijer waren zonder uitzondering leuk en verhelderend. Hakan Öksüzŏglu verleende veel hulp bij de visualisatie van de modeldata. Caroline Katsman, Maurice Schmeits en Ernst van der Avoird droegen bij aan een fijne sfeer in onze groep. I have enjoyed scientific and non-scientific discussions with Nathalie Rittemard. Marcel Portanger en Henk Mos boden uitkomst bij talloze computerproblemen. Ook bedank ik het secretariaat, in het bijzonder Yvonne Wouda en Ellen Berger-Okkels, voor hun ondersteuning.

I thank the staff of the Geophysical Fluid Dynamics Summer Program of the Woods Hole Oceanographic Institution (Woods Hole, U.S.A.) for giving me the opportunity to participate

in their program. I thank my ‘fellow fellows’ Fiona, Ed, Helén, Shreyas, Matt, Taka and Chiara for their friendship and support during this enjoyable summer.

Naast alle werkzaamheden was er ook ruimschoots tijd voor ontspanning. Johan, Sonja, Jeroen, Janine en Roland, bedankt voor jullie vriendschap en voor de gezellige ‘Catan’-avonden. De steeds wisselende leden van het ‘IMAU-zwemclubje’ droegen bij aan de sportieve ontspanning. Sonja verdient in dit verband een bijzondere vermelding, voor de ontelbare malen dat ze mij achter mijn computer vandaan plukte om tussen de middag te gaan zwemmen. Marian, Yvonne, Thierry, Ellen, Jojanneke, Freek, Karen, Astrid en Arja bedank ik voor hun interesse in waar ik mee bezig was en voor de jarenlange vriendschap.

Mijn ouders en mijn broer lazen zorgvuldig de Nederlandse samenvatting, die door hun suggesties sterk verbeterd is. Hun bijdrage aan dit proefschrift omvat echter zoveel meer dan dat. Ik bedank hen voor het vertrouwen dat ze altijd in me hebben gehad en voor hun voortdurende steun en liefde. Pappa, mamma en Robbert Jan, daarmee hebben jullie de basis gelegd voor dit proefschrift. Dank jullie wel!

Curriculum Vitae

Ik ben geboren op 26 juni 1975 in Eindhoven. In 1993 behaalde ik mijn VWO-diploma aan het Eckartcollege te Eindhoven. Aansluitend ben ik natuurkunde gaan studeren aan de Universiteit Utrecht. Na het behalen van de propedeuse in 1994 koos ik voor de bovenbouwstudie Meteorologie en Fysische Oceanografie aan dezelfde universiteit. Het doctoraaldiploma behaalde ik cum laude in 1998. Van oktober 1998 tot december 2002 heb ik als onderzoeker in opleiding bij het Instituut voor Marien en Atmosferisch onderzoek Utrecht (IMAU), onderdeel van de Universiteit Utrecht, aan mijn promotieonderzoek gewerkt. De belangrijkste resultaten van dat onderzoek staan beschreven in dit proefschrift. De maanden juni tot en met augustus 2001 heb ik doorgebracht aan het Woods Hole Oceanographic Institution (Woods Hole, U.S.A.), dankzij een Geophysical Fluid Dynamics Fellowship van dat instituut. Sinds januari 2003 heb ik een aanstelling als post-doc onderzoeker bij het IMAU.

Publications

Te Raa, L. A. and Dijkstra, H. A. Instability of the thermohaline ocean circulation on inter-decadal time scales, *J. Phys. Oceanography*, vol **32**, pp. 138-160, 2002.

Te Raa, L. A. and Dijkstra, H. A. Sensitivity of North-Atlantic multidecadal variability to freshwater-flux forcing, accepted for publication in *J. Climate.*

Te Raa, L. A. and Dijkstra, H. A. Modes of internal thermohaline variability in a single-hemispheric ocean basin, submitted to *J. Mar. Res.*

Te Raa, L. A., Gerrits, J. and Dijkstra, H. A. Identification of the mechanism of inter-decadal variability in the North-Atlantic Ocean, submitted to *J. Phys. Oceanography.*